

Surface Properties of Graphite for Efficient Electrocatalysis of Vanadium Redox Reactions

Zur Erlangung des akademischen Grades eines
DOKTORS DER INGENIEURWISSENSCHAFTEN (Dr.-Ing.)

von der KIT-Fakultät für Maschinenbau des
Karlsruher Instituts für Technologie (KIT)
angenommene

DISSERTATION

von

M. Sc. Hannes Radinger

Tag der mündlichen Prüfung	14.06.2022
Hauptreferent	Prof. Dr. rer. nat. Michael J. Hoffmann
Korreferent/Korreferentin	Prof. Dr. rer. nat. Helmut Ehrenberg Prof. Dr.-Ing. Christina Roth

“Without deviation from the norm, progress is not possible.”
— Frank Zappa

Acknowledgements

My first heartfelt thanks go to my committed dissertation advisors. I owe the supervision and general help in all life and career issues to Prof. Helmut Ehrenberg. The freedom in research that I have enjoyed at the Institute of Applied Materials is probably not to be found anywhere else. Thanks also go to Prof. Michael Hoffmann, who took on the technical role of my PhD supervisor. I would like to thank Prof. Christina Roth from the University of Bayreuth for creating a welcoming atmosphere at all virtual project meetings, for supporting this work as an examiner and assisting in the postdoctoral application processes.

It is equally important to thank my group leader, Dr. Frieder Scheiba, who has provided a friendly and supportive relationship over the past three years. He has perfectly struck the right balance between thematic guidance and freedom of research. It is because of his perfectionist personality that not only research papers in which results are dryly presented have been produced, but literary works of sophisticated communication. For the friendly collaborations and discussions, I thank my carbon group members Marina Bauer, Jessica Pfisterer, Bijian Deng, and Philip Richter.

For all the preliminary work, additional experiments, and creative ideas, I acknowledge several students (in chronological order of appearance): Marius Ast (measurements presented in Figure 7-2), Manuel Moser, Mattes Renner, Adrian Lindner, Linfeng Miao, and Felix Bauer (several measurements in Chapter 10). Many experiments could not have been performed without the expertise of more experienced graduate students. Therefore, I would like to thank Mark Hartmann from Martin Luther University Halle-Wittenberg for performing the polarization curves in Figure 7-6 and Sören Dreyer from the Institute of Nanotechnology for the DEMS measurements in Figure 6-3. Further thanks go to PD Dr. Bernhard Kaiser from the Technical University of Darmstadt for his supervision during the publication process of my master thesis. His patience and helpfulness will remain in my best memory.

The research presented in Chapter 9 would not have been possible without the significant support of Prof. Heine A. Hansen of the Technical University of Denmark. His willingness to host an experimentalist who imagined he could learn density functional theory calculations and produce presentable results within three months was encouraging. Many thanks to all the nice and smart people I had the pleasure to meet in and around Copenhagen.

I gratefully acknowledge financial support for this research from the German Federal Ministry of Education and Research (BMBF) as part of the Flow3DKat project under grant number 03EK3053C. Thanks to the Karlsruhe House of Young Scientists (KHYS) and Andreas Hahmann for financial support under the Networking Grant to perform a trip to the Netherlands, which he secured over a long period because of the harsh travel restrictions. I thank the Center for Electrochemical Energy Storage (CELEST) and the Graduate School Electrochemical Energy Storage (GS-EES) for financial support during my research stay in Denmark.

Udo Geckle's technical assistance with the SEM and in performing several sputter depositions is highly credited. Thanks to Vanessa Trouillet for guidance concerning photoelectron spectroscopy. Liuda Mereacre always knew where to find even the smallest equipment. Luis Sanchez was my white knight when I desperately needed a replacement for my dying laptop. A very important thank you goes in the direction of Almut Kriese, whose organizational talent is probably unsurpassed anywhere in the world.

Thank you, Aliena, for giving me all the love and warmth I desperately needed from time to time. Thank you for being patient, lovely, smart, and funny.

Abstract

The results of this work contribute to a deeper understanding of the kinetic processes in vanadium flow batteries. For this purpose, the electrocatalytic and physicochemical properties of industrially relevant graphite felt and related carbon-based materials were investigated. The use of several spectroscopic and microscopic methods allowed the mapping of the microstructure at different scales, the chemical composition, the electronic structure and finally the sorption and charge transfer processes by means of theoretical calculations and spectro-electrochemical investigations.

Due to contradictory results in the literature regarding oxygen functional groups, this work aimed to establish clear relationships between surface structure and electrocatalysis. The analysis of chemically and structurally modified electrodes before and after electrochemical tests led to the identification of graphitic defects as active centers. After complete removal of oxygen, hydrogen terminated defects instead of surface groups were found to be the cause of catalytic activity. The attachment of pyrenes with different functionalities on the graphite surface served to demonstrate the effects of individual oxygen groups.

To specify the effect of the different defect geometries, carbon atoms were substituted by phosphorus in model and real electrodes through thermochemical activation. The electrochemical performance was significantly increased by carefully considering all the electrode properties changed in the process. The investigation of the electronic structure of polycyclic aromatic hydrocarbons linked the electrocatalytic activity to the electrode architecture and the work function. Theoretical modeling defined interactions between the solvated vanadium ions and the substrates across various hydrogen- and oxygen-terminated edges. Finally, the thesis formulates an experimentally and computationally supported innovative reaction mechanism by studying the electrode-electrolyte interface at an applied potential.

Zusammenfassung

Die Ergebnisse dieser Arbeit tragen zu einem tieferen Verständnis der kinetischen Prozesse in Vanadium-Redox-Flow-Batterien bei. Dafür wurden die elektrokatalytischen und physikochemischen Eigenschaften von industriell relevantem Graphitfilz und verwandten kohlenstoffbasierten Materialien untersucht. Der Einsatz von mehreren spektroskopischen und mikroskopischen Methoden ermöglichte die Abbildung verschiedener Skalen der Mikrostruktur, die chemische Zusammensetzung, die elektronische Struktur und schließlich die kinetischen Vorgänge mittels theoretischen Berechnungen und spektro-elektrochemischen Untersuchungen.

Aufgrund widersprüchlicher Ergebnisse in der Literatur im Themenkomplex funktionelle Sauerstoffgruppen hat sich die Arbeit zum Ziel gesetzt, eindeutige Zusammenhänge zwischen Oberflächenstruktur und Elektrokatalyse herzustellen. Die Analyse von Eigenschaften chemisch und strukturell modifizierter Elektroden vor und nach elektrochemischen Tests führte zur Identifizierung graphitischer Defekte als aktive Zentren. Nach der vollständigen Entfernung von Sauerstoff ergaben sich wasserstoffterminierte Defekte anstelle von Oberflächengruppen als Ursache für die katalytische Aktivität. Die Anbringung von Pyrenen mit unterschiedlichen Funktionalitäten auf der Graphitoberfläche diente zum Nachweis der Effekte einzelner Sauerstoffgruppen.

Um die Auswirkung der verschiedenen Defekt-Geometrien zu spezifizieren, wurden durch thermochemische Aktivierungen Kohlenstoffatome in Modell- und realen Elektroden durch Phosphor substituiert. Unter gezielter Berücksichtigung aller dabei veränderten Elektrodeneigenschaften konnte so die elektrochemische Aktivität deutlich gesteigert werden. Die Untersuchung der elektronischen Struktur von polyzyklischen aromatischen Kohlenwasserstoffen verband die elektrokatalytische Aktivität mit der Elektrodenarchitektur und der Austrittsarbeit. Theoretische Modellierungen definierten Wechselwirkungen zwischen den solvatisierten Vanadium-Ionen und der Substrate durch verschiedene wasserstoff- und sauerstoffterminierte Kanten. Schließlich formuliert die Arbeit durch die Untersuchung der Elektrode-Elektrolyt-Grenzfläche bei angelegtem Potential einen experimentell und rechnerisch gestützten, innovativen Reaktionsmechanismus.

Table of Contents

Acknowledgements	i
Abstract	iii
Zusammenfassung	v
Table of Contents	vii
1 Guiding Principles	1
1.1 Role of Flow Batteries	1
1.2 Working Principle of Flow Batteries	2
1.3 Graphite Electrodes for Vanadium Flow Batteries	4
1.4 Surface Properties of Graphite.....	6
1.5 Analysis of the Structural and Electrochemical Properties.....	8
1.6 Outline of this Thesis	9
2 Review of Electrode Activation Treatments	11
2.1 Thermal Activation.....	11
2.2 Chemical and Thermo-Chemical Activation.....	14
2.3 Electrochemical Activation	15
2.4 Plasma/Radiation Activation.....	17
2.5 Perspective.....	18
3 Experimental Methods	21
3.1 Electrochemistry	22
3.2 Microstructure	25
3.3 Electronic Structure	28
3.4 Electrical Conductivity.....	29
3.5 Density Functional Theory.....	30
4 Influence and Electrochemical Stability of Oxygen Groups and Edge Sites	33
4.1 Preparation and Characterization of MWCNT Dispersions	33
4.2 Morphological and Structural Characterization.....	34
4.3 Surface Chemistry.....	37
4.4 Electrical Conductivity.....	38
4.5 Electrocatalytic Half-Cell Activity	39
4.6 Evolution of OFGs and Defects in Electrochemistry	42
4.7 Conclusions.....	45
5 Origin of the Electrocatalytic Activity at Graphite	47
5.1 Influence of the Deoxygenation on the Electronic Structure.....	48
5.2 Microstructural Properties	50

5.3	Influence of OFGs on the Electrochemical Half-Cell Performance	52
5.4	Chemical and Structural Changes During Electrochemistry	55
5.5	Long-Term Half-Cell Cycling	57
5.6	New Scheme for the Vanadium Redox Reactions	59
5.7	Conclusions	60
6	Pyrene-Modified Graphite Felts as Model Electrodes	63
6.1	Improving the Attachment of Pyrenes to GF	64
6.2	Electrochemical Stability of Modified GF	66
6.3	Electrocatalytic Activity of Pyrene-Modified GF	68
6.4	Chemical and Structural Changes by the Modification	70
6.5	Conclusions	72
7	Understanding Efficient Phosphorus-Functionalization of Graphite	73
7.1	Graphene Powder Attached to GF	74
7.2	Electrocatalytic Activity of Doped Graphene	75
7.3	Physicochemical Characterization of Doped Graphene	77
7.4	Directly Phosphorus-Functionalized GF	79
7.5	Conclusions	83
8	The Work Function Describes the Electrocatalytic Activity of Graphite	85
8.1	Electrocatalytic and Microstructural Properties of GF	85
8.2	Electronic Structure of GF	87
8.3	HOPG as Model System	90
8.4	Influence of Edge Geometry	90
8.5	Conclusions	93
9	Structural and Electronic Properties of Vanadium Complexes at Graphite Electrodes	95
9.1	Structure of Solvated Vanadium Ions and Graphene Nanoribbons	95
9.2	Adsorption Properties of Vanadium Complexes at Graphite	97
9.3	Electron Transfer Described by the Density of States	101
9.4	Desorption of $[V^VO_2(H_2O)_4]^+$	104
9.5	Conclusions	106
10	Vanadyl Oxidation Elucidated by <i>Operando</i> Raman Spectroscopy	107
10.1	Raman Spectra of Electrolyte and Electrodes	107
10.2	Electrocatalytic Activity of the Substrates	110
10.3	<i>Operando</i> Raman Spectra	111
10.4	Conclusions	117
11	Concluding Remarks	119
11.1	Summary and Final Conclusions	119
11.2	Outlook on Future Research Possibilities	122
References	125

List of Abbreviations	139
List of Symbols.....	141
Appendix A: Experimental Details	143
Sample Preparation	143
Analytical Methods.....	145
Appendix B: Supporting Information.....	151
Appendix C: List of Publications and Presentations.....	185

1 Guiding Principles

1.1 Role of Flow Batteries

The flow battery is a relatively new type of electrochemical energy storage system compared to other technologies, and its various forms are becoming increasingly popular in research and development right now. Flow batteries can be described as a form of rechargeable fuel cells, in which energy is stored *via* electroactive species dissolved in a solution. There is a wide variety of technologies and chemistries available for their design, ranging from inorganic full-flow (vanadium^[1], iron–chromium^[2]), inorganic semi-flow (zinc–cerium^[3], lead–acid^[4]), to aqueous^[5] as well as aprotic^[6] organic electrolytes. Assuming it takes about 20 years for a technology to penetrate the market, the biggest time for flow batteries is probably yet to come; this also means that there is a race in development between different electrolyte chemistries. For comparison, 2019 Nobel Prize in Chemistry winners Goodenough, Whittingham and Yoshino conducted the most significant part of their research on lithium-ion batteries in the 1970s to 1980s.^[7–9] Commercialization of the lithium-ion battery followed in 1991 in small-scale devices, and the first electric vehicle saw the light of day in 2010. While there are approaches to potential vanadium-based flow batteries (VFBs) dating back to the 1930s and 1970s, successful demonstration took Maria Skyllas-Kazacos and colleagues until the late 1980s to implement a technology not far away from that used today.^[1,10–12] It is therefore unclear what can be considered the biggest obstacle to commercialization so far, but several points could be responsible: the high system costs, which only lead to profit with >20,000 charging and discharging cycles, the lack of a globally known and charismatic figurehead of the caliber of Elon Musk, or perhaps the nonexistent acceptance towards further complex energy storage systems to complement the market offering by the population.

While some newspapers try to promote a contest of supply not only between fossil fuels and the electrification of large parts of civilization—which requires green power from renewable resources such as wind energy, solar radiation or hydro power—but also between modern storage systems themselves, researchers around the world must refrain from considering one technology in competition with another. Rather the complementary capabilities of multiple systems that rely on a variety of materials and provide energy on demand at widely different scales should be emphasized. If all available lithium is on the road, other technologies, whose upscaling is also a lot easier and tremendously less dangerous, should be considered for

stationary energy storage. Salt water batteries can be installed near the coast to store offshore wind and tidal energy,^[13] fuel cell technologies can be tailored for multiple purposes and scales to reach places not well-connected to the grid,^[14] while aqueous flow batteries will be located near settlements and residents to benefit from energy generated by their own photovoltaic systems and the wind turbines next door.

Especially when considering the capacity required to power an electrical society, it is crucial to have as many complementary technologies as possible. To illustrate the orders of magnitude: the capacity necessary to power electric vehicles is about 10,000 times greater than that required for personal battery devices. Meaningful storage systems for our electric grid then still require up to 10,000 times the capacity of a battery powered vehicle.^[15] Flow batteries have the potential to close an existing gap for large-scale storage with their arbitrarily scalable energy density. To understand what this means and what makes the flow battery so unique, the next chapter explains how it works.

1.2 Working Principle of Flow Batteries

In comparison to many other energy storage systems, the installment of a flow battery is more complex because of the plenty components and the interplay of many engineering aspects. In this thesis, the VFB, one of the few commercialized technologies^[16], has been the subject of investigation. Its general working principle and the most relevant cell parts are displayed in **Figure 1-1a**. The heart of each system is the symmetric power cell, whose two half-cells are divided by a proton exchange membrane, which guarantees charge separation between the two vanadium-based electrolytes. Each half-cell comprises two important components: (i) the porous electrode, which acts as an electrocatalyst to reduce or oxidize the dissolved vanadium ions with as little energy input as possible; (ii) the bipolar plate, which separates the single cells in a stack and connects the electrode to the current collector. Both must withstand the harsh environments of the acidic electrolyte and the continuous exchange of electrons. The resulting requirements are manifold, as the corrosion resistance and electrical conductivity should be high. Therefore, the manufacturing material for electrode and bipolar plate is most commonly graphite-based. For the bipolar plate, a polymeric binder is usually added to guarantee a dense and robust cell part which is not brittle and does not allow leakage.

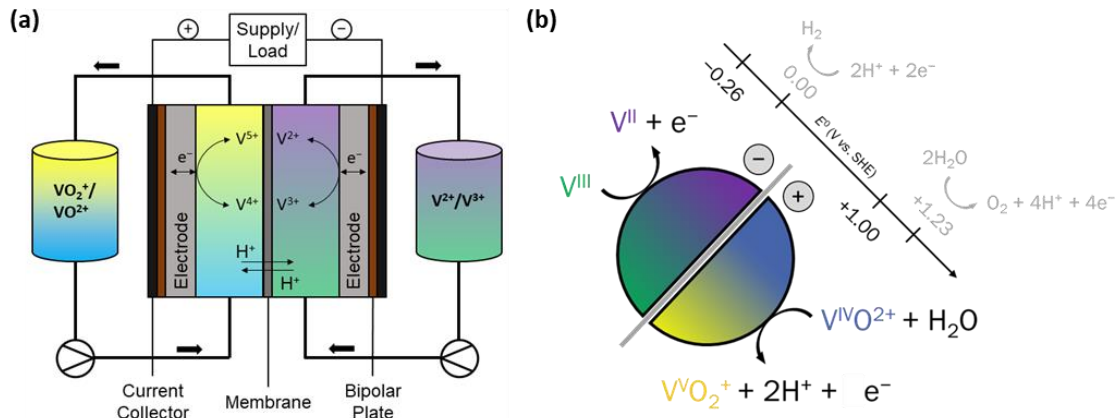
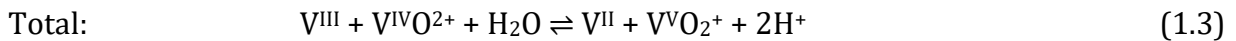
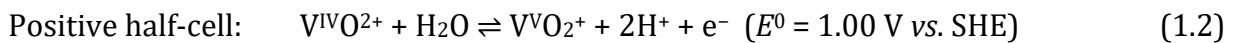
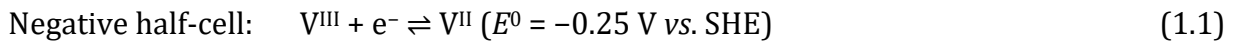


Figure 1-1. Working principle of a VFB. **(a)** Schematic depiction, indicating the most relevant cell parts. **(b)** Redox reactions undergoing at the surface of the electrode in comparison to the electrolyte stability window.

The concept of the VFB is based on the use of four oxidation states of vanadium ions— V^{II} , V^{III} , $V^{IV}O_2^+$ and $V^{VO}_2^+$ —which are present as electrochemically active species dissolved in an aqueous solution, the electrolyte. Usually, it comprises 2 to 3 M sulfuric acid with 1.5 to 2 M solvated vanadium ions. In the tank reservoir for the negative half-cell, V^{III}/V^{II} species can be found, whereas for the positive half-cell a $V^{VO}_2^+/V^{IV}O_2^+$ redox couple is used (**Figure 1b**). During the operation of the battery, the following reactions take place:



To charge the battery, electrons provided by the oxidation of $V^{IV}O_2^+$ are transferred through an external circuit from the positive to the negative half-cell and can thus reduce V^{III} . In a fully charged battery, only V^{II} and $V^{VO}_2^+$ are present in the electrolyte reservoirs. To equalize the charge imbalance, protons diffuse through the membrane to the negative side. The same reactions take place in reverse when discharging. The power density of a VFB depends on the electrode area, while the capacity of the system is determined by the amount of electrolyte, *i.e.*, the number of vanadium ions available. In this way, both can be scaled independently and adjusted according to the surrounding and its requirements. The comparably low energy density is limited by the low solubility of highly oxidized vanadium and lies around 20 to 35 Wh kg^{-1} . The temperature of the system must be monitored to prevent the precipitation of $V^{VO}_2^+$ to V_2O_5 . Since power electronics are required to operate the battery besides tanks, pipes and pumps, the energy efficiency of the overall system makes up 70 to 80%. In comparison, commercial lithium ion batteries reach up to 200 Wh kg^{-1} while offering an efficiency over 90%.^[17] Since

VFBs are usually operated with an aqueous electrolyte, the potential window is limited by its side reactions, as depicted in **Figure 1b**. At higher potentials than 1.2 V vs. SHE, carbon corrosion under the formation of CO and CO₂ at the electrode and the oxidation of water to O₂ must be considered in the positive half-cell. Below a potential of -0.3 V vs. SHE on the other side, hydrogen evolution is a limiting factor. The VFB should furthermore be operated in the absence of oxygen because V^{II} oxidizes immediately and V^{III} slowly, resulting in efficiency losses. Contamination due to the migration of vanadium ions across the membrane, which are then correspondingly oxidized or reduced in the other half-cell, also leads to capacity fading.

1.3 Graphite Electrodes for Vanadium Flow Batteries

The efficiency of the electrochemical cell is heavily defined by the electrocatalytic properties of the electrode. To meet the above-mentioned requirements, such as redox activity, acidic stability, and low selectivity towards the parasitic side reactions, the most commonly used electrode material in VFBs is graphite. Carbonaceous electrodes are becoming increasingly popular for electrochemical energy storage and conversion devices such as batteries, supercapacitors and fuel cells.^[18-20] Especially graphite scores with its low cost, abundance and high electrical conductivity. For VFBs, a few millimeter-thick graphite felt (GF) is used for the flow through configuration, in which electrolyte is continuously pumped through the electrode. Because of its porosity of up to 90%, a high surface area is available to facilitate the vanadium redox reactions. To produce GF, polyacrylonitrile (PAN) is usually blended with co-monomers such as methyl acrylate for production and fabricated either by wet spinning or melt spinning. The product is oxidatively stabilized in air at 210 to 300 °C to allow ring closure of the nitrile groups. The fibers are then carbonized under inert gas at a temperature of 1100 °C, which leads to a controlled decomposition of the material to products such as H₂, CH₄, CO, and NH₃. During the heating procedure, turbostratic carbon is formed, whose disorder in the z-direction decreases with higher temperature until the fibers are graphitized above 2500 °C.

In graphitic materials, the surface structure determines the electrocatalytic activity and thus the efficiency of conversion from electrical to chemical energy and *vice versa*. To understand the structure and thus the properties of GF, we start with the fundamental building block of graphite, finite single-layer graphene (**Figure 1-2a**). It comprises two atoms per unit cell (A, B) forming a network of hexagonal *sp*² hybridized carbon rings.^[21] Only three electrons are required to form a covalent bond, resulting in the formation of a π-conjugated system. At its edges, graphene either has A and B as neighbors in an armchair configuration, or it exposes

one of the atoms in a zigzag formation.^[22] The primitive cell in reciprocal space (**Figure 1-2b,c**) shows the high symmetry points Γ in the center, M in the middle of the sides, and K and K' at the edges. The electronic structure can be described by two π -states (π , π^*) each belonging to a sublattice formed by A and B, respectively. These cone-shaped bands touch at the edges, defining the Fermi level (E_F) and making graphene a semiconductor with zero bandgap (**Figure 1-2d**). Stacking multiple layers in z-direction widens the cone and increases the overlap area of the bonding and anti-bonding states (**Figure 1-2e**).^[23] However, most of the charge carriers are located within a small energy gap from E_F , the cutoff of their highest occupied molecular orbital being described as the valence band maximum (E_{VBM}).

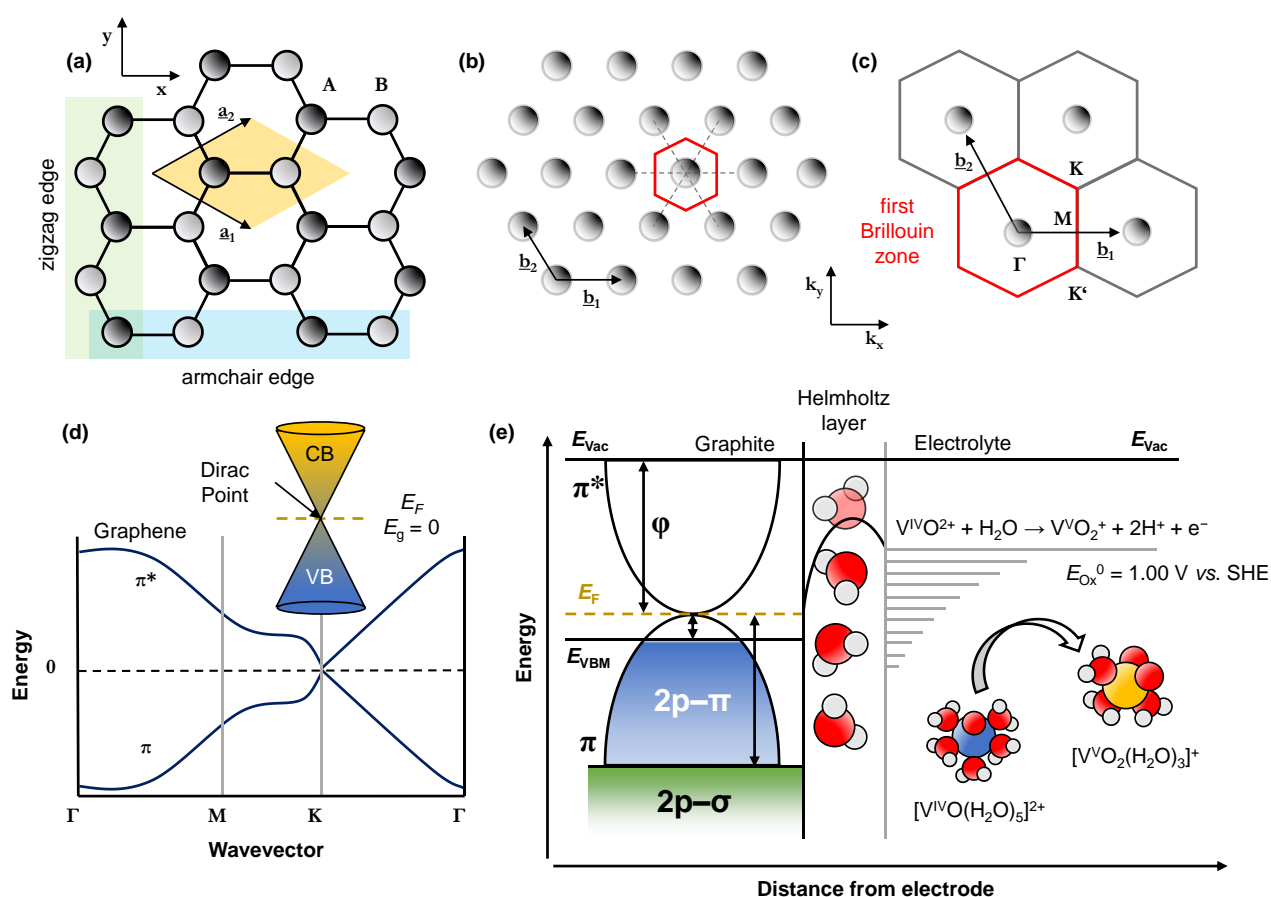


Figure 1-2. The structure of graphite-based material. **(a)** Top view of a monolayer graphene in the real space, showing the two inequivalent atoms A and B, the vectors a_1 and a_2 spanning the unit cell, and the two possible carbon edge site configurations. **(b,c)** The reciprocal space unit cell with the first Brillouin zone (red hexagon), revealing the high-symmetry points: the Γ point within the center, the M point in the middle of a hexagonal side, and the K and K' point at its corners. **(d)** Schematic band structure of graphene, showing the symmetric dispersion of the π and π^* bands. **(e)** Schematic depiction of the graphite–electrolyte interface.

The important properties of the electronic structure for electrochemical processes shall be illustrated by describing the interface between graphite and vanadium-containing electrolyte (**Figure 1-2e**). At the surface of an immersed electrode, the so-called electrical double layer

forms.^[24] While E_F would theoretically match the equilibrium redox state of the solution, the arrangement of molecules and ions in the double layer as well as the alignment of the vacuum level (E_{Vac}) create a potential barrier, which must be overcome for successful charge transfer. The total number of electron donor or acceptor levels of the electrolyte, which are accessible to graphite (horizontal gray lines in **Figure 1-2e**), could thus be increased by shifting E_F upwards, which is in theory achieved by doping^[25,26], or by decreasing the work function ($\Phi = E_{Vac} - E_F$) which is debated based on the electrode material and the reaction under consideration.^[27-31]

Since GF consists mostly of sp^2 hybridized basal planes at the surface which possess low charge transfer kinetics, their reactivity must be tailored by a prior activation treatment, which damages the material.^[32,33] The integration of surface defects such as edge sites has been shown to be a reliable way to improve its activity towards the vanadium redox couples.^[34-36] Chemical stability and electrical conductivity of the material are preserved, while ions in the electrolyte find reaction sites with lower adsorption barriers.^[37,38] For graphite, the edge orientation (**Figure 1-2a**) can play a role for its catalytic and electronic properties.^[39,40] Due to the complicated interactions between morphology, surface chemistry, micro- and electronic structure, conclusions in the literature diverge, making it difficult to find common activity descriptors.^[41] Complexity increases as one moves from model systems such as graphene or highly ordered pyrolytic graphite (HOPG) to heterogeneous, three-dimensional GF. However, a thorough understanding of these real electrodes is necessary to advance the development of systems that rely on their use. The influence of the surface structure and chemistry for graphite-based material on the electronic structure must be investigated to understand the activity-determining factor for the charge transfer across the interface.

1.4 Surface Properties of Graphite

For many electrochemical devices that use carbon-based materials such as electrolyzers, supercapacitors, and batteries, oxygen functional groups (OFGs, **Figure 1-3a**) are essential to facilitate electron transfer.^[40,42-45] Nearly 30 years ago, a few years after the first successful demonstration of a VFB, a reaction mechanism based on hydroxyl groups was postulated.^[10,12,33] The research afterwards stagnated until the late 2000s, when the number of publications for (vanadium) flow batteries climbed exemplarily in a short time (Figure S1). It is thus more remarkable that the original proposed reaction mechanism *via* OFGs is still regularly cited and reproduced in literature up to this year.^[46-49] A lot of scientific and industrial activity

regarding VFBS focuses on improving GF by introducing OFGs through oxidative treatments.^[32,50–57] The later observed performance enhancement is then ascribed to an elevated quantity of surface oxygen.^[45,58] However, there are contradictory results about the specific type of OFG, which should be responsible for the increased activity.^[48,52,55,58,59] Only a few research groups express serious doubt and discuss that especially the $V^{VO_2^+}/V^{IV}O^{2+}$ reduction is obstructed by OFGs.^[60–63] Both half-cell reactions should be investigated separately, since positive and negative electrodes respond differently to the surface oxygen concentration, which can mislead in symmetric full cell characterizations.^[64–66]

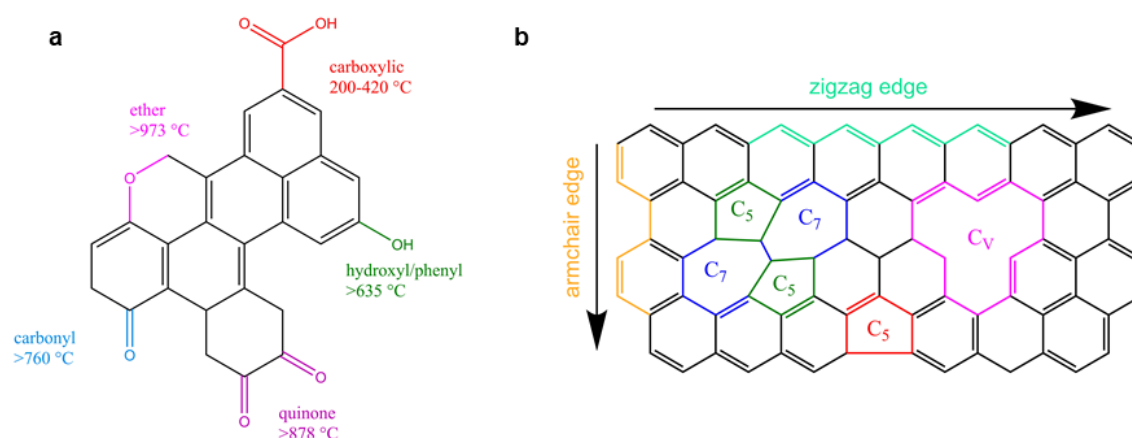


Figure 1-3. Schematic representation of the graphite structure. **(a)** Selection of graphitic oxygen functional groups that can be distinguished with XPS, and their respective decomposition temperature under inert gas. **(b)** Defective graphite cluster displaying a Stone–Wales defect (C₅–C₇), a single vacancy (C_v), a disturbed ring at the edge (C₅), and two types of edge sites (armchair and zigzag).

A further complicating factor is that most of the oxidative procedures use harsh environments that as well damage the surface of the material and create defects such as edge sites and vacancies (**Figure 1-3b**). Edge sites provide faster electron transfer kinetics for redox reactions, which was also demonstrated specifically for the vanadium chemistry.^[34,67,68] Theoretical calculations have concluded that the graphitic basal plane is basically inactive and only edge sites, which form carbonyl groups because of dissociated water, serve as active sites.^[69,70] Also in experimental work, the activity in both half-cells has so far been associated with oxidized edge sites.^[68,71] However, in the evaluation of electrocatalysts, often only the properties before electrochemistry are inspected, therefore neglecting the change in surface chemistry and microstructure induced by the electrolyte and the electric potential. It remains to be showed whether predictions on the activity can be made based alone on physicochemical characterizations after preparing an electrode. Based on multiple investigations after electrochemical testing, more

conclusions on the correlation between surface properties and catalytic activity might be drawn.

1.5 Analysis of the Structural and Electrochemical Properties

In **Figure 1-4**, the topmost surface layer of a graphitized GF is divided into three different classes according to the preparation procedure and can either preserve a graphene, a graphene-oxide, or a reduced graphene oxide-like structure. The electrode shown in **Figure 1-4a** comprises an intact sp^2 hybridized basal plane with a π -conjugated system and lacks contamination and functional groups. The structure of carbon-based materials is regularly studied by Raman spectroscopy, in which the intensity ratio of the defect-induced D and graphitic G band is used to quantify and qualify disorder.^[72,73]

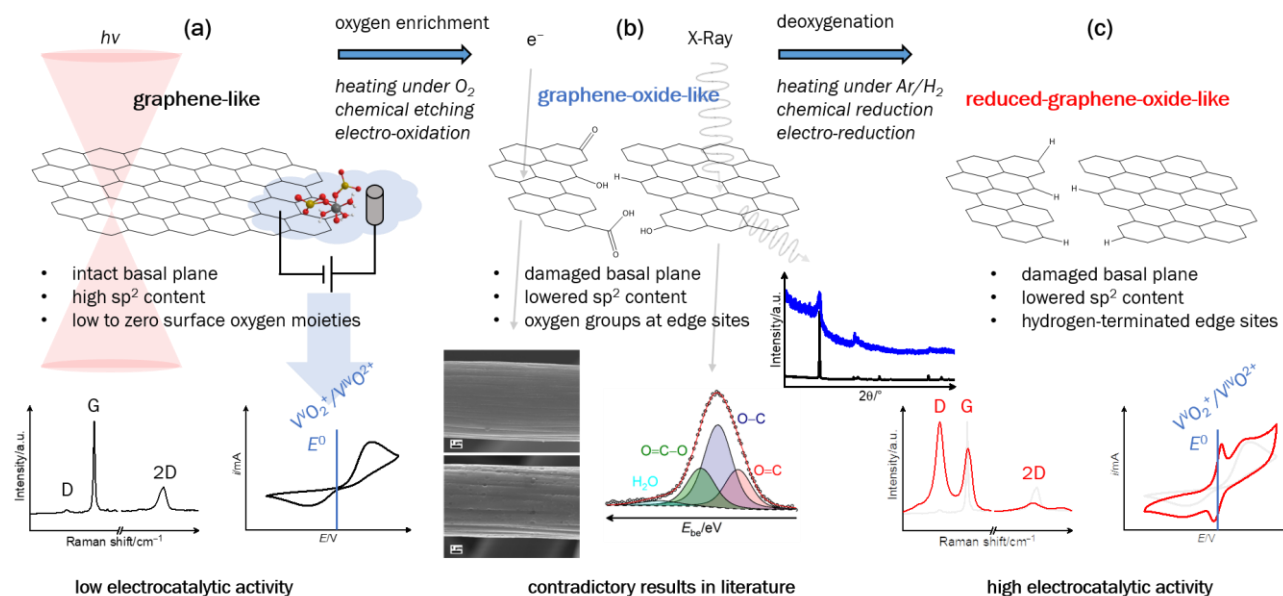


Figure 1-4. Illustration of three fundamental graphitic surface structures commonly used to describe electrocatalysis in vanadium flow batteries, and typical characterization tools used for their analysis. **(a)** Graphene-like electrodes characterized by Raman spectroscopy and positive half-cell CV. **(b)** Graphene oxide-like electrodes imaged by SEM and investigated by XPS. **(c)** Reduced graphene oxide-like electrodes studied by XRD, Raman spectroscopy and positive half-cell CV.

The catalytic activity of an electrode is studied in a three-electrode half-cell comprising the electrolyte with vanadium-containing species, *e.g.*, $V^{IV}O_2^+$ for the positive or V^{III} for the negative half-cell. An electrode is considered active when reversible cyclic voltammetry (CV) curves close to the thermodynamic standard potential E^0 can be obtained. For graphene, the overpotential is high since the basal plane is electrochemically inert for vanadium.^[34,71] Oxidative treatments such as thermal, chemical, or electrochemical activation introduce OFGs, classifying

the subsequently obtained surface as graphene oxide-like material (**Figure 1-4b**), which reveals a damaged surface with a decreased sp^2 content. The presence of OFGs as hydroxyl, carbonyl, and carboxyl moieties can be investigated by photoelectron or IR spectroscopy. Oxidative activation furthermore creates pores and corrosion-like pits on the otherwise smooth pristine GF, as it can be observed by electron microscopy. If the damaging exceeds the mechanical tolerance of the material, its structural properties change and the long-range order is lost, resulting in an amorphous material with low electrical conductivity.^[74] This material failure cannot be studied by surface sensitive methods, but requires bulk techniques such as X-ray diffraction (XRD). A deoxygenated electrode has a reduced graphene oxide-like structure with hydrogen-terminated edges (**Figure 1-4c**). The material surface is damaged by the ripping of carbon–oxygen moieties and reveals a more intense D to G ratio. In the displayed CV curves, a higher catalytic activity can be observed by a $V^{VO_2^+}/V^{VO^{2+}}$ redox peak, which lies at lower potentials compared to graphene and originates from the more active edge sites compared to the basal plane.

1.6 Outline of this Thesis

The underlying thesis contributes to a fundamental understanding of the charge transfer processes occurring at the graphite–electrolyte interface in VFBS. A major part of this work deals with the characterization of graphite-based materials such as GF, graphene, HOPG or polycyclic aromatic hydrocarbons (PAHs), putting special emphasis on finding activity-determining properties. For an in-depth understanding of this flamboyant material and its electrocatalytic activity, several analytical techniques to describe the microstructural properties on various scales, the surface chemistry and the electronic structure were used.

The journey starts with diving into the available literature dividing the research community. I will provide an essayistic overview of important studies dealing with surface functionalization in Chapter 2, as well as formulating general and especially my personal research goals on the electrocatalysis of solvated vanadium ions at graphite. Chapter 3 introduces the experimental methods used in this thesis to provide the background necessary. A basic understanding of the goals and directions of each methodological approach will be sketched. The research presented in Chapter 4 can be considered the catalyst of my project: By investigating the surface properties of electrodes, such as chemistry and microstructure, before and after electrochemical testing, I will discover several contradictions with the literature. My observations and theories will subsequently falsify the current reaction mechanism by using deoxygenated electrodes in

Chapter 5. In that manner, the electrocatalytic activity could be ascribed to hydrogen-terminated defects instead of OFGs. PAHs as model electrodes are subsequently introduced in Chapter 6 in the form of pyrenes. These PAHs bearing different OFGs were used to modify the basal plane of GF. While this study clearly shows that some moieties are detrimental to the electrocatalytic activity, it is not always easy to fully link the surface chemistry to the activity, since still the microstructural characteristics of electrodes differ based on the pyrene used. How important it is to keep an in-depth view of all physicochemical properties is especially illustrated in Chapter 7. Heteroatom functionalization using boron and phosphorus is examined as active site. However, commercial doped graphene will show surprisingly low electrochemical performance in half-cell electrochemistry due to its low long-range order and high degree of functionalization. A rational design to efficient heteroatom functionalization of GF is subsequently developed and tested using polarization curves.

Graphitic defects can meanwhile be considered the origin of the electrocatalytic activity of graphite for the vanadium redox reactions. However, defects come in various forms, such as the previously mentioned point defects which are partly tackled by doping. In Chapter 8, I will explore the influence of different edge geometries using multiple PAHs as model electrodes. Modified graphene powders show electrocatalytic variations regarding the architecture of the PAH, such as size of the conjugated system and edge geometry. By combining the results of different GFs and PAHs, it will be possible to link the activity not only to the micro- but also to the electronic structure of the material. The basal plane of graphite and edge sites comprising hydrogen and oxygen groups are furthermore investigated by density functional theory (DFT) calculations in Chapter 9. These simulations were conducted during a research stay at the Technical University of Denmark. Interactions between different surfaces and the vanadium ions will be modeled in vacuum to derive adsorption energies. The charge transfer probabilities will be estimated by investigating overlapping molecular orbitals close to E_F . Differences regarding the edge orientation and the oxidation state of the vanadium ion will be described. In Chapter 10, *operando* Raman spectroscopy on different graphite-based substrates is introduced to study the structural changes of the electrode and identify intermediates under reaction conditions. Only at active edge sites, an early conversion of the vanadium species will be followed by visible reaction intermediates and a direct interaction between the electrode and the electrolyte. To sum up the impact of my research and sketch interesting matters to be explored in the future, a concise summary and a general outlook are provided in Chapter 11.

2 Review of Electrode Activation Treatments

Important previous research that specifically addressed OFGs and defects is summarized herein. The current state of knowledge is considered, and the previous conclusions are critically evaluated. The literature is divided into segments based on the electrode treatment, including thermal, (thermo-)chemical, electrochemical, and plasma/radiation activation. However, it is not the aim to only review electrode treatments. Instead, attention is paid to the material used, its modified properties as concluded by the authors, and the associated interpretation of performance enhancement or degradation. The literature was selected by paying special attention to interpreting the physicochemical data and which material properties were made responsible for activity alterations. The findings and how they build on or contradict each other are outlined in a chronological order. In the end, a perspective on how to advance research on the fundamental catalysis of graphite electrodes while avoiding contradictions is given, which will set the direction of this dissertation.

2.1 Thermal Activation

Oxidation at elevated temperature in ambient is the most used method for the activation of GF. The studies discussed in the following paragraphs are summarized in **Table 1**. Other treatments must stand comparison with thermal activation for its simplicity and effectiveness. A major drawback, however, is the unreliability of the process, whose parameters not only depend on the material but can even change within two supply batches.^[75] Thermal activation increases the electrical double layer capacitance (EDLC) and improves the wetting properties, but these important parameters can diverge between two studied charges, which is related to their different surface chemistries.

To improve its electrochemical performance, Sun and Skyllas-Kazacos thermally treated GF, which improved the energy efficiency by 10% in a symmetrical full cell.^[32] This increase was attributed to surface-active hydroxyl and carbonyl functional groups. A reaction sequence involving the formation of C–O–V intermediates facilitating electron and oxygen transfer was first proposed. However, the suggested half-cell mechanism was based solely on full cell measurements. Therefore, Choi and co-workers aimed to separate the half-cells by investigating pristine and heat-treated carbon felt (CF) using impedance spectroscopy.^[64] They found that the negative electrode was much more sensitive to heat treatment, and the highest charge and

discharge capacities were obtained by using activated CF as the negative and untreated CF as the positive electrode. They consequently suggested an inner-sphere mechanism for the V^{III}/V^{II} , and an outer-sphere mechanism for the $V^{VO_2^+}/V^{IVO^{2+}}$ redox pair. This raises questions about whether there is a relationship between total oxygen content and activity or even specific OFGs are necessary. Certain groups could complement the mechanism of the V^{III}/V^{II} reaction but not work accordingly for the $V^{VO_2^+}/V^{IVO^{2+}}$ reaction, which would explain previous results.

Different OFGs and their effects on CF were thus investigated, showing that thermal activation increased the hydroxyl, decreased the carbonyl, but did not affect the carboxylic group concentration.^[52] In half-cell experiments with rotating disk electrodes, the V^{III}/V^{II} reaction rate constant and exchange current density were enhanced, but reduced for the $V^{VO_2^+}/V^{IVO^{2+}}$ reaction by heat treatment. Subsequent single-cell tests achieved a by 15% increased energy efficiency after exchanging the negative electrode for a heat-treated sample. In contrast, by changing the positive electrode, the efficiency was decreased by 2%. The improvement of the negative electrode was attributed to the oxygen concentration supporting the inner-sphere electron transfer process of the V^{III}/V^{II} redox reaction, which was often discussed since electrodes without activation seemed to support the theory of an outer-sphere mechanism.^[76] It was concluded that the efficiency of a full cell depends more on the negative than on the positive half-cell reaction. However, this was proven incorrect by Fink *et al.* and Friedl and Stimming, who considered the rate constants of both vanadium redox reactions and proposed that they were of the same order of magnitude in both half-cells.^[60,61] By studying different OFGs after thermal activation, they also concluded that all groups increase the wetted surface area and catalyze the V^{III}/V^{II} but hinder the $V^{VO_2^+}/V^{IVO^{2+}}$ kinetics. To investigate the limits of oxygenation, Pezeshki and co-workers doubled the atmospheric oxygen concentration during carbon paper (CP) heat treatment.^[53] Since this resulted in an increased number of OFGs but lower cell performance, they concluded it is rather the increase in surface area responsible for the reduction of the activation overpotential.

It can be expected that the variety of materials studied is crucial, as different intrinsic and surface properties must be considered. Even with the same graphitized felt material, the influence of thermal activation varies depending on the fiber precursor. This was shown by Schweiss and colleagues, who studied pristine and activated GF produced of PAN and cellulose (Rayon) fibers.^[65] The oxygenated felts had no or only slightly adverse effects on the cell resistances and polarization curves using the positive electrolyte, which was shown by double half-cell

measurements. Because of the different results depending on the felt precursor, another influencing factor was highlighted: the degree of graphitization. This was further explored by Langner *et al.* who graphitized and thermally activated felt electrodes at different temperatures.^[77] The peak currents and peak potential separation in the negative half-cell were increased after thermal activation, regardless of the previous graphitization temperature. The treated samples exhibited an increased surface area, abundant OFGs, and a higher percentage of sp^2 hybridized carbon by the removal of amorphous carbon during the heat treatment. In addition, increased disorder was characterized by Raman spectroscopy. The specific influence of one factor was difficult to isolate, so no conclusive statement could be made whether it is OFGs, edge sites, or the sp^2 content that controls the V^{III}/V^{II} redox activity.

Table 1. A chronologically ordered list of literature that dealt with thermal activation and claimed to as a result change the electrochemical performance of the investigated material.

Material	Environment	Investigated System	Improvement related to	Year	Ref.
GF	200–500 °C, 10–50 h, air	full cell	OFGs	1992	[32]
carbon-based ^a	400 °C, 20 h, air	$V^{VO_2^+}/V^{IVO_2^+}$	sp^2 content	2014	[74]
GF (PAN)	403–575 °C, n/a, air	EDLC	surface chemistry	2015	[75]
CP	400 °C, 15–35 h, 0–42% O ₂	single flow cell	surface area	2015	[53]
carbon-based ^b	400 °C, 30 h, air	V^{III}/V^{II} , $V^{VO_2^+}/V^{IVO_2^+}$, single flow cell	edge sites and OFGs	2015	[34]
GF (PAN) ^c	400–600 °C, n/a, air	V^{III}/V^{II}	OFGs, edge sites	2016	[77]
GF (PAN, Rayon)	400 °C, 1–20 h ^d , air	V^{III}/V^{II} , $V^{VO_2^+}/V^{IVO_2^+}$	OFGs, sp^2 content	2016	[60]
GF (PAN, Rayon) ^e	n/a, air	V^{III}/V^{II} , $V^{VO_2^+}/V^{IVO_2^+}$ (single flow cell)	OFGs, none	2017	[65]
GF (Rayon)	400–600 °C, 9 h, air	V^{III}/V^{II} , $V^{VO_2^+}/V^{IVO_2^+}$, full cell	OFGs, none, OFGs	2018	[66]
CF	520 °C, 9 h, air	full cell (impedance)	OFGs ^f	2018	[64]
CF	400 °C, 30 h, air	V^{III}/V^{II} , $V^{VO_2^+}/V^{IVO_2^+}$, single cell	OFGs, none, OFGs	2019	[52]

^a carbon black, graphite flakes, carbon fiber

^b graphite foil, highly oriented pyrolytic graphite, carbon felt

^c graphitized at 1500 and 2000 °C for 1 h

^d PAN- and Rayon-based activated for 20 and 1 h, respectively

^e carbonized and graphitized

^f improvements are reported mainly for the negative electrode

Model electrodes such as HOPG are used to distinguish the electrocatalytic properties of the basal and edge plane, with the latter providing faster electron transfer for both vanadium redox pairs. Building on this knowledge, Pour *et al.* explored defects on heat-treated CP and recognized higher peak currents and smaller peak separations for the negative half-cell, associating the enhanced activity with oxygen-containing defects.^[34] The positive half-cell reaction could not be enhanced by heat-treatment for vanadium concentrations typically used in

battery cells. Mazúr and colleagues specifically studied OFGs on GF and observed increased EDLC, disorder, and oxygen coverage, all of which subsided at higher temperatures because of destruction of the graphite structure.^[66] They similarly observed a decrease in faradaic resistances in the negative half-cell for functionalized electrodes. Whereas the oxygen-rich sample also had the best performance in the positive half-cell, in their full-cell impedance study using higher vanadium concentrations, the oxygen-rich GF did not show decreased charge transfer resistances.

2.2 Chemical and Thermo-Chemical Activation

To conduct chemical or thermo-chemical activation, the sample is treated in an aggressive environment or soaked in a solution and subsequently heated. Studies focusing on this technique are summarized in **Table 2**. Similar to their former study on thermal activation, Sun and Skyllas-Kazacos treated GF with hot sulfuric and nitric acid.^[33] The full cell efficiencies were increased afterwards, and the activity of the best performing electrode was attributed to the higher number of OFGs. Gao and co-workers used iron-containing H_2O_2 solution to selectively hydroxylate GF.^[78] They attributed the enhanced peak potential separation and cell efficiencies mainly to the increased number of surface oxygen, but found severely damaged electrodes using SEM. Jiang *et al.* made use of this damaging process and combined thermal activation with chemical etching to enable bi-porous GF.^[79] The resulting electrode had more than twice the number of OFGs compared to thermally activated felt only, which was suspected to be the electrocatalytic motif in both half-cell reactions over the seven times larger surface area and changed morphology. However, their thermally activated sample for comparison had no defined redox peaks in the negative half-cell and was activated for a shorter period than the thermo-chemically treated felt.

Carbon cloth (CC) as possible electrode material was investigated by Zeng and colleagues using alkaline hydrothermal treatment.^[80] In their SEM results, the surface was not affected by the activation, but defects were observed in Raman spectroscopy. An increase in OFGs, mainly as hydroxyl and carbonyl groups, was revealed, and the active surface area, approximated by EDLC measurements, was nearly doubled for the treated material. In the positive half-cell, the treated and untreated sample was indistinguishable, which was explained by the lower number of OFGs compared to the literature. Activity enhancement in the negative half-cell reaction was fully attributed to OFGs, although the activity had a local maximum and decreased again at higher degrees of oxidation.

Table 2. A chronologically ordered list of literature that dealt with chemical or thermochemical activation and claimed to as a result change the electrochemical performance of the investigated material.

Material	Environment	Investigated System	Improvement related to	Year	Ref.
GF	H ₂ SO ₄ , HNO ₃ , 3–15 h, inert gas	full cell	OFGs	1992	[33]
GF (PAN)	Fenton's reagent	V ^{VO} ₂ ⁺ /V ^{IVO} ₂ ⁺ , full cell	OFGs	2013	[78]
MWCNTs	H ₂ SO ₄ , HNO ₃ , 3–18 h, inert gas	V ^{VO} ₂ ⁺ /V ^{IVO} ₂ ⁺	none	2013	[81]
GF (PAN)	KOH, 800 °C, 2 h, inert gas	V ^{III} /V ^{II} , V ^{VO} ₂ ⁺ /V ^{IVO} ₂ ⁺ , full cell	OFGs, edge sites	2016	[56]
CC	KOH, 6–12 M, 150 °C, autoclave	V ^{III} /V ^{II} , V ^{VO} ₂ ⁺ /V ^{IVO} ₂ ⁺ , full cell	OFGs	2017	[80]
GF (Rayon)	FeCl ₃ , 0.5 M, 400 °C, 6 h, air	V ^{III} /V ^{II} , V ^{VO} ₂ ⁺ /V ^{IVO} ₂ ⁺ , full cell	OFGs, surface area	2017	[79]
graphitic carbon powder	H ₂ SO ₄ , HNO ₃ , KMnO ₄ , 100 °C, 1h, inert gas	V ^{VO} ₂ ⁺ /V ^{IVO} ₂ ⁺	choice of material	2018	[63]

Various research groups expressed doubts about the necessity of OFGs after chemical activation. Rümmler and colleagues studied graphitic carbon powders activated by oxygenating agents and found the activity of the electrode was not reflected by the respective oxygen concentration.^[63] They concluded that the choice of material was more important than oxygenation, but activation was still necessary to create hydrophilic surfaces for improved diffusion and sorption kinetics. Friedl *et al.* studied the electron transfer kinetics of the positive redox couple on multi-walled carbon nanotubes (MWCNTs).^[81] While functionalization for the Fe^{III}/Fe^{II} system led to a tenfold increase in current density, the activity of the V^{VO}₂⁺/V^{IVO}₂⁺ reaction was decreased by OFGs. They concluded these groups played no role in the vanadium electrocatalysis, but slowed the mobility of vanadium ions. Zhang *et al.* modified GF with KOH and attributed increased wettability, lower peak potential separation and higher peak current ratios for both half-cells and higher efficiencies and capacities in the full cell to OFGs.^[56]

2.3 Electrochemical Activation

Electrochemical activation is attractive for commercial applications, as it allows the input of pristine material followed by activation within the assembled cell. Many researchers therefore performed potential-driven activation directly in the battery electrolyte. However, there are differences in terms of electrolyte concentration, electrochemical protocols, and the material studied, as shown in **Table 3**. The positive half-cell reaction kinetics were investigated by Wang *et al.* on oxidized graphite disks activated by anodic polarization.^[82] The higher rate constant and activation energy was attributed to an increased number of OFGs, enhancing the

wetting properties of the material and promoting charge transfer. With the applied potential, the damage to the material increased. Kabir and co-workers studied the negative half-cell using electrochemically oxidized HOPG.^[83] Their sample exhibited several oxygen-related functional groups after activation, which were held responsible for the enhanced electron transfer properties.

Table 3. A chronologically ordered list of literature that dealt with electrochemical activation and claimed to as a result change the electrochemical performance of the investigated material.

Material	Environment	Investigated System	Improvement related to	Year	Ref.
GF (PAN)	1 M H ₂ SO ₄ , 5–15 V ^a	VVO ₂ ⁺ /V ^{IV} O ₂ ⁺ , full cell	OFGs (carboxylic) and surface area	2007	[84]
graphene oxide	PBS ^b , -0.8 to -1.6 V vs. SCE, 3 min	V ^{III} /V ^{II} , VVO ₂ ⁺ /V ^{IV} O ₂ ⁺ , full cell	OFGs (carbonyl)	2013	[50]
CF, GF	2 M vanadium, 4 M H ₂ SO ₄ , -2.0 to 1.5 V, 60 s	V ^{III} /V ^{II} , VVO ₂ ⁺ /V ^{IV} O ₂ ⁺ , full cell	OFGs	2016	[85]
carbon based ^c	1.5 M vanadium, 4.5 M H ₂ SO ₄ , -2.25 to 1.6 V vs. Hg/Hg ₂ SO ₄ , 60 s	V ^{III} /V ^{II} , VVO ₂ ⁺ /V ^{IV} O ₂ ⁺	OFGs	2016	[86]
graphite disc	0.1 M V ^{IV} O ₂ ⁺ + 3 M H ₂ SO ₄ , 1.5–1.9 V vs. SCE, 10 min	VVO ₂ ⁺ /V ^{IV} O ₂ ⁺	OFGs	2016	[82]
HOPG	1.0 M H ₂ SO ₄ , 2.1 V vs. Ag/AgCl, 1 min	V ^{III} /V ^{II}	OFGs	2017	[83]
GC	2 M H ₂ SO ₄ , 0.5–2 V vs. Hg/Hg ₂ SO ₄ , 30 s	V ^{III} /V ^{II} , VVO ₂ ⁺ /V ^{IV} O ₂ ⁺	OFGs (hydroxyl), OFGs (carboxylic)	2018	[59]
Graphite disc ^d	2 M H ₂ SO ₄ , 2.2 V vs. RHE, 5 min	V ^{III} /V ^{II}	OFGs and edge sites		[71]

^a a two-electrode setup was used (titanium as counter electrode)

^b PBS: phosphate buffer solution (KH₂PO₄/K₂HPO₄, pH 5.1–5.5)

^c GC: glassy carbon, carbon paper, carbon xerogel, carbon fibers

^d edge and basal plane exposed

Many scientists who agree on the functionality of surface oxygen still discuss the differences in specific OFGs and believe that only one or two catalyze the vanadium redox reactions. Li *et al.* attributed an improvement of the positive half-cell reaction by oxidized GF to the increased number of carboxyl groups.^[84] Other researchers reduced graphene oxide electrochemically and observed increased activity in both half-cells by implementing carbonyl groups.^[50] Noack and co-workers studied polarized GF and found that the reaction rates increased.^[59] However, the negative half-cell reaction was steadily improved with applied potential, while the positive half-cell reaction had a local kinetic minimum. A correlation was found between the activity of the VVO₂⁺/V^{IV}O₂⁺ redox couple and the number of hydroxyl groups. No such correlation was present for the negative half-cell, but because of the lack of links with roughness factors or surface area, the activity of carboxylic groups was discussed.

More detailed studies note the difference between the vanadium half-cells and investigate the influence of activation conditions. It was demonstrated by Bourke *et al.* for several carbon-based materials that the V^{III}/V^{II} reaction is enhanced by anodic, and the $VVO_2^+/V^{IV}O^{2+}$ reaction by cathodic polarization.^[86] In both cases, they suspected the influence of OFGs whose oxidized or reduced state would not correspond to the state in which the respective redox reaction occurs. In a later study, they reported their results were not related to a change in surface area, but to altered surface chemistry.^[85] Anodic treatment, which inhibits the positive half-cell reaction, leads to a highly oxidized surface. In contrast, cathodic treatment, which enhances the $VVO_2^+/V^{IV}O^{2+}$ redox reaction, resulted in a composition like the untreated sample with rather low oxygen content.

The role of defective sites after electrochemical treatment is less prominently discussed, but Taylor and coworkers studied basal and edge exposed electrodes before and after electrochemical oxidation and stated that edges provide faster redox kinetics in the initial state.^[71] After oxidation, the edge surfaces catalyzed the parasitic hydrogen evolution reaction and were subsequently less active for the V^{III}/V^{II} redox couple. For the oxidized basal surface, prolonged cycling resulted in a sharp drop in activity, which was attributed to unstable OFGs.

2.4 Plasma/Radiation Activation

To integrate abundant OFGs on the surface of GF, plasma or irradiation exposure, occasionally followed by a chemical treatment, is explored (**Table 4**). Kim *et al.* investigated the influence of mild oxidation, plasma treatment and gamma-rays on the electrochemical performance of CF.^[87] They concluded that the number and type of OFGs are crucial for the redox kinetics. The importance of hydroxyl groups is emphasized to enhance the efficiency of the $VVO_2^+/V^{IV}O^{2+}$ reaction. In a later study, they enriched the surface of GF with OFGs by combining a plasma procedure to create dangling bonds with a subsequent H_2O_2 treatment to saturate these bonds with oxygen.^[45] According to their interpretation, OFGs provided faster charge transfer and improved the wettability. However, only an effect on the negative half-cell and almost no improvement of the peak current and potential separation in the positive half-cell was observed.

Table 4. A chronologically ordered list of literature that dealt with plasma treatment or radiation and claimed to as a result change the electrochemical performance of the investigated material.

Material	Environment	Investigated System	Improvement related to	Year	Ref.
CF (PAN)	300–600 °C, 5 h, air; O ₂ plasma, 1–10 min; gamma-ray, 50–200 kGy, RT, air	full cell	OFGs and surface area	2011	[87]
CF (PAN)	Corona discharge, 4 A, 15 s, air; H ₂ O ₂ (30%), 1 h	V ^{III} /V ^{II} , V ^{VO} O ₂ ⁺ /V ^{IVO} O ₂ ⁺ , full cell	OFGs	2014	[45]
GF (PAN)	O ₂ plasma, 2–60 min; H ₂ O ₂ , 1 h	full cell	OFGs (carboxylic) ^a	2016	[58]
GF (PAN)	N ₂ plasma, 40 min,	V ^{III} /V ^{II} , V ^{VO} O ₂ ⁺ /V ^{IVO} O ₂ ⁺ , full cell	defects	2019	[88]

^a negative effect for hydroxyl and carbonyl groups

Estevez *et al.* combined oxygen plasma and chemical treatment and found that carboxylic groups improved the energy efficiency by about 8%, while hydroxyl and carbonyl groups had a negative impact.^[58] No microstructural changes were observed on the electrodes by SEM after the procedure compared to the untreated felt. By switching from an oxygen to a nitrogen plasma treatment, Dixon and coworkers showed that the induction of structural defects can improve the half-cell redox kinetics, especially for the V^{III}/V^{II} reaction.^[88] Since the oxygen content on the surface remained unchanged, the increased charge and discharge capacities in a full cell were attributed to a higher disorder.

2.5 Perspective

The literature dealing with how the catalytic properties of carbon-based materials for vanadium redox reactions are affected by integrating surface oxygen was summarized. The selected publications differed in their activation method, the material studied, the systems explored, and the data interpretation. The conclusions drawn based on a physicochemical characterization of the procedures are contradictory. OFGs are regularly held responsible for the showed increased electrochemical performance.

When discussing surface chemistry and associated changes after a treatment, it is important to note that oxidized or reduced states are likely to be unstable over the potential ranges examined. When the oxygenated sample activated at positive potential is cycled in the negative half-cell, most of the previously introduced OFGs are expected to be removed, explaining the reduced concentration of surface oxygen after electrochemistry.^[85] The surface chemistry and structure must thus be analyzed after electrochemical testing to gain a more in-depth view of the relevant material properties. In contrast, OFGs are more persistent or are generated in the positive half-cell, which is why the importance of their presence on a treated electrode might

be overestimated. It was calculated that the $V^{VO_2^+}/V^{IVO_2^+}$ redox reaction does not require the transfer of an oxygen atom, as several studies suggested.^[70] Instead, proton exchange could occur *via* the oxygen atoms surrounding the vanadium ion or without the involvement of oxygen at all. A recent computational study suggests that sp^3 groups at the surface handle the acceleration of the positive half-cell redox reaction and oxygen groups can be considered a by-product of this hybridization.^[38] Instead, the authors propose non-oxidative activations should be performed to maximize this effect. Further computational studies should also consider the energy barriers for electron transfer at oxygen-free graphite defects.

Once a scientific theory is established in a community, it is difficult to challenge it. Phenomenological observations by studying the physicochemical properties of catalysts are used to explain aspects of the electrocatalytic activity. However, for complex systems such as graphite, not only one property should be held responsible, since lots of changes can be monitored. Established theories might be reproduced while other properties are neglected. In catalysis research, it is common for mechanistic studies to examine the material after it is used to draw reliable conclusions. However, this is rarely done within the VFB community, also because of the complexity of the surface of GF. To develop reliable mechanisms, one must paint a picture of the changing material properties during electrochemistry. Therefore, *operando* techniques should be applied to learn more about solid–liquid interactions and how molecules and atoms adsorb and migrate, how their coordination spheres change, and how ions and charges are exchanged.

There are lots of open questions that need to be discussed, especially when it comes to graphitic defects: it is unclear how edge sites and vacancies behave differently in catalysis and how we can selectively introduce them into real electrodes. Armchair edges might have different properties than zigzag edges, which affects activity in other reactions such as oxygen evolution or reduction.^[40,89] These effects on vanadium redox reactions remain to be investigated. Furthermore, the size contribution of the π -conjugated system must be evaluated more precisely. This might help in finding the correct balance between electrical conductivity and enough defect sites for electron transfer. In addition, the interplay between microstructure and electronic structure needs to be understood. With an efficient activity descriptor from an electronic point of view that can be evaluated experimentally and theoretically, other parameters will be easier to compare.

3 Experimental Methods

This chapter is intended to provide the reader with enough information to follow the discussion of the results. It is not meant to be a copy of textbook information that is widely available in more detail. Therefore, the emphasis of a method will be less on the working principle and its physical and chemical background, but more on the capability of the method explicitly on the herein studied system. Experimental details on the techniques covered in this chapter and other methods used can be found in the Appendix A.

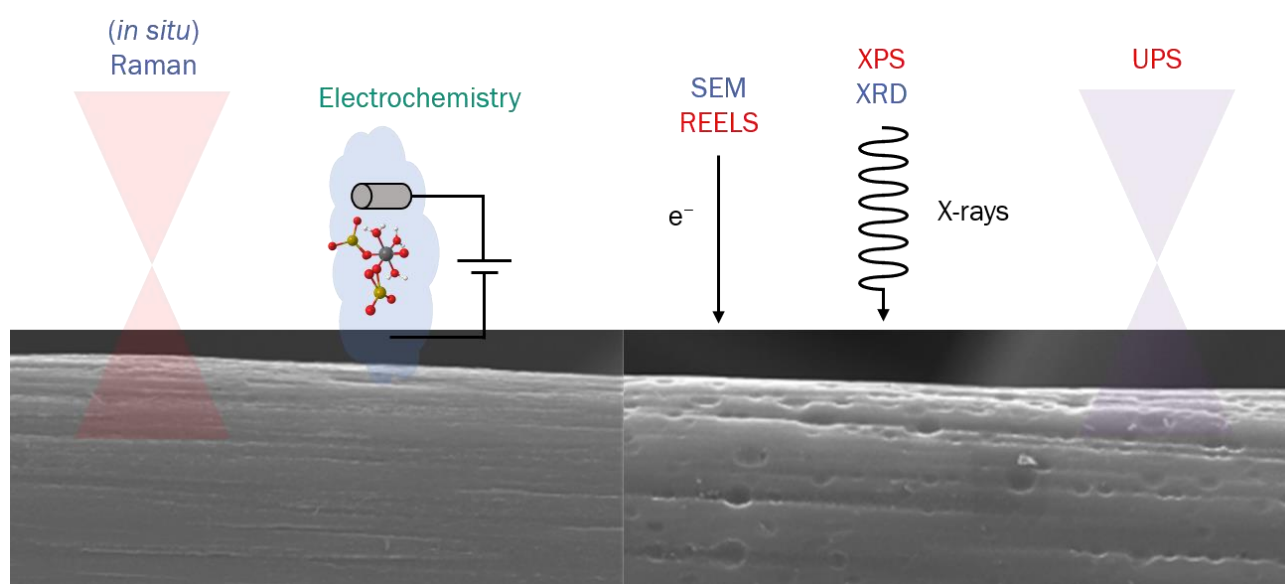


Figure 3-1. Schematic depiction of the analytical techniques used in this thesis. Physicochemical techniques for the investigation of microstructural properties are written in blue, and for the evaluation of the electronic structure in red.

Figure 3-1 provides an overview of the main analytical techniques used in this work. The goal was to obtain a holistic view on the characteristics of the carbon-based electrode material by combining half-cell electrochemistry with techniques to study the microstructure and electronic structure. For the investigation of the microstructural properties on several scales, SEM, Raman spectroscopy, and XRD were employed. The electronic structure was studied by X-ray and UV photoelectron spectroscopy and reflection electron energy loss spectroscopy (REELS). Furthermore, the electrical conductivity under compression was investigated. The chapter concludes with a description of the DFT calculations performed during a research stay at the Technical University of Denmark.

3.1 Electrochemistry

Electrochemical reactions use electrons (*i.e.*, a current flow) as an educt to enable chemical change. To advance the charge transfer at the interface, an external potential is applied. A reaction takes place at the interface between an electrode and the ion-containing electrolyte, when the free reaction enthalpy G , which can be calculated according to

$$G = -nFE_{Redox}, \quad (3.1)$$

is lower or equal to zero. F stands for the Faraday constant ($96,485 \text{ C mol}^{-1}$) and n for the number of electrons involved in the reaction. The concentration of the redox couple in the electrolyte changes due to reactions and so does the redox potential. To determine this, the Nernst equation is used:

$$E_{Redox} = E^0 + \frac{RT}{nF} \ln\left(\frac{a_{ox}}{a_{red}}\right). \quad (3.2)$$

E^0 is the standard potential of the reactants, a is the activity of the redox couple, T the temperature and R the universal gas constant ($8,314 \text{ J K}^{-1} \text{ mol}^{-1}$). The standard potential is usually expressed regarding the standard hydrogen electrode (SHE), which marks the zero point, but can be shifted for convenience (*e.g.*, $E_{Vac} = E_{SHE} - 4.44 \text{ V}$ or $E_{Ag/AgCl} = E_{SHE} + 0.21 \text{ V}$).

The Nernst equation describes the potential at an electrode in the equilibrium case and without a current flow. However, electrochemical reactions rarely proceed at the thermodynamic standard potential because of kinetic hindrances. To lower the activation energy, which describes the interfacial barrier that must be overcome to transfer charges effectively, electrocatalysts are used. The primary figures of merit to evaluate the suitability of a catalyst are activity, stability, and selectivity. Even though all three are equally important, in this work mostly the activity is considered. The goal is therefore to reduce the overpotential η necessary to drive the reaction. It is crucial to know how much current per electrode area (*i.e.*, current density j) is received regarding the potential applied. This relationship is described by the Butler-Volmer equation:

$$j = j_0 \left\{ \exp\left[\frac{\alpha n F \eta}{RT}\right] - \exp\left[\frac{(1 - \alpha) n F \eta}{RT}\right] \right\}. \quad (3.3)$$

The equation comprises an anodic and a cathodic term, in which the charge transfer coefficient α , a dimensionless symmetry factor ranging from 0 to 1, determines the direction of the

reaction which is biased by the applied potential. The exchange current density j_0 describes the current density without an overpotential present.

Abundant electrochemical methods have found their way into multiple branches of materials science, chemistry, and engineering. Several electrochemical cells for this purpose are available in specialized shops and were partly also used for this work. However, the classical aqueous electrochemical measurements, which are usually performed in these cells, either use rod electrodes with just a small area exposed to the electrolyte, or disperse small amounts of powder on top of an (inert) electrode. For the investigation of GF, these cells do not quite meet the requirements for several reasons: Because of the inhomogeneity of GF, it makes sense to measure a large surface area of the material to receive good approximations. However, since the counter electrode should not be the limiting factor of the reaction, the size of the piece used must be significantly larger than that of the working electrode, which must be considered in the resulting size of the apparatus. It is furthermore common practice in the RFB community to attach GF to a thin wire, which is then connected to the potentiostat with a crocodile clip. However, this leads to considerable contact resistances, especially for high currents.

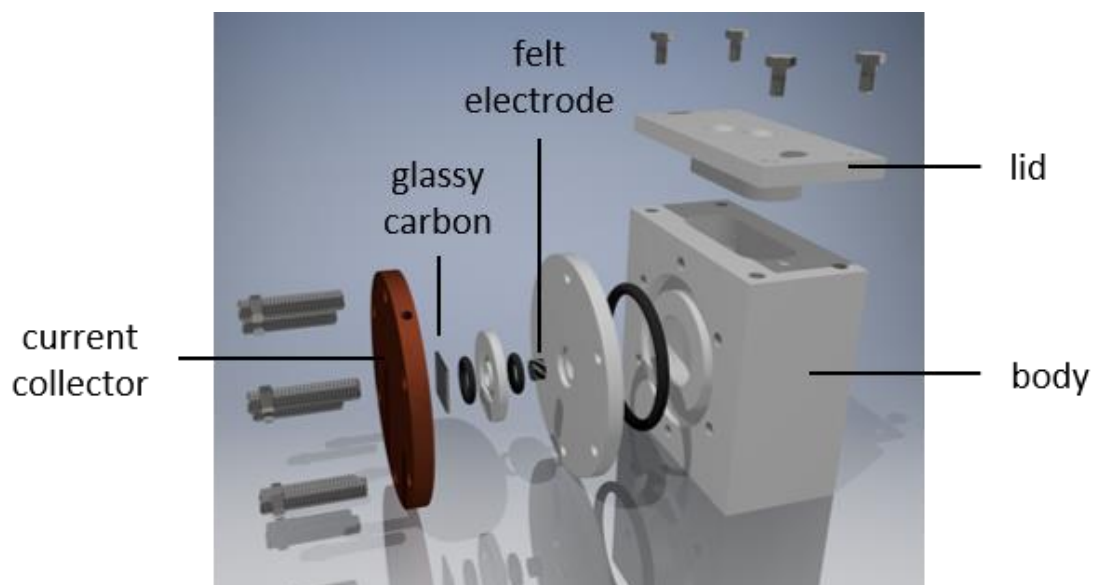


Figure 3-2. Three-electrode cell used for electrochemical half-cell experiments with porous felt electrodes.

The three-electrode setup shown in **Figure 3-2** was constructed by computer-aided design using the Autodesk Inventor software, and solves these problems. The main part of the cell consists of the body, which serves as an electrolyte reservoir. While the working electrode is fed by specially cut pieces from the side of the device, there is plenty of room in the body for a large piece of felt as a counter electrode. Slightly offset in the direction of the sample, a commercial

or custom-built reference electrode can be attached from the top. Since GF is thicker compared to its backing plate, one entire side of the felt can be contacted to the gold-coated copper current collector *via* a GC plate as a bridge, improving the electrical contact. Since each part of the cell can be replaced and designed individually, it is possible to vary the geometry of the working electrode as required.

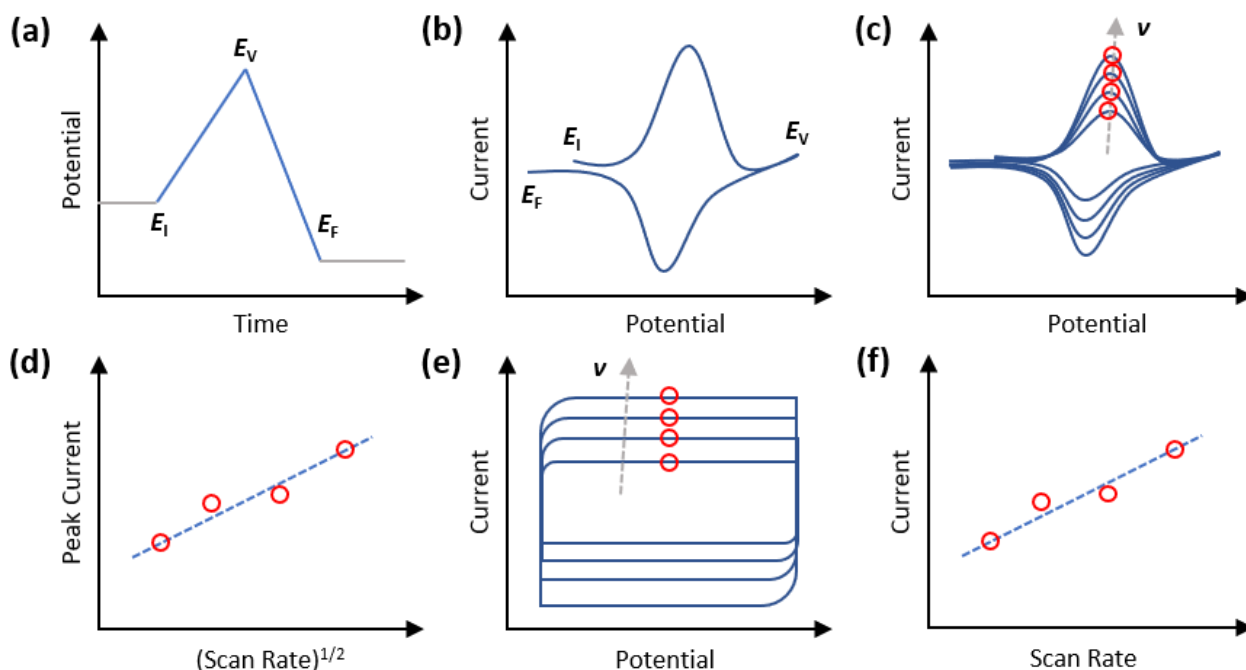


Figure 3-3. Schematic depiction of experiments involving the CV technique. **(a)** Evolution of the potential with time during an experiment, starting the experiment at an initial potential (E_i), increasing the potential up to the vertex potential (E_v), before decreasing the potential again toward the final potential (E_f). **(b)** Current–voltage profile for the experiment in (a). **(c)** CV curves of the same redox reaction recorded at different scan rates. **(d)** Linear relationship between the peak currents in (c) and the square root of the scan rate. **(e)** Current–voltage curves for a non-faradaic potential region at different scan rates. **(f)** Linear relationship between the current at an arbitrary potential from (e) and the scan rate.

In a three-electrode configuration, the current flow is measured between the working and the counter electrode, while the potential is measured between the working and reference electrodes. This arrangement allows the half-cell reactions to be studied only at the sample, without considering the electrochemical reactions at the counter electrode. The reference is used as a second half-cell with a fixed potential to monitor the changes in cell voltage. Mostly two standard techniques, CV and Electrochemical Impedance Spectroscopy (EIS), were used in this work.

CV: a special technique to record current–voltage curves at a specific scan rate in one direction of the potential and backward (**Figure 3-3a**). This allows to not only record an

oxidation/reduction but also the corresponding reduction/oxidation back reaction (**Figure 3-3b**). An advanced form of CV is, for instance, alternating the scan rate in the same potential window (**Figure 3-3c**). The resulting current behavior of a redox wave as a function of the scan rate can provide important information about the limiting factor of a reaction (diffusion vs. mass transfer) according to the Randles–Sevcik equation (**Figure 3-3d**). In a non-Faradaic potential window, the same technique can evaluate the EDLC of an electrode, which is closely related to the electrochemically active surface (**Figure 3-3e,f**).

EIS: allows the determination of the electrical resistivity of the electrolyte when recorded at no applied potential, or the charge transfer resistance (R_{CT}) of a redox reaction when recorded at a potential where charges are exchanged between the electrode and electrolyte. The spectra were fitted using the equivalent circuit diagram displayed in Figure S25 or a slightly modified version of it.

3.2 Microstructure

Scanning electron microscopy (SEM): Conventional SEM images are created by screening the surface of a sample with an electron beam and detecting the yield of secondary electrons (<50 eV) ejected. The contrast in a picture is created by the different height and orientation of particles. SEM can thus determine the size and shape of structures, but also reveals information on the composition by the diffraction pattern of the electrons or the investigation of backscattered electrons or the detection of characteristic X-rays. Unmodified GF comprises $\sim 10 \mu\text{m}$ thick randomly entangled graphitized fibers, which show a smooth surface with visible stripes from the wet-spinning process (**Figure 3-4a**).

Raman spectroscopy: Collecting the inelastically scattered photons of a sample, which is irradiated by monochromatic light, with a detector and filtering the intense signals due to elastic Rayleigh scattering characterizes a sample. Raman spectroscopy is one of the most versatile techniques for studying carbon-based materials such as disordered and amorphous carbon, fullerenes, nanotubes, diamonds, graphene, and graphite. By searching the Web of Science with the keywords "Raman carbon," readers can choose from >57,000 publications since 1945. The technique is fast, nondestructive, offers high resolution, and provides very detailed structural information. Disadvantages are a direct consequence thereof: Due to the small number of scattering features in a graphite-based sample and the high information content in each vibrational band, the interpretation process is complicated. Depending on the properties of a material,

spectral features can vary in shape, position, and relative intensity. Often these individual peaks overlap and must first be separated in a deconvolution process.

The main features in a Raman spectrum of GF (**Figure 3-4b**) comprise the G band at ~ 1590 cm^{-1} , associated with a first order E_{2g} longitudinal optical phonon mode, resembling the in-plane stretching of C=C bonds, and the D band at ~ 1335 cm^{-1} , induced by disorder such as edges, stacking fault, or atomic defects, corresponding to an A_{1g} breathing mode of a six-atom C-ring.^[90-93] At higher wavenumbers, the spectrum is dominated by the second-order D band (2D) at 2660 cm^{-1} , which is a result of two D band phonons with opposite momentum. The intensity ratio of the D and G band provides useful information such as the degree of disorder in the sample.^[73,94] The origin of the observed defects is evaluated by the ratio of the D and the D' band, in which a ratio of ~ 3.5 corresponds to grain boundary defects such as edge sites, and higher ratios to vacancy-like (~ 7) or sp^3 type (~ 13) defects.^[95]

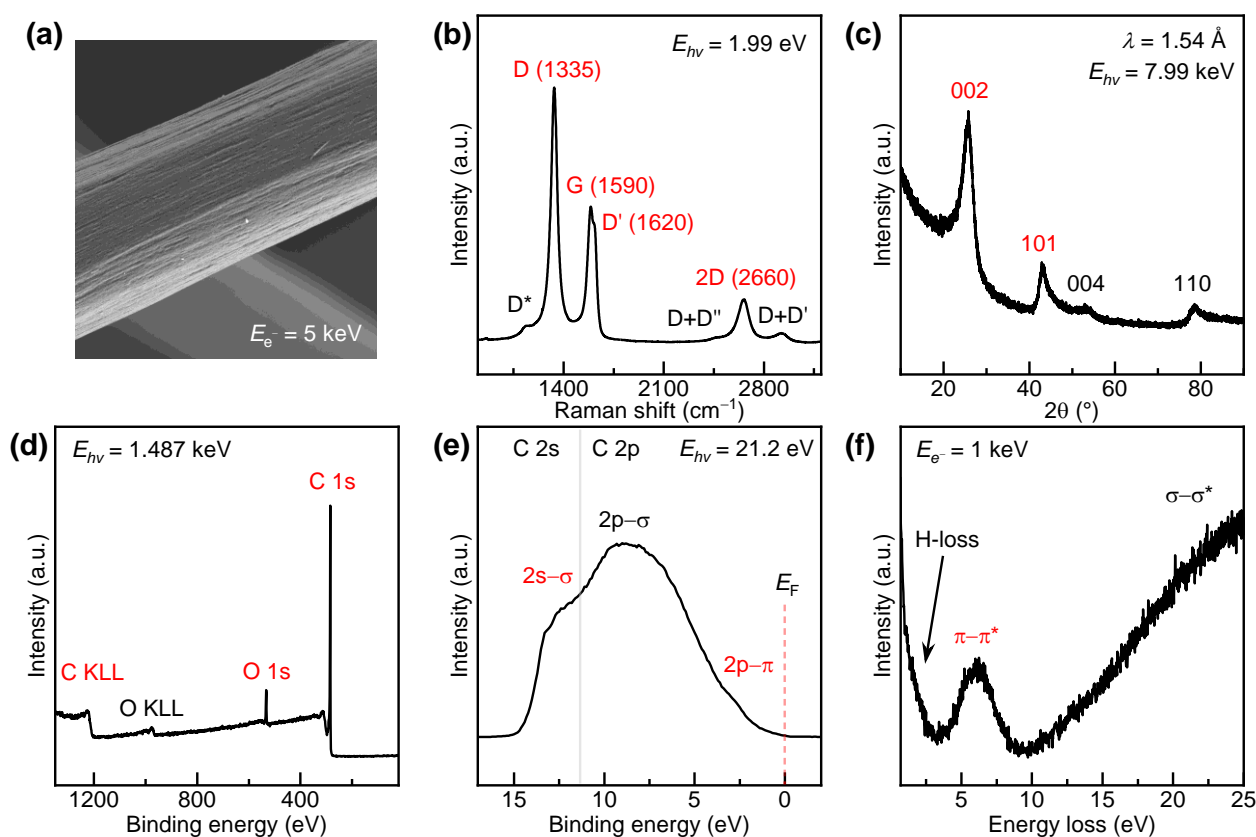


Figure 3-4. Analytical techniques used in this work, exemplary illustrated for pristine GF. **(a)** SEM, **(b)** Raman spectroscopy, **(c)** XRD, **(d)** XPS, **(e)** UPS, and **(f)** REELS.

Operando Raman spectroscopy: There is a growing interest in the development of analytical tools to study chemical processes occurring on an active catalyst under working conditions

through the use of *in situ* characterization techniques.^[96,97] The term *in situ* is commonly used to describe the acquisition of spectra at the same location where the sample is treated, while *operando* more precisely describes the simultaneous use of an additional analytical technique to determine a chemical change under working conditions.^[98] The difficulty is to apply techniques that not only detect the bulk of a material, but allow monitoring of surface changes, reaction intermediates or adsorption processes. Nowadays, *in situ* spectroscopy of catalysts is done by using by a variety of techniques such as IR, Raman, X-ray absorption, nuclear magnetic resonance, UV-vis, and Mössbauer spectroscopy.^[99]

Raman spectroscopy is particularly suitable for *operando* investigations as it uses visible light and allows observation of catalysts by irradiation through transparent windows. It is also applicable at higher temperatures and enables monitoring of thermal decomposition or experiments at elevated pressure.^[98,100] In particular, it provides strong signals for typical catalytically active sites, such as molecular metal–oxygen vibrations.^[101] A review of the literature from about 1970 to 2010 revealed that Raman studies on catalysts increased greatly after 1995 due to the growing interest and applicability of *in situ* techniques to determine the active site.^[101] About 25% of the available Raman literature today deals with *in situ* spectroscopy and considers the dynamic response of the Raman signal to environmental factors such as concentration, temperature or pressure.

X-ray diffraction (XRD): X-rays have wavelengths in the Ångstrom range and are energetic enough to penetrate solids, allowing characterization of their internal structure. Conventional X-ray sources consist of a target (*e.g.* copper), which is bombarded with high-energy electrons. Taking the characteristic Cu–K α line as an example, an electron can create a core hole in the K-shell of the target, which is then filled by an electron from the L-shell under emission of an X-ray quantum. Diffraction is accounted for by the elastic scattering of these X-rays by periodically arranged atoms in a lattice. The design interference of these scattered X-rays allows the lattice spacing d to be derived using Bragg's law:

$$n\lambda = 2d \sin \theta, \quad (3.4)$$

in which the integer n describes the order of reflection, λ the wavelength, and θ the angle between the incoming X-rays and the reflecting lattice plane. A diffractogram is measured as a function of the angle 2θ . Polycrystalline samples must be rotated during the measurement to increase the number of particles participating in the diffraction process. In this work, XRD was not used to distinguish between different phases or structures. The goal was to characterize

subtle variations in the long-range order after a modification procedure or between several graphitic materials to characterize differences not only at the surface but also in the bulk. Pristine GF reveals Bragg reflections corresponding to the 002, 101, 004, and 110 planes located at $2\theta = 26.5, 42.4, 54.6$ and 77.5° , respectively (**Figure 3-4c**).^[102]

3.3 Electronic Structure

X-ray photoelectron spectroscopy (XPS): XPS provides information about the elemental composition of a sample and the oxidation state of the elements present. The technique is based on the photoelectric effect: an atom absorbs a photon and subsequently emits an electron, which can be collected by a detector measuring its kinetic energy E_{Kin} . Knowing the work function Φ of the spectrometer, according to the equation

$$E_{Kin} = h\nu - E_{Bin} - \Phi \quad (3.5)$$

the binding energy E_{Bin} of the electron is calculated, allowing the determination of its elemental origin. Additionally, the ion which released an electron can be de-excited by receiving an electron from a higher shell. The energy released in this process can be enough to emit another electron with lower kinetic energy, the so-called Auger electron. GF reveals a prominent C 1s and O 1s signal at ~ 285 and ~ 533 eV due to carbon and oxygen, respectively (**Figure 3-4d**). Furthermore, their corresponding Auger lines C KLL and O KLL are visible at higher binding energies. The deconvolution to separate overlapping peak signals is in detail described in the Appendix A.

UV photoelectron spectroscopy (UPS): The difference between UPS and XPS is the use of UV light instead of X-rays. Consequently, the excitation energy is a lot lower which limits the emission of photoelectrons to valence electrons. Therefore, UPS is extremely powerful in probing the electronic structure close to E_F on the surface of a material, the density of states (DOS). The threshold close to E_F allows the evaluation of the E_{VBM} . In that manner, the energy gap between the upper limit of the $2p-\pi$ electrons and E_F can be evaluated for GF (**Figure 3-4e**). The degree of graphitization can be estimated by the relative intensity of the $2s-\sigma$ signal. The spectrum can be shifted to higher binding energies by applying a bias voltage. As a result, a clear energy cut-off allows the determination of the sample's work function Φ since $E_{Kin} = h\nu - \Phi$ equals zero at that point.

Reflection Electron Energy Loss Spectroscopy (REELS): involves a beam of monoenergetic electrons, which regarding to its energy can excite lattice vibrations, molecular vibrations of adsorbents, or electronic transitions. In the spectrum it is shown how much energy the inelastically scattered electrons have lost due to the previously mentioned scattering processes. For GF, a peak arising due to the π - π^* transition at ~ 6 eV can be seen (**Figure 3-4f**), whose intensity and position depends on the defectiveness of the carbon surface.

3.4 Electrical Conductivity

The electrical conductivity of GF is of vital importance for the battery efficiency. Due to the thickness of the flow-through electrodes, charges must be transferred from the reaction centers close to the membrane all the way toward the current collector. The number of conductive pathways should thus be high to reduce ohmic losses in the cell. GF is due to its predominantly sp^2 hybridization already an excellent electrical conductor. It is thus important to maintain this outstanding property during a surface modification. The electrodes in flow batteries are usually compressed to ensure enough contact area between GF and the bipolar plate. As a downside, porosity is lost in this process.

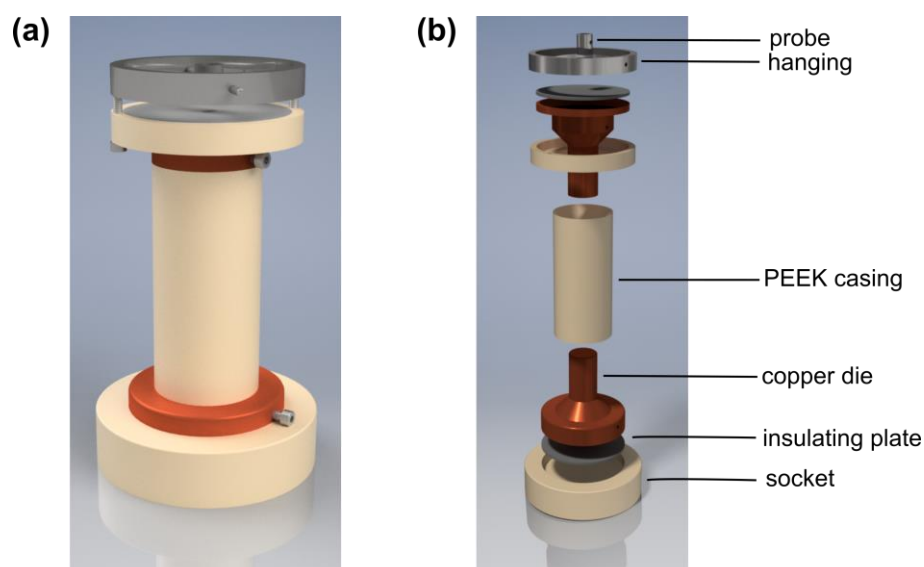


Figure 3-5. Test setup to probe the electrical conductivity of a sample at an applied pressure. **(a)** Assembled device and **(b)** explosion drawing, indicating the individual components of the cell.

It is thus important to balance ohmic losses during charge transport and pump losses due to reduced macro-porosity in the felt. Several studies suggest that a compression of $\sim 20\%$ of the original felt thickness offers a satisfactory tradeoff. The electrical conductivity of an electrode should thus neither be investigated under full pressure like a metal plate nor without any

compression which would lead to high contact resistances not occurring in the battery. Therefore, a device which can be coupled with a pressure test machine to allow compression-dependent measurements of the electrical resistance was developed (**Figure 3-5**). In principle, two copper dies coupled to a potentiostat ensure the loss-free evaluation of the electrical conductivity of a felt placed in between. The system is then electrically insulated from the test machine by aluminum oxide plates. At the bottom, a tight-fit socket mounts the setup to the machine to prevent a shift of the construction. At the top, a metal probe connected to a hanging by a thin rod transfers the pressure of the machine directly to the copper die. A leak-proof casing can be used to perform measurements of wet felts.

3.5 Density Functional Theory

For many fields in natural sciences and engineering, the key to scientific progress is understanding material properties at an atomic scale. Electronic structure calculations were the key to a row of groundbreaking discoveries, illustrated by the following three prominent examples^[103]: (i) It was shown that ammonia synthesis, one of the most important catalytic reactions, proceeds *via* at least twelve distinct steps on a metal catalyst, of which the most important is breaking of the N₂ bond. On atomically flat regions, a high amount of energy is required for this reaction, whereas at edges, the energy expense is much lower.^[104] (ii) Researchers have described the embrittlement of copper by small amounts of bismuth. Several explanations were proposed over the years, including the introduction of strain, electronic bond weakening, and size effects. Using DFT, it was shown that significant changes in the material properties were due to the much larger bismuth atoms.^[105] (iii) Finally, DFT can investigate material under misanthropic conditions as they exist in the center of planets. By investigating the stability and properties for phase transformations of crystal structures, it was demonstrated that MgSiO₃ can be found in the center of Uranus and Neptune, but not inside Jupiter or Saturn.^[106]

DFT describes the quantum behavior of atoms by solving the Schrödinger equation. Atoms comprise nuclei and electrons. If one wants to understand the properties of matter, it is important to know where the atoms are located and how their energy changes when being moved around. Because nuclei are much heavier than electrons and therefore react delayed to a displacement, their wave functions Ψ can be separated according to the Born–Oppenheimer approximation.^[107] As a result, a static electronic state of a molecule can be described by solving the many-electron time-independent Schrödinger equation.

In one of two important theorems formulated by Hohenberg and Kohn, they proclaim that the ground state energy of the Schrödinger equation is a functional of the electron density.^[108] The second theorem defines that the true energy density minimizes the overall functional and corresponds to the true solution of the Schrödinger equation. Knowing that it is not an easy task to solve the Schrödinger equation fully, Kohn and Sham developed a method to express the correct electron density by solving a set of equations describing single electrons as:

$$\left[-\frac{\hbar}{2m_i} \nabla_i^2 + V(\mathbf{r}) + V_H(\mathbf{r}) + V_{XC}(\mathbf{r}) \right] \Psi_i = \varepsilon_i \Psi_i. \quad (3.6)$$

The first potential V describes the interaction of an electron and all atomic nuclei; the Hartree potential V_H defines the Coulomb repulsion between the considered electron and the total electron density. V_{XC} means the exchange and correlation contributions to the single electron equations and can formally be defined as a “functional derivative” of the exchange–correlation energy. Since solving the Kohn–Sham equation is a circular problem, an initial guess for the electron density must be made to solve the problem iteratively.

Kohn–Sham DFT calculations were performed using GPAW.^[109] All calculations were based on the projector augmented wave (PAW) method.^[110,111] The structures were built and visualized by using the atomic simulation environment (ASE) package.^[112] Adsorption energies E_{ads} of H_2O and vanadium ions with solvation shell are determined using the following equation:

$$E_{ads} = E_{(surface+adsorbant)} - (E_{surface} + E_{adsorbant})$$

To retrieve the respective energy values, a plane-wave cutoff energy of 400 eV was used in the calculations. A $5 \times 5 \times 1$ mesh of k-points was chosen for the calculations using basal plane graphene, and a $1 \times 1 \times 5$ mesh for the graphene nanoribbons. The lattice constant a of single-layer graphite was set to 2.46 Å.^[113] For the ribbons, the initial C–H and C–C bond lengths were set to 1.09 Å and 1.42 Å, respectively.^[114] The Bayesian error estimation functional with van der Waals correlation (BEEF-vdW) was used as the exchange–correlation functional.^[114] Electron wave functions were represented on a real space grid with a spacing of 0.2 Å. The tolerance for geometry optimization was set to 0.05 eV Å⁻¹. Vanadium ions were initialized to possess charges and magnetic moments according to the occupation of their d -orbitals. The smearing of the occupation numbers was controlled by a Fermi–Dirac function with a width of 0.1 and 0.0 eV for systems with and without periodic boundaries, respectively.

4 Influence and Electrochemical Stability of Oxygen Groups and Edge Sites

The flow battery community widely accepts that OFGs on graphite work as an effective catalyst for the occurring vanadium redox reactions as it was broadly discussed in Chapter 2. The mere number of studies may explain why the literature is contradictory, especially when the material characterization after the respective surface treatment is directly related to the electrochemical activity. Most of the used oxidative treatments are as well expected to damage the material and create graphitic defects as edge sites. Clear discrimination between OFGs and defects is difficult and thus the observed activity can hardly be attributed to one specific property. More questions about the functionality of surface groups arise when carbon-based nanomaterials, such as graphene or MWCNTs, are used for GF modifications. Prior treatment to increase the activity is therefore often considered as hydroxylation or carboxylation, sulfonating, or heteroatom doping.^[115-121] The activity enhancement of the treatment is hard to separate from the pure addition of the nanomaterial.

In this chapter, the respective role of OFGs and edge sites for the electrocatalysis of GF were disentangled. Owing to their intact sp^2 structure and wide modification potential, MWCNTs serve as a good substrate for studying the influence of defects in more detail. A KOH activation was chosen to create edge sites effectively and introduce OFGs on the material as described in literature. Morphological changes were investigated by SEM, the chemical composition by XPS, and the defective structure by Raman spectroscopy to draw conclusions about the electrocatalytic activity studied by CV and EIS. The felts were characterized again after electrochemistry to monitor changes in the surface moieties and the stability of defects. A set of four different samples with varying defect density and concentration of OFGs was prepared by refining conventional modification techniques. Pristine GF was decorated with MWCNTs (GF/CNT), treated in a 4 M KOH solution (GF/KOH), and subsequently immersed in a dispersion of MWCNT in 4 M KOH (GF/CNT/KOH).

4.1 Preparation and Characterization of MWCNT Dispersions

Ready-made MWCNTs must be disentangled and dispersed in a solution to profit from their intrinsic properties, making the use of solvents and surfactants inevitable.^[122-124] As a surfactant, a polymer can be used to non-covalently functionalize MWCNTs by a wrapping

mechanism.^[125-129] This approach allows a combination of dispersion, functionalization, and bonding of MWCNTs to a substrate.^[130,131] Carboxymethyl cellulose (CMC) was identified as the most suitable agent for a homogeneous coating of MWCNTs on GF. The stability and quality of the CNT/CMC dispersion in water were studied by UV-Vis spectroscopy and dynamic light scattering. **Figure 4-1a** reveals two absorption bands at ~ 265 and ~ 225 nm which can be assigned to an $n-\pi^*$ and a $\pi-\pi^*$ transition, corresponding to C=O groups, and C-C bonds in aromatic carbon rings, respectively, demonstrating the successful dispersion of MWCNTs.^[132]

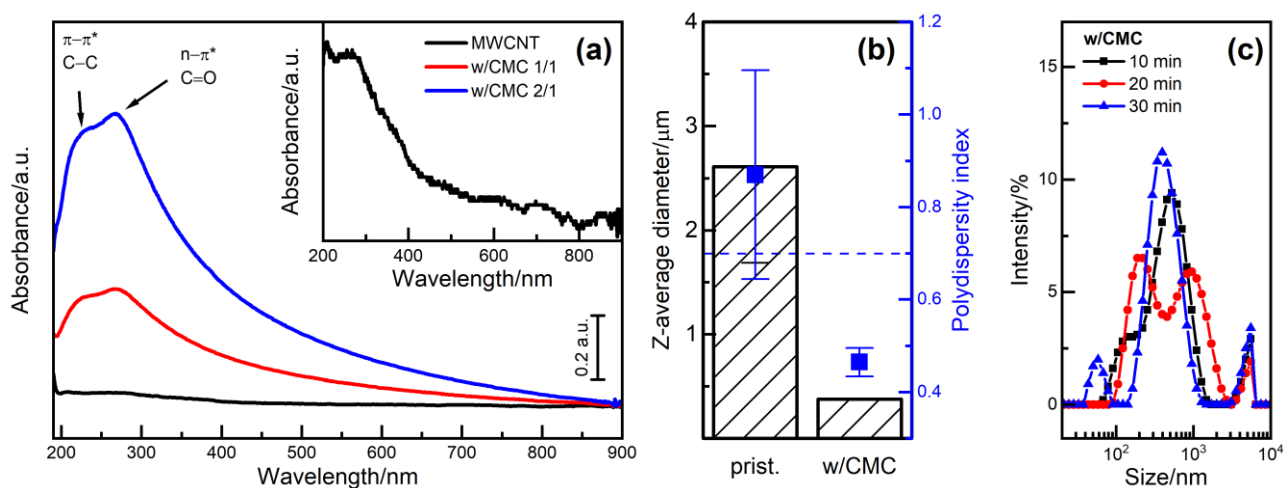


Figure 4-1. Optical property examination of CNT/CMC dispersions by **(a)** UV-Vis spectroscopy with different MWCNT contents, **(b)** DLS analysis of improved dispersion properties by addition of CMC, and **(c)** time-resolved particle size distribution of a successful dispersion.

The average particle diameter of the dispersions has been investigated by DLS (**Figure 4-1b**). By the addition of CMC, the average particle size is reduced from ~ 2600 to ~ 380 nm. The polydispersity index is a dimensionless factor that qualifies the size distribution of a dispersion. For the used device, dispersions showing an index < 0.7 are considered stable, which is fulfilled by the CNT/CMC (0.46) but not the pure MWCNT dispersion (0.87). The size distribution of the particles has been evaluated as a function of time (**Figure 4-1c**), showing that a small fraction of aggregates > 5000 nm is always present, whereas a major part of the particles is sized between 120 to 960 nm.

4.2 Morphological and Structural Characterization

The influence of the MWCNT impregnation and the KOH activation on the morphology, the samples were examined by SEM. Pristine GF (**Figure 4-2a-c**) consists of randomly entangled fibers with an average diameter of ~ 10 μm , possessing a smooth surface with narrow stripes

resulting from the spinning production process. The images of GF/CNT (**Figure 4-2d–e**) display no visible MWCNT aggregates in the pore space between the fibers. Instead, a uniform coating on the surface with smaller agglomerates of $<5\ \mu\text{m}$ in between is visible. High magnification images (**Figure 4-2f**) demonstrate the distribution of single MWCNTs and binder particles, which contribute to a rougher appearance. Out of all tested polymers, CMC showed the best distributing properties to obtain a homogeneous coating (**Figure S3**).

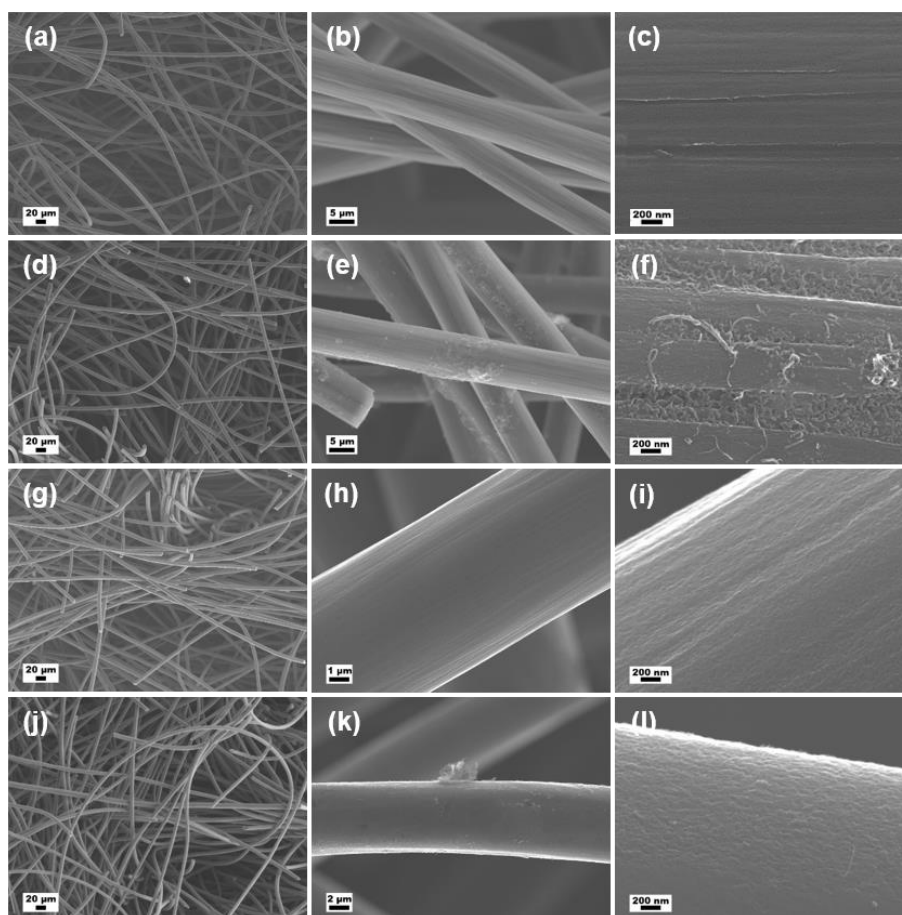


Figure 4-2. SEM images at different magnifications of (a–c) pristine GF, (d–e) GF/CNT, (g–i) GF/KOH, and (j–l) in combination treated GF/CNT/KOH.

The high magnification image of GF/KOH (**Figure 4-2i**) shows thorough roughening of the surface due to the activation process, revealing pores on the nanometer scale.^[56,133] In combination with the MWCNT impregnation, the roughening disguises the visibility of single MWCNTs because of the high edge surface contrast. However, smaller agglomerates of $\sim 3\ \mu\text{m}$ as in **Figure 4-2k** are visible. A close comparison of GF/KOH with and without MWCNTs (see **Figure 4-2i,l**) reveals a slightly fuzzier and fluffier appearance of the MWCNT impregnated fibers indicating that the GF/CNT/KOH sample is also homogeneously decorated with MWCNTs.

The influence on the microstructure was further investigated by XRD (Figure S4). After the KOH treatment, a weak Bragg reflection is located at $2\theta \cong 31^\circ$, which is associated with the residual K_2CO_3 formed during the activation. While the peak width of the graphitic 002 reflection ($2\theta \cong 26^\circ$) changes only slightly by $+0.3^\circ$, the interlayer distance is expanded from 3.48 to 3.63 Å according to Bragg's law due to intercalation of metallic potassium.^[134]

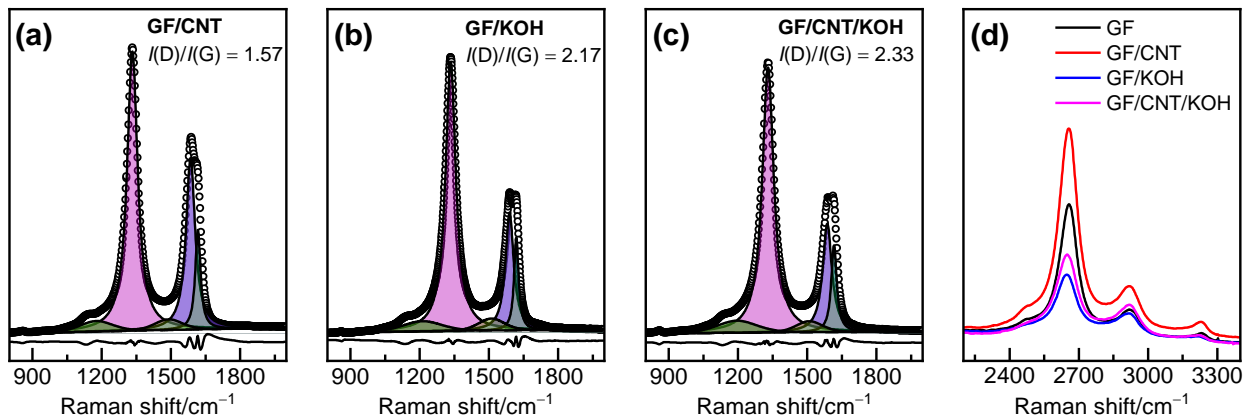


Figure 4-3. Deconvoluted Raman spectra of pristine and modified GF. **(a–c)** Detail spectra of the modified GF, and **(d)** the overtone modes in comparison. The given $I(D)/I(G)$ ratio is the average of at least three measurements per sample

Raman spectroscopy was used to investigate the degree of disorder, which is introduced on the felts by the used modifications (Figure S5). **Figure 4-3a–c** displays the deconvoluted first-order spectra of the modified felts, showing that the initial $I(D)/I(G)$ ratio of pristine GF (1.85) is increased to 2.17 by KOH etching, but to an even higher extent for GF/CNT/KOH (2.33). The reduction of disorder on GF/CNT (1.57) is attributed to the high graphitic character of single MWCNTs attached to the fiber, and probably their preferred attachment to fiber defect sites (such as to the spinning stripes in **Figure 4-2f**). The highly defective structure of GF/CNT/KOH is associated with additional defects created on the MWCNTs by KOH, and the different interaction characteristics between the basal plane of GF, and the nanostructured surface of GF/KOH with MWCNTs. The latter assumption is based on the analysis of the second-order modes (**Figure 4-3d**), where a more intense 2D band for GF/CNT indicates a strong interaction between single-atom graphitic layers.^[94] The aggressive attack on the structure induced by KOH is also visible in a decreased 2D band for GF/KOH and GF/CNT/KOH. As it was visible by SEM (**Figure 4-2i**), the KOH activation creates a nanostructured surface, thus providing access to the underlying edge site-oriented planes, and introducing defects into the basal plane on the outer surface of the felt. The origin of the observed defects is evaluated by the ratio of the D and the D' band, in which a ratio of ~ 3.5 corresponds to grain boundary defects such as edge

sites, and higher ratios to vacancy-like (~ 7) or sp^3 type (~ 13) defects.^[95] The ratios of our samples are between 2.56 (GF/CNT) and 2.91 (GF/CNT/KOH), which is why we characterize the defects as edge site like. Due to a ratio < 3.5 , there are multiple edge sites present in a so-called loop configuration.^[135]

4.3 Surface Chemistry

The surface chemical composition was studied by XPS to compare the OFGs qualitatively and quantitatively (Figure S6). Detail spectra were recorded for the core level regions O 1s and C 1s (**Figure 4-4**). Three main oxygen species were identified: O–C (hydroxyl groups) at binding energies of ~ 532.8 eV, O=C (carbonyl groups) at ~ 531.6 eV, and O=C–OH (carboxylic groups) at 533.9 eV.^[136] Adsorbed water is present on all felts above 535 eV. The water content increases after KOH activation from below 0.2 to 0.5 at%, suggesting improved wetting properties.^[56] After the KOH treatment, residual carbonate groups are present at 530.6 eV and 292.9 eV. The concentration of oxygen in comparison to the total carbon–oxygen content and the share in one specific oxygen group within the three OFGs was evaluated (**Table 5**). By the attachment of MWCNTs to GF (~ 11 at%), the overall oxygen content is reduced to ~ 8 at%, and a higher amount of sp^2 hybridized carbon (~ 81 at%) is present (Figure 4-4d). After the KOH etching, the oxygen concentration is further reduced to ~ 6 and ~ 7 at% for GF/KOH and GF/CNT/KOH, respectively. According to the C 1s region, the relative amount of sp^2 hybridized carbon is even increased from ~ 57 at% on GF to about 60 and 62 at%. This can be explained by the exposure of underlying graphite sheets due to the etching treatments, which reveal a lower oxygen coverage than the pristine surface layers of GF.

Table 5. Initial chemical composition of the pristine and modified GF regarding the amount of OFGs. The composition compared to all surface species (including carbon, rounded to 0.5 at%) and the relative composition regarding the three main functional groups (O–C, O=C, O=C–O, rounded to the full percentage) is given.

Sample	O–C (at%)	O=C (at%)	O=C–O (at%)	O–C (rel. at%)	O=C (rel. at%)	O=C–O (rel. at%)
GF	4.5	6	1	40	53	7
GF/CNT	4.5	1	2	59	17	25
GF/KOH	2	2.5	0.5	53	34	15
GF/CNT/KOH	2	1.5	0.5	40	47	13

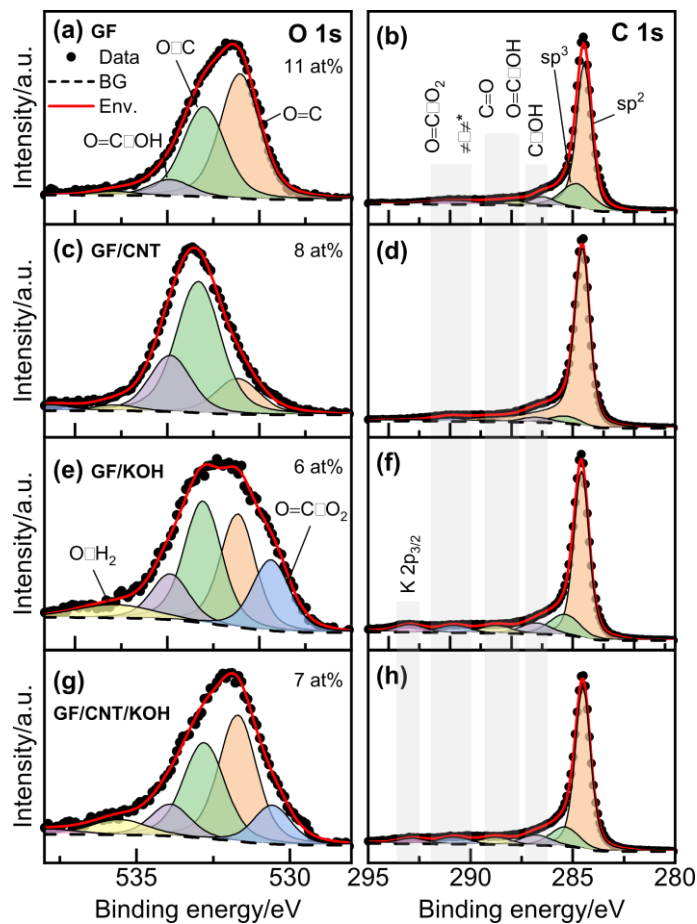


Figure 4-4. Deconvoluted XPS data of the O 1s and C 1s regions of **(a–b)** pristine GF, **(c–d)** GF/CNT, **(e–f)** GF/KOH, and **(g–h)** GF/CNT/KOH. The regions were subtracted by a Shirley background and single species fitted by Gaussian–Lorentzian peak shapes. The concentration of surface oxygen for each sample is given.

The C 1s region exhibits five different carbon components, related to sp^2 and sp^3 hybridized carbon at ~ 284.5 eV and ~ 285.2 eV, along with hydroxyl, and carbonyl/carboxylic groups at ~ 286.6 eV and ~ 287.8 eV.^[58,137] It was not further differentiated between carbonyl and carboxylic groups since the assignment of binding energies for the respective species is ambiguous in literature.^[78,138–141] The discrimination is further impeded by the relatively low intensity of the single oxygenated (carbon species (<5 at%) compared to the strong signal of sp^2 carbon (>57 at%). At higher binding energies of 289.0 to 291.7 eV, it was close to impossible to distinguish between carbonate, adsorbed atmospheric carbon components, and the shake-up satellite feature associated with graphitic carbon, all present at about 291 eV.^[136,138]

4.4 Electrical Conductivity

The influence of the felt modifications on the electrical properties has been evaluated by performing pressure-dependent conductivity measurements (**Figure 4-5**). To guarantee a

homogeneous potential distribution for a felt electrode, the fiber conductivity, which relies heavily on the fiber–fiber interface, should be high.^[142,143] The compression inside a battery minimizes ohmic losses, while the permeability of flowing electrolyte through the pores should be maintained.^[144]

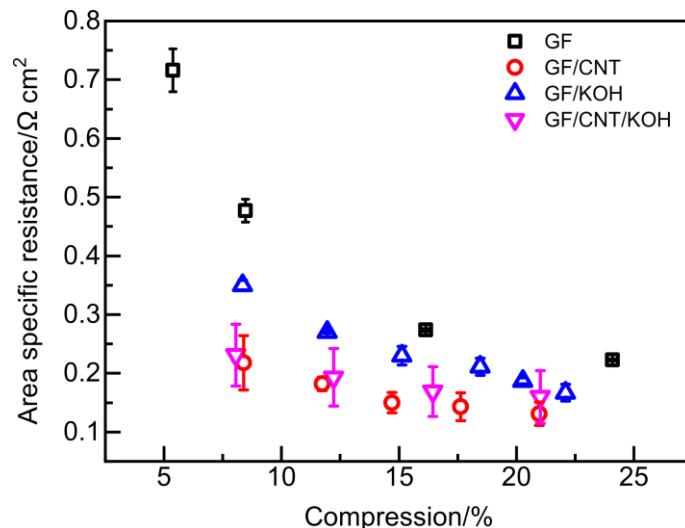


Figure 4-5. Electrical area specific resistance of pristine and modified GF under compression.

The felts reveal an initial resistivity drop, which is associated with the creation of interfacial contact between the fibers and the measurement device. Subsequently, the mere electrical property of the felt material is observed.^[145–147] GF shows a severe resistivity decrease when compressed by 15% of the total thickness, followed by a slight decrease thereafter to 22 mΩ cm². The MWCNTs decrease not only the contact resistance of GF/CNT (22 mΩ cm² at ~8% total compression) but also increase the intrinsic conductivity (13 mΩ cm² at ~21% total compression). The nanostructured surface of GF/KOH creates more contact points between the fiber and the measurement device, which reduces the interfacial contribution to the resistance. For GF/CNT/KOH, the resistivity at ~20% total compression is decreased from 19 for GF/KOH to 16 mΩ cm². Considering the deviation of GF/CNT/KOH, the MWCNTs cannot enhance the electrical conductivity of the felt electrode completely homogeneously, which might arise because of the lower mechanical stability in the investigated region (Figure S7).

4.5 Electrocatalytic Half-Cell Activity

To study the influence of the sample modifications, which created edge sites and OFGs in various concentrations, electrochemical half-cell tests were performed. The electrocatalytic properties were studied by CV. In each obtained voltammogram, the peak separation potential (ΔE_p)

and the peak current ratio of the oxidation and reduction peaks are used to study the activity and redox reversibility.

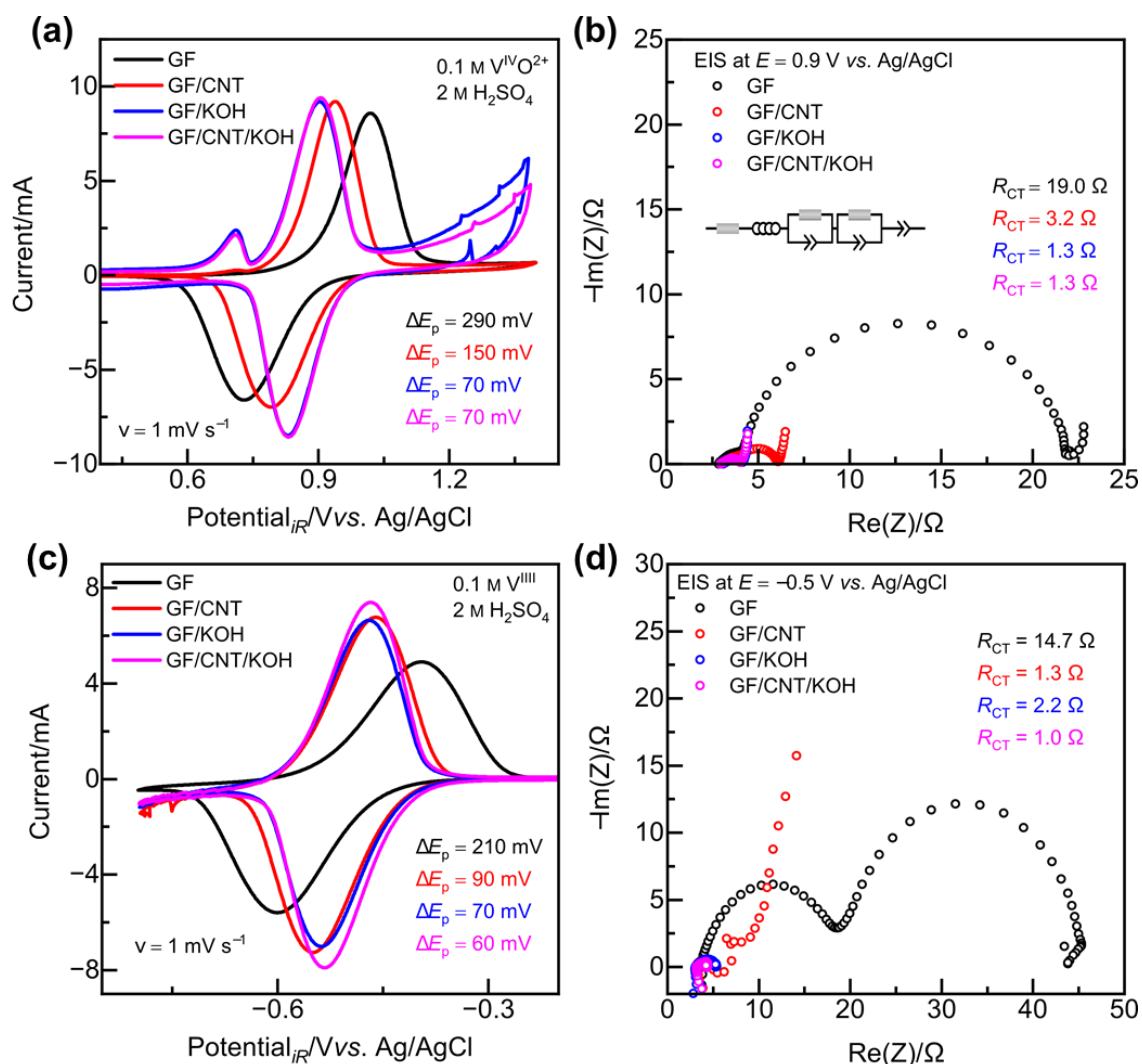


Figure 4-6. Electrochemical characterization of the pristine and the modified GF electrodes in the **(a,b)** positive and **(c,d)** negative half-cell. (a) iR -corrected CV with 1 mV s^{-1} ; (b) EIS at $0.9 \text{ V vs. Ag/AgCl}$, also displaying the equivalent circuit diagram used for spectral deconvolution; (c) iR -corrected CV with 1 mV s^{-1} , (d) EIS at $-0.5 \text{ V vs. Ag/AgCl}$.

For the positive half-cell, a reduction of ΔE_p from GF (290 mV) to GF/CNT (150 mV) is observed, which is according to the XPS, Raman spectroscopy, and resistivity results a consequence of the higher electrical conductivity of the felt electrode (**Figure 4-6a**). For catalytically more active samples, a sharp oxidation signal at $0.7 \text{ V vs. Ag/AgCl}$ and a broad reduction at 0.2 to $0.6 \text{ V vs. Ag/AgCl}$ corresponds to the $V^{IV}O_2^+/V^{III}$ redox reaction (Figure S9). The electrochemical performance of GF/KOH depends on the molarity of the KOH solution, the drying procedure, and subsequent heating temperature, and has an optimized ΔE_p of 70 mV (Figure S10).^[56,133,148] No further electrocatalytic improvement is observed by combining the KOH activation and the

impregnation with MWCNTs. Compared to the XPS and Raman results, the samples exhibiting the highest electrocatalytic activity showed low oxygenation and an increased number of edge sites.

The R_{CT} was evaluated by EIS at an applied potential. In the Nyquist representation (**Figure 4-6b**), the main semicircle corresponds to the R_{CT} , which is significantly reduced from 19.0 Ω (GF) over 3.2 Ω (GF/CNT) to 1.3 Ω (GF/KOH and GF/CNT/KOH). The R_{CT} is decreased by all modifications, but to the highest extent for those samples that revealed a lot of edge sites and a lower oxygen concentration. The MWCNTs provide good charge transfer, which could be related to the high electrical conductivity and low interfacial resistance since fewer edge sites were observed for this sample. A more detailed discussion on the reversibility of the redox reaction and the mass-transfer properties can be found in Figure S12 and Figure S13.

Based on the electrochemical analysis of the positive half-cell, it can be concluded that the activity of GF is enhanced both by the MWCNT application and KOH activation. There was almost no difference observed between the KOH treatment of GF only and in combination with the MWCNTs. For these two samples, neither the relative amount of one specific OFG (O–C on GF/KOH and O=C on GF/CNT/KOH), nor the difference in defect density (2.17 and 2.33) has a major impact on the $V^{VO_2^+}/V^{IVO^{2+}}$ redox reaction. If one considered carboxylic groups to drive the positive half-cell redox reaction, GF/CNT would outperform the other samples, which was not the case.

The negative half-cell reaction was also inspected by the same electrochemical techniques. The CV curves in **Figure 4-6c** display an improvement of the redox activity, reducing the peak potential separation in the order GF (210 mV) > GF/CNT (90 mV) > GF/KOH (70 mV) > GF/CNT/KOH (60 mV). This proves that all modifications also have a positive effect on the electrocatalytic activity for the V^{III}/V^{II} redox reaction. In the Nyquist plots (**Figure 4-6d**), R_{CT} decreases from 14.7 Ω (GF) to 2.2 Ω (GF/KOH), 1.3 Ω (GF/CNT), and 1.0 Ω (GF/CNT/KOH). At lower frequencies, a second semicircle is visible for GF, which is assigned to a $V^{IVO^{2+}}/V^{III}$ reduction process of residual higher oxidized vanadium species. In summary, the combination of KOH etching and MWCNT impregnation has a positive effect compared to only one of the methods, which one might therefore ascribe to either the higher (or lower) concentration of one specific OFG or additional edge sites on the electrode which are beneficial for the charge transfer and electrocatalytic activity since the defect-poor GF/CNT with the higher oxygen concentration reveals the lowest improvement.

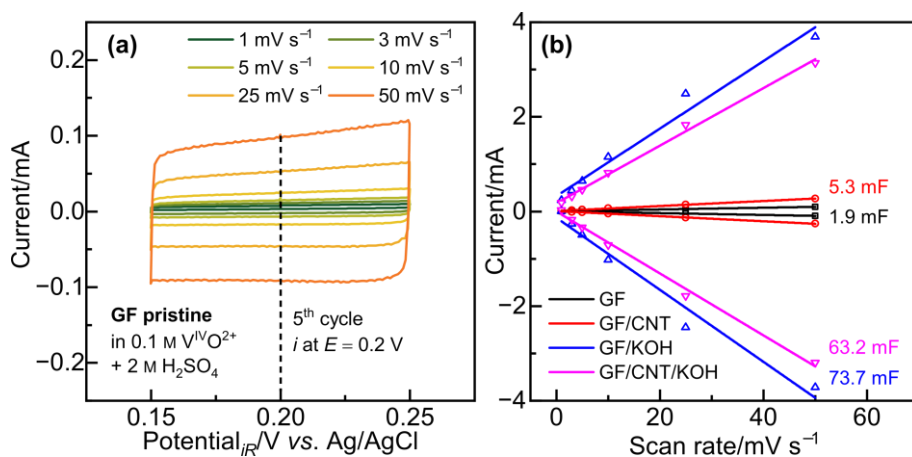


Figure 4-7. EDLC of pristine and modified GF. **(a)** CV in a non-faradaic potential range at different scan rates. **(b)** Plot of currents at a potential of 0.2 V vs. Ag/AgCl for each given scan rate.

In addition to the electrocatalytic activity, the electrochemical active surface area has been investigated in a non-faradaic potential region to probe the electrochemical double-layer capacitance (EDLC, **Figure 4-7**). A relatively low initial EDLC of ~ 2 mF (GF) is significantly enhanced by more than 30 times for GF/CNT/KOH (~ 63 mF). The increase is attributed to the enhancement of the overall surface area by etching a microporous structure and by attaching high surface MWCNTs, which can provide additional active sites. Furthermore, more edge sites are introduced to the graphitic structure of the electrode as well as on the MWCNTs, which relates to the higher EDLC of edge planes ($\sim 70 \mu F cm^{-2}$) compared to basal planes (1 to $2 \mu F cm^{-2}$) of graphite.^[56,149,150] For this reason it is surprising that the EDLC of GF/KOH is even higher (~ 74 mF), though it revealed a lower number of defects in Raman spectroscopy. Further studies towards the phenomena of the EDLC, its relation to the active surface area, and the influencing factors are intended. The XPS results already implied that the initial relative amount of oxygen does not play a major role when the active surface area is explored.

4.6 Evolution of OFGs and Defects in Electrochemistry

The initial concentration of oxygen or the number of specific functional groups did not explain the differences in half-cell activity. Considering ΔE_p and R_{ct} , the activity for the positive half-cell would be in the order GF/CNT/KOH = GF/KOH > GF/CNT > GF, and likewise (the first exceeding GF/KOH) in the negative half-cell. Based on the XPS analysis (**Table 5**), one would expect activities for the positive half-cell in the order GF/CNT > GF > GF/CNT/KOH > GF/KOH for carboxylic groups. For hydroxyls as active species, it would be GF > GF/CNT > GF/KOH > GF/CNT/KOH. However, none of these sequences is reflected in electrochemistry. Moreover,

by comparing the relative stoichiometry of OFGs to each other, it is not possible to reflect the above-mentioned sequences. On the contrary, an increase of surface groups rather seems to impede the electrocatalytic activity. To better understand the influence of the electrochemical conditions on the OFGs, their evolution was studied by XPS after cycling. The deconvoluted O 1s and C 1s detail spectra of all samples are displayed in **Figure 4-8a-d** and Figure S14.

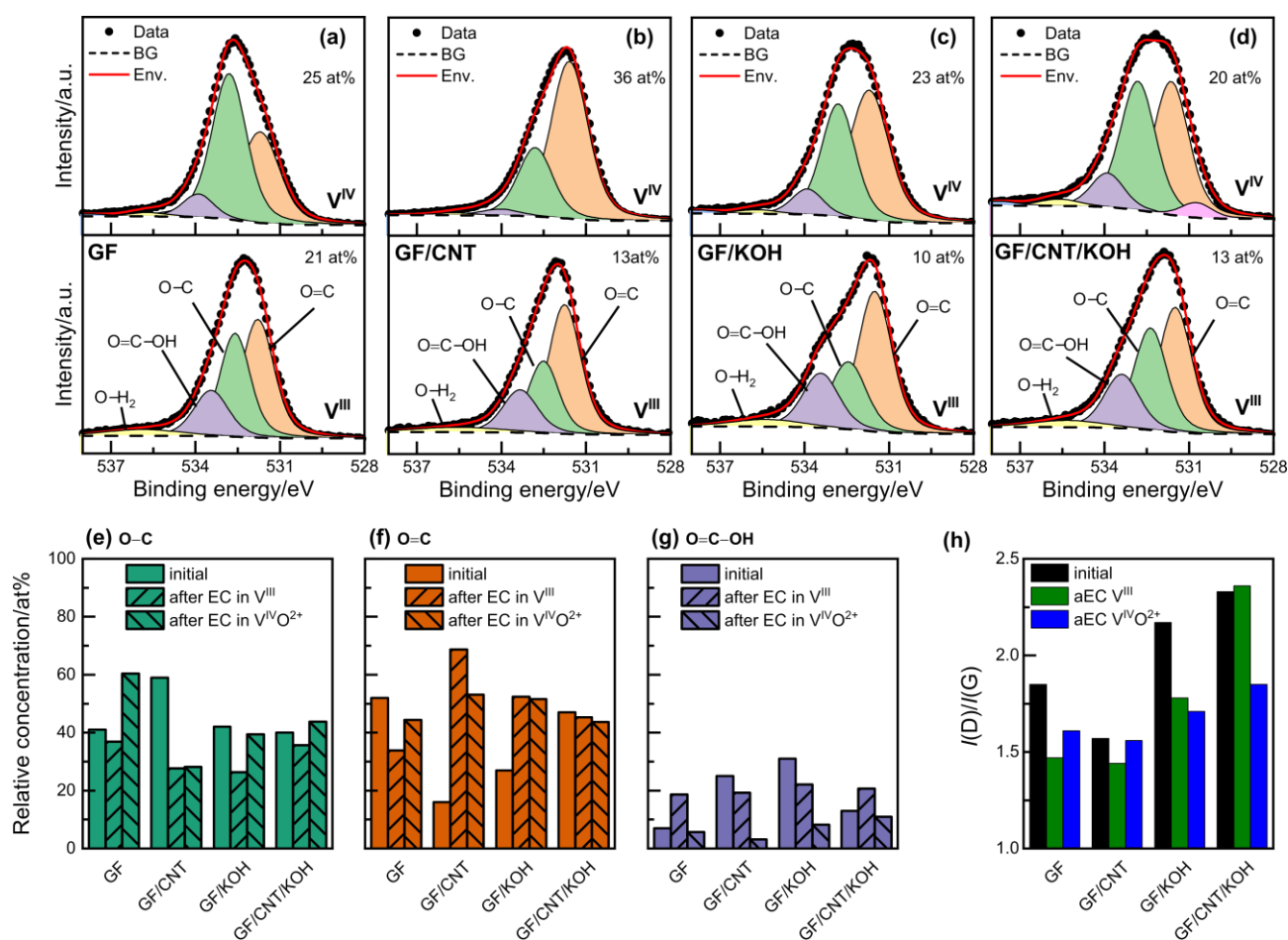


Figure 4-8. Analysis of pristine and modified GF after cycling regarding their number of OFGs and defects. O 1s spectra of (a) GF, (b) GF/CNT, (c) GF/KOH, (d) GF/CNT/KOH. Comparison of the relative number of OFGs, namely (e) hydroxyl, (f) carbonyl, and (g) carboxylic groups. (h) The defect structure studied by Raman spectroscopy, evaluating the $I(D)/I(G)$ ratios before and after cycling in each half-cell.

After cycling in the positive half-cell, the relative oxygen content increases from ~ 6 to 11 at% for the initial samples by around a factor of three for the cycled electrodes. This effect is most pronounced for GF/CNT with >35 at%, whereas the other samples have a very similar quantity of surface oxygen (~ 20 to 24 at%). Therefore, the oxygen concentration alone cannot explain the different electrochemical activities. To study the influence of single OFGs, their concentration profile has been analyzed quantitatively, comparing the relative percentage values of O-C, O=C, and O=C-OH in the initial state and after electrochemistry (**Figure 4-8e-g**).

On the one hand, GF/CNT has the lowest relative number of hydroxyls after cycling (28%). On the other hand, the highest concentration of hydroxyls after electrochemistry is present on GF (60%), which revealed the lowest half-cell activity. Both GF/KOH and GF/CNT/KOH, which showed an equal electrochemical performance, have values in between. Most of the oxygen on GF/CNT consists of carbonyl (~69%) and only ~3% of carboxylic groups. GF/KOH and GF/CNT/KOH developed lower amounts of carbonyls (52% and 45%) with more persistent carboxylic groups (8% and 11%). It is seen that the relative concentration of GF/KOH undergoes some severe changes during cycling (especially for C=O and O=C-OH groups), while GF/CNT/KOH has a similar share in OFGs compared to the initial sample. One might argue that the higher activity of GF/CNT compared to GF is attributed to the severe reduction of electrical resistance, which compensates for the lower number of active carboxylic groups. However, this would be expected to mainly influence the R_{CT} , but also an impact on the EDLC was observed.

Since the XPS results were not in itself conclusive, the degree of disorder after electrochemistry has been investigated by Raman spectroscopy (**Figure 4-8h** and Figure S15). The stability of edge sites is important even for OFGs, since they are far more stable on edges rather than on basal planes.^[71] After cycling in the positive half-cell, all samples lose a severe number of edge sites, reflected by a decrease of the $I(D)/I(G)$ ratio. Considering the degree of disorder, the minor electrochemical performance of GF mostly is related to its lower number of defects (1.61). More persistent carboxylic groups are formed on GF/KOH and GF/CNT/KOH, which correlates with their increased defect density (1.71 and 1.85). Conclusively, the degree of disorder accounts for the higher electrocatalytic activity of these samples in the positive half-cell. The minor differences in the chemical composition regarding the number of carboxylic groups are not expected to drive such high discrepancies in the electrochemical performance. It is much rather a consequence of their primary formation on edge sites if the correlation to the overall disorder is considered. Due to the decrease of edge sites during oxidative treatment in the positive half-cell, we suppose that other oxygen groups, as the concentration of carboxylic groups also decreases, are attached to active edge sites and hinder the electron transfer subsequently.

The negative half-cell was analyzed in the same manner. Cycling in V^{III} introduces fewer oxygen moieties (~10 to 13 at%) for the modified felts, while pristine GF had a considerably larger oxygen content of >20 at%. This observation suggests that, also for the negative half-cell, the relative amount of oxygen is a property that describes the activity of the graphite felt electrodes poorly. Therefore, the composition of single OFGs has been evaluated, showing that the surface composition of all felts is relatively similar, with about 19 to 22% carboxylic, 44 to 53%

carbonyl, and 26 to 37% hydroxyl groups. Again, no clear correlation between the relative concentration of a certain OFG and the electrochemical activity of the electrodes could be established. A possible explanation for this observation might be that the activity of certain OFGs for the V^{III}/V^{II} redox reaction seems to depend on whether they are attached to basal or edge site positions and the higher catalytic activity was attributed to oxygen-containing edge site defects.^[34,68,151] Hence, it is important to further examine the change in disorder after electrochemistry. The $I(D)/I(G)$ ratio is affected by cycling, which leads to a decrease of defects on GF (1.47), GF/CNT (1.44), and GF/KOH (1.78) while the amount of edge sites is increased on GF/CNT/KOH (2.36). Recalling the previous discussion on the positive half-cell, the observations again seem to be consistent with the importance of stable edges. Due to the minor differences in the surface chemical composition observed by XPS, we conclude that graphitic edge sites appear to be the major driving force for the negative half-cell reaction. Even though OFGs form on the surface of GF during electrochemical cycling, their positive influence on the negative half-cell reaction cannot be confirmed by our study. Instead, the evolution of the defect density on the surface appears to be a more important indicator for the electrocatalytic activity.

4.7 Conclusions

The role of graphitic edge sites and OFGs and their electrochemical stability in both half-cells of a VFB was examined. My chosen GF treatments resulted in samples with a different concentration of oxygen moieties and disorder. The disorder was characterized as edge site defects for all samples. By XPS and Raman spectroscopy after half-cell tests, it was confirmed that the OFGs and edges evolve dynamically during cycling. The electrochemical performance of an electrode can thus not only be correlated with its physicochemical properties in the pristine state. Neither the total concentration of OFGs nor the presence of a certain bonding type could be made responsible for the electrocatalytic activity. Instead, the more active electrodes revealed a lower oxygen concentration and simultaneously a higher number of edge sites. There was a correlation between the activity and the electrochemical stability of edges and attribute this as beneficial towards the $V^{VO_2^+}/V^{IVO_2^+}$ and V^{III}/V^{II} redox reactions. Consequently, this study highlights the importance of edge site defects for the vanadium redox kinetics. Although it cannot be ruled out that certain OFGs are active during the reaction, edge site defects seem to play an essential role either by stabilizing favorable OFGs or by directly assisting the charge-transfer process.

5 Origin of the Electrocatalytic Activity at Graphite

After having conclusively shown that electrochemically stable graphitic edge sites are required to successfully change the oxidation states of solvated vanadium ions, the role of OFGs will now be clarified. By conventional electrode activations, it is not possible to completely rule out the influence of OFGs at the start of electrochemical cycling. Therefore, a different approach was taken: While usually the oxygen concentration is increased by a pretreatment, GF herein was thermally deoxygenated according to a procedure specified in **Figure 5-1a** to investigate the changes in activity thereafter.

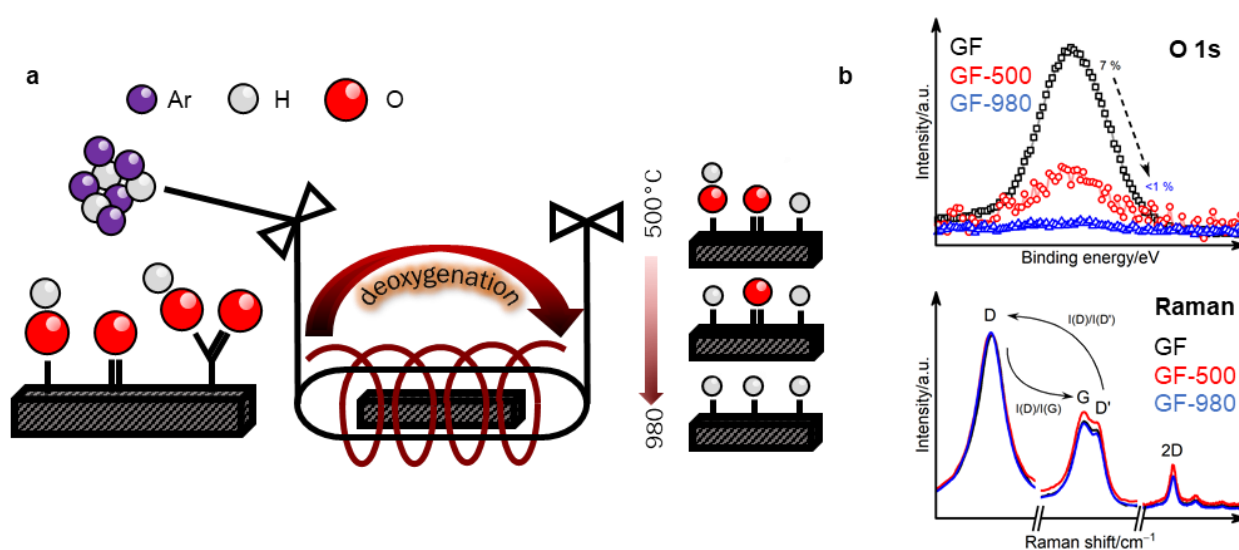


Figure 5-1. Schematic representation of the experimental procedure. **(a)** Deoxygenation of GF in a sealed glass tube under Ar/H₂ atmosphere at different temperatures. **(b)** Subsequent *quasi in situ* XPS and Raman spectroscopy.

This procedure allowed to observe chemical surface changes without attacking the structure and to study the influence of various OFGs because of their different decomposition temperatures (**Figure 1-3**). The influence of the deoxygenation procedure on rather inactive pristine GF and highly performant, surface activated felt (GF-SA) which was thermally oxidized by the manufacturer, was considered. The evolution of the electronic structure and the microstructure was monitored by *quasi in situ* XPS and Raman spectroscopy (**Figure 5-1b**). After the evaluation of the respective half-cell activity, the evolution of OFGs and defects was selectively characterized after immersion in the electrolyte and polarization experiments to tackle the relevant conditions for the formation of surface oxygen. Furthermore, the long-term cycling effect and stability of the deoxygenation procedure was studied.

5.1 Influence of the Deoxygenation on the Electronic Structure

After thermal deoxygenation, the chemical composition of GF was studied by *quasi in situ* XPS (Figure 5-2 and Figure S16–Figure S18). The thermal, chemical, or hydrothermal deoxygenation of graphene oxide has been intensely studied by multiple methods.^[152–154] A precise understanding of these mechanisms on GF is given for the first time. The C 1s region of mixed sp^2/sp^3 hybridized carbon is difficult to evaluate, which is why a semi-quantitative method by the first derivative of the C KLL Auger region (Figure 5-2a) is used to approximate the overall carbon bonding state. For sp^3 hybridized carbon-based materials such as diamond, the so-called D-parameter has a minimum of ~ 13 eV, while graphite-like materials have higher energy gaps of up to 23 eV.^[155–157]

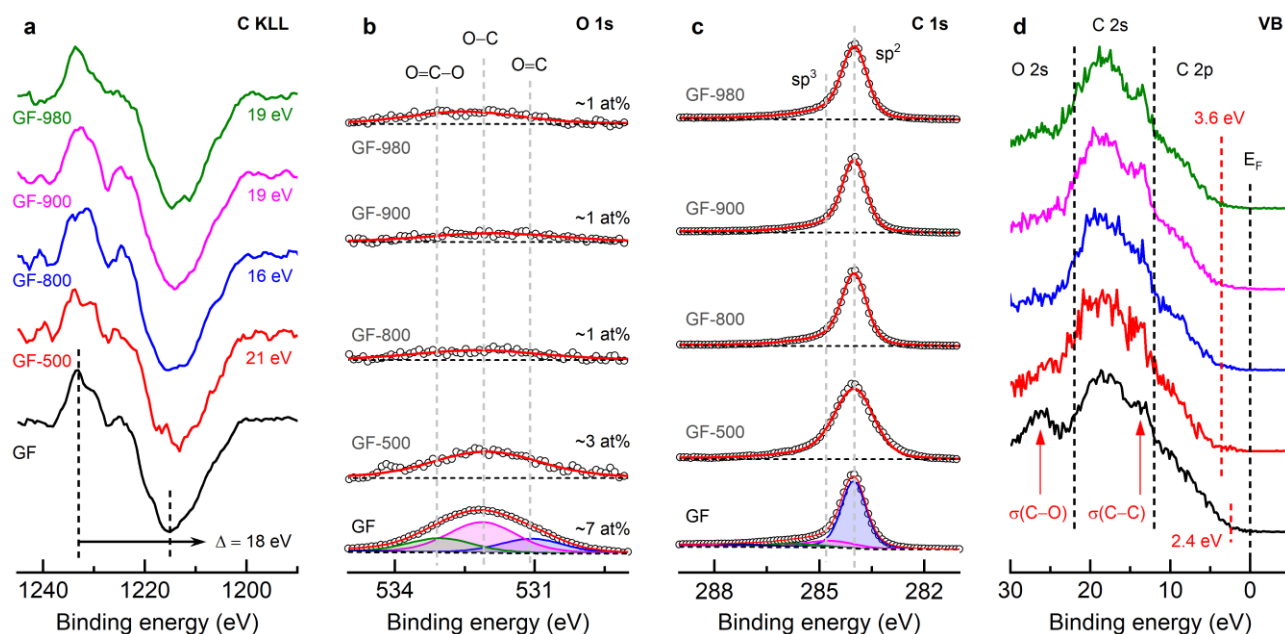


Figure 5-2. XPS investigation of thermally deoxygenated GF. **(a)** First derivative of the C KLL Auger region to determine the D-parameter. **(b)** O 1s detail spectra, showing the position of the respective oxygen group and the relative oxygen content. **(c)** C 1s detail spectra, indicating the position of sp^2 and sp^3 hybridized carbon. **(d)** VB region, displaying the O 2s, C 2s and C 2p regions and the E_{VB} .

At temperatures ≤ 500 °C mostly basal plane bound hydroxyl and carboxylic groups, and amorphous carbon are removed, while the π -conjugated structure of graphite is restored, resulting in the high sp^2 content for GF-500 (21 eV).^[158,159] At higher temperatures, the relative sp^3 content increases (16 eV) because of the conversion of covalently bound ether (C–O–C) to edge site located carbonyl and phenyl groups.^[152] Above 900 °C (19 eV), some of these oxygen groups are removed, and the share in sp^2 carbon rises again.

In the O 1s spectra, it is observed that the overall oxygen concentration on the surface decreases with temperature (**Figure 5-2b**). On the initial sample, three different oxygen components were identified: O=C (oxygen doubly bounded to carbon in carbonyls) at ~ 531.1 eV, O-C (singly bounded oxygen, C-O-C in ether and C-OH in hydroxyls) at ~ 532.1 eV, and O=C-O (oxygen bound as carboxylic acid) at ~ 533.1 eV.^[137,160,161] The high binding energy oxygen component is regularly also assigned to phenyl groups (oxygen singly bounded to aromatic carbon).^[152,162,163] Even temperatures >1000 °C do not sufficiently remove phenyl groups because of their thermodynamically stable presence between layers of graphite.^[163-165] Six different peak contributions in the C 1s region (**Figure 5-2c** and **Figure S17**) are visible on GF: sp^2 hybridized carbon at 284 eV, sp^3 carbon at 284.8 eV, ether and hydroxyl groups at 286.3 eV, carbonyls at 287.6 eV, carboxylic groups at 289.2 eV, and the sp^2 carbon-related shake-up satellite at 291.2 eV.^[58,152,166,167] The regions after deoxygenation were deconvoluted by one sp^2 component and the high binding energy $\pi-\pi^*$ feature. At temperatures ≥ 800 °C, the full width at half maximum (FWHM) of sp^2 carbon decreases from 1.3 eV (GF-500) to 0.8 eV (as originally on GF), indicating the absence of sp^3 hybridized components. All three regions, in conclusion, suggest the conversion of oxygen from surface groups (sp^3) to ether (sp^2) to terminal groups (sp^2) and their removal thereafter.

Additional information is gained by the low binding energy and valence band (VB) region (**Figure 5-2d**). The domain at 2 to 12 eV above E_F is occupied by C 2p, up to 22 eV by C 2s, and beyond contributions from O 2s electrons are observed.^[152,168,169] The onset of the C 2p threshold-edge allows the evaluation of the electronic DOS close to E_{VBM} . All samples show a non-zero DOS between 0 to 3 eV because of $2p-\pi$ electrons present in the π -conjugated basal plane.^[170] The heat-treated samples show an increased E_{VBM} of 3.6 eV compared to the pristine material (2.4 eV), since the deoxygenation increases the sp^2 content, which itself has a positive effect on the in-plane electron transfer, but not perpendicular to the plane because of the absence of bridging bonds. At ~ 13 eV the 2s σ (C-C) electron states are identified as an especially distinct feature ≥ 900 °C instead of merging with the subsequent C 2s signal, followed by the main C 2s peak at ~ 18 eV.^[168,170,171] A prominent signal in the O 2s region associated with oxygen bound to the aromatic carbon lattice [σ (C-O)] disappears after deoxygenation.^[152,170,172] Interestingly, this feature reappears on GF-980 with a lower separation to the C 2s peak because of phenyl instead of primarily C-O-C or C=O groups being present.^[152]

The same investigation was conducted for GF-SA (**Figure S18**). This material initially has a lower sp^2/sp^3 ratio (D-parameter = 17 eV), attributed to the prior oxidative heat treatment.

The sp^2 character is then restored on GF-SA-980 (21 eV). For GF-SA-800 and above the oxygen concentration decreases (from 10 at% to ~ 1 at%), and the overall appearance of the O 1s and C 1s region is like the GF row. GF-SA has a higher populated DOS ($E_{\text{VBM}} = 1.9$ eV), shifting to 3.7 eV directly after the first heating step and not changing thereafter. The 2s $\sigma(\text{C-C})$ contribution is less distinct, which we contribute to irreversible damage of the graphitic network because of the oxidative treatment.

5.2 Microstructural Properties

The difference in morphology between pristine GF and thermally activated GF-SA was visualized by SEM (**Figure 5-3a-c**). The felts consist of randomly entangled fibers of ~ 10 μm in diameter (**Figure 5-3a**). Singular fibers of both felts were directly compared, which revealed numerous porous defects induced by the thermal activation on GF-SA (**Figure 5-3b,c**).

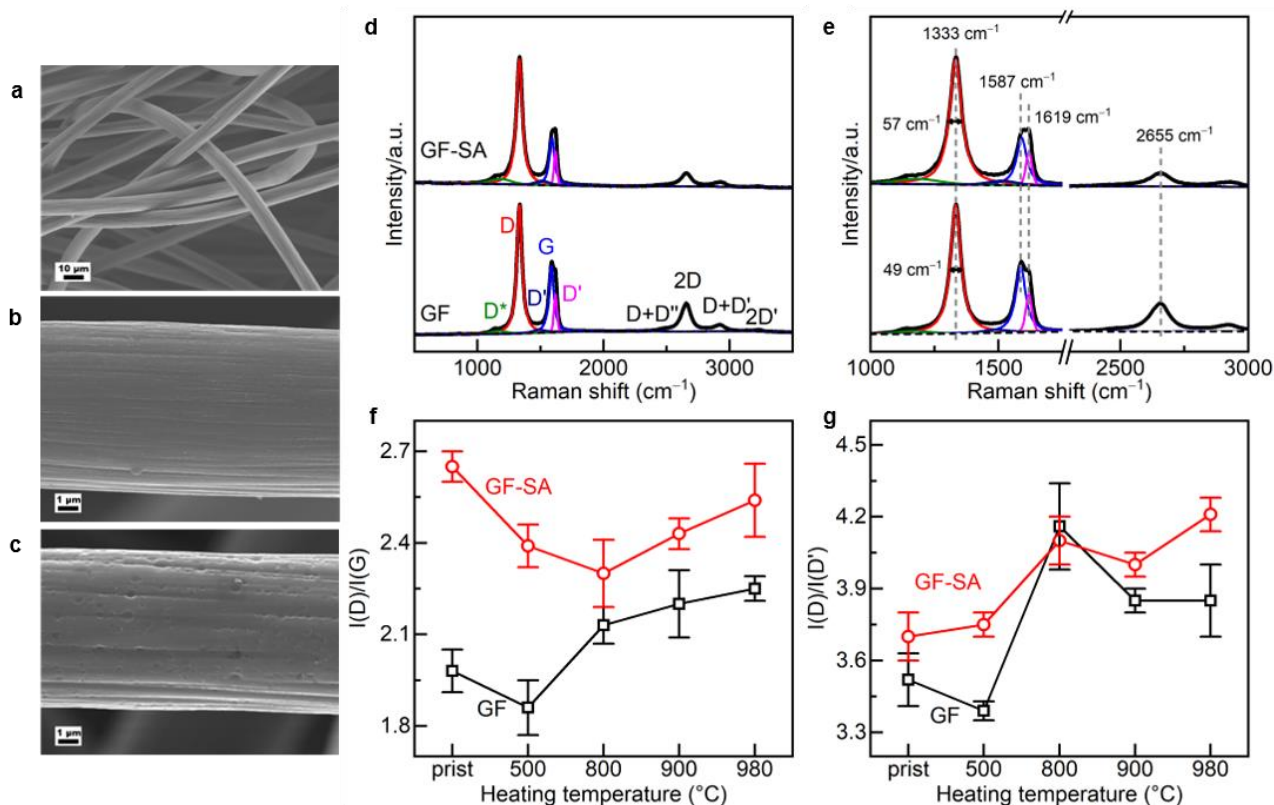


Figure 5-3. Microstructural properties of GF before and after deoxygenation. (a-c) SEM images of (a,b) GF and (c) GF-SA. (d-g) Raman spectra of GF, GF-SA, and the thermally deoxygenated felts. (d,e) First- and second-order modes of GF, indicating the respective vibrational features and their positions; additionally, the FWHM values of the D band is given. (f) $I(\text{D})/I(\text{G})$ ratio and (d) $I(\text{D})/I(\text{D}')$ ratio of the felts regarding the prior heating temperature.

These pores greatly enhance the surface area, which was verified by BET measurements. An increase by a factor of 5.3 (from about 0.64 m^2 g^{-1} to 3.41 m^2 g^{-1}) was observed, indicating that

the oxidative attack exposes additional graphite layers. To make sure that the deoxygenation treatment had no influence of the microstructure, GF-980 and GF-SA-980 were analyzed by SEM (Figure S19), revealing no visible difference compared to the initial samples.

To analyze the induced disorder, the oxidized and deoxygenated felts were investigated by Raman spectroscopy (**Figure 5-3d,e** and Figure S20). The $I(D)/I(G)$ value (**Figure 5-3f**) of GF (1.98) first decreases to 1.86 (GF-500), but then steadily rises to 2.25 (GF-980). In accordance with the XPS results, the first deoxygenation of the material results in a higher share of sp^2 carbon due to the removal of basal plane bound oxygen and the rearrangement of graphitic layers. Continuous deoxygenation creates more defects, which are recognized as disorder in contrast to oxygenated edge sites which do not always correspond to a high D to G ratio.^[173,174] The increased $I(D)/I(D')$ ratio of GF (3.52 to 4.20) in **Figure 5-3g** suggests the generation of vacancies at 800 °C. Higher temperatures counteract and heal these vacancies partly which is seen by a decreased ratio.

The band positions on both original samples are the same, but for GF-SA the D band is more, and the 2D signal is less pronounced, which indicates a higher degree of disorder and weaker interaction between intact graphitic layers for the activated felt.^[94] The higher FWHM of the D band for GF-SA (from 49 to 57 cm^{-1}) is attributed to its more defective structure. With ongoing deoxygenation, the FWHM of the D band does not change by more than $\pm 1 \text{ cm}^{-1}$ for GF, but decreases by 4 cm^{-1} for GF-SA which indicates partial healing of oxygenation damage (Figure S20). The evolution of the $I(D)/I(G)$ ratio of GF-SA (2.65) follows a similar trend as GF with a decrease up to 800 °C (2.30), followed by an increase to 2.54 at 980 °C confirming an increase of deoxygenated defects also for the GF-SA sample series. The higher D to D' ratios suggests that even before deoxygenation, the defects on GF-SA (3.70) are more related to edge sites, but deoxygenation further increases the number of vacancies up to GF-SA-980 (4.21).

In summary, up to a certain deoxygenation temperature (500 °C for GF and 800 °C for GF-SA, seemingly depending on the initial defect density) the disorder is first reduced, and rearrangement of the basal plane occurs. At higher temperatures, two effects were observed: (i) the deoxygenation of edge sites leads to an increased D to G ratio due to their larger Raman scattering cross-section. (ii) Defects created at higher temperatures can be partially attributed to vacancies. Furthermore, the comparison with the XPS results demonstrates that this occurs while a high sp^2/sp^3 ratio is maintained.

5.3 Influence of OFGs on the Electrochemical Half-Cell Performance

To study the correlation between the electrocatalytic properties and the decreasing degree of deoxygenation, the electrochemical half-cell performance was examined in a three-electrode cell. Several features of the recorded CV data (Figure S21) were examined. The reversibility of the redox reaction was investigated by the peak current ratio between the oxidation and reduction reaction (Figure 5-4a,b), while the electrocatalytic activity was studied using ΔE_p (Figure 5-4c). Furthermore, the influence of the deoxygenation on the electrochemical active surface area, which is linked to the EDLC, was examined (Figure 5-4d and Figure S22).^[175,176] In addition, the R_{CT} values were assessed in both half-cells by EIS (Figure 5-4e,f and Figure S24/Figure S25) at the start and the end of cycling.

The samples of the GF series all show peak current ratios well above 0.85 in the negative half-cell (Figure 5-4a). However, in the positive half-cell (Figure 5-4b) a rise in reversibility with increasing scan rate and deoxygenation is observed for GF. The desorption kinetics, often identified as the rate-limiting step in the positive half-cell, are therefore accelerated by an oxygen-free surface.^[69,70] This is attributed to the higher electrostatic attraction between surface oxygen groups and the $V^{VO_2^+}$ molecule compared to the V^{II} ion. An acceleration of the desorption process is further supported by a steeper slope in the Randles–Sevcik plots (Figure S26). The ΔE_p values of GF decrease from 230 mV (positive half-cell) and 270 mV (negative half-cell) to almost identical values for both half-cell reactions of 140 mV for GF-980. The initial activity enhancement is attributed to the removal of OFGs since no additional edge sites were created. Subsequently, a lower ΔE_p is associated with additional disorder since no change in the chemical composition was observed. The active surface area slightly increased according to the EDLC from about 1 (GF) to 1.25 mF (GF-980).

The redox reversibility of GF-SA is higher, but for both half-cell reactions, no significant changes because of the deoxygenation were observed. For the positive half-cell, the ΔE_p of GF-SA slightly decreases at temperatures >800 °C (from 100 mV to 80 mV). Even though an overall healing of disorder was observed by Raman spectroscopy up to this temperature, the creation of vacancies balances this loss of active edge sites, keeping ΔE_p constant. At higher temperatures, the defect density rises, which lowers the ΔE_p . In the negative half-cell, ΔE_p rises from 60 mV to a nearly constant peak separation of 80 mV after deoxygenation at 500 °C, which agrees with the lower $I(D)/I(G)$ ratio of GF-500. Since the additional removal of oxygen has no further influence on this value, it can be deduced that the overall lower disorder of deoxygenated GF-

SA (2.30 to 2.54) compared to its initial state (2.65) handles the activity drop. The further loss of edges on GF-800 is compensated by an increased presence of carbon vacancies, which is evident in the D to D' ratio, resulting in a constant ΔE_p .

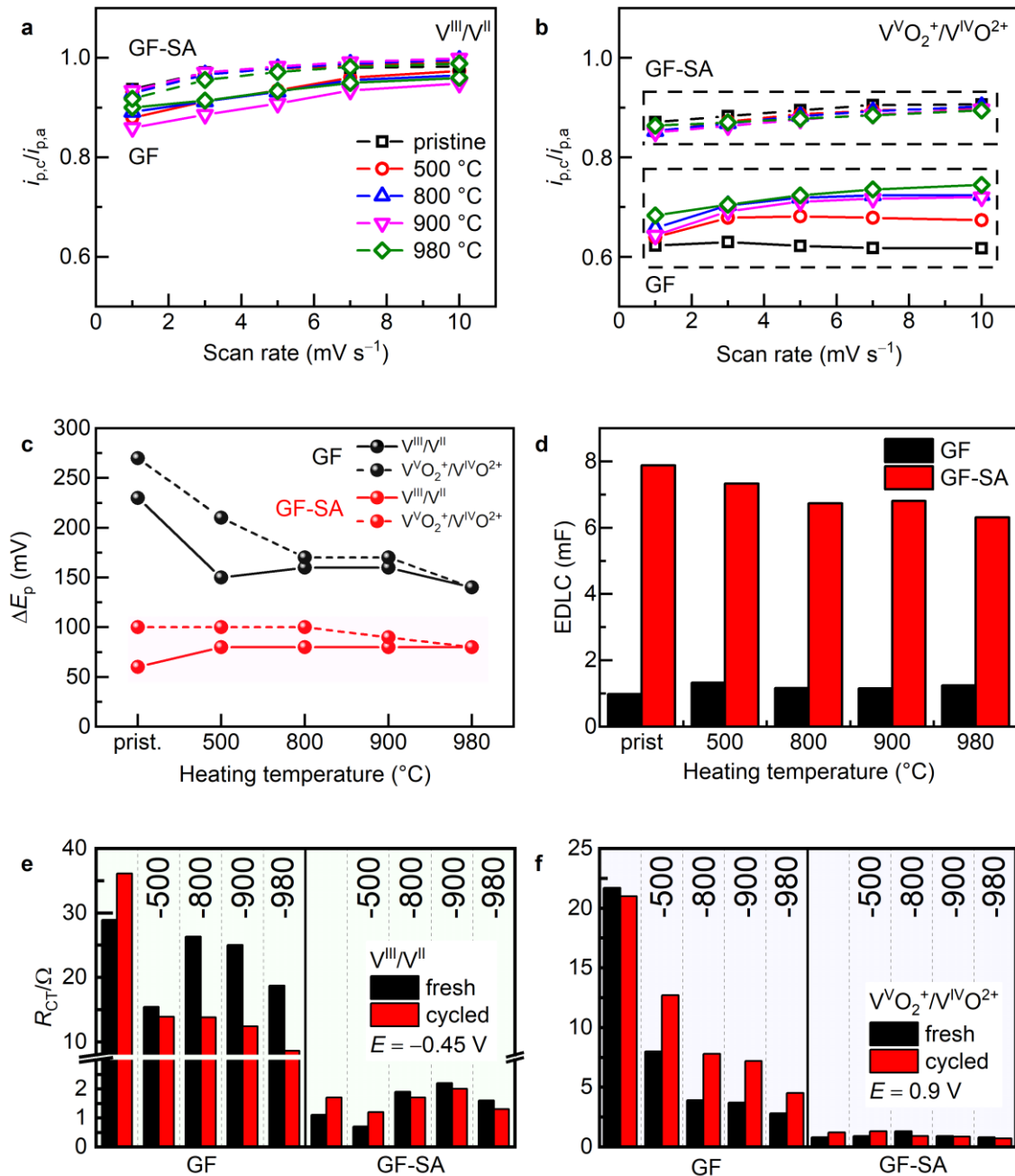


Figure 5-4. Electrochemical investigation of pristine and deoxygenated GF and GF-SA by CV and EIS in both half-cells. **(a,b)** The peak current (i_p) ratio of the oxidation and reduction signals in the (a) negative and (b) positive half-cell, determined at different scan rates; **(c)** ΔE_p between the oxidation and reduction signal; **(d)** EDLC. **(e,f)** R_{CT} , determined by EIS before (fresh) and after (cycled) CV in the (e) negative and (f) positive half-cell.

The EDLC of GF-SA corresponds to about eight times the value of GF (**Figure 5-4d**), but the surface area is only higher by a factor of ~ 5.3 . Additional active sites, commonly associated

with oxygen groups, have been generated on GF-SA during the thermal activation.^[177,178] The EDLC of GF-SA steadily declines from about 7.9 to 6.3 mF with increasing deoxygenation temperature, while it increased on GF. The removal of OFGs can therefore not be held responsible for the observed change in active surface area. However, our results indicate, that the different EDLC of the two sample sets is related to the number of defects, which is in accordance with previous studies on graphitic disorder.^[149,150,179] After normalizing the EDLC to the real surface area (Figure S23), GF-980 has a higher value than its more active counterpart GF-SA-980. This was attributed to the different distribution of defects per area, and believe that non-edge defects, which were proven to have the highest capacitance per area, are more dense on GF-980.^[179]

The electrochemical impedance of the electrodes was evaluated before and after cycling to study the influence of the deoxygenation on the charge transfer kinetics (**Figure 5-4e,f**). The R_{CT} of GF-SA is consistently lower than GF, regardless of the inspected half-cell or deoxygenation temperature. This is based on the overall higher defect density, which is evident from the Raman results and the much higher EDLC. Two observations are made for the deoxygenated GF: first, the strongest decrease of R_{CT} for GF-500 is associated with the removal of the major part of OFGs. Even though for higher temperatures the oxygen concentration further decreases, active defects are partially healed (**Figure 5-3f**), which explains the relative increase for GF-800 in the negative half-cell. However, additional deoxygenation decreases the R_{CT} for the cycled samples, which is not observed for pristine GF since the degree of oxidation at this material is high as it was demonstrated in the previous chapter.^[180] The oxygen-free electrodes further decrease R_{CT} during cycling. In the positive half-cell, R_{CT} steadily declines with higher deoxygenation temperatures. All cycled samples of the GF row show an increase in R_{CT} because of oxidation by the electrolyte, which is reduced by higher degree of deoxygenation. The removal of basal plane bound oxygen and formation of hydrogen-terminated edges at higher temperature, which are more stable against re-oxidation and hence against the formation of new OFGs, leads to a more rapid electron conductivity across the basal plane and an increased charge transfer rate at the solid–liquid interface.^[68,69] In general, the R_{CT} of the GF-SA row remains much lower due to the overall higher degree of disorder throughout all temperature stages. For GF-SA in both half-cells, the evolution of R_{CT} with temperature resembles the $I(D)/I(G)$ ratio (**Figure 5-3f**), showing a higher resistance for a lower number of defects.

5.4 Chemical and Structural Changes During Electrochemistry

By the investigations discussed so far, it was possible rule out a significant contribution of OFGs to the charge transfer reaction of both half cells. Instead, the importance of graphitic defects was highlighted. However, as discussed previously all deoxygenated samples show a certain degree of re-oxidation when being exposed to the electrolyte or electrochemically cycled. This raises the question how well the initial surface structure obtained by an activation treatment is maintained in the cell or if surface structures of differently treated samples converge after some time irrespective of their initial treatment.

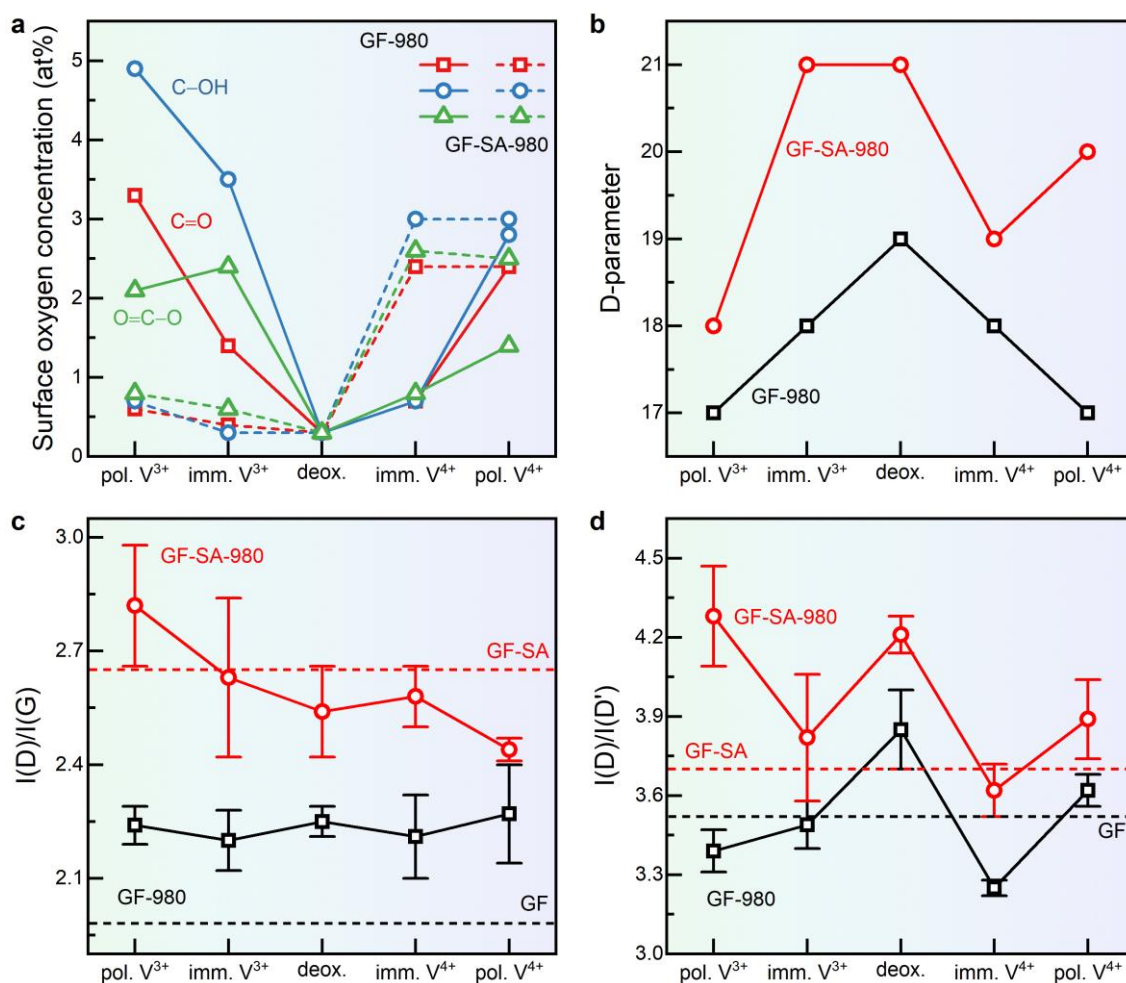


Figure 5-5. Photoelectron and Raman spectroscopy of GF thermally deoxygenated (deox.) at 980 °C after immersion (imm.) and polarization (pol.) in each half-cell electrolyte. **(a)** Change in surface concentration of different OFGs; **(b)** D-parameter; **(c)** degree of disorder given by the $I(D)/I(G)$, and **(d)** type of graphitic defects expressed by the $I(D)/I(D')$ ratio.

Therefore, the evolution of OFGs after exposure to the positive and negative electrolyte and electrochemical polarization of the deoxygenated electrodes (GF-980 and GF-SA-980) was analyzed by XPS to probe the chemical composition and the sp^2/sp^3 ratio (Figure 5-5a,b).

Furthermore, Raman spectroscopy was used to monitor possible changes of their microstructural properties (**Figure 5-5c,d**).

The amount of oxygen increases considerably for GF during immersion (~ 7 at%) and polarization (~ 10 at%) in the negative electrolyte (**Figure 5-5a** and Figure S27). The major part consists of hydroxyl groups formed at basal planes, whereas carbonyls and carboxylic groups develop at edge sites.^[69,181,182] This is consistent with the decrease of the D-parameter (from 19 to 17 eV, **Figure 5-5b**), which is ascribed mostly to the formation of oxygen groups at edges or defects of the sp^2 planes, resulting in sp^3 carbon–oxygen bonds. The higher amount of oxygen is also observed in the increased $\sigma(\text{C-O})$ signal of the O 2s region in the VB spectra (Figure S27).

The oxygen concentration on GF is rather low after immersion in the positive electrolyte (~ 2 at%), while the oxidative polarization generates more oxygen moieties (~ 7 at%), specifically carbonyl and carboxylic groups. An attack of basal planes is reflected by the decreased D-parameter (19 to 17 eV) and the disappearance of the peak corresponding to $\sigma(\text{C-C})$ bonding states (Figure S27). During immersion and polarization in both electrolytes, the $I(\text{D})/I(\text{G})$ ratio of GF-980 remains almost unchanged (**Figure 5-5c**), but a decrease of vacancies is observed by a change in the $I(\text{D})/I(\text{D}')$ ratio (**Figure 5-5d**). This shows that vacancies are more easily oxidized and consumed in contact with the electrolyte. However, the increase of the D to D' ratio after polarization in $\text{V}^{\text{IV}}\text{O}^{2+}$ suggests that vacancies can also be deoxygenated electrochemically and therefore be available as active sites.

Less surface oxygen (~ 2 at%) is formed on GF-SA-980, even after polarization, and there appears to be no recognizable preference for the formation of one specific type of OFG. This may seem surprising, given the significantly higher surface area of GF-SA. However, in contrast to GF less oxidation resistant carbon structures on the surface of GF-SA have already been removed due to the oxidative treatment of GF-SA prior to deoxygenation, which increases its stability towards re-oxidation. Nevertheless, also for GF-SA an attack of basal planes by the negative polarization is witnessed by a decrease of the D-parameter from 21 to 18 eV. Considering the improved electrochemical performance of GF-SA-980, the higher concentration of oxygen on GF does not result in an increased activity in the negative half-cell. GF-SA-980 shows a significantly increased disorder which grows even further for the polarized electrode (from 2.57 to 2.82). Consequently, it can be concluded that the activity is more affected by the presence of structural defects acting as active sites rather than by OFGs. Many of these structural defects are linked to vacancies, as indicated by the high $I(\text{D})/I(\text{D}')$ ratio of GF-SA-980 (**Figure 5-5d**).

The density of vacancies at first decreases after immersion, indicating the reactivity with electrolyte species. In contrast to GF, negative polarization results in the activation of the electrode by inducing more vacancies than on GF-SA-980, showing that these previously occupied sites are not only freed but also additional point defects are created on the electrode. Hence, given that less noble carbon species at the surface have been removed, a low number of OFGs is beneficial for application in the negative half-cell, and polarization under operation further increases the number of favorable edge sites and vacancies.

Re-oxidation of GF-SA-980 is stronger after immersion and polarization (~8 at%) in the positive electrolyte. Again, a similar increase for all types of OFG can be observed. Since reoxidation occurs already mainly upon immersion into the positive electrolyte, a participation of OFGs in the charge transfer reaction of the positive electrode cannot be fully ruled out. However, comparison with GF-980 which shows a further increase of OFGs due to polarization along with an increase in R_{CT} for cycled electrodes (**Figure 5-4f**). In contrast, the R_{CT} for GF-SA-980 remains almost constant, which indicates that OFGs may not only not play the dominant electrocatalytic role but even hamper the charge transfer.

By the evolution of the D-parameter for GF-SA-980 it is seen that the immersion results in the formation of OFGs at the basal plane (21 to 19 eV), which are then during polarization removed and formed at edge sites (19 to 20 eV). The restoration of sp^2 carbon is also observed in the decreased $I(D)/I(G)$ ratio after polarization (from 2.57 to 2.44). Like the negative half-cell, vacancies are oxidized during polarization, given by the evolution of the $I(D)/I(D')$ ratio (from 4.2 to 3.62 to 3.89).

5.5 Long-Term Half-Cell Cycling

Since immersion and polarization in the positive electrolyte leads to partial re-oxidation of the surface, the effect of deoxygenation was studied during repetitive cycling. For this purpose, GF (~7 at% OFGs, $I(D)/I(G) = 1.98$) and GF-980 (<1 at% OFGs, $I(D)/I(G) = 2.25$) were cycled 100 times and ΔE_p (**Figure 5-6a,b**) as well as R_{CT} were determined at the start and after every 10th cycle (**Figure 5-6c**). Subsequently, the electronic structure and microstructure were studied again by XPS and Raman spectroscopy (**Figure 5-6d,e**).

For pristine GF, ΔE_p slightly increases over the first 50 cycles (from 310 to 320 mV) and decreases again thereafter (300 mV). GF-980 initially has a much lower ΔE_p (170 mV), which also increases to around 50 cycles (190 mV) and remains constant thereafter. This trend is equally

observed for GF and GF-980 by comparing their R_{CT} values, which shows a growth from 35 and 6.5 Ω before CV up to 49 and 12 Ω after 50 to 60 cycles, respectively, and a subsequent reduction at higher cycle numbers to 40 and 10 Ω . These results prove that the previous deoxygenation has a positive effect on the long-term cycling performance. The increase of the values for the first 50 cycles is associated with the oxygen-enrichment of the electrode due to the oxidative electrolyte and potential, which relates to the previous results showing an increased oxygen concentration after polarization in the positive half-cell (**Figure 5-5a**). After this saturation point, OFGs are removed due to the harsh environment, as it will be seen by the investigation after long-term cycling.

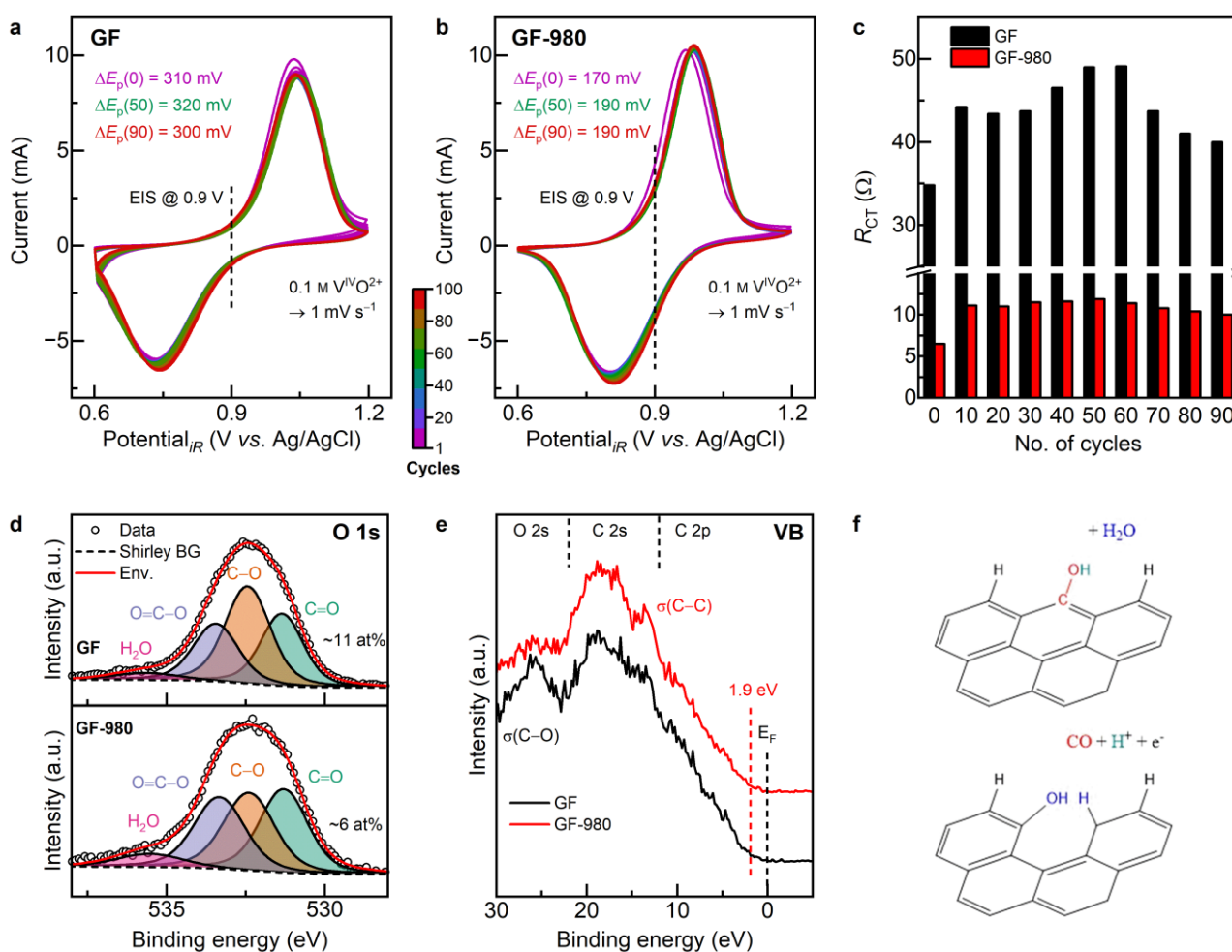


Figure 5-6. Long-term cycling and physicochemical investigation of GF and GF-980. Half-cell electrochemistry: **(a,b)** CV curves of the positive half-cell, displaying ΔE_p before and after 50 and 100 cycles. The color bar indicates the number of cycles. **(c)** Evolution of the R_{CT} during cycling, measured initially and after each 10th cycle. Physicochemical characterization after 100 cycles: **(d)** deconvoluted O 1s detail spectra and the respective relative oxygen content; **(e)** VB spectra. **(f)** Carbon corrosion mechanism on GF.

After performing 100 cycles, the oxygen concentration of GF is higher (~11 at%) than of GF-980 (~6 at%, **Figure 5-6d** and Figure S28). On GF-980 the different types of OFGs have similar

concentrations, while OFGs on GF are dominated by hydroxyl groups (~5 at%). Carboxylic groups and carbonyls are present to a lesser extent (~3 at%). The deoxygenation procedure apparently prevents the formation of basal plane OFGs, because physisorbed oxygen species readily desorb again on large sp^2 sites with far away edges.^[69] Hydrogenated edge sites, as they are facilitated by the deoxygenation, are less prone to water adsorption.^[183,184]

The oxygen content is further reflected in the O 2s region (**Figure 5-6e**) by a less pronounced $\sigma(\text{C-O})$ signal and a more distinct peak related to 2s $\sigma(\text{C-C})$ electrons on GF-980. A VBM of 1.9 eV signifies an increase of occupied states close to E_F (compare **Figure 5-2d**) due to increased electron transfer between layers of graphite, facilitated by intercalated electrolytic species such as water molecules, vanadium ions, or sulfuric acid.^[185,186] The more active GF-980 exposes a lower number of defects ($I(\text{D})/I(\text{G}) = 2.06$) compared to the less active GF (2.21, **Figure S30**). The origin of defects on both electrodes, which are mainly edge sites, is not affected by the electrochemical cycling. Combined with the higher hydroxyl concentration and the declining R_{CT} , the increasing disorder is associated with incipient carbon corrosion (**Figure 5-6f**), resulting in more active sites on the electrode. It was concluded that the positive half-cell vanadium redox reaction relies on an oxygen-free, intact sp^2 basal plane in combination with enough hydrogen-terminated defects as active sites. The prevention of oxygenation, equally on basal and edge sites, is beneficial for the electron transfer and the lifespan of the electrode.

5.6 New Scheme for the Vanadium Redox Reactions

In summary, the previously ascribed electrocatalytic role of OFGs on GF as driving force for the vanadium redox reactions was disproved. Therefore, a new reaction mechanism for both half-cells that allows the redox reaction to occur at hydrogen-terminated edge sites rather than through the support of hydroxyl groups, as it was suggested by the previous mechanism, was proposed (**Figure 5-7** and **Figure S31**). The activity and effective charge transfer are mainly determined by the number and stability of the (hydrogenated) graphitic edge sites and vacancies in combination with an oxygen-free and intact basal plane.

The reduction in the negative half-cell proceeds *via* three steps: (i) ion exchange of hydrogen bound to an edge site of the electrode and a dissolved V^{III} ion from the electrolyte; (ii) electron transfer from the electrode to reduce the oxidation state of the vanadium ion; (iii) a second ion exchange between vanadium and a proton from the electrolyte, which releases V^{II} and creates a new active site. In the positive half-cell, four steps are required in the oxidation reaction: (i)

ion exchange of hydrogen and a dissolved $V^{IV}O_2^+$ ion from the electrolyte; (ii) oxygen from water molecules in the solvation shell is transferred to the positively charged vanadium ion; (iii) an electron is transferred to the electrode under the release of a proton to oxidize the tetra to a pentavalent ion; fourth, vanadium reacts with the free proton by an ion exchange and consequently $V^{VO}_2^+$ is released under the recreation of the active site.

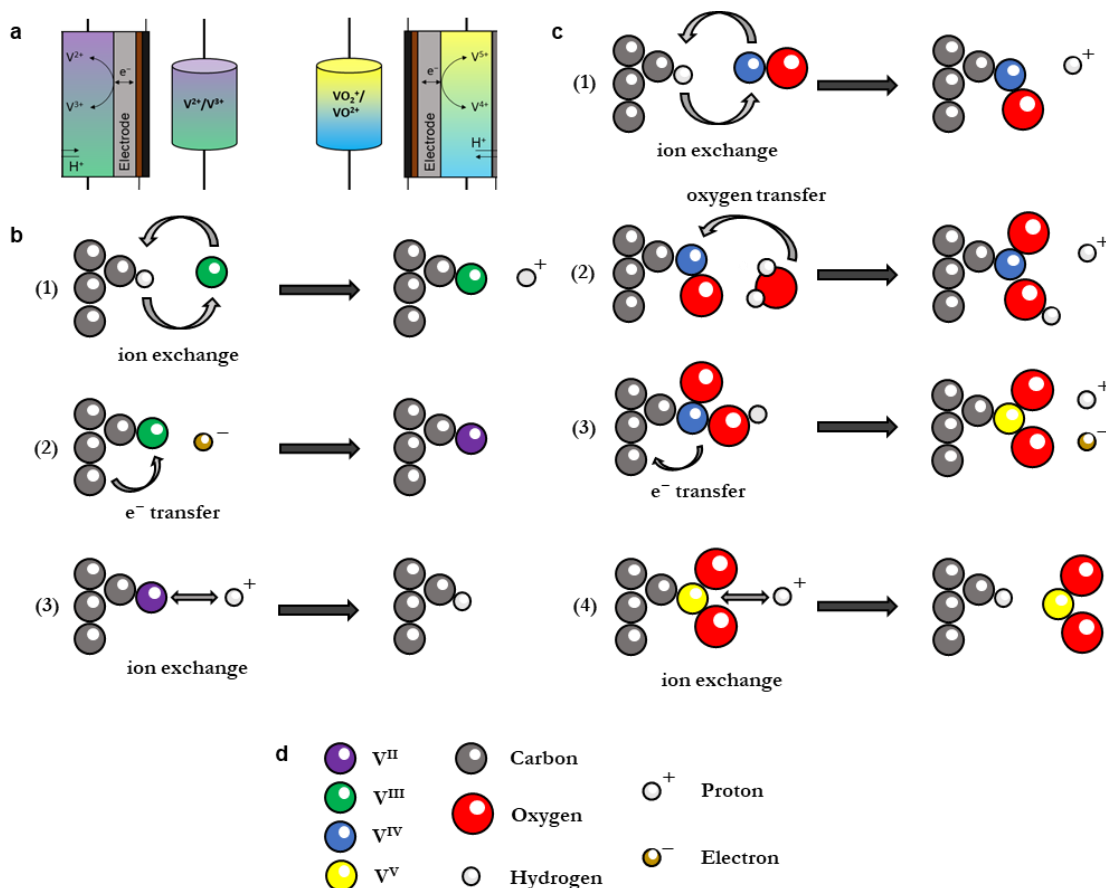


Figure 5-7. New reaction scheme for the half-cell reactions in VFBs. **(a)** Illustration of the reactions in the negative and positive half-cell. **(b)** Three-step reaction mechanism in the negative half-cell. **(c)** Four-step reaction mechanism in the positive half-cell. **(d)** Legend for the depiction in (b,c).

5.7 Conclusions

The influence of OFGs and surface defects on the electrocatalytic activity of GF was analyzed by a novel deoxygenation procedure. The removal of specific OFGs, subsequent defect healing, followed by creating disorder under the preservation of sp^2 planes was confirmed by XPS and Raman spectroscopy. The oxygen-free electrodes, as opposed to the predominant opinion, had an overall better half-cell performance than the oxygen-rich starting material. New active edge sites are induced, further enhancing the activity. No correlation between the concentration of oxygen or of certain OFGs with the electrocatalytic activity could be established, while instead

the presence of certain carbon defects correlates well with the observed electrochemical properties. Oxidation through the electrolyte is much more pronounced in the positive half-cell. During long-term cycling, it was shown that the benefit of the deoxygenation treatment is stable. It resulted in a lower oxygenation, which guaranteed high activity and rapid charge transfer. A decreasing charge transfer resistance of oxygen-rich GF is associated with carbon corrosion because of a higher hydroxyl concentration, which subsequently increases the number of edge sites.

6 Pyrene-Modified Graphite Felts as Model Electrodes

The last chapter demonstrated that OFGs most likely negatively affect the electrocatalytic activity of GF for the vanadium redox reactions. However, differences could arise from the specific type of OFG, which is difficult to introduce specifically by a pretreatment. Pyrenes are a class of PAHs consisting of four highly condensed benzene rings in a plane. Due to their wide availability with different functional groups, they are an attractive candidate for electrochemical energy systems which rely on redox-active species. However, these PAHs suffer from low electrical conductivity and dissolution in the electrolyte, requiring a supporting substrate to guarantee electron transport and chemical stability.^[187,188] As possible substrates, several materials such as polymers, enzymes, and metals have been investigated.^[189-191] The most prominent example for non-covalent surface modification is graphite, since pyrenes allow strong π - π interactions with sp^2 hybridized carbons due to their aromatic character.^[192] The non-covalent attachment of pyrenes to carbon surfaces has already led to success concerning the dispersion of nanotubes and conductivity tuning of graphene.^[193-196] Modification of MWCNTs using pyrenes with nitrogen- and oxygen-containing functional groups demonstrated different redox activities and improved energy and power densities for lithium-ion anodes.^[197] The electro-grafting of nitropyrenes onto onion-like carbon resulted in a change of capacitive behavior from double layer-like to the introduction of a redox capacitance.^[198] There is subsequently a lot of work to be done to understand and tailor the effect of pyrenes on the vanadium redox reaction and explore them as an easy to facilitate technique to tune the properties of GF.

In this work, GF was modified by various pyrene derivatives to study their electrocatalytic activity for the vanadium redox couples. After a survey of several available pyrenes, the previously introduced deoxygenation was used as a facile pretreatment to improve the loading and electrochemical responsiveness of pyrenes. The electrochemical stability of modified GF was investigated under the harsh vanadium oxidation conditions by differential electrochemical mass spectrometry (DEMS). Subsequently, their capacitive as well as faradaic electrochemical behavior in both vanadium half-cells was studied. The physicochemical surface properties of the modified GF were analyzed by XPS and Raman spectroscopy.

6.1 Improving the Attachment of Pyrenes to GF

Pyrenes containing OFGs were studied as electrocatalysts for the vanadium redox reaction by modifying the basal plane of GF *via* π - π stacking.^[192] This method has been chosen since it does not affect the structure of the electrode and was already successfully applied in the functionalization of graphene for other energy storage devices.^[199] In a first approach, pristine GF was dipped into pyrene-containing DMSO solution, allowing the pyrenes to stack to the graphite surface overnight. The modified GFs were subsequently tested in electrochemical half-cell experiments to investigate the redox peak shapes and positions, as well as the charge transfer resistances. This approach allowed to quickly survey the available pyrenes in terms of their electrocatalytic activity.

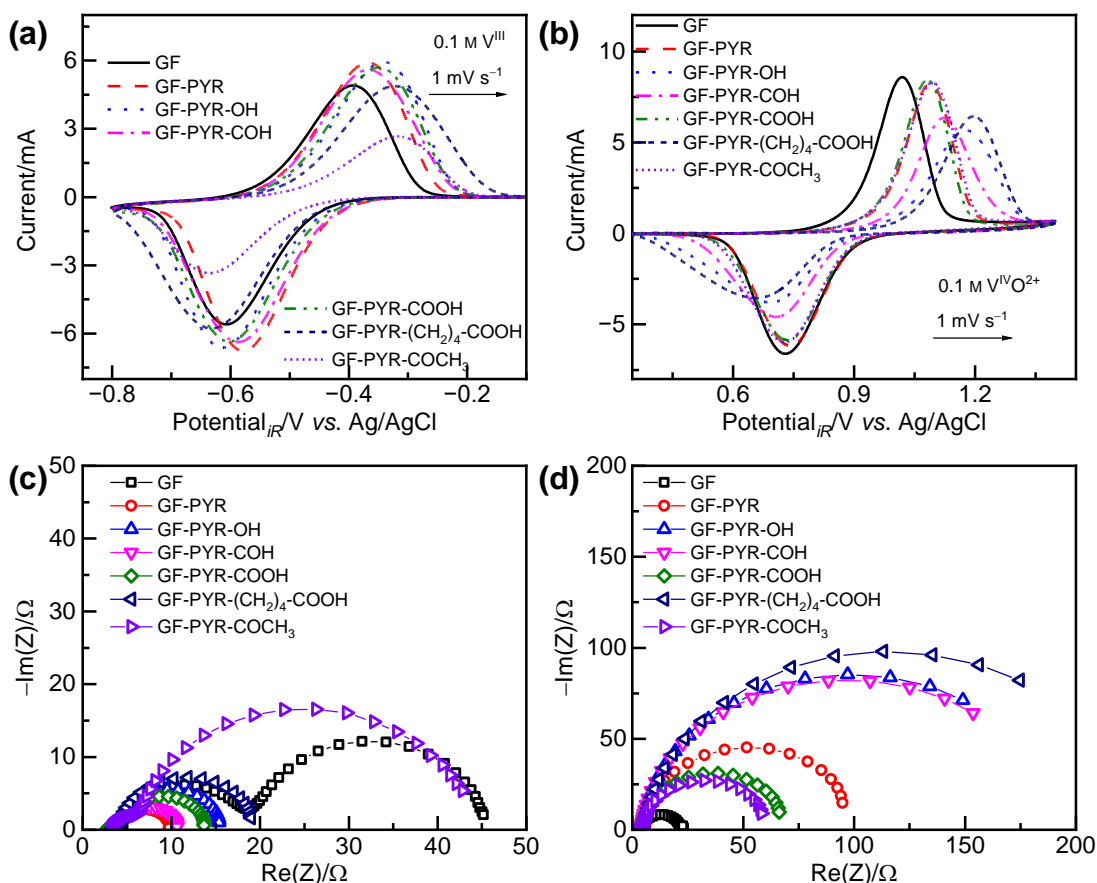


Figure 6-1. Qualitative survey of the electrocatalytic activity of functionalized pyrenes. **(a,b)** Vanadium redox reactions in the (a) negative and (b) positive half-cell. **(c,d)** EIS at an applied potential of -0.45 and 0.9 V vs. Ag/AgCl in the (c) negative and (d) positive half-cell, respectively.

In the negative half-cell (**Figure 6-1a**), the V^{III}/V^{II} reduction was enhanced by using the pristine pyrene and functionalized 1-Hydroxypyrene (GF-PYR-OH), 1-Pyrenemethanol (GF-PYR-COH), or 1-Pyrenecarboxylic acid (GF-PYR-COOH). However, the observed electrocatalytic activity of

the carboxylic group was absent for pyrene exposing the functional group bridged *via* four carbon atoms in 1-Pyrenebutyric acid [GF-PYR-(CH₂)₄-COOH]. The peak currents were also reduced by ~40 % for the 1-Acetylpyrene functionalized GF (GF-PYR-COCH₃). Pure pyrene could provide additional edges for redox reactions, which would explain the increased performance in the negative half-cell. There is also an increased activity observable by the oxygen-containing pyrenes compared to GF, which might have several origins: (i) active oxygen groups; (ii) three C₆ rings without OFGs working as active sites; (iii) partially unstable OFGs which are reduced during cycling at negative potentials, leaving behind hydrogen-terminated edges. For the positive half-cell reaction, all pyrene modifications deteriorated the activity of GF (**Figure 6-1b**). There was almost no difference visible between pyrene, 1-Acetylpyrene, and 1-Pyrenecarboxylic acid. Instead, the peak position of the V^{VO}₂⁺/V^{VO}₂²⁺ oxidation was shifted by ~0.2 V to more positive potentials for 1-Pyrenemethanol and 1-Pyrenebutyric acid. The functionalization with different pyrenes showed that using pristine GF, OFGs were not beneficial for the positive half-cell reaction. The *R*_{CT} values acquired by EIS at an applied potential reflected the activity changes observed by CV (**Figure 6-1c,d**).

Pyrenes stack to the basal plane of graphite. Consequently, a higher share of *sp*² hybridization of the material could result in increased loading. Since unmodified GF with a considerable amount of covalently bound and atmospherically adsorbed oxygen at its surface was used, the pyrene stacking capabilities were improved by using deoxygenated GF as a precursor. However, it must be taken into account that this deoxygenation procedure itself provides a higher number of active sites due to the introduction of microstructural defects.^[200] This can be demonstrated by CV (**Figure 6-2a**), showing the decreased ΔE_p from 230 and 270 (GF) to 140 mV (GF-980) in the negative and positive half-cell, respectively. Additionally, higher peak currents for the deoxygenated GF are observed. The increased electrocatalytic properties is ascribed mainly to two observations (**Figure 6-2b**): (i) the removal of activity-inhibiting OFGs, resulting in an almost oxygen-free surface comprising *sp*² hybridized carbon exclusively, and (ii) to the introduction of edge sites and carbon vacancies as microstructural defects. The thus obtained GF electrodes were treated in the same manner as mentioned above by simple immersion in pyrene-containing DMSO solutions. Following the results of the pyrene survey in **Figure 6-1**, 1-Pyrenebutyric acid and 1-Acetylpyrene were disregarded for further experiments and concentrated on the derivatives displayed in **Figure 6-2c**.

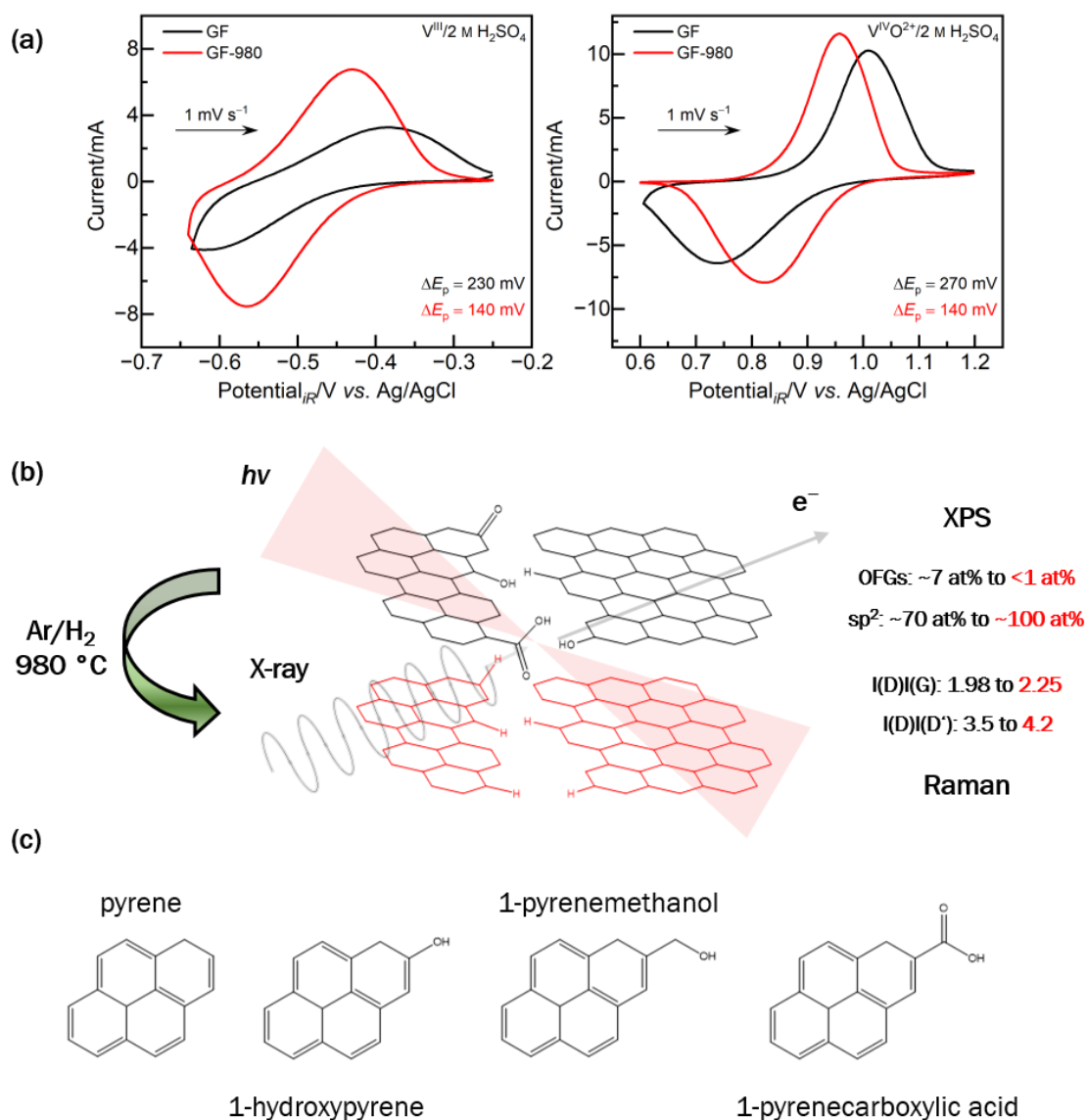


Figure 6-2. Experimental procedure to attach pyrene derivatives to a highly sp^2 hybridized GF. **(a)** Changing electrocatalytic activity of GF because of the prior deoxygenation in both half-cells. **(b)** Alteration of the surface chemical composition and microstructural properties. **(c)** Pyrenes used to modify GF.

6.2 Electrochemical Stability of Modified GF

At first it was made sure that the electrochemical observations could in fact be ascribed to the modification with the pyrene derivatives. Therefore, DEMS investigated the stability of treated and untreated GF to analyze the gas evolution during electrode operation. These experiments were conducted in the positive half-cell because of the harsher oxidative conditions. In the voltage range of vanadium oxidation (0.7 V to 1.1 V vs. Ag/AgCl), the only detected gas is H_2 , which likely stems from the reduction of water at the counter electrode (**Figure 6-3a**). The high variation in the evolution rates can be explained because the evolution of H_2 is not the only possible reaction at the counter electrode, which was not located close to the carrier gas

bubble stream, so that the detachment of H₂ bubbles from the electrode itself has happened with different rates. The effect of the sudden detachment also explains the wobbling behavior in the H₂ detection at higher potentials. At the end of the potential scan range, O₂ evolution is observed, showing the onset of water electrolysis at the working electrode (**Figure 6-3b**). As the O₂ signal is weak against its background (see Figure S33), the difference in absolute values is likely because of calibration deviations.

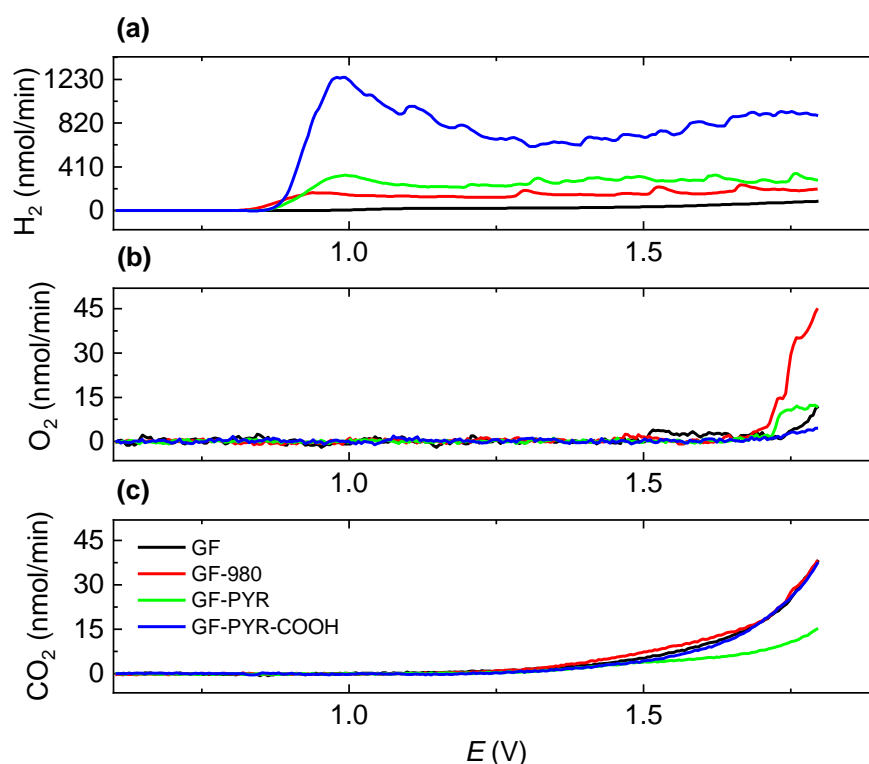


Figure 6-3. Gas evolution of pristine and modified GF monitored by DEMS. Evolution of **(a)** H₂, **(b)** O₂ and **(c)** CO₂.

The CO₂ evolution at the working electrodes is depicted in **Figure 6-3c**. Within the potential range for vanadium oxidation, no CO₂ release is detected irrespective of the sample, thus showing stability of graphite, surface carboxylates and pyrene coatings against oxidation at these potentials. At potentials >1.25 V vs. Ag/AgCl, an exponential increase of CO₂ evolution with the electrode potential is observed, indicating oxidation of the graphite electrode, in line with literature observations.^[201,202] For GF-PYR, a slightly lower evolution of CO₂ was found for a similar electrode mass. It can be assumed that the higher chemical stability of unsubstituted pyrene slows either the degradation reaction itself or the dissolution of CO₂ from the electrode surface. The total charge passed during the measurement varied between different working electrodes. To confirm that higher currents are not entirely because of degradation reactions,

Table S2 shows the total amount of charge passed, the total amount of CO₂ evolved, and the ratio between them, showing that no proportionality exists. Signals for fragments of pyrene or substituted pyrene were also monitored, but no evolution was detected. The DEMS measurements thus confirm that pyrenes are stable in the range relevant for the V^{VO}₂⁺/V^{IV}O₂²⁺ redox reaction.

6.3 Electrocatalytic Activity of Pyrene-Modified GF

Another indicator for successful modification and the electrochemical response of pyrene-modified GF can be seen in a potential range without vanadium-related redox activity. CV curves show a higher current response for the pyrene-modified than for the pristine surface of GF-980 (**Figure 6-4a**). 1-Hydroxypyrene furthermore has a distinct redox peak at 0.36, GF-PYR-COOH at 0.28 and 0.43, and GF-PYR and 1-Pyrenemethanol at 0.23 V vs. Ag/AgCl.

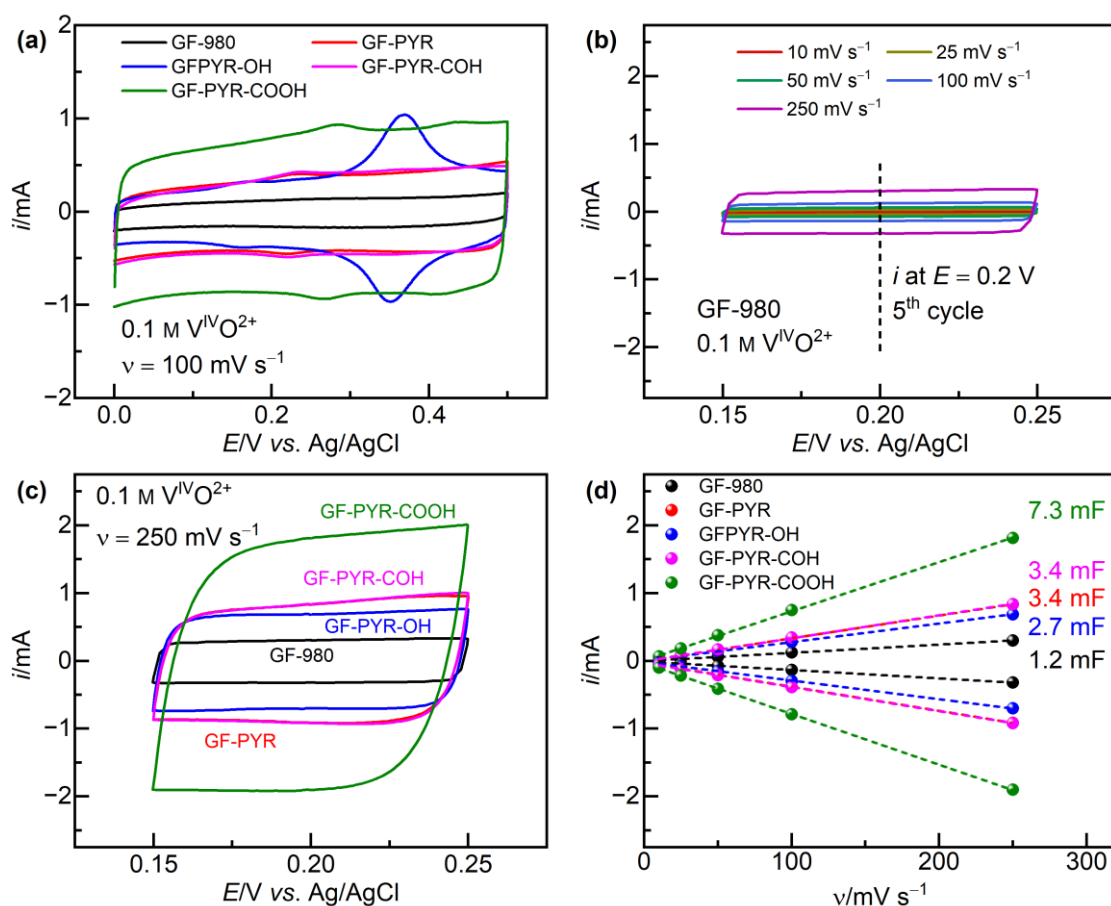


Figure 6-4. Capacitive behavior of pyrene-modified GF-980. **(a)** CV in the electrochemical double layer region; **(b)** exemplary EDLC measurement on GF-980; **(c)** EDLC currents at the highest scan rate used; **(d)** EDLC results.

To investigate the electrochemical active surface area, EDLC measurements were conducted. To this end, the electrode was cycled in a narrow potential window at different scan rates, exemplary displayed for GF-980 in **Figure 6-4b**. It is shown in **Figure 6-4c** that at the highest scan rate chosen no redox peaks interfere with the capacitive behavior of the modified electrodes. The curves in **Figure 6-4d** thus reveal a linear relationship of the current at 0.2 V vs. Ag/AgCl in relation to the scan rate. The slope of the curves, which represents the EDLC, yields a relatively low value of 1.2 mF for GF-980 that is increased for pyrene and 1-Pyrenemethanol modified GF-980 to 3.4 mF. While 1-Hydroxypyrene reveals a lower EDLC than non-functionalized pyrene (2.7 mF), the capacitance is more than doubled for GF-PYR-COOH (7.3 mF).

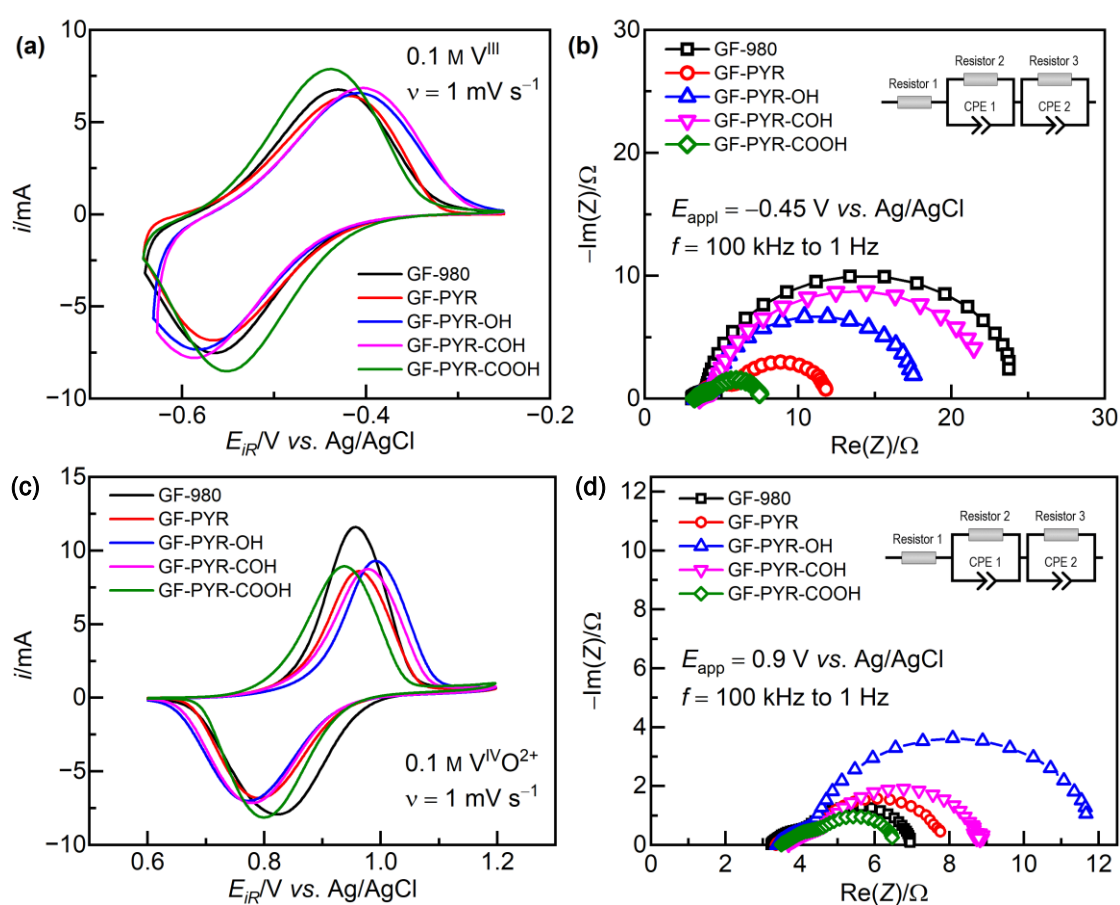


Figure 6-5. Electrocatalytic activity of pyrene-modified GF-980. CV and EIS in the **(a,b)** negative and **(c,d)** positive half-cell.

As a next step, the electrocatalytic activity of the modified GF-980 electrodes in both half-cells was analyzed by CV and EIS (**Figure 6-5**). The ΔE_p of GF-980 regarding the V^{III}/V^{II} redox reaction (140 mV) remains unchanged for GF-PYR (**Figure 6-5a**), demonstrating that subsequent changes can well be associated with the additional functionalization. While the ΔE_p extended for 1-Hydroxy and 1-Pyrenemethanol modified GF to 170 mV, GF-PYR-COOH revealed a

decreased value of only 110 mV. It is thus surprising that for all samples the R_{CT} (**Figure 6-5b**) is lower than for the unmodified GF-980 ($\sim 20 \Omega$). However, the lowest value is observed for GF-980 modified with pyrene ($\sim 6 \Omega$) and 1-Pyrenecarboxylic acid ($\sim 3 \Omega$). It is suspected that in fact the pyrenes might provide additional active sites but deteriorate the sorption kinetics of the reacted species, thus resulting in variances between voltammetry and impedance values.

In the positive half-cell, the ΔE_p of GF-980 (140 mV) is increased for GF-PYR to 170 mV, but even more by 1-Hydroxypyrene to 220 mV (**Figure 6-5c**). While the $V^{VO_2^+}/V^{VO^{2+}}$ oxidation for GF-PYR-COOH is kinetically enhanced, the corresponding reduction is hindered, resulting in an unchanged ΔE_p of 140 mV in comparison to GF-980. It is thus clear that a different responsiveness of one specific group with the oxidation and reduction of the vanadium species exists. The oxidation behavior in the CV is very well represented by the impedance, showing increased R_{CT} values for GF-PYR-OH ($\sim 8 \Omega$) and a by 0.5Ω lowered barrier for 1-Pyrenecarboxylic acid in comparison to GF-980 ($\sim 3 \Omega$, **Figure 6-5d**). The electrochemical half-cell tests demonstrated that the electrocatalytic activity differed regarding the functionalization of the pyrene. For both vanadium redox reactions, the overall activity was improved or at least not deteriorated by modifying GF-980 with 1-Pyrenecarboxylic acid. It is furthermore possible to use the pyrene modification as a basis for more sophisticated treatment studies such as electrochemical activation. A detailed description of a subsequent activation of GF-PYR using phosphate buffer solution to introduce carbonyl groups can be found in Figure S34.

6.4 Chemical and Structural Changes by the Modification

To gain a deeper understanding about the changes in surface chemistry and microstructure associated with the pyrene modification technique, GF-980 and the treated samples were investigated by XPS and Raman spectroscopy. XPS yields information about the oxygen-containing surface groups of GF-980, comparing all pyrene-functionalized felts after deoxygenation, dipping in DMSO, washing, and drying (Figure S35). No signals other than carbon and oxygen were detected. The oxygen-free GF-980 became oxygenated by the procedure; even for the non-functionalized pyrene the oxygen concentration raised to ~ 6 at%. For 1-Pyrenemethanol and 1-Pyrenecarboxylic acid functionalized pyrene, the surface oxygen content increased to ~ 8 at%. XPS does not seem to be a suitable method to discriminate between different pyrenes: After the functionalization, the surface of the sample did not necessarily possess the chemical composition that one would expect based on the oxygen group on the pyrene derivative used. The deconvoluted spectra showed that the concentration of single species did not correspond

to the initially introduced functional group. However, the high E_{VBM} of GF-980 (3.6 eV) was lowered to 2.1 eV for all pyrene-modified samples, indicating the introduction of additional charge carriers close to E_{F} regardless of the surface oxygen concentration or predominant type of oxygen group. At ~ 13 eV the $2s$ $\sigma(\text{C-C})$ electron states can be identified, which does not majorly change in relative intensity, demonstrating the integrity of the graphitic system on the surface after the modification.^[168,170,171]

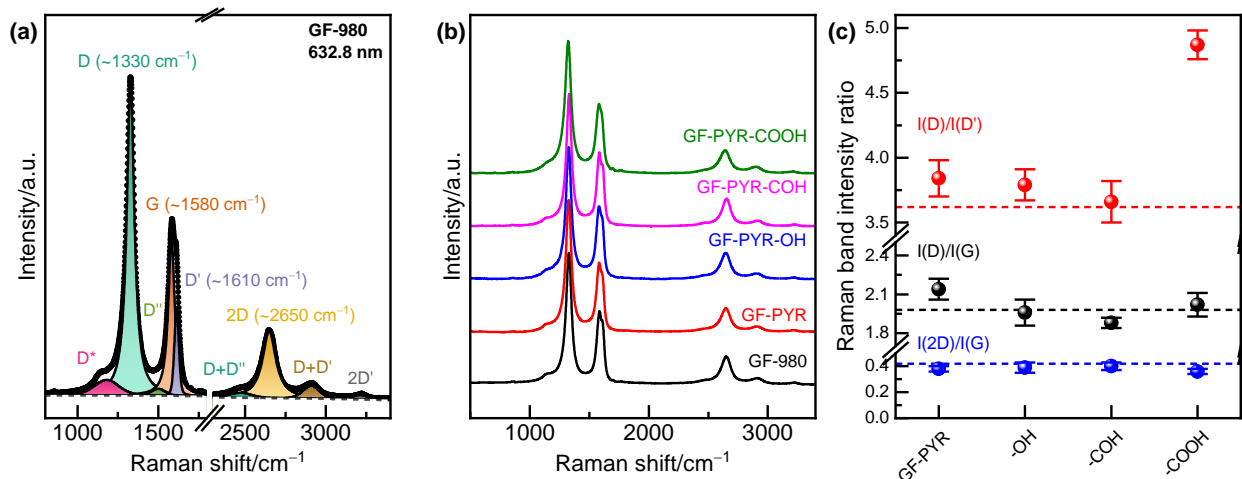


Figure 6-6. Microstructural properties of pyrene-modified GF-980. **(a)** Raman spectrum of GF-980, displaying all relevant scattering features. **(b)** Survey spectra of all samples in comparison. **(c)** Intensity ratios for the degree of disorder and type of defects. The dotted lines represent the mean values of GF-980.

Changes in microstructural properties after the electrode modification were monitored by Raman spectroscopy. An exemplary spectrum is given in **Figure 6-6a**, in which all scattering features are assigned to the corresponding modes. **Figure 6-6b** displays a survey spectrum for every sample, showing that the pyrene modification itself cannot be detected by Raman spectroscopy despite the multitude of signals which pyrene powder possesses.^[203] However, important differences in the resulting structural properties were discovered by the evaluation of the various intensity ratios of the D, G, D' and 2D bands (**Figure 6-6c**). On each sample, several points were acquired to account for the fluctuations resulting from the heterogeneous felt material. It can be observed that the 2D to G ratio of GF-980 (0.42) is only slightly decreased up to 0.36 after the modification, which matches the almost unchanged $\sigma(\text{C-C})$ signal in the C $2s$ region. However, it additionally shows the sensitivity of Raman spectroscopy and that even small changes of the sample, such as attaching a monolayer of pyrenes, directly affects the spectral features. The famous $I(\text{D})/I(\text{G})$ ratio of GF-980 (1.98) is increased for GF-PYR to 2.14 and slightly for GF-PYR-COOH to 2.02, whereas it is lowered for samples modified by 1-Hydroxy-

and 1-Pyrenemethanol to 1.96 and 1.88, respectively. Moreover, the type of defect for all samples but GF-PYR-COOH can be characterized as mainly edge sites due to a ratio close to 3.5 (3.62 to 3.84). For GF modified with 1-Pyrenecarboxylic acid, this ratio increased to 4.87, signifying a considerable number of vacancy-type defects whose role as active sites is very underrepresented in literature but was already suspected to play a significant role in Chapter 5.

Considering the absence of any meaningful differences in the surface chemistry and the previous results about the importance of graphitic defects for efficient electrocatalysis of the vanadium redox reaction, once again the activity corresponds to the microstructural properties resulting from the Raman characterization. While all pyrenes conserved the graphitic structure of GF-980, the highest degree of disorder was characterized for the more active samples GF-PYR and GF-PYR-COOH. However, one cannot disregard the functionalization of the pyrenes, since also GF-PYR-OH showed additional surface defects but especially in the positive half-cell a decreased activity.

6.5 Conclusions

In this chapter, the successful modification of GF electrodes with pyrenes, a special class of PAHs which can possess different functional groups, was demonstrated. It was shown that an oxygen-free graphite surface enhanced the adhesion and subsequently the electrochemical response of the pyrenes. The electrochemical stability of the pyrene-modified GF in a potential range relevant for the vanadium redox reactions in the positive half-cell was demonstrated by DEMS measurements. The electrocatalytic activity was subsequently tested in half-cell experiments, which showed that pyrenes varying regarding their functional groups exhibit different redox properties and charge transfer kinetics, highlighting the non-functionalized pyrene and the oxidative properties of the GF modified with 1-Pyrenecarboxylic acid. However, it was not possible to discriminate the modified electrodes based on their surface chemistry or electronic structure. Instead, GF-PYR and GF-PYR-COOH exhibited a higher number of microstructural defects, such as edge sites and carbon vacancies, which could be responsible for their elevated reactivity.

7 Understanding Efficient Phosphorus-Functionalization of Graphite

The direct integration of heteroatoms into the surface of GF will increase the electron donor or acceptor level, which in theory should enable more efficient charge transfer. This is a topic of general concern for a wide variety of energy technologies but has seldomly be considered for VFBs. Whereas OFGs and defects can be unstable during electrochemistry, and the binding of electroactive particles is difficult because the flowing electrolyte can wash away the valuable catalyst, heteroatom functionalization might be able to reliably integrate active sites into the lattice of graphite. Theoretical calculations already predicted improved electrocatalytic activity of doped graphene for the negative vanadium half-cell reaction.^[204] Regarding the electrical conductivity, wettability, and calculated energy barriers, phosphorus-modified graphene was considered a promising approach. Some experimental studies meanwhile characterized an electrode treated with boron, phosphorus, nitrogen, or multiple elements for VFBs.^[141,205–208] For boron-doped GF it was shown that not the total number of atoms is defining (all samples exhibited <1 at%) but the type of bonding, since the activity was most improved for the sample with the highest share in graphitic boron groups.^[205] Thermochemical treatment of GF with phosphoric acid resulted in an increased electrode activity, revealing the formation of abundant pores in the range of 0.2 to 20 μm on the surface in addition to phosphorus-containing functional groups, which heavily impedes retraction of elevated reaction kinetics to the heteroatom only.^[206]

It is thus crucial to consider the effect of other activity-influencing properties. Often by the thermochemical treatments, the specific surface area is increased or additional edge sites are introduced which catalyze both vanadium half-cell reactions.^[34,88,180] Some researchers discussed the role of the heteroatom since even bird dung was used to improve the electrocatalytic activity of graphene.^[209] For doped materials, the increased activity is therefore often secondary associated with the creation of OFGs.^[141,210] These, however, do not assist in the charge transfer process for the vanadium redox couple, as it was demonstrated previously.

To achieve a better understanding of heteroatom functionalization of graphite, at first commercial boron (electron-withdrawing) and phosphorus (electron-donating) doped graphene alongside homemade samples were studied by half-cell electrochemistry to elaborate on a prospective candidate. To establish correlations between the electrocatalytic and physicochemical characteristics, the bulk and surface properties of the material were studied in detail by XRD,

XPS and Raman spectroscopy. Based on the thereby gained knowledge, GF was directly phosphorus-functionalized and additionally characterized by full cell polarization curves. The underlying study thus provides evidence for the influence of heteroatom functionalization and paints a clear picture about the properties which are often changed as a side effect and can additionally have an enhancing or detrimental influence on the electrocatalytic activity.

7.1 Graphene Powder Attached to GF

To examine the influence of doped graphene on the electrochemical performance, the commercial powders (graphene: G, phosphorus-doped: PG-1, boron-doped: BG) were successfully attached to GF by the method introduced for MWCNTs in Chapter 4.^[180] SEM images visualized the distribution of small particles at the intersection of fibers or on single fiber surfaces, and the absence of big aggregates in the pores (Figure S36). In the P 2p spectrum of GF-PG (Figure S37), <1 at% phosphorus is identified, predominantly bound to three carbon and one oxygen atoms (C_3PO).

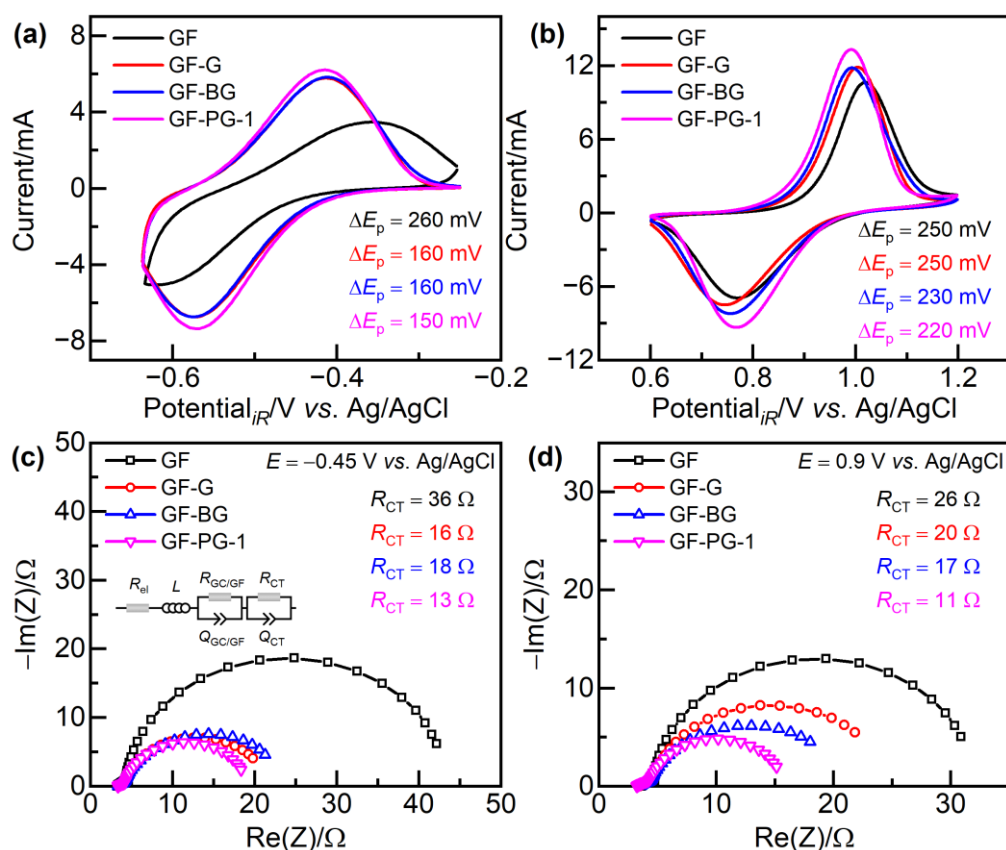


Figure 7-1. Electrocatalytic activity of graphene-modified GF. **(a,b)** CV of the (a) negative and (b) positive half-cell reaction with ΔE_p being indicated. **(c,d)** EIS in the (c) negative and (d) positive half-cell to assess R_{CT} .

CV was used to study the values for the ΔE_p of the V^{III}/V^{II} and $V^{VO_2^+}/V^{IVO_2^2+}$ redox couple (**Figure 7-1**). The activity of pristine GF (260 mV) in the negative half-cell (**Figure 7-1a**) was improved by the attached graphene (160 mV). No major additional improvement was observed using the doped material. GF-PG-1 revealed a slightly lowered ΔE_p (150 mV) and higher peak currents. The $V^{VO_2^+}/V^{IVO_2^2+}$ oxidation (**Figure 7-1b**) was enhanced for GF-G, but the reduction was kinetically hindered, which results in the same ΔE_p as for GF (250 mV). Minor improvements were monitored for the doped material (230 and 220 mV). In the negative half-cell, the R_{CT} of GF was 36 Ω , while GF-PG-1 showed a much lower value (13 Ω , **Figure 7-1c**). For GF-BG (18 Ω) no improvement was found in comparison to the felt modified using undoped graphene (16 Ω). The R_{CT} was also reduced in the positive half-cell from 26 to 11 Ω , especially by the attached phosphorus-doped graphene (**Figure 7-1d**). Even though the electrocatalytic activity of GF could be improved by attaching doped graphene, the possibilities of heteroatom functionalization must be studied in more detail to understand the important material properties for efficient electrode improvement.

7.2 Electrocatalytic Activity of Doped Graphene

The electrocatalytic activity of the pure commercial material was studied. For referential purpose, a CV curve was recorded for a blank GC electrode and drop-cast graphene powder (**Figure 7-2a**). Two commercial graphene powders, of which one was heat-treated under inert gas at 3000 °C to heal defects and remove surface groups, were used. In contrast to heat-treated G3000, pristine graphene showed a pre-located sharp redox peak below 1 V vs. Ag/AgCl, which is caused by a splitting of the redox signals when vanadium is reduced/oxidized either at basal planes or more active edges sites. The higher catalytic activity of graphene was associated with an increased disorder, which resembled active defects such as edge sites. To demonstrate this, basal and edge plane exposed HOPG electrodes were investigated, revealing improved redox kinetics for the edge plane exposed electrode (Figure S11).^[34,71] The additional active defects of graphene were furthermore well-visible in the corresponding Raman spectra (Figure S38). The defect-poor G3000 was thus chosen as a reference for the doped material to omit falsifying alterations in the activity.

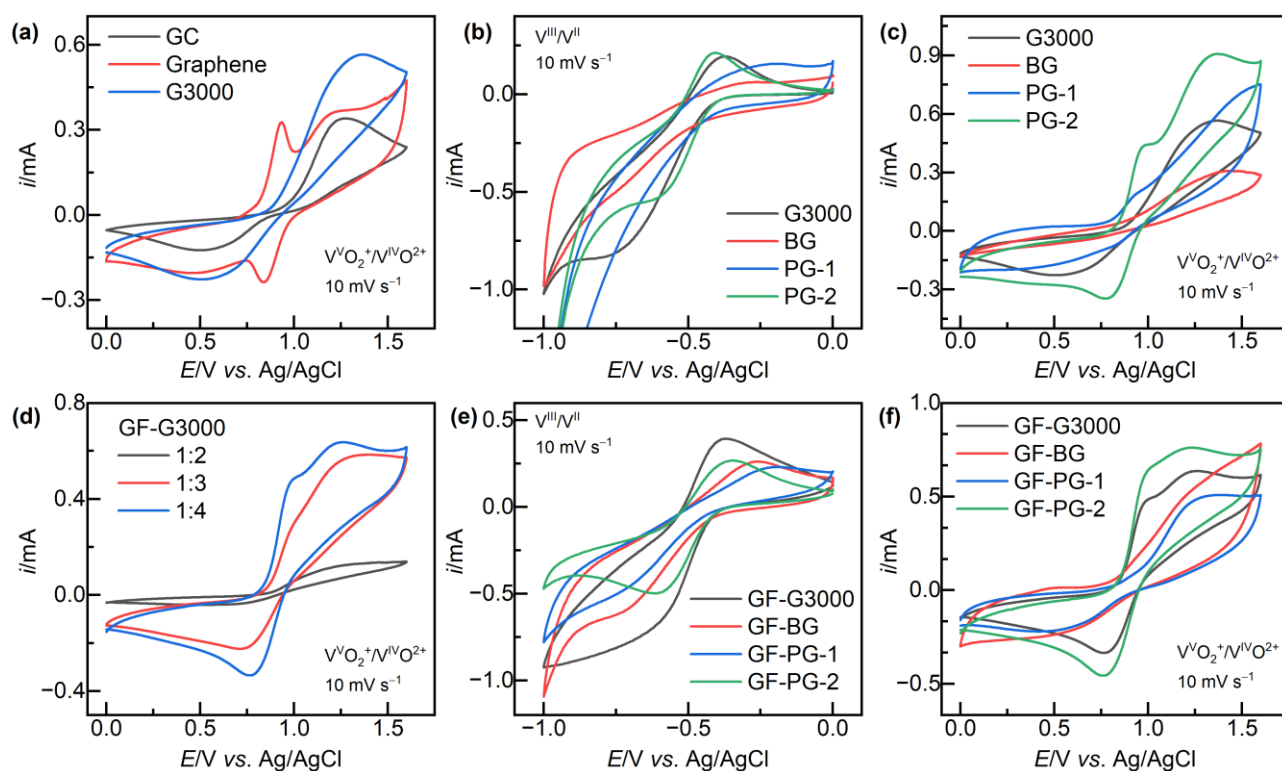


Figure 7-2. CV of drop-coated carbon-based material. **(a)** Blank GC and two different graphene powders. **(b,c)** Defect-free graphene (G3000) and doped graphene in the (b) negative and (c) positive half-cell. **(d)** A mixture of pulverized GF and G3000 at different mass ratios. **(e,f)** G3000 and doped graphene mixed with GF in a ratio of 1 to 4 in the (e) negative and (f) positive half-cell.

In both half-cell electrolytes (**Figure 7-2b,c**), the boron-doped graphene provided a lower activity than G3000, observed by a low current response and undefined peaks. Although PG-1 was rather inactive towards both half-cell reactions, a small $VVO_2^+/VIVO_2^{2+}$ oxidation peak like defective graphene was visible. Due to these promising results, phosphorus-doped graphene (PG-2) was synthesized using a known method.^[211] It showed improved redox kinetics and developed distinct redox peaks in both half-cells. However, rising currents towards the hydrogen and oxygen evolution reaction were detected. This was further examined in a vanadium-free sulfuric acid electrolyte, exposing the activity of PG-2 for these side reactions (Figure S39).

As a next step, the activity of the doped material interacting with a graphite-based matrix, *i.e.*, in contact with the felt, was inspected to converge the results observed for graphene-modified GF. GF was pulverized but could not be dispersed in a variety of solvents such as H_2O , DMSO, or IPA even with the addition of a surfactant and binder. Therefore, it was mixed with G3000 in different ratios to force a homogeneous dispersion of aggregates by π - π stacking, followed by drop coating on GC to study the catalytic activity (**Figure 7-2d**). By adding four times the mass of G3000 to GF, a homogeneous dispersion was obtained, which was directly observed in

the CV by the formation of two distinct redox peaks. This ratio was thus chosen for the investigation of the doped material in both half-cell electrolytes (**Figure 7-2e,f**). PG-2 showed well-defined redox peaks in the negative electrolyte, lower selectivity towards hydrogen evolution, and the highest currents in the positive electrolyte, whereas BG and PG-1 remained rather inactive.

7.3 Physicochemical Characterization of Doped Graphene

To establish relationships between chemical and microstructural properties and the electrocatalytic activity of the material, XRD, Raman spectroscopy and XPS were employed. By XRD, the degree of graphitization was analyzed (**Figure 7-3a**). Graphite powder was used as a reference, showing Bragg reflections corresponding to the 002, 100, 101, 004, 110, and 112 planes located at $2\theta = 26.5, 42.4, 44.7, 54.6, 77.5, \text{ and } 83.6^\circ$, respectively.^[102] These reflections were equally present for G3000 and PG-2. In contrast, the commercial PG-1 and especially BG revealed an amorphous appearance.

Structural differences were further studied by Raman spectroscopy (**Figure 7-3b**). The main features of graphite are the G band at $\sim 1580 \text{ cm}^{-1}$, resembling the in-plane stretching of C=C bonds, and the D band at $\sim 1330 \text{ cm}^{-1}$, induced by disordering such as edge sites.^[92,93] The intensity ratio of the D and G band provides useful information about the degree of disorder in the sample.^[73,94] Heat-treated G3000 had a low $I(\text{D})/I(\text{G})$ ratio of 0.07, which was slightly increased to 0.13 due to the doping procedure for PG-2. In contrast, the commercial BG (1.89) and PG-1 (1.76) showed a high number of defects and a vanishing 2D signal, correlating to the amorphous XRD pattern.

The chemical composition was analyzed by XPS (**Figure 7-3c-g**, Figure S40). In the O 1s detail spectra of G3000 (**Figure 7-3c**), three different carbon-oxygen components were identified: carbonyls (O=C) at $\sim 531.1 \text{ eV}$, hydroxyls (O-C) at $\sim 532.1 \text{ eV}$, and carboxylic groups (O=C-O) at $\sim 533.1 \text{ eV}$.^[137,160,161] An additional oxygen component was present for BG and PG-1 at ~ 530.9 and 530.7 eV , arising from oxygen bound to boron or phosphorus, respectively. Six different contributions in the C 1s region (**Figure 7-3d**) were visible for all samples: sp^2 hybridized carbon at $\sim 284.4 \text{ eV}$, sp^3 related carbon at $\sim 285.2 \text{ eV}$, and carbonaceous components at $\sim 286.7\text{--}289.6 \text{ eV}$.^[141,212] For BG, boron ($\sim 3.1 \text{ at}\%$) was equally bound to three carbon atoms in the basal plane (190.9 eV), and at the edge site to two carbon and one oxygen atom (192.4 eV).^[213,214] PG-1 reveals phosphorus ($\sim 2.4 \text{ at}\%$) majorly coordinated to one or two carbon

atoms (133.4 eV), and the lesser amount covalently substituted in the graphite lattice (132.1 eV). Elemental phosphorus was present (129.6 eV). In contrast, PG-2 had a lower doping concentration of <1 at%, further exhibiting a lower share in edge site located and no elemental phosphorus (Figure S41).

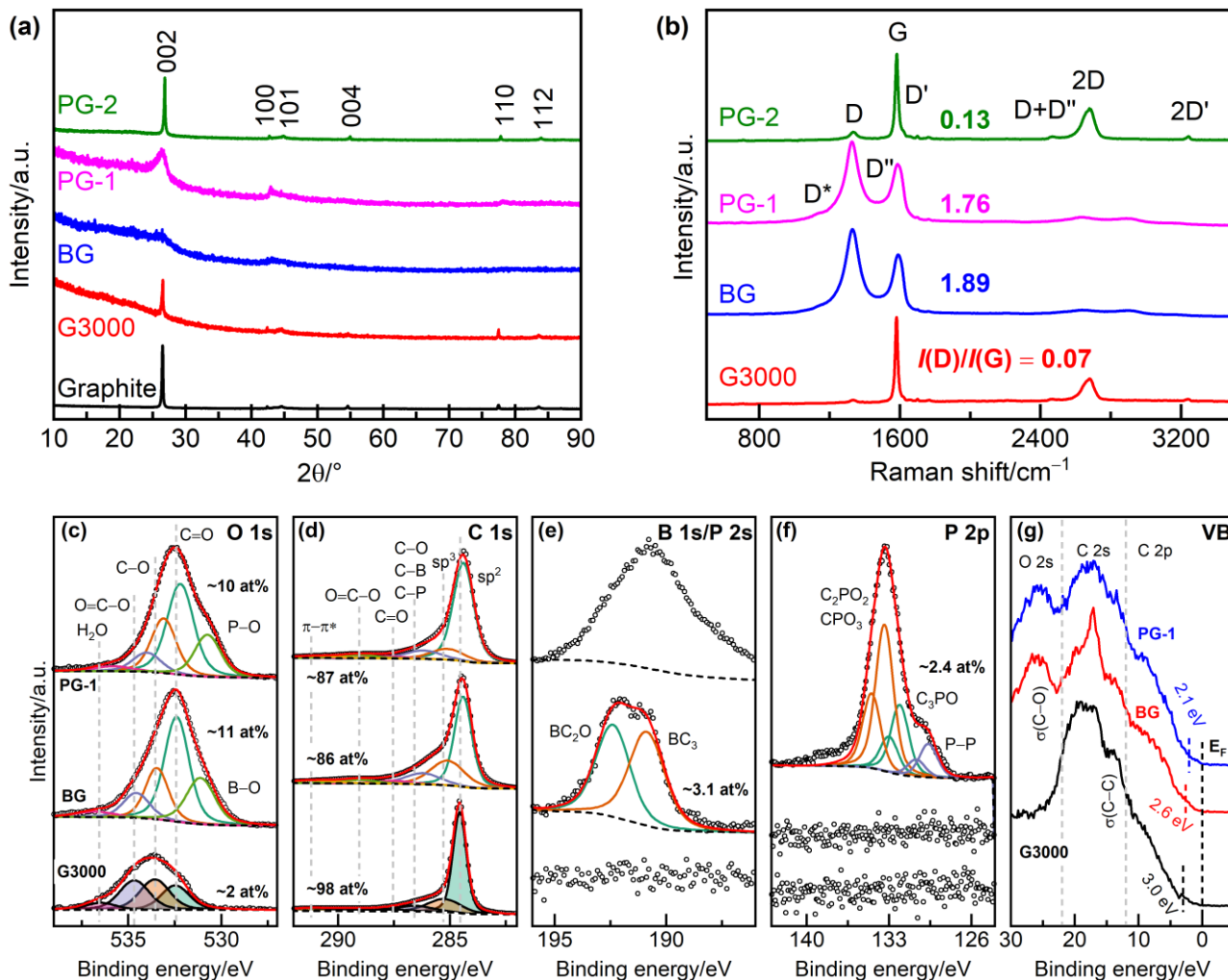


Figure 7-3. Physicochemical characterization of pristine and doped graphene. **(a)** XRD pattern with graphite as a reference. **(b)** Raman spectra with the assigned vibrational features, and the evaluated D to G ratio. **(c–f)** Deconvoluted detail spectra of the (c) O 1s, (d) C 1s, (e) B 1s/P 2s, and (f) P 2p signals. The respective concentration of each element is indicated. **(g)** The VB region close to E_F .

Close to E_F , more information about the electronic structure of the material was assessed (**Figure 7-3g**). The domains below E_F are occupied by C 2p (2 to 12 eV), C 2s (to 22 eV), and O 2s (above 22 eV) valence electrons.^[152,168,169] A sharp signal for BG at ~16 eV corresponds to the B 2s core level. All samples showed a non-zero state between 0 to 3 eV because of 2p- π electrons in the basal plane.^[170] The steep onset of electron density for G3000 (~3 eV) shifted to lower values for BG (2.6) and PG-1 (2.1). This suggests that a higher electron density exists

close to E_F and therefore the electrode could in theory more easily take part in charge transfer reactions. Especially for PG-1, this uplift was not reflected in the catalytic activity.

In contrast to the electron enrichment in the VB (**Figure 7-3g**) and the high number of defects for the doped graphene, several properties were observed which influence the activity negatively. It was already demonstrated that surface oxygen inhibits the electron transfer, which could explain the poorer performance of BG (~10 at%) and PG-1 (~11 at%) compared to PG-2 (<1 at%).^[180,200] In an elemental analysis (Table S3), an even lower carbon content for the commercial powders (76 to 78 %) was revealed. The high degree of bulk oxygen is suspected to impede the electrical conductivity. The amorphous XRD pattern and a broadened sp^2 carbon feature (from 0.8 to 1 eV) in the photoelectron spectra demonstrated low long-range order and decreased graphitic character at the surface, both detrimental for the catalytic activity.^[74,77] Considering the higher dopant concentration of PG-1 (~2.4 at%) compared to PG-2 (<1 at%), the number of foreign atoms in the structure might not define the electrocatalytic activity. Instead, it could be more important how the phosphorus is embedded in the lattice. In my case, a low number of mainly graphitic coordinated phosphorus (C_3PO) was responsible for a remarkable change of the electrochemical performance. In summary, for a material which maintains low degree of oxygenation and high long-range order, phosphorus-doping could be a suitable strategy to improve the activity.

7.4 Directly Phosphorus-Functionalized GF

After the previous investigation, phosphorus-doped material stood out as a promising candidate to improve the activity, suggesting that electron-donating species could be beneficial. The discrepancy between our and previous published results may be resolved considering that most modification techniques go along with significant changes not only to the surface chemistry, but also alter morphology and the nature and density of other graphitic defects. As it has been shown by my previous works, these changes alone may explain a significant part of the observed catalytic improvement, either by increasing the active surface area or by improving the kinetics of charge transfer. The significance to prevent changes in morphology and to monitor the density of graphitic defects when the effect of heteroatom functionalization is evaluated is therefore expressed.

To study the effect of phosphorus-functionalization for GF, a slightly modified method used for PG-2 was employed. To exclude any influence on other felt properties of the obtained GF-P,

various analytical tools were used. By SEM, it was ruled out that the treatment damaged the material visibly (Figure S42). In the XRD pattern (Figure 7-4a), four out of six graphene reflections were present for both pristine GF and GF-P that did not differ concerning their positions, relative intensities, or FWHM values, proving that the modification had no effect on the degree of graphitization.

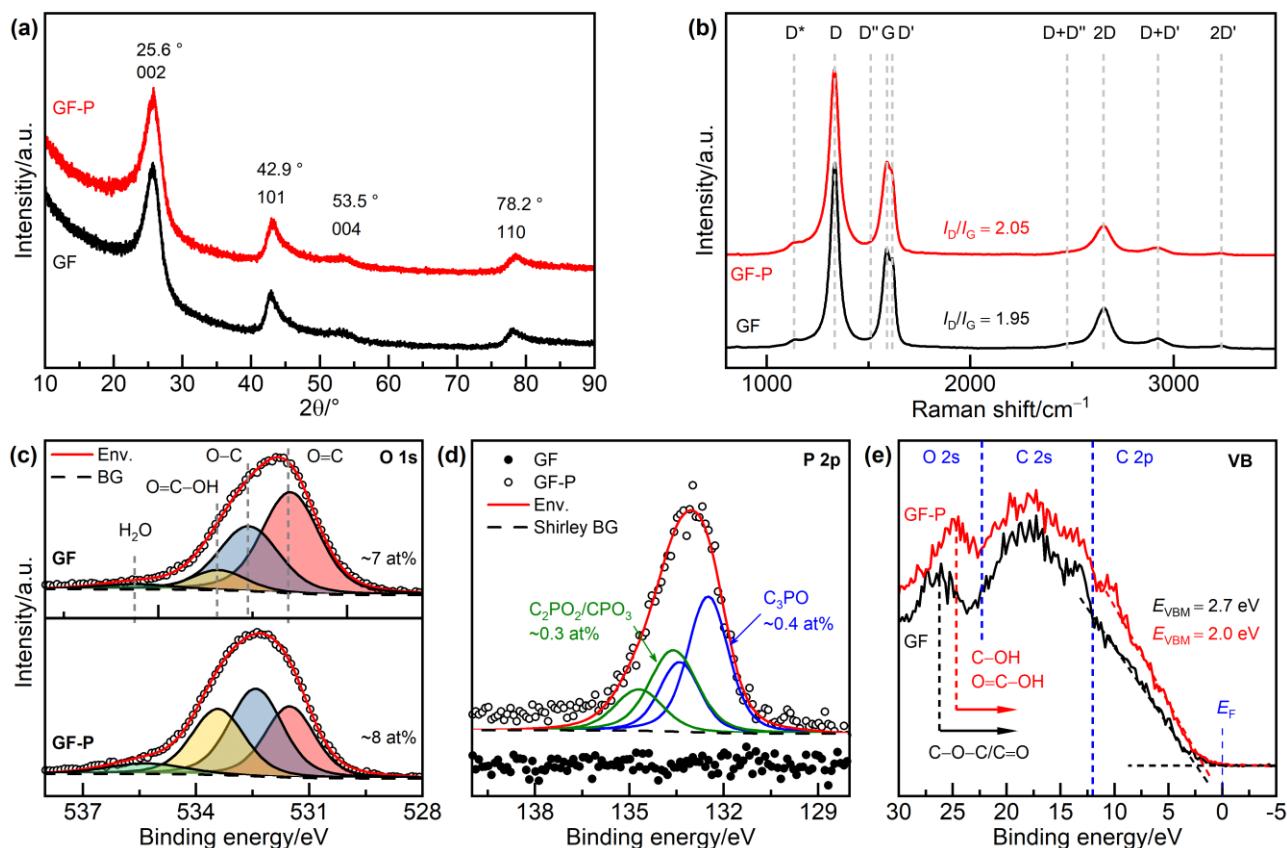


Figure 7-4. Physicochemical characterization of GF and GF-P. Microstructural properties analyzed by (a) XRD and (b) Raman spectroscopy. (c–e) XPS detail spectra of the (c) O 1s, (d) P 2p and (e) VB region.

The change of disorder was monitored by Raman spectroscopy (Figure 7-4b). The D to G ratio of GF slightly increased from 1.95 to 2.05 due to the modification. Additional defects were also reflected in the relatively less intense 2D band. By XPS, the level of oxygenation was studied (Figure 7-4c), since it was proposed that oxygen-rich phosphate groups can enhance the activity of GF, which had to be excluded as a possible influence.^[210] The low oxygen content of the pristine felt (~7 at%) was maintained by the functionalizing treatment. The phosphorus concentration was estimated to <1 at% by the analysis of the P 2p region (Figure 7-4d). In contrast to other publications that deal with phosphorus functionalization of GF, herein it was not bound to carbon by an oxygen bridge as a functional group but directly substituted for a carbon atom in the graphite lattice, either in the basal plane (C₃PO) or at the edges

(C_2PO_2/CPO_3).^[206,210] Due to the low increase in disorder and the absence of pores in the SEM images, it can be concluded that the changes in the electrochemical performance of GF-P are associated mainly with the substitution. Similar to the doped graphene powders, it was seen in the VB region that the treatment increased the DOS by ~ 0.7 eV (**Figure 7-4e**). Furthermore, a shift of the $\sigma(C-O)$ signals toward the C $2p$ region was determined which corresponds to the presence of majorly hydroxyl and carboxylic groups over carbonyl and ether groups and agrees well with observations in the O1s spectrum (**Figure 7-4c**).^[152]

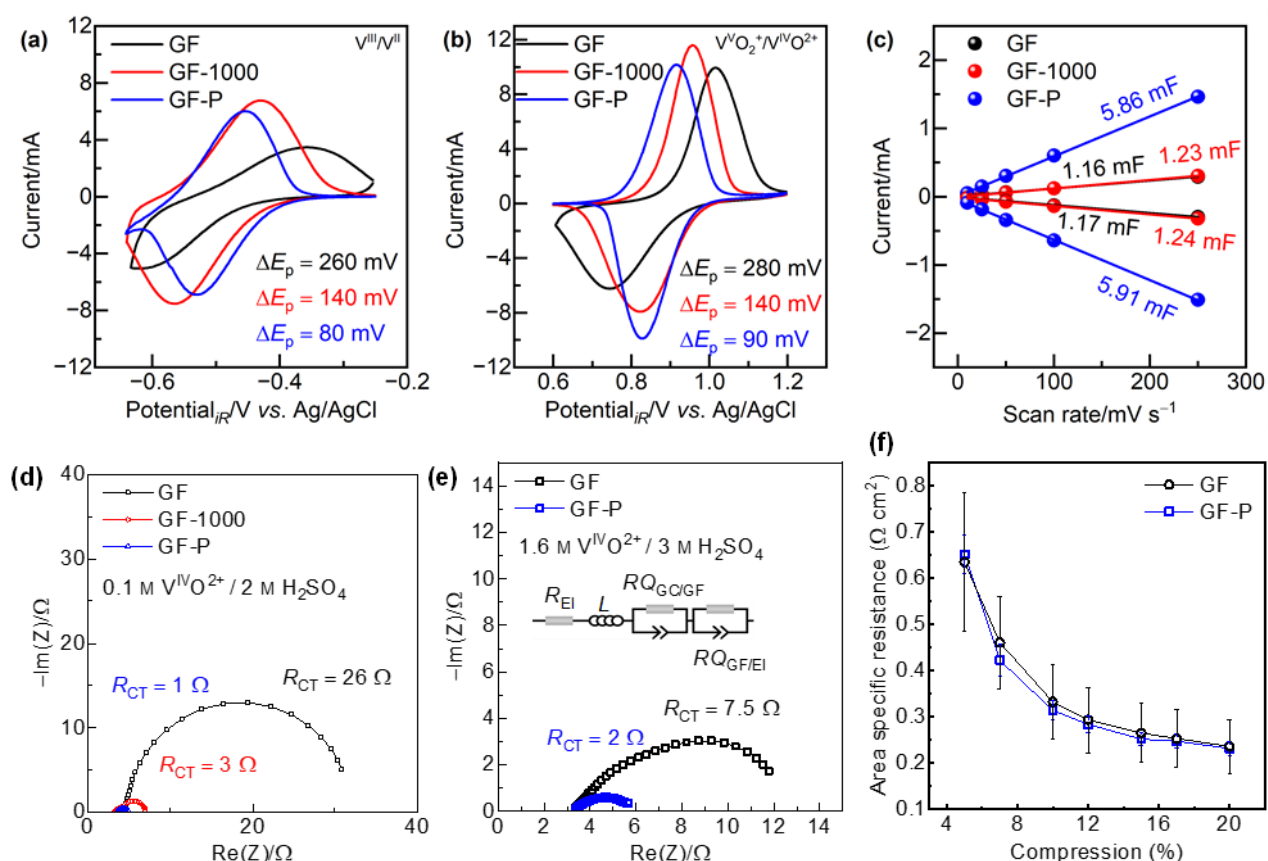


Figure 7-5. Electrochemical half-cell performance and electrical conductivity of pristine and modified GF. CV in the (a) negative and (b) positive half-cell with ΔE_p being indicated; (c) EDLC for the anodic and cathodic current responses. (d,e) EIS at an applied potential of 0.9 V vs. Ag/AgCl in (d) half-cell and (e) full cell battery electrolyte. (f) Electrical conductivity under compression.

The electrochemical half-cell performance of GF-P was studied in comparison to pristine GF and a felt treated analogous to GF-P, but in the absence of a phosphorus source (GF-1000). This was conducted since the performance of GF is already improved by a surface cleaning at high temperatures under argon atmosphere.^[200] This could be seen by an improved ΔE_p for GF-1000 from 260 (GF) to 140 mV in the negative half-cell (**Figure 7-5a**). However, the ΔE_p was further decreased to 80 mV for GF-P. Similarly, in the positive half-cell GF-P showed a lower ΔE_p (90

mV) than the less active GF (280 mV) and the thermally treated GF-1000 (140 mV, **Figure 7-5b**). The EDLC was studied to qualitatively compare the electrochemically active surface area.^[215] The low value of GF (~ 1.2 mF) was increased by a factor of ~ 5 due to the phosphorus-functionalization (**Figure 7-5c**). The EDLC is mainly related to the graphitic disorder, as the basal plane has low values, followed by edge sites and carbon vacancies or point defects, as it is the case for GF-P.^[179]

A further investigation of the electrochemical impedance confirmed the success of the modification (**Figure 7-5d,e** and Figure S43) by lowered R_{CT} values for the $V^{VO_2^+}/V^{VO_2}$ redox reaction from 26 to 1 Ω . Additionally, EIS measurements were repeated using the electrolyte composition of the full cell experiments. Whereas the R_{CT} value of GF-P remains almost unchanged at ~ 2 Ω , the slow reaction kinetics of pristine GF become less relevant, exposing a much lower R_{CT} of 7.5 at higher vanadium and sulfuric acid concentrations. To study in more detail whether reduced R_{CT} values are a consequence of higher electrical conductivity, the area specific resistance under compression was evaluated (**Figure 7-5f**). It is seen that there is no significant difference between GF and GF-P, marking faster reaction kinetics to be responsible for the enhanced electrocatalytic activity. The experimental procedure regarding the heating temperature (Figure S44), the concentration of the precursor solution, and the reaction environment (Figure S45) were optimized for the synthesis of the herein presented GF-P.

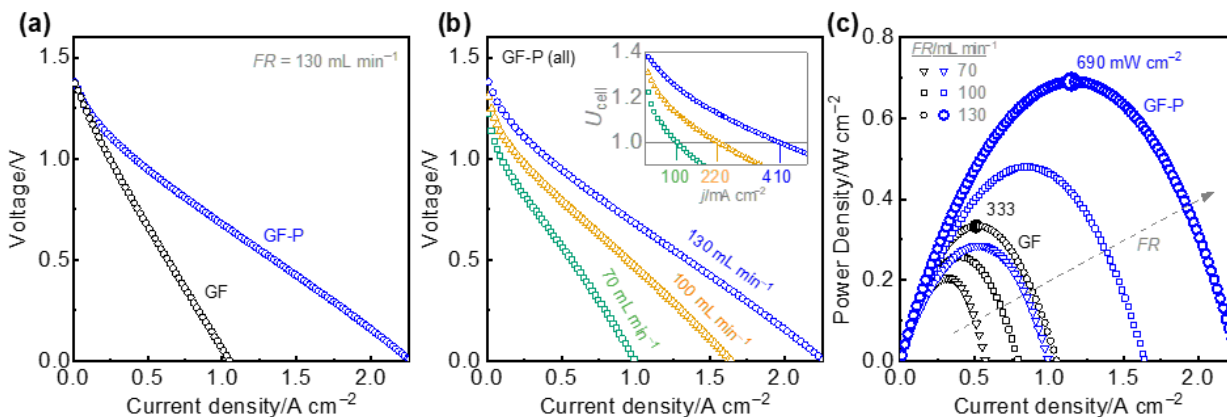


Figure 7-6. Electrochemical full cell performance of GF and GF-P. **(a,b)** Polarization curves **(a)** at a flow rate (FR) of 130 mL min⁻¹ and **(b)** at different FRs. **(c)** Power curves at different FRs.

To investigate the electrochemical performance of GF-P under nearly realistic operation conditions (*i.e.*, forced convection of the electrolyte through the electrodes), VFB test cells were equipped with the samples and the polarization curve method was conducted at SoC $\gtrsim 50$ %. Thus it can be quantitatively and qualitatively distinguished between different types of voltage

losses of kinetic activation, ohmic and mass-transport overpotentials.^[216] The polarization curves of GF and GF-P at a flow rate of 130 mL min⁻¹ are displayed in **Figure 7-6a**. The progression of the U vs. i curves of GF-P and GF at low current densities shows the polarization losses due to the kinetic activation of the electrodes. While GF reaches a cell voltage of 1.0 V at already 240 mA cm², a current density of 410 mA cm² is required for GF-P. While GF-P clearly transits into a linear Ohmic loss region at about 1.2 V, this behavior is not very pronounced for GF. The phosphorus-functionalized felt further shows improved reaction kinetics in that region by a lower slope compared to pristine GF. A precise observation of the progressions of the U vs. i curves of GF-P especially reveals a decent exponential-like decrease at high current densities above 1.5 A cm², which is an indicator for mass transport overpotentials. For GF, a progression from a linear to an exponential-like region cannot be observed without uncertainty. This shows that the cell voltage was lowered by kinetic activation and by mass-transport overpotentials, which likely resulted from the slow kinetics of the V^{II} oxidation in comparison to the fast V^{VO}₂⁺ reduction.^[217] A cell voltage of 0.0 V was reached at current densities of 1.05 and 2.30 A cm², respectively, demonstrating the ability of GF-P to tolerate higher limiting currents. Despite of high educt availability (high in theory due to a high flow rate and high vanadium concentration), the lowering of the flow rate caused a ‘forking’ of the polarization curves even at very low current densities (**Figure 7-6b**). The current density which is necessary to reach a potential of 1.0 V is dependent on the flow rate, increasing from 100 over 220 to 410 for flow rates of 70, 100, and 130 mL min⁻¹, respectively. In summary, we conclude that under realistic operational conditions, the superior GF-P electrode material scores by lower polarization losses, faster redox kinetics, and an improved availability/removal of educt/product, respectively, during the VFB discharge reaction. This is further expressed by the high peak power density in **Figure 7-6c** of GF-P (690 mW cm⁻²), which is more than twice as for GF (333 mW cm⁻²).

7.5 Conclusions

In this chapter, the influence of phosphorus heteroatom functionalization on the electrochemical performance of graphene and GF was studied. By using commercial in comparison to synthesized phosphorus-functionalized graphene, the important physicochemical properties for an active electrocatalyst for the vanadium redox reactions were assessed. A high degree of graphitization and low number of surface and bulk oxygen groups were considered necessary to profit from phosphorus as additional active site. The amorphous appearance and high

surface as well as bulk oxygen content of the commercial powders were detrimental to the activity of the material. Consequently, rationally synthesized phosphorus-doped graphene showed a high catalytic activity. This knowledge was transferred to realistic battery electrodes to successfully functionalize GF, which showed high electrocatalytic activity for both half-cell reactions. Full cell polarization curves demonstrated a lower iR -drop and reduced kinetic and mass transport overpotentials. Retaining important graphite properties such as a highly ordered sp^2 carbon content, low concentration of OFGs, and incorporating phosphorus directly into the graphite lattice matters more than the sheer concentration of the heteroatom. This project highlights the importance of an in-depth view on the surface properties of GF since one altered property cannot be made responsible for changes in the activity, when other material characteristics are not monitored equally.

8 The Work Function Describes the Electrocatalytic Activity of Graphite

In Chapter 7, it was shown that enrichment with electrons near E_F by functionalization with electron-donating elements such as phosphorus might be responsible for improved charge transfer kinetics of GF for the vanadium redox reactions. Recalling the scheme on the graphite–electrolyte interface in **Figure 1-2e**, a different strategy seems appropriate as well: If the vacuum energy (E_{Vac}) is defined as zero, a lower work function (WF, $\Phi = E_{Vac} - E_F$) brings E_F closer to the redox potential of the electrolyte. This was demonstrated for metals, such as copper or silver, yielding improved charge transfer properties for the electrocatalytic CO_2 reduction.^[27] However, experimental results on the influence of the WF vary and therefore cannot be readily extrapolated from one system to another. One study of Au–Ag alloys suggests more efficient CO_2 reduction by increasing the WF, while another work claims the opposite for silver electrodes.^[28,29] For carbon-based electrodes used in the oxygen reduction reaction, a lower WF has been found to be beneficial.^[30]

Herein, pristine and activated GF for the $V^{VO_2^+}/V^{IVO_2^+}$ redox reaction is investigated to elaborate the correlation between electrocatalytic activity, physicochemical properties and electronic structure by combining results from half-cell electrochemistry, SEM, XPS and UPS, as well as Raman spectroscopy and REELS. Argon ion bombardment on HOPG was considered as a possible model to find interactions between graphitic defects and the electronic structure. Finally, PAHs were attached to graphene to observe electrochemical changes associated with the architecture of carbon edge sites, linking micro- and electronic structure in detail.

8.1 Electrocatalytic and Microstructural Properties of GF

Two activation procedures were used to compare felt electrodes that differed in their electrocatalytic activity and structural properties. (i) a deoxygenation process introduced in Chapter 5 using a mixture of argon and H_2 gas was employed to purify the surface of oxygen (GF- H_2).^[200] (ii) a thermally activated sample oxidized in air (GF-TA) was chosen to consider a conventional treatment relevant to industrial scale. The electrocatalytic activity for the vanadium redox reaction was evaluated in electrochemical half-cell experiments. In this chapter, the focus lies on the $V^{VO_2^+}/V^{IVO_2^+}$ reaction as an example because it is kinetically sluggish and in general harder to facilitate. It should be mentioned that the relevant parameters obtained for the oxidation of

vanadium species in the positive half-cell do not necessarily correspond to those driving reductive reactions in a VFB such as the V^{III}/V^{II} reduction reaction in the negative half-cell.

To describe the activity of an electrode, ΔE and R_{CT} were determined. It was found that ΔE decreased from 230 (GF) to 140 (GF- H_2) to 100 mV (GF-TA) after activation (**Figure 8-1a**). Correspondingly, R_{CT} decreased from 22 to 3 to 1 Ω in the same order (**Figure 8-1b**). This demonstrated that both activation methods increased the electrocatalytic activity of GF, but thermal oxidation did so to a higher extent.

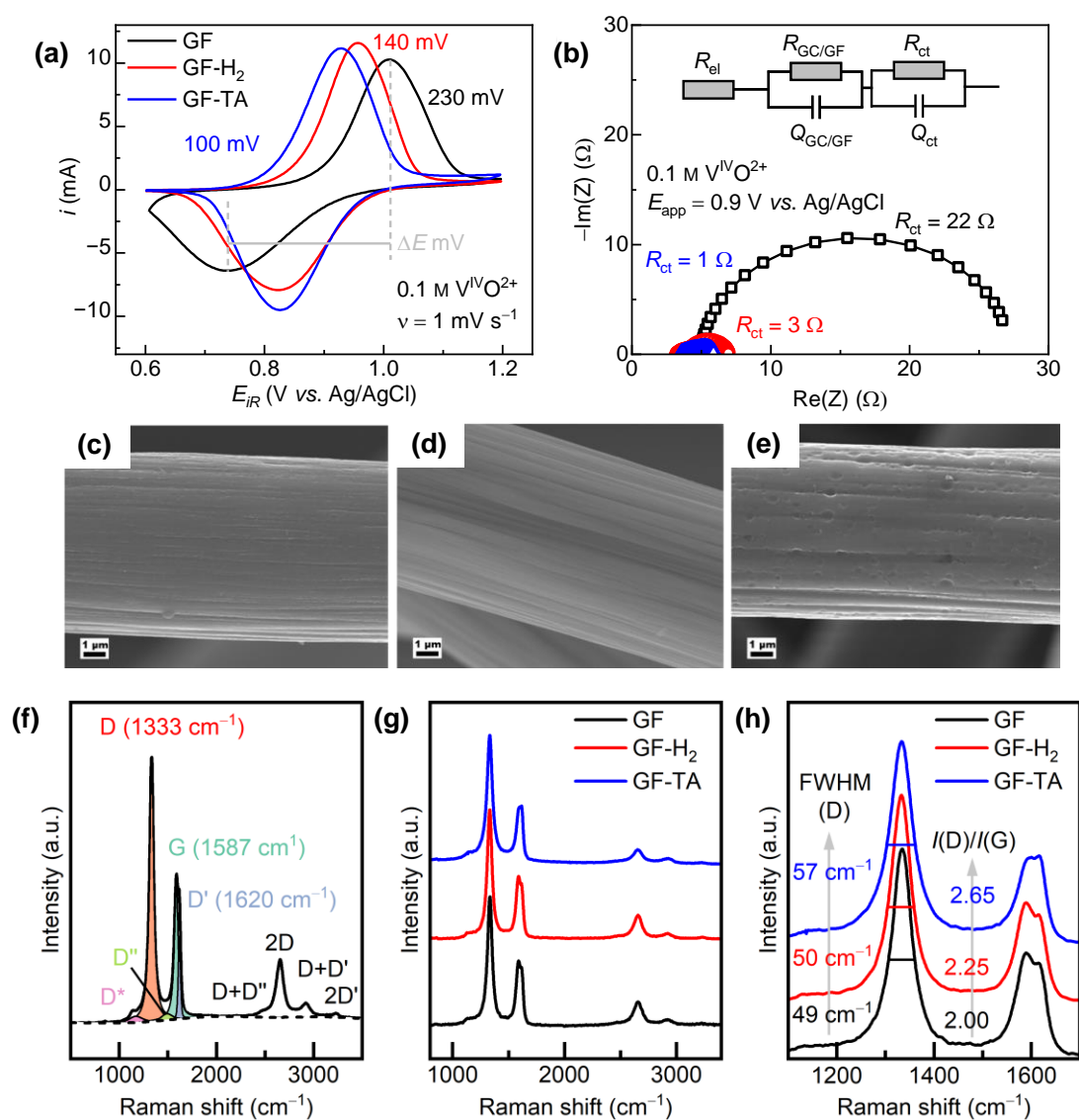


Figure 8-1. Electrochemical and structural characterization of GF. **(a)** CV in the positive half-cell, displaying ΔE between the $VVO_2^+/V^{IV}O_2^{2+}$ redox peaks. **(b)** EIS at an applied potential to assess R_{CT} . **(c-e)** High-magnification SEM images showing the morphology of **(c)** GF, **(d)** GF- H_2 , and **(e)** GF-TA. **(f-h)** Raman spectra, illustrating **(f)** an exemplary deconvolution of the characteristic vibrational features of GF; **(g)** each felt stacked for comparison, and **(h)** the results of the deconvolution.

To explain the differences in electrocatalytic activity, the physicochemical properties of the felts were studied. Structural defects and morphological changes on the microscale resulting from the treatments were visualized by SEM. **Figure 8-1c–e** shows that the smooth surface of GF was preserved after deoxygenation, but additional pores were created by thermal activation. While the total surface area of GF-TA ($3.41 \text{ m}^2 \text{ g}^{-1}$) is larger than that of GF ($0.64 \text{ m}^2 \text{ g}^{-1}$) and GF-H₂ ($0.69 \text{ m}^2 \text{ g}^{-1}$), previously it was demonstrated that the active surface area normalized to the electrochemical double layer is higher for the latter due to a higher density of defects.

A deeper investigation down to the nanoscale was achieved by Raman spectroscopy. The additional presence of defects on GF-H₂ was detected by evaluating the intensity ratio of the D and G bands in the spectra.^[218] The $I(\text{D})/I(\text{G})$ ratio increased from 2.00 (GF) to 2.25 (GF-H₂) to 2.65 (GF-TA), indicating that both activation methods introduced additional defects, but thermal activation yielded more disorder. In addition, the half-width of the D band increased from 49 to 57 cm^{-1} for GF-TA, which can be attributed to the increased number of defects.

The chemical composition studied by XPS showed surfaces consisting of carbon and oxygen only (Figure S46). No oxygen was present on GF-H₂ due to the deoxygenation process. The oxygen concentration decreased after thermal oxidation from 6.0 at% on GF to 4.5 at% on GF-TA, which can be attributed to the removal of the atmospherically oxidized upper graphite layer, exposing an underlying, less oxidized layer. To quantitatively describe the degree of graphitization of a carbonaceous sample, the D-parameter, evaluated in the C KLL Auger region, was used.^[219] In this case, the D-parameter of GF (22 eV) was increased after deoxygenation (23 eV) and decreased for GF-TA (21 eV). Accordingly, deconvolution of the C 1s spectra revealed that the sp^2 content increased for GF-H₂ (81 to 88 at%) and decreased after thermal activation (to 79 at%). This agreed well with the disorder characterized above by SEM and Raman spectroscopy.

8.2 Electronic Structure of GF

Another method to study the integrity of the graphite structure, especially the upper surface layers, is REELS. A beam of electrons with a certain energy is scattered on the surface of the sample. Most of the electrons are scattered elastically, but a small fraction transfers energy to the system by exciting internal energetic transitions. In graphitic materials such as HOPG, a well-defined $\pi-\pi^*$ transition can be observed at 6.6 eV (Figure S47). The relative intensity and

position of the loss feature characterize the graphitic degree, as demonstrated by argon ion bombardment: the inelastic scattering feature was weakened and shifted to lower energy loss values. A higher degree of graphitization for GF-H₂ was therefore indicated by REELS through the higher relative intensity of the π - π^* transition, in contrast to the low-intensity signal for GF-TA (**Figure 8-2a**).^[220] However, both samples showed a slight shift from 6.1 eV (GF) to lower energy values of 6.0 (GF-H₂) and 5.9 (GF-TA) due to the damaging pretreatment.

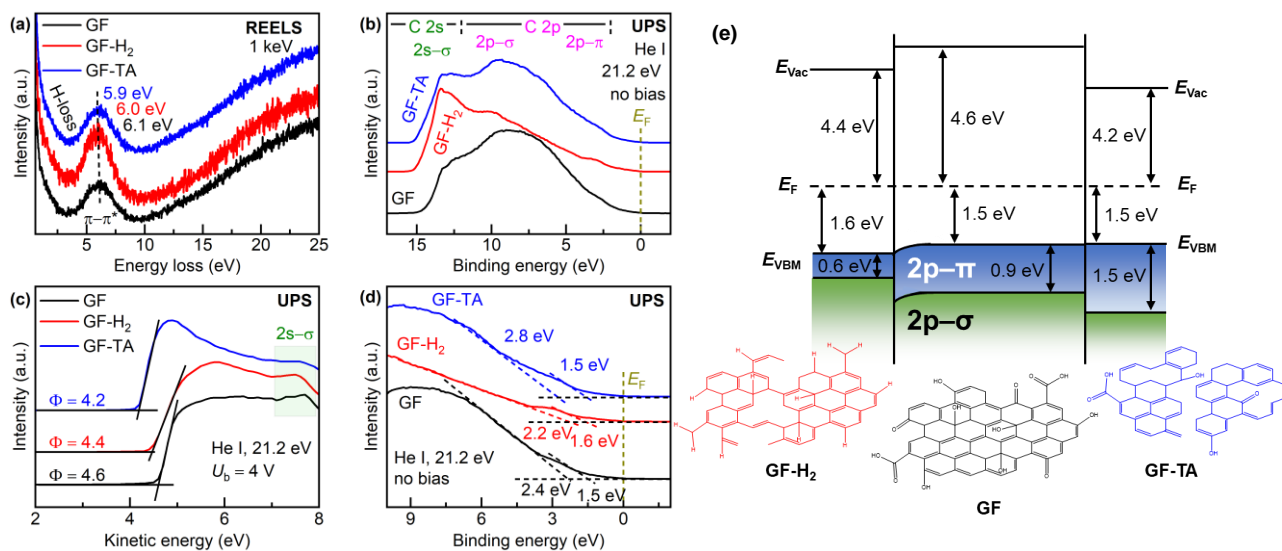


Figure 8-2. The electronic structure of GF. **(a)** The integrity of the π -conjugated system is analyzed by the π - π^* transition using REELS. **(b)** The electronic DOS below E_F is probed by UPS. **(c)** At an applied external bias, the cutoff energy of the valence electrons yields the WF. **(d)** Detailed investigation of the threshold energies close to E_F to determine the VBM. **(e)** By combining the information retrieved from UPS, an electronic band diagram is constructed.

To establish correlations between the previously evaluated characteristics and the electronic structure, UPS was used to study the DOS near the Fermi level. Compared to XPS, which permits the emission of electrons from the first 10 nm of a sample, UPS is much more surface sensitive, penetrating only the first 2.5 nm due to the lower excitation energy of UV light. Consequently, the electronic structure of the surface can be evaluated with high resolution. For graphitic materials, the range from 2 to 12 eV below E_F is occupied by C 2p electrons and above by C 2s electrons (**Figure 8-2b**).^[152,169] The region of the C 2p orbital can be divided into two contributions originating from $2p$ - π and $2p$ - σ electrons. The DOS extends until E_F where the π and π^* bands touch, characterizing graphite as a zero bandgap semiconductor (compare **Figure 1-2d**).^[170] For GF-H₂, a strong $2s$ - σ signal at ~ 13 eV was detected due to the higher graphitic degree of the sample.^[171] In addition to differences in VB occupation which describe the electronic structure of the material, an energy cutoff at higher binding energies can be used to determine the WF. This value can be accurately evaluated with a bias voltage applied to the

specimen, increasing the slope of the cutoff (**Figure 8-2c**). In addition, an energy threshold near E_F was used to define the E_{VBM} of the respective atomic orbital to describe from which energetic level on charge carriers are located (**Figure 8-2d**).

The values of the UPS characterization were used to draw a schematic band diagram, in which E_F is defined as the reference point for the comparison of the samples (**Figure 8-2e**). It was assumed that underlying graphite layers, which were not affected by the treatment, resemble the surface of untreated GF. Therefore, an energetic passage between the different materials at E_F was defined as shown in the scheme. It is observed that the WF decreased from 4.6 eV for GF through 4.4 eV for the more active GF-H₂ to 4.2 eV for GF-TA, which revealed the highest electrocatalytic activity. Moreover, an inverse correlation between the WF and the degree of disorder characterized by Raman spectroscopy can be established: a lower WF corresponds to a higher $I(D)/I(G)$ ratio. The VBM of the $2p-\pi$ electrons is slightly increased after deoxygenation (1.5 to 1.6 eV) due to the increased sp^2 content.^[200] In contrast, the values for GF-TA remain unchanged, indicating that the disorder introduced through deoxygenation and thermal activation does not have a large effect on the electronic structure in the VB.

Charge accumulation was detected at the interface between the untreated felt and the deoxygenated surface by a shifted C 1s signal (+0.1 eV). In the drawing, this is sketched as a downward band bending behavior typically known from semiconductors. Since GF and GF-H₂ both exhibit the properties of a semiconductor and GF resembles the bulk beneath the modified surface layers, two semiconducting materials touch at the interface between the surface and bulk. This bending is thus attributed to a lower electrical conductivity in the direction perpendicular to the surface, in which the graphene layers are arranged, due to their higher degree of graphitization. To confirm that differences in the electronic structure are mainly linked to structural disorder and not the concentration or presence of surface oxygen groups, the thermally activated felt (GF-TA) was subjected to the deoxygenation and analysis procedure (Figure S48). Only slight changes in the electronic structure were observed for deoxygenated GF-TA: the treatment resulted in a further decrease of the WF and VBM to 4.1 eV and 1.6 eV, respectively. In agreement with the previous study on GF-TA, which showed that charge transfer properties can be enhanced by the removal of surface oxygen, this is further evidence that WF and electrocatalytic activity are linked.^[180,200]

8.3 HOPG as Model System

To study the effects of disorder on the electronic structure in more detail, HOPG was chosen as a model substrate. Initially the HOPG surface was contaminated by atmospheric oxidation and thus exhibited oxygen (~ 4 at%), a low D parameter (17 eV), and a reduced sp^2 carbon content of ~ 78 at% (Figure S4). In a second step the surface was cleaned with argon ion clusters, which increased the D-parameter to 24 eV and the sp^2 content to ~ 93 at% as expected for almost perfect graphitic material. Subsequently, defects were introduced by bombardment with monoatomic argon ions. This resulted in an additional contribution in the C 1s spectra due to the formation of carbon vacancies.^[221] At all three stages of the substrate (untreated, cleaned, etched), UPS was used to follow the evolution of the electronic structure and sketch a band diagram (Figure S47 and Figure S50). Removal of oxygen and sp^3 carbon resulted in a sharp drop in the WF from 4.9 to 4.2 eV. However, this value was maintained after ion bombardment, which illustrates that vacancies do not affect the level of the WF. Instead, the E_{VBM} of the $2p-\pi$ electrons was raised from 0.9 to 0 eV, indicating a metallic character for the damaged HOPG. This highlights the different influences of various defects on the electronic properties of graphite. Point defects introduced by ion bombardment altered the E_{VBM} similarly to the introduction of additional charge carriers by doping. Argon ions implanted in the material during ion bombardment cannot be held responsible for the changes in the electronic structure, since at the time of the UPS measurements, the volatile argon has already escaped through the defects into the atmosphere. This is confirmed by the absence of argon-related signals in the spectra after bombardment. The presence of predominant edge defects on GF is evident from previous studies in which we considered the nature of disorder by Raman spectroscopy, and from the absence of an additional peak in the C 1s spectra after the activation (Figure S46) that would correspond to vacancies.^[180,200] The edge sites on GF-H₂ and GF-TA, on the other hand, decrease the WF but leave the VB level unchanged.

8.4 Influence of Edge Geometry

The importance of edge sites for the electrocatalysis of vanadium redox reactions is demonstrated by CV curves of pyrolytic graphite electrodes exposing either predominately basal or edge planes (**Figure 8-3a**). For the HOPG electrode with edge site orientation, the $\text{V}^{\text{VO}_2^+}/\text{V}^{\text{VO}^{2+}}$ oxidation wave exhibited higher peak currents and was shifted to lower potentials, confirming the higher reactivity of these regions compared to the basal plane. However, since edge sites have both armchair and zigzag configuration in real electrodes, their individual contribution

cannot be assessed by this measurement. Therefore, graphene was modified with PAHs that differ in their orientation and the number of conjugated rings. Two PAHs with armchairs, phenanthrene (P-G) and chrysene (C-G), and two with zigzag edges, anthracene (A-G) and tetracene (T-G), with three and four rings, respectively, were chosen to account for the edge type and size effect. The successful modification was observed by redox signals in a region where graphene otherwise shows no faradaic potential (**Figure 8-3b**).

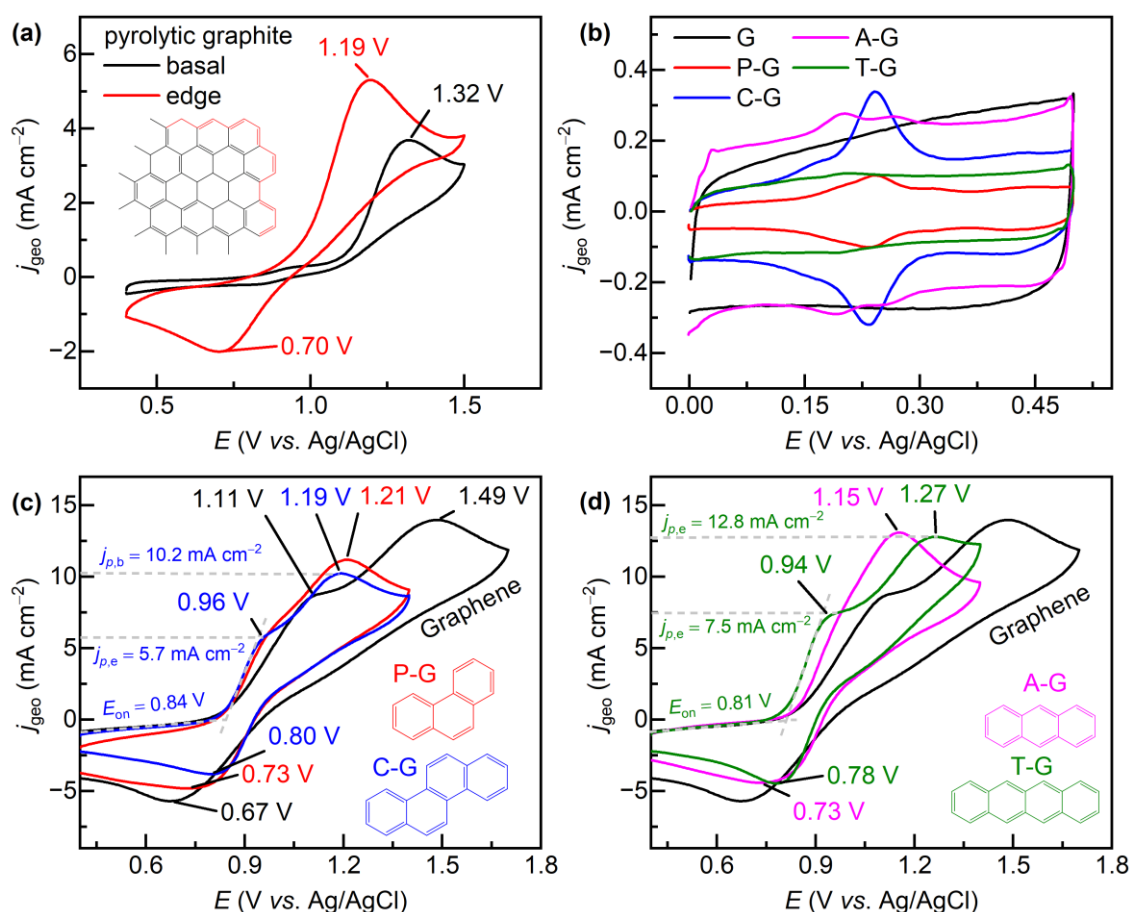


Figure 8-3. Electrochemical characterization of carbon edge sites in 0.1 M $\text{V}^{\text{IV}}\text{O}_2^{2+}/2 \text{ M H}_2\text{SO}_4$ electrolyte. (a) Comparison of the basal and edge plane of pyrolytic graphite; (b) current response in the double layer region. (c,d) Comparison of the catalytic activity of (c) armchair and (d) zigzag edge site PAH-modified graphene.

The modified graphene powders were then used to evaluate their electrocatalytic activity (**Figure 8-3c,d**). In the CV curves, pure graphene shows two oxidation peaks. We assume these signals do either correspond to the basal plane (1.49 V) and the more active edges (1.11 V) of its finite platelets like the observations on pyrolytic graphite, or they arise because of two edge-related carbon atoms: There could be an electrochemical difference between sp^2 and sp^3 bound carbon at the edge of one C_6 ring and in between two conjugated rings. The electrocatalytic activity was increased for all PAH-modified electrodes, evidenced by a shift of both oxidation

signals to lower potentials. However, differences were observed for the onset and peak potential of the oxidation, as well as in the maximum peak current. A larger π -conjugated system as four conjugated rings shows a more defined first signal (C-G and T-G), while for the three-ring PAHs the two peaks almost merge. It was shown by the comparison of armchair (C-G) to zigzag edges (T-G) with four rings that the onset potential decreases from 0.84 to 0.81 V, the first peak potential increases from 0.96 to 9.94 V and its peak current from 5.7 to 7.5 mA cm⁻². These results highlight two important findings: (i) the role of edge geometry, with zigzag edges being superior to armchair edges, and (ii) the importance of π -conjugation, showing that larger graphitic systems can use their edges more effectively.

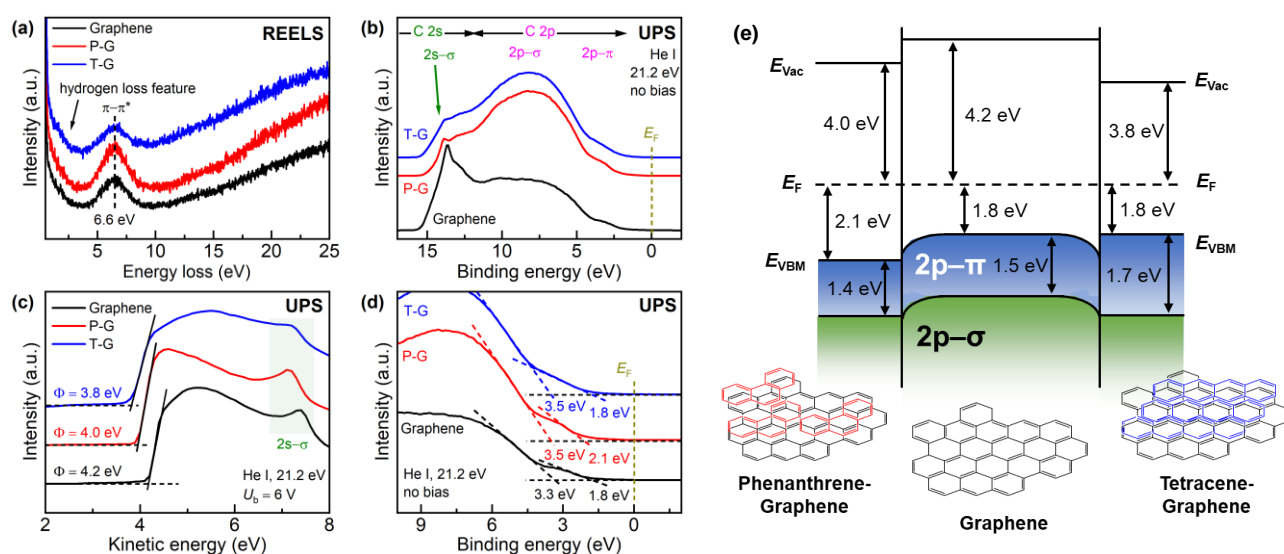


Figure 8-4. The electronic structure of natural vs. armchair vs. zigzag carbon edge sites. **(a)** The π - π^* transition in REELS. **(b)** The electronic density below E_F , probed by UPS. **(c)** At an applied external bias, the cutoff energy of the valence electrons yields the WF. **(d)** Detailed investigation of the threshold energies close to E_F . **(e)** Model of the electronic band diagram.

The structural and electronic properties of the modified powders were then examined to find a descriptor for the differences in activity. Raman spectroscopy revealed no discernible differences between the samples (Figure S51) which can be attributed to the strong signal contribution of the underlying graphene. In contrast, due to the high surface sensitivity of REELS and UPS, the changes in the electronic properties could be well observed. To establish meaningful correlations, the least and most reactive PAHs, P-G and T-G, were analyzed in detail and compared with pristine graphene. It was first made sure that the chemical composition of the surface remained almost unchanged after modification. Only T-G showed a slight increase in oxygen content, which can be attributed to the higher chemical reactivity of the zigzag edges (Figure S52).^[222] However, as demonstrated using GF-TA, even surface oxygen contents of >4

at% did not significantly affect the results of the electronic structure analysis. As for GF-H₂, charge accumulation at the interface between graphene and PAH is evidenced by a slight shift in the *sp*² carbon peak in the C 1s spectra (+0.2 eV), which could be attributed to the electrically insulating property of the PAH. The π - π^* transition recorded by REELS was more pronounced in P-G because a layer of fully π -conjugated electrons has been added (**Figure 8-4a**). In contrast, the transition peak of T-G decreased due to the perturbation of the system (see **Figure 1-2a** for comparison), forming π -radicals responsible for the higher chemical reactivity of the zigzag edges.^[223]

Graphene showed a strong contribution of 2s- σ electrons in the UPS spectra, which was drastically reduced after modification with non-graphitic PAH (**Figure 8-4b**). Again, the WF and E_{VBM} were extracted from the UPS spectra by careful examination of the cutoff energy at applied bias and the threshold near E_{F} (**Figure 8-4c,d**). In the band diagram in **Figure 8-4e** it is seen that the WF of graphene is the same as that of cleaned HOPG (4.2 eV) but it is significantly reduced by the attached PAHs. Charge accumulation at the interface of graphene and PAH was again sketched as band bending behavior. Armchair edges have a semiconducting and zigzag edges a metallic character.^[224] This explains why E_{VBM} is reduced for P-G (from 1.8 to 2.1 eV); however, it is not further increased for T-G.^[224-226] Again, the electrocatalytic activity of the materials corresponds well with their respective WF levels, reconfirming the importance of this parameter previously derived from the analysis of the modified GF electrodes. The WF is reduced by the additional armchair edges of the P-G (4.0 eV), but even more by the zigzag edges of the highly active T-G (3.8 eV). In summary, these results show a clear correlation between the electronic structure, microstructure, and electrocatalytic activity and prove that a decrease of the WF, which can be achieved by the introduction of (preferably zigzag) edge sites effectively increases the electrocatalytic activity of graphite.

8.5 Conclusions

Pristine, thermally activated and deoxygenated GF electrodes were studied to establish correlations between electrocatalytic activity, structural and electronic properties. Morphological defects, such as edge sites, form the basis for successful charge transfer in the redox reactions occurring in vanadium flow batteries. These defects were investigated by Raman spectroscopy and SEM to establish a correlation between the electrocatalytic activity and the microstructure. By examining the electronic structure using UPS, we found that the catalytic activity correlates with the WF level of the material. Argon bombardment of HOPG showed that point defects do

not affect the WF, but instead increase the DOS near the E_F . PAHs exhibiting armchair and zigzag edges were used to explore the importance of edge site configuration on catalytic activity and electronic structure. The zigzag edges, which required the lowest overpotential and provided the highest current densities for the oxidation of $V^{IV}O^{2+}$ to $V^{VO_2^+}$, also showed the lowest WF. These results clearly demonstrate the dependencies between structural, electronic and electrochemical properties. From an engineering perspective, strategies need to be developed for targeted integration of zigzag edges into the material surface.

9 Structural and Electronic Properties of Vanadium Complexes at Graphite Electrodes

In the last chapter, it was conclusively demonstrated the superior activity of zigzag *versus* armchair edges and identified the WF as a possible descriptor for the electrocatalytic activity of graphite electrodes. In a next step, the properties of edge geometry shall be elucidated in more detail using DFT calculations. These computational methods can provide theoretical insight into situations where experiments are difficult to perform or evaluate.^[69,70,204,227] First, it is important to build reliable models of the complexes formed by dissolved vanadium ions in an aqueous electrolyte. Molecules containing vanadium ions in all four different oxidation states were constructed, including their solvation shell to account for the effects in both half cells. To investigate the sorption properties related to the architecture of the electrode, the basal plane of single-layer graphene was used as a reference system and fabricated graphene nanoribbons with zigzag and armchair edges. To elaborate on the functionalization of the electrode, the terminal hydrogen on the edges was also replaced with different OFGs such as carbonyl and hydroxyl groups. To model the properties describing efficient charge transfer between the atoms in the electrode and the solvated molecule, DOS calculations for the adsorbed system were performed. By examining overlapping molecular orbitals near E_F , conclusions can be drawn about the effectiveness of electron transfer.

9.1 Structure of Solvated Vanadium Ions and Graphene Nanoribbons

Both the chemistry and coordination of ions in aqueous solution are important to understand fundamental processes at solid–liquid interfaces. Therefore, the coordination spheres of the vanadium ions fabricated for this research will be briefly discussed. The relaxed structures are displayed in **Figure 9-1**, the most important bond lengths summarized in **Table 6**, whereas a full analysis on bond lengths and angles can be found in Table S4 for $[V^{II}/V^{III}(H_2O)_6]^{2+/3+}$, in Table S5 for $[V^{IV}O(H_2O)_5]^{2+}$, and in Table S6 for $[V^{VO}_2(H_2O)_4]^+$.

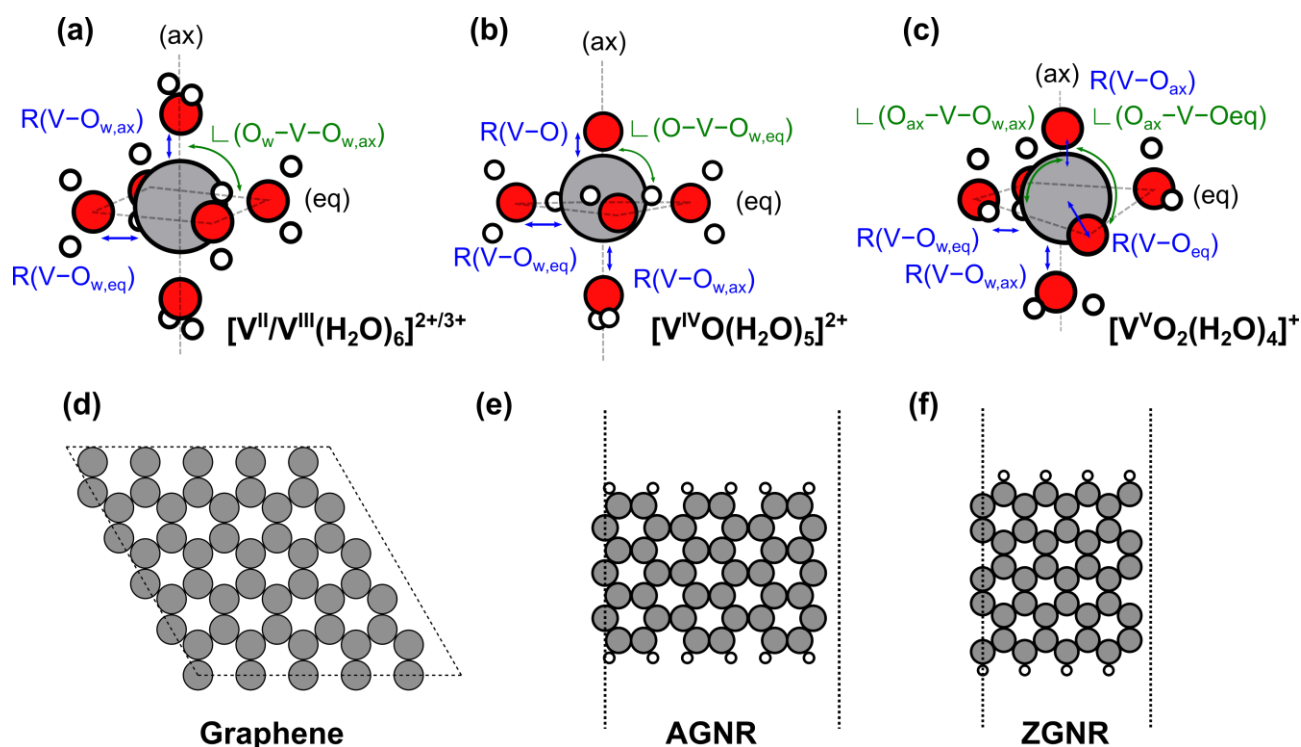


Figure 9-1. Relaxed structures under consideration. **(a–c)** Dissolved vanadium ions including solvation shell: (a) Hexa-aqua octahedral complex of $[V^{II}/V^{III}(H_2O)_6]^{2+/3+}$. (b) Penta-aqua distorted octahedra of $[V^{IV}O(H_2O)_5]^{2+}$. (c) Distorted octahedral $[V^VO_2(H_2O)_4]^+$ complex. **(d–f)** Nanoribbons used as substrates: (d) basal plane graphene, and edge-site exposed ribbons with (e) armchair and (f) zigzag edges.

Table 6. Average distances (R in Å) for the first hydration shell of dissolved vanadium ions compared to calculations and experimental data (XRD).^[228,229] The type of oxygen atom is specified according to its geometric position and coordination, where O_w describes the classification of the oxygen atom in a water molecule, “ax” denotes axial and “eq” equatorial (see **Figure 9-1a–c**).

Complex	R(V–O _{ax})	R(V–O _{eq})	R(V–O _{w,ax})	R(V–O _{w,eq})
$[V^{II}(H_2O)_6]^{2+}$			2.19–2.20	
Lit.			2.13–2.23	
$[V^{III}(H_2O)_6]^{3+}$			2.19–2.21	
Lit.			2.00–2.10	
$[V^{IV}O(H_2O)_5]^{2+}$	1.68		2.44	2.19/2.22
Lit.	1.57–1.72		2.20–2.36	2.03–2.12
$[V^VO_2(H_2O)_4]^+$	1.68	1.69	2.35	2.26/2.51
Lit.	1.61–1.73		2.22–2.32	2.01–2.13

For both the V^{III} and V^{II} ions, their coordination can easily be described by a stable hexa-aqua octahedral complex with four equatorial and two axial water molecules (**Figure 9-1a**). The distance from the vanadium ions to the oxygen in the first coordination sphere is ~ 2.20 Å (lit.: 2.13 to 2.23 Å).^[228] In good approximation, the angles comprise 90° within the plane and 180° along the axes.^[230] A characteristic feature of the $[V^{IV}O(H_2O)_5]^{2+}$ complex is a V=O bond with a distance of 1.68 Å (lit.: 1.57 to 1.72, **Figure 9-1b**).^[231] This exceptionally strong bond is one of

the most stable diatomic cations in aqueous complex chemistry, as it can exist in solid, liquid, and even gas phases.^[232] $[\text{V}^{\text{IV}}\text{O}(\text{H}_2\text{O})_5]^{2+}$ appears in acidic solution ($\text{pH} < 4$) as a penta-aqua complex, a distorted octahedron, which precipitates at a pH of ~ 5 to the insoluble $\text{VO}(\text{OH})_2$. The equatorial water molecules are within a distance of ~ 2.20 Å (lit.: 2.03 to 2.12 Å), slightly offset below the equatorial plane because of electrostatic repulsion of the oxygen atoms.^[228] The axial water molecule moves at a distance of 2.44 Å (lit.: 2.20 to 2.36 Å) further away from the ion than its equatorial equivalents.^[233] Both values are larger in my case than in the literature, but this could be because of the new exchange–correlation functional used with which the publications do not allow comparison.

Vanadium ions in their pentavalent oxidation state also exhibit pH -dependent behavior, with the $[\text{V}^{\text{VO}_2}(\text{H}_2\text{O})_4]^+$ complex found in acidic solution and oligomeric vanadate ions predominating in alkaline environments.^[231] In this work, $[\text{V}^{\text{VO}_2}(\text{H}_2\text{O})_4]^+$ reveals the structure of a distorted octahedra (**Figure 9-1c**).^[229] In comparison to $[\text{V}^{\text{IV}}\text{O}(\text{H}_2\text{O})_5]^{2+}$, the distance of vanadium to the covalently bound oxygen remains at ~ 1.68 Å (lit.: 1.63 to 1.73 Å), however, a wider range of distances to the coordinated water molecules becomes obvious: while the axial H_2O is 2.35 Å away (lit.: 2.23 to 2.32 Å), the equatorial, which is opposite the equatorial $\text{V}=\text{O}$ bond, has a large distance of 2.51 Å. In contrast, the remaining water is located within 2.26 Å and thus shows good agreement with literature (lit.: 2.23 to 2.32 Å).^[228,231,234–236]

As a reference structure for the substrate, single-layer graphene with C–C bond lengths of 1.42 Å was constructed (**Figure 9-1d**). To account for the two different edge defects on the surface of an activated GF electrode, a layer of an armchair and zigzag graphene nanoribbon was fabricated (**Figure 9-1e,f**). At the armchair edges, the neighboring carbon atoms are 1.36 Å apart, while the other bonds are between 1.42 and 1.43 Å distant, resulting from variations in the charge density.^[237] At the zigzag edges, the exposed carbon atom is 1.41 Å away from its neighbors in the ring.

9.2 Adsorption Properties of Vanadium Complexes at Graphite

The affinity of the vanadium complexes for the electrode surface as a function of their structure is studied *in vacuo*. Considering the important interplay of solvents, cations, and electrode at the interface, we first separately investigated how the substrates interact with the water molecules in the solvation shell of the vanadium ions. For each structure, a water molecule was placed 2 Å above the substrate in two different orientations: toward the electrode *via* the

oxygen atom or the two hydrogen atoms. The adsorption energy (E_{ads}) of H_2O at the basal plane of graphene is -0.07 eV regardless of the position of the hydrogen atoms (Figure S53). However, when the hydrogen atoms face the graphene plane, the water approaches the substrate from 3.34 to 2.94 Å.

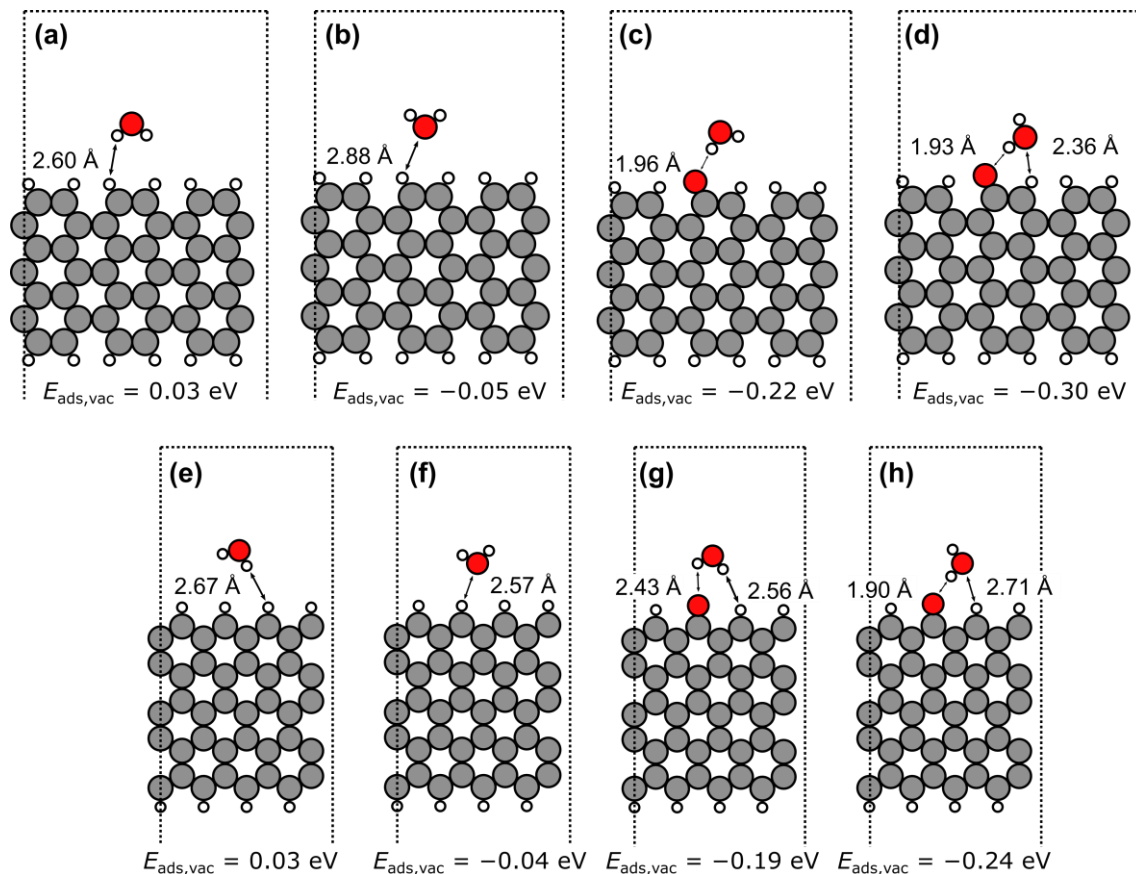


Figure 9-2. Relaxed structures of adsorbed water in two different orientations (H_2 and O) facing graphene edges: **(a)** H_2 and **(b)** O at H-terminated armchair edges; **(c)** H_2 and **(d)** O at O-terminated armchair edges; **(e)** H_2 and **(f)** O at H-terminated zigzag edges. **(g)** H_2 and **(h)** O at an O-terminated zigzag edge.

Several interesting effects can be observed during adsorption at the nanoribbons (**Figure 9-2**). Relaxation at hydrogen-bounded edges is more favorable for the water molecule, which moves its hydrogen dipole away from the structure (**Figure 9-2b,f**). While there is almost no energetic difference between armchair and zigzag edges, the distance between structure and adsorbent is smaller for the zigzag (2.57 Å) than for the armchair edge (2.88 Å). However, adsorption is clearly stronger at the edges with oxygen termination. It can be observed that the water molecule moves slightly to the side to bring its hydrogen atom close to the O-terminus and, at the same time, its oxygen atom closer to an H-terminated edge (**Figure 9-2d,h**). Consequently, the water molecule tilts about 45° , stretching the second hydrogen atom far away from the electrode. The orientation of the water molecules and both the geometry and functionalization of

the carbon substrate influence the adsorption properties of water in the solvent and the solvation shell around the vanadium ions.

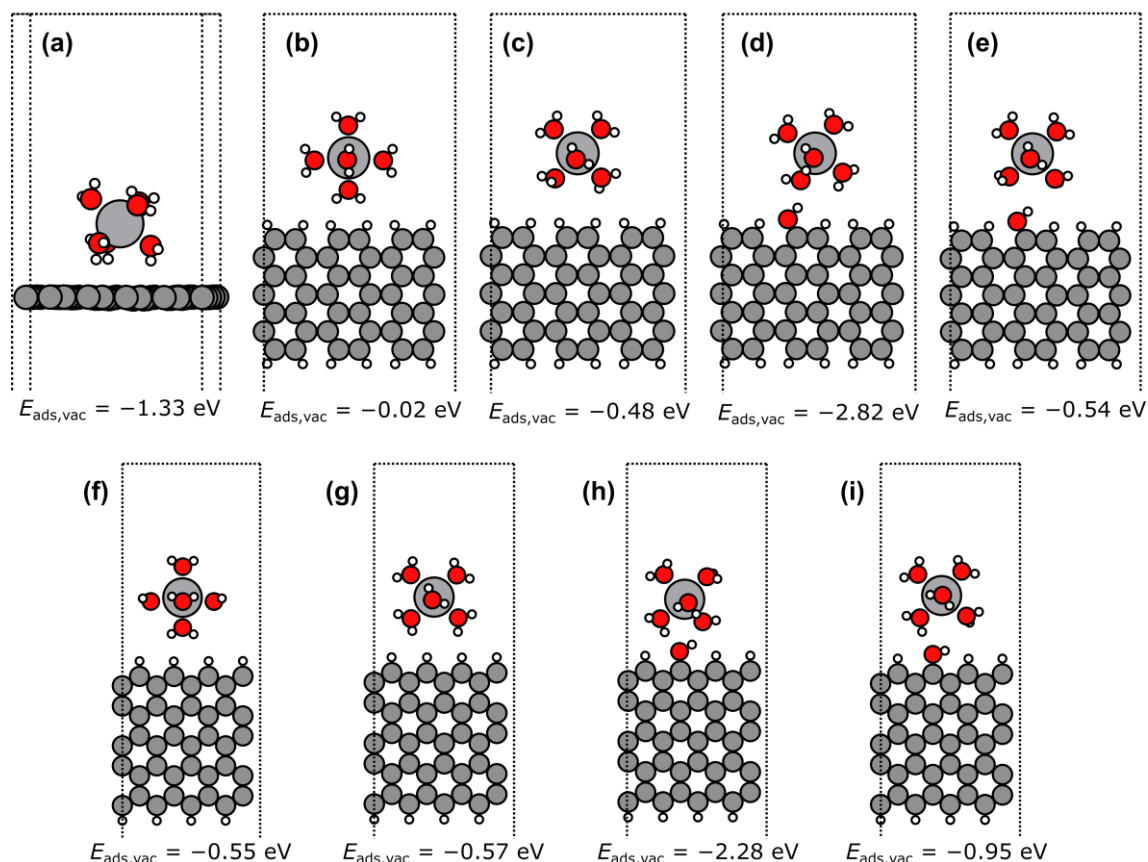


Figure 9-3. Relaxed structures of adsorbed $[V^{III}(H_2O)_6]^{3+}$: **(a)** at the basal plane of graphene; **(b,c)** at H-terminated armchair edges in two different orientations; at an **(d)** O- and **(e)** OH-terminated armchair edge. **(f,g)** Two different orientations at H-terminated zigzag edges; at an **(h)** O- and **(i)** OH-terminated zigzag edge.

There were almost no differences observed for the relaxation of $[V^{II}(H_2O)_6]^{2+}$ and $[V^{III}(H_2O)_6]^{3+}$ in terms of E_{ads} . Therefore, only the adsorption of the latter will be described (**Figure 9-3**). Several possibilities to relax the complex at the basal plane of graphene exist: E_{ads} decreased from -0.9 over -1.18 to -1.33 eV for bringing one, two, and three, respectively, coordinated water molecules close to the surface (**Figure 9-3a**). While the comparison of H-terminated edges with two water molecules forming a 45° angle is much more convenient for armchair edges (-0.48 instead of -0.02 eV), there is almost no difference noted for zigzag edges (**Figure 9-3b,c** and **f,g**). In both edge geometries, the vanadium complex at the carbonyl group is unstable. The water in the vanadium coordination sphere loses a hydrogen atom and forms a hydroxyl group. This ketone-to-alcohol formation is energetically favored at an O-terminated armchair (-0.91 eV), but not normally at the zigzag edge (0.21 eV); yet it has been observed (**Figure 9-3d,h**). This can be explained by the E_{ads} of $[V^{III}(H_2O)_6]^{3+}$ at OH-terminated edges,

which voluntarily occurs at armchair (-0.54 eV) but even stronger at zigzag edges (-0.95 eV, **Figure 9-3e,i**). Furthermore, it is observed that the orientation of H_2O varies with the edge geometry; while the hydrogen atoms move away from the H-terminated armchair, there is no electrostatic repulsion near the zigzag edges (**Figure 9-3c,g**). Similar effects can be detected at the OH-terminated armchair edge: water from the solvation shell near the OH-terminated armchair edge is repelled, while it is strongly attracted to the zigzag structure (**Figure 9-3e,i**).

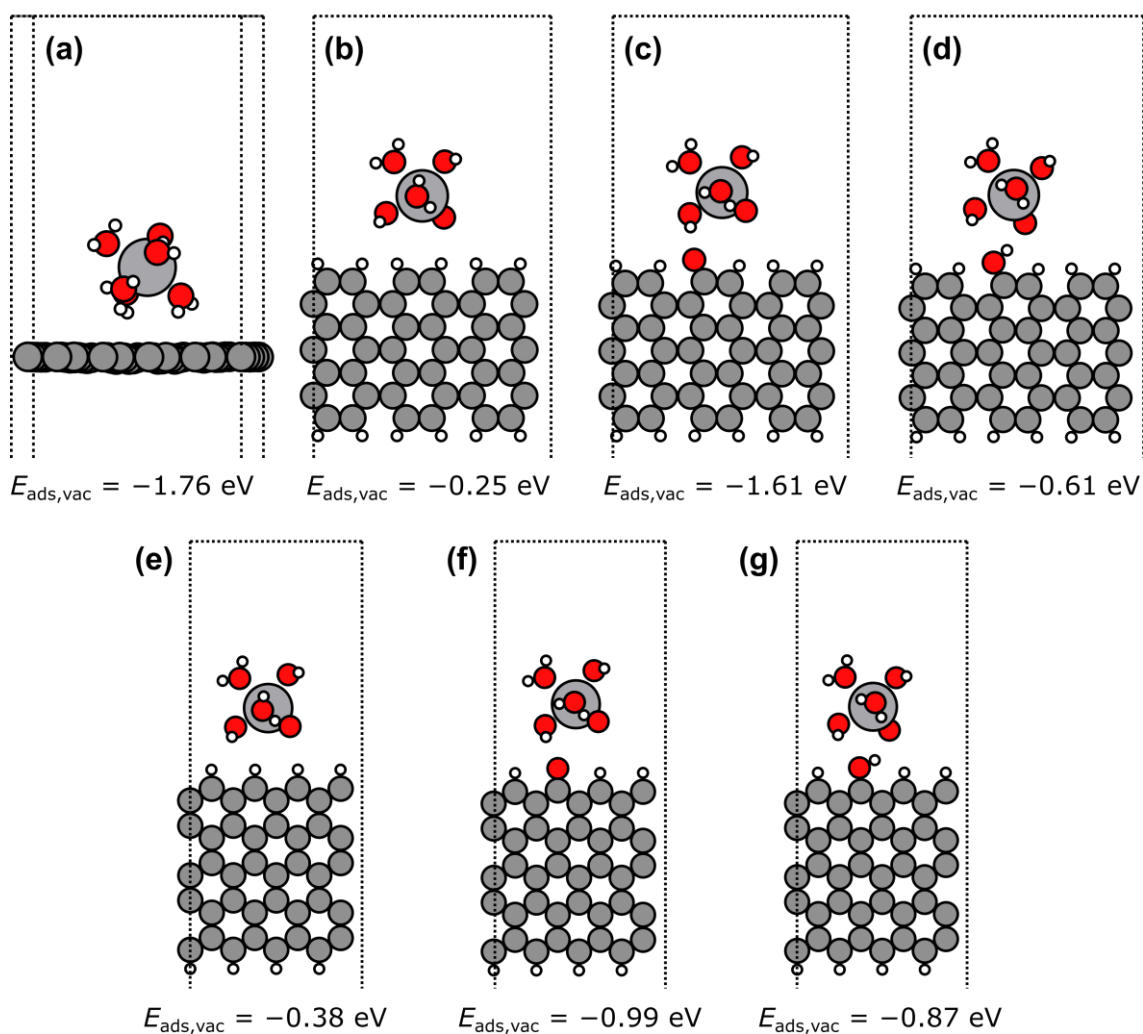


Figure 9-4. Relaxed structures of adsorbed $[\text{V}^{\text{IV}}(\text{H}_2\text{O})_5]^{2+}$: **(a)** at the basal plane of graphene; **(b)** at H-terminated armchair edges; at an **(c)** O- and **(d)** OH-terminated armchair edge. **(e)** at H-terminated zigzag edges; at an **(f)** O- and **(g)** OH-terminated zigzag edge.

To charge a VFB, in the positive half-cell $[\text{V}^{\text{IV}}(\text{H}_2\text{O})_5]^{2+}$ is oxidized to $[\text{V}^{\text{VO}_2}(\text{H}_2\text{O})_4]^+$. In general, this reaction is considered the kinetic bottleneck in terms of reaction rates.^[61,238] A precise understanding of the positive redox reaction is thus important. The relaxed adsorbed structures and their corresponding E_{ads} can be found in **Figure 9-4**. The lowest energy barrier is presented by adsorption of $[\text{V}^{\text{IV}}(\text{H}_2\text{O})_5]^{2+}$ onto the basal plane of graphene, confronting the

substrate with three water molecules in a triangular geometry, resulting in an even lower E_{ads} of -1.67 eV than for the $[\text{V}^{\text{III}}(\text{H}_2\text{O})_6]^{3+}$ complex (-1.33 eV). At all edges, adsorption is strongest when the adsorbent faces the substrate with the V=O bond and a water molecule from the hydration shell at a 45° angle. Adsorption at the H-terminated edge is again favored by -0.38 eV compared to the armchair edge (-0.25 eV, **Figure 9-4b,e**). Even though $[\text{V}^{\text{IV}}\text{O}(\text{H}_2\text{O})_5]^{2+}$ shows a similar structure at both O-terminated edges, its adsorption is stronger at armchair (-1.61 eV) over zigzag geometries (**Figure 9-4c,f**). In contrast to $[\text{V}^{\text{III}}(\text{H}_2\text{O})_6]^{3+}$, no proton transfer was observed. In agreement with this observation, the tetravalent complex shows weaker adsorption properties at the hydroxyl than at the carbonyl group, favoring the zigzag edges (-0.87) over the armchair edges (-0.61 , **Figure 9-4d,g**).

The previous observations can be summarized: for $[\text{V}^{\text{III}}(\text{H}_2\text{O})_6]^{3+}$, the bare H-terminated zigzag edge shows stronger adsorption properties than the functionalized armchair edge. However, E_{ads} is even lower for the OH-terminated zigzag edge. Considering the adsorption of $[\text{V}^{\text{IV}}\text{O}(\text{H}_2\text{O})_5]^{2+}$, the O-terminated edges are preferred, which is due to the strong adsorption of a water molecule from the solvation shell to the oxygen-functionalized edge and, at the same time, the strong adsorption from the V=O bond to the direct hydrogen-terminated neighbor. In this sense, the armchair is strongly preferred over the zigzag geometry. Furthermore, adsorption on H-terminated edges bearing an additional OH group (H-C-OH) was investigated. However, this functionalization was not stable at armchair edges. Adsorption of $[\text{V}^{\text{III}}(\text{H}_2\text{O})_6]^{3+}$ (-0.97 eV) and $[\text{V}^{\text{IV}}\text{O}(\text{H}_2\text{O})_5]^{2+}$ (-0.90 eV) was little different from adsorption on the OH-functionalized edges (Figure S54).

9.3 Electron Transfer Described by the Density of States

It cannot be overlooked that the adsorption of the vanadium complexes is most favored at the basal plane of graphene, which is known not to be an active site for the vanadium redox reactions, as demonstrated by the CV curves in Figure 1a. Therefore, it is important to investigate the electronic properties of the adsorbed structures, which could provide an explanation for the different charge transfer kinetics observed in electrochemical experiments. Projected density of states (PDOS) calculations were performed for the carbon atom to which a functional group (H, O, OH) was attached and the vanadium atom in the center of the complex. The PDOS measures the relative probability of an electron being in the different atomic orbitals at each energy. We evaluated the DOS for the *s* and *p*-orbitals of carbon and the *d*-orbital of vanadium. For successful electron transfer with low-energy input, the occupied states of the outer shells

should be located close to E_F . Thus, we can estimate the readiness of the adsorbed system to transfer electrons by an overlap of the p -orbital of carbon and the d -orbital of vanadium.

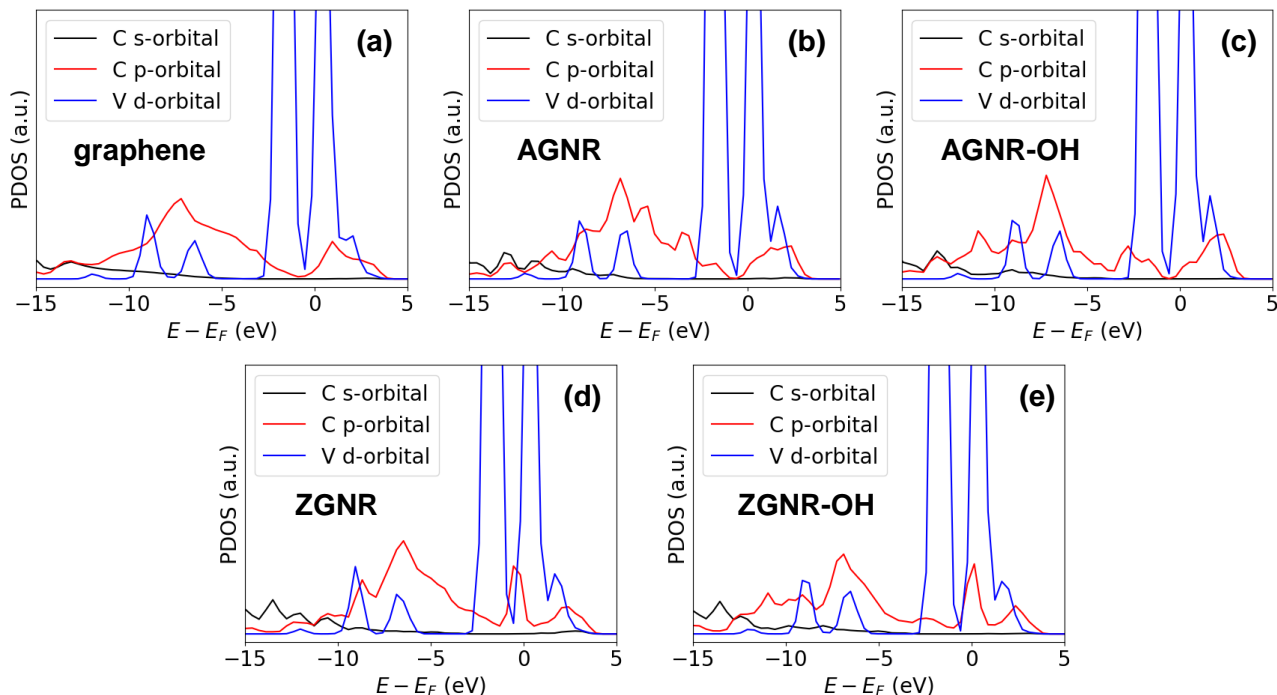


Figure 9-5. PDOS of adsorbed $[V^{III}(H_2O)_6]^{3+}$ at various nanoribbons: **(a)** at the basal plane of graphene; **(b,c)** at armchair edges bearing **(b)** H- and **(c)** OH-termination; **(d,e)** at zigzag edges bearing **(d)** H- and **(e)** OH-termination.

For the investigation of the $[V^{III}(H_2O)_6]^{3+}$ complex, we considered bare graphene as well as H- and OH-terminated edge sites since the solvation shell of V^{III} was unstable at carbonyl groups. It can be seen in **Figure 9-5** that the vanadium ion has many electronic states near E_F due to its metallic nature. In contrast, at the basal plane of graphene, a slowly rising DOS can be observed at lower energies, with most electrons lying between -5 and -10 eV (**Figure 9-5a**). Both the H- and OH-functionalized armchair edges exhibit a local maximum near E_F , but the higher occupied states are located at elevated energies compared to the occupied states of vanadium (**Figure 9-5b,c**). This means that energy would have to be applied to the system to achieve an overlap of the orbitals and subsequently increase the possibility of charge transfer. In contrast, the H-terminated zigzag edge shows a high number of occupied states near E_F , which could indicate a low energy barrier for charge transport between the structures (**Figure 9-5d,e**). For the OH-functionalized edge, this high DOS shifts beyond E_F into the conduction band of the electrode, which indicates that electrons move freely through the material. Since for the reduction of $[V^{III}(H_2O)_6]^{3+}$ to $[V^{II}(H_2O)_6]^{2+}$ providing electrons is the key, there is no major difference expected in the kinetics of an H-terminated compared to a hydroxyl-functionalized zigzag edge.

However, it is questionable whether oxygen termination is stable at reducing potentials, since surface analysis of electrodes subjected to negative polarization has revealed very low oxygen coverage.^[85,200]

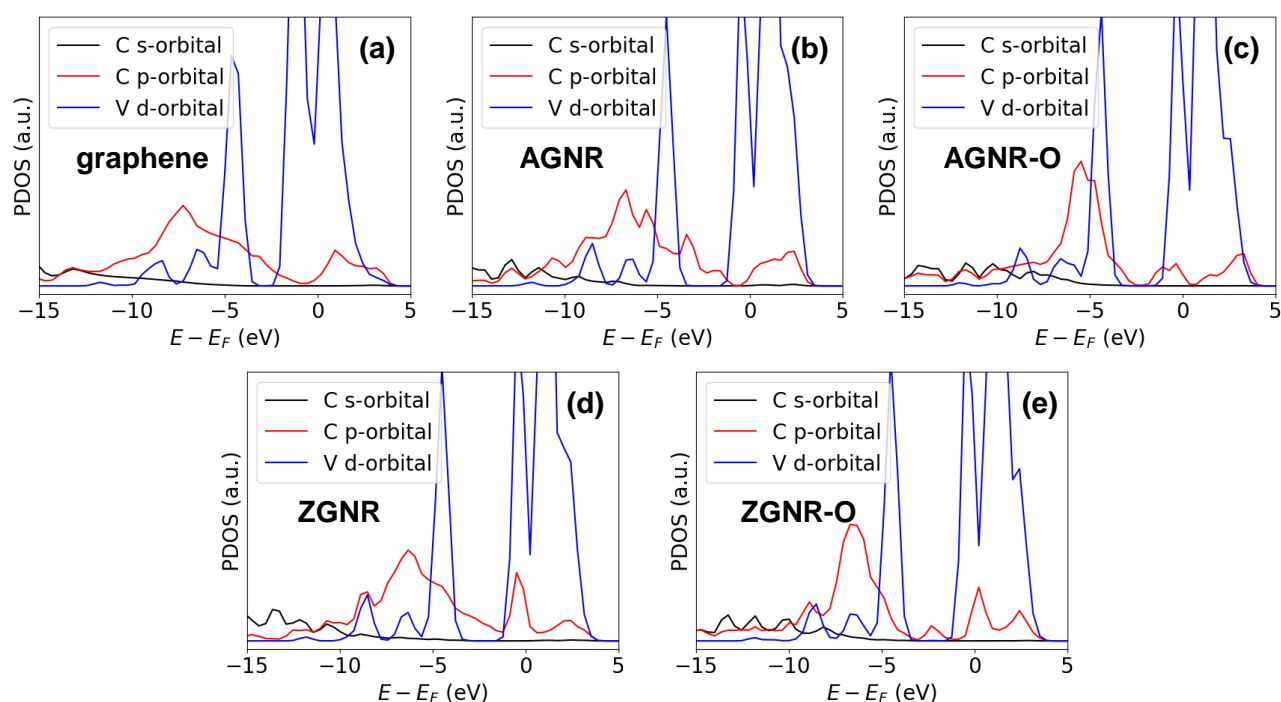


Figure 9-6. PDOS of adsorbed $[\text{V}^{\text{IV}}(\text{H}_2\text{O})_5]^{2+}$ at various nanoribbons: **(a)** at the basal plane of graphene; **(b,c)** at armchair edges bearing **(b)** H- and **(c)** O-termination; **(d,e)** at zigzag edges bearing **(d)** H- and **(e)** O-termination.

A similar investigation was conducted for the $[\text{V}^{\text{IV}}(\text{H}_2\text{O})_5]^{2+}$ complex, although in this case the OH-functionalization was disregarded due to its lower adsorption energies compared to the O-terminated edges (**Figure 9-6**). The observations for positive half-cell oxidation are very similar to the negative half-cell reduction. The basal plane of graphene and the armchair edges do not provide increased DOS near E_F in contrast to the high number of occupied states for the H-terminated zigzag edges. However, it is worth noting that the O-functionalized armchair edges exhibit a small local minimum, while the H-termination shows little overlap of the p -orbital of carbon and the d -orbital of vanadium (**Figure 9-6b,c**). In a similar manner as for $[\text{V}^{\text{III}}(\text{H}_2\text{O})_6]^{3+}$, the occupied states shift upward beyond E_F but in this case the number of charge carriers decreases compared to the H-termination. Moreover, for efficient oxidation of $[\text{V}^{\text{IV}}(\text{H}_2\text{O})_5]^{2+}$ to $[\text{VO}_2(\text{H}_2\text{O})_4]^+$, holes must be created in the electrode to successfully accept electrons from the solvated vanadium ions. Thus, a large overlap of occupied states in the valence and conduction bands could promote rapid recombination within the electrode rather than filling the existing holes with electrons from the electrolyte.

Based on the PDOS observations, it was shown why the basal plane of graphene cannot be considered as an active site for the vanadium redox reactions due to the lack of overlap of the occupied states of the molecular orbitals. While there is some possibility of charge transfer between H- and OH-functionalized armchair edges and $[\text{V}^{\text{III}}(\text{H}_2\text{O})_6]^{3+}$ molecules, as well as for O-terminated armchair edges and $[\text{V}^{\text{IV}}\text{O}(\text{H}_2\text{O})_5]^{2+}$ complexes, the highest overlap between the p -orbital of carbon and the d -orbital of vanadium near E_{F} is always present for the H-terminated zigzag edges.

9.4 Desorption of $[\text{V}^{\text{V}}\text{O}_2(\text{H}_2\text{O})_4]^+$

Since the energetic differences between $[\text{V}^{\text{III}}(\text{H}_2\text{O})_6]^{3+}$ and $[\text{V}^{\text{II}}(\text{H}_2\text{O})_6]^{2+}$ are in a range of 0.02 eV, we will only look at the desorption properties of the $[\text{V}^{\text{V}}\text{O}_2(\text{H}_2\text{O})_4]^+$ complex after the oxidation of $[\text{V}^{\text{IV}}\text{O}(\text{H}_2\text{O})_5]^{2+}$ in detail to understand trends regarding the orientation and functionalized of edge sites. One should be aware that in the reverse direction, the edge type best suited for vanadium oxidation may be different from that needed for efficient vanadium reduction in the positive half-cell when the battery is discharged again.

The relaxed structures of the adsorbed $[\text{V}^{\text{V}}\text{O}_2(\text{H}_2\text{O})_4]^+$ complex at the different carbon substrates are displayed in **Figure 9-7**. The strongest E_{ads} of -0.48 eV at the basal plane of graphene was obtained by placing the complex in a triangular position above the electrode, facing the surface with the two $\text{V}=\text{O}$ bonds and one water molecule from the solvation shell (**Figure 9-7a**). Placement of three water molecules or two water ligands and one $\text{V}=\text{O}$ bond over graphene resulted in higher energies of -0.32 and -0.38 eV, respectively. With bare H-terminated armchair edges, the adsorption energies were negative regardless of the orientation of $[\text{V}^{\text{V}}\text{O}_2(\text{H}_2\text{O})_4]^+$. Two water molecules above the edge showed weaker adsorption properties (-0.04 eV) while they were strong for one or two covalently bound $\text{V}=\text{O}$ (-0.38 eV, **Figure 9-7**). It must be noted that it is unlikely for the structure to face the reaction site with two water molecules. According to the reaction equation, the oxidation of $[\text{V}^{\text{IV}}\text{O}_2(\text{H}_2\text{O})_5]^{2+}$ includes the transfer of two protons. The complex would have to be rotated at least 90° at the surface before it can desorb with only water molecules pointing toward the edge. The desorption for the case in **Figure 9-7b** at an O-terminated edge reveals only a low energy barrier of -0.05 eV. In contrast, the structure becomes unstable when water from the solvation shell is near the functionalized edge (**Figure 9-7c**). As it was observed similarly for $[\text{V}^{\text{III}}(\text{H}_2\text{O})_6]^{3+}$ in **Figure 9-3d,h**, a proton from the solvation shell is transferred to saturate the oxygen group and one water molecule even dissociates away from the vanadium complex. Adsorption on the OH-functionalized

edge, however, is very strong both for the $\text{V}=\text{O}$ bond (-0.63 eV, **Figure 9-7d**) and for water from the solvation shell (-0.29 eV) as adsorbing agent.

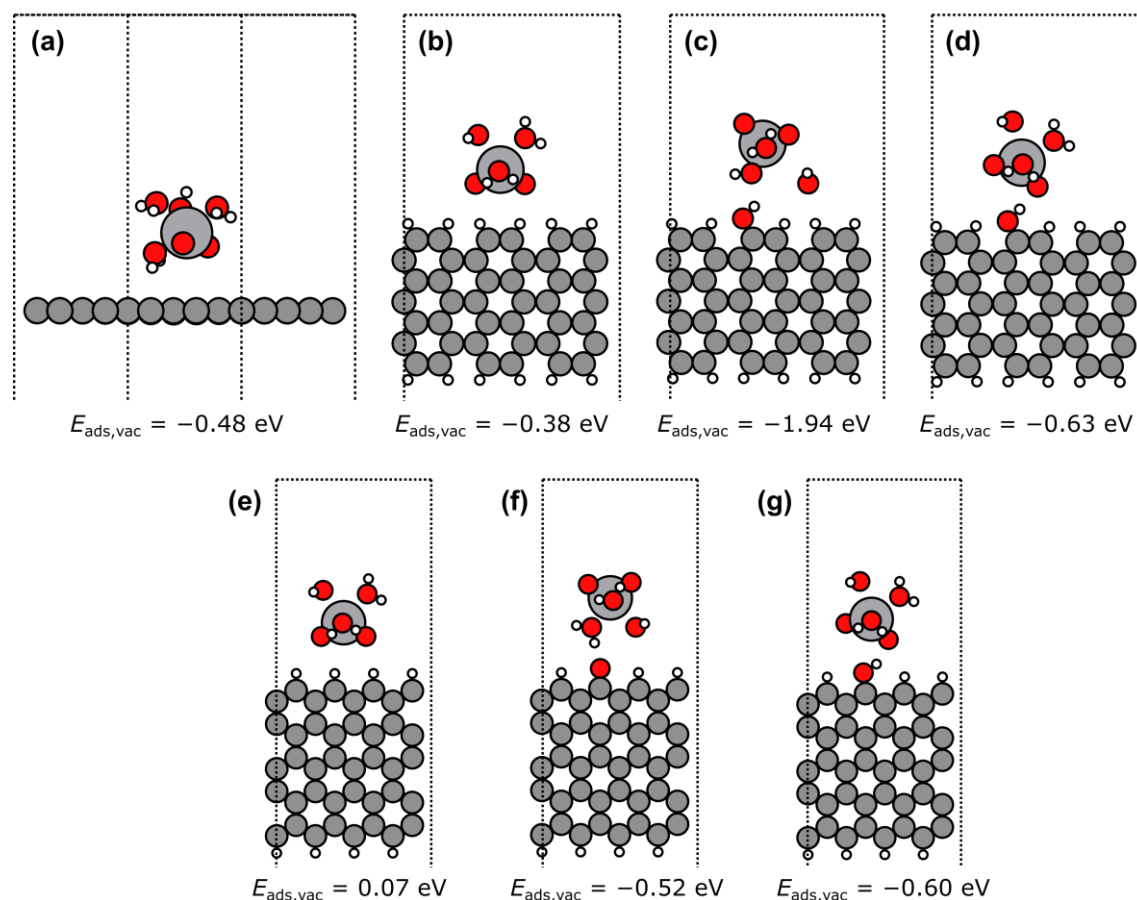


Figure 9-7. Relaxed structures of adsorbed $[\text{VVO}_2(\text{H}_2\text{O})_4]^+$: **(a)** at the basal plane of graphene; **(b)** at H-terminated armchair edges; at an **(c)** O- and **(d)** OH-terminated armchair edge. **(e)** at H-terminated zigzag edges; at an **(f)** O- and **(g)** OH-terminated zigzag edge.

The adsorption energies of $[\text{VVO}_2(\text{H}_2\text{O})_4]^+$ at H-terminated zigzag edges are positive regardless of the orientation of the adsorbent. From the comparison of two water molecules to one H_2O and one $\text{V}=\text{O}$ to two $\text{V}=\text{O}$ bonds, E_{ads} decreases from 0.14 to 0.10 to 0.07 eV (**Figure 9-7e**). In contrast to the O-terminated armchair edges, the structure adsorbs strongly and stably on the functionalized zigzag edge (-0.52 eV) through the water from the solvation shell (**Figure 9-7f**) but not *via* the double $\text{V}=\text{O}$ bonds (0.12 eV) which is the more likely case directly after the oxidation. However, the adsorption of the latter is very strong at the OH-terminated zigzag edges (-0.60 , **Figure 9-7g**). The calculated adsorption barriers for $[\text{VVO}_2(\text{H}_2\text{O})_4]^+$ on different functionalized structures clearly show that voluntary desorption of the reactant, independent of its orientation, and thus the release of an active site can only occur reliably at the H-terminated zigzag edge sites. It is important to keep in mind that for an effective reduction of

$[\text{VO}_2(\text{H}_2\text{O})_4]^+$ to $[\text{V}^{\text{IV}}(\text{H}_2\text{O})_5]^{2+}$ a negative E_{ads} might be favorable. However, for all calculated structures of the reduced state which were discussed previously, also very low adsorption energies were found, especially at the functionalized surfaces (see **Figure 9-4** for comparison). Thus, even for the reduction reaction during the discharge of a VFB, it might be favorable for the system to accept the small adsorption energy barriers at the H-terminated zigzag edges to benefit later from the lower barriers during the desorption of the reactant.

9.5 Conclusions

Vanadium ions including their first coordination sphere in aqueous medium and graphite-based electrode surfaces were modeled. The sorption and charge transfer properties of these solvated vanadium ions were investigated using DFT calculations. Water molecules adsorbed more readily to carbonyl groups by exhibiting lower E_{ads} and smaller distances from the substrate. The adsorption energies of $[\text{V}^{\text{III}}(\text{H}_2\text{O})_6]^{3+}$ and $[\text{V}^{\text{IV}}(\text{H}_2\text{O})_5]^{2+}$ varied based on the geometry of the substrate and the orientation of the molecule. The lowest barriers were always located at the basal plane of graphite. For both vanadium complexes, functionalized zigzag edges had lower adsorption barriers than the corresponding armchair geometry. Charge transfer properties were subsequently investigated by PDOS calculations comparing the overlap of the p -orbital of the (functionalized) carbon atom and the d -orbital of the vanadium ion. Despite the strong adsorption at the basal plane, electron transfer is not likely due to the lack of occupied states near E_{F} . Similarly, armchair edges provide lower DOS regardless of the functionalization. In contrast, H-terminated zigzag edges exhibit a high number of occupied states near E_{F} , which explains their experimentally observed higher reactivity for the vanadium redox reaction. For oxidized zigzag edges, the DOS shifts beyond E_{F} , which could be an indication of the reaction-inhibiting properties for oxidative reactions. Additionally, by studying the sorption properties of $[\text{VO}_2(\text{H}_2\text{O})_4]^+$, it was shown that reliable desorption can only occur at H-terminated zigzag edges, freeing up an active site to promote the oxidation process.

10 Vanadyl Oxidation Elucidated by *Operando* Raman Spectroscopy

Operando Raman spectroscopy enjoys great popularity for many electrochemical systems and was used to study the oxygen evolution reaction on metal oxides^[239,240], lithiation^[241] and sodiation^[242] into carbon-based electrodes, or carbon dioxide reduction on copper^[243,244]. In contrast, only one very recent study examined the oxidation of $V^{IV}O_2^+$ to $V^VO_2^+$ on carbon paper.^[245] On strongly oxidized electrodes, the reaction was reported to proceed *via* the formation of dimers of vanadium ions on oxygen-functionalized surfaces, which complements the old, meanwhile refuted reaction mechanism.^[200] In the cited study, only a small wavenumber range of low intensity at 700 to 1100 cm^{-1} is investigated. The region below, which probably includes more relevant vanadium–oxygen vibrations and the higher wavenumber range, which contains the carbon-related modes, was not resolved.

In this chapter, a knowledge gap about vanadium oxidation kinetics in the positive half-cell of a VFB was filled. By using different carbon-based materials (GF, graphene, and HOPG), laser excitation wavelengths (532 and 633 nm), and electrolyte concentrations, variations in the reaction kinetics regarding the structural properties of the electrode were explicitly explored. A focus will lie on the kinetics at the basal plane of graphite, in contrast to its active edge sites.

10.1 Raman Spectra of Electrolyte and Electrodes

Prior to a meaningful analysis of the spectra recorded under *operando* conditions, the dissolved vanadium oxide species were studied separately in sulfuric acid. A systematic analysis of the characteristic scattering pattern of each component allows the assignment of new signals for the identification of reaction intermediates and products. **Figure 10-1a,b** shows the electrolyte used on the positive side of a vanadium flow battery in the uncharged and charged/oxidized states compared to the salt and sulfuric acid used to prepare the solutions; **Table 7** lists the observed modes and their assignment. Strong signals correspond to the symmetric stretching of HSO_4^- (590 cm^{-1} and 1050 cm^{-1}), and the total symmetric stretching of SO_4^{2-} (985 cm^{-1}). The weaker asymmetric stretching of HSO_4^- and its overtone are located at 895 and 1085 cm^{-1} , respectively.^[246–248]

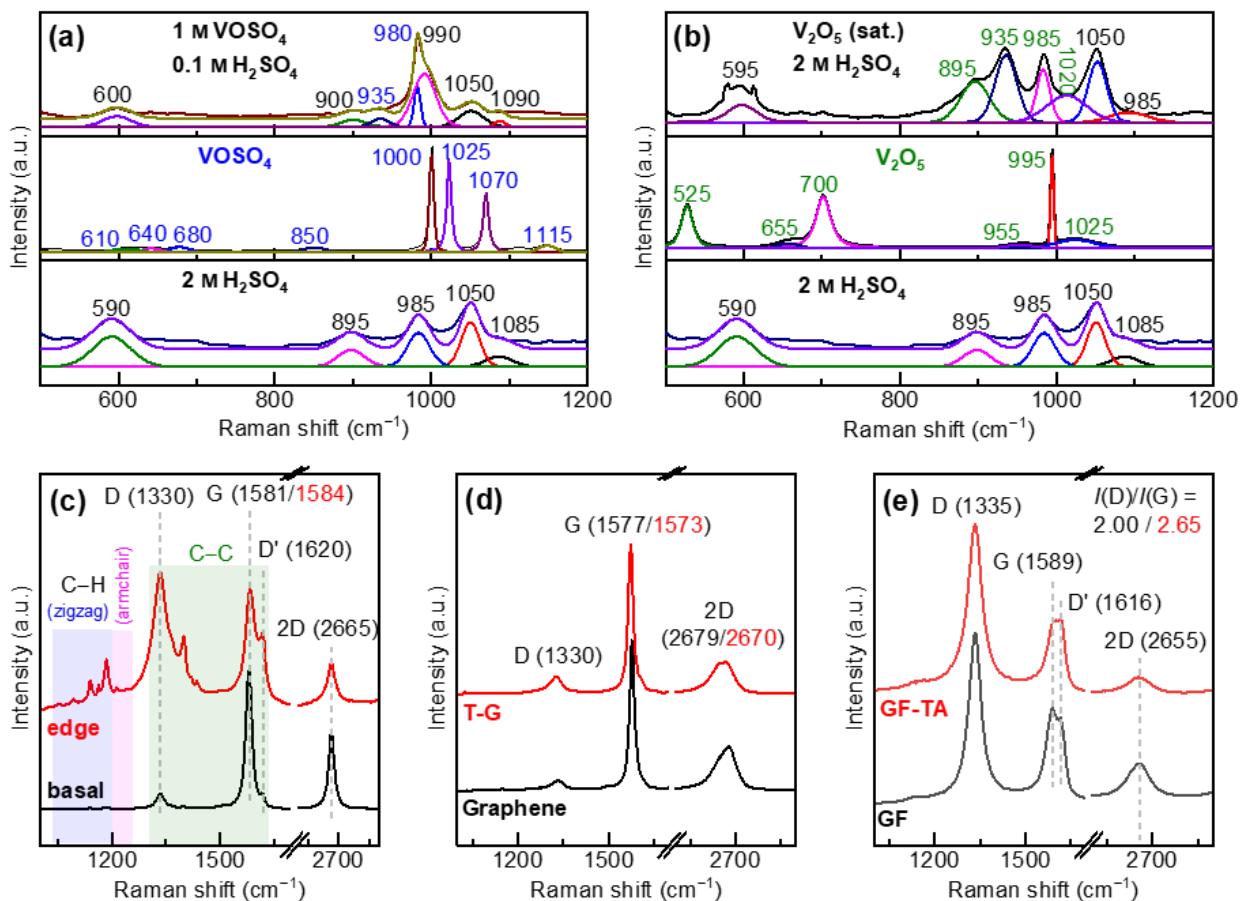


Figure 10-1. Raman spectra of solid and dissolved vanadium oxides and the carbon-based substrates used. **(a)** Uncharged and **(b)** charged positive electrolyte compared to its corresponding salt and sulfuric acid. **(c)** Basal and edge plane exposed HOPG; **(d)** pristine and tetracene-modified graphene (T-G); **(e)** pristine (GF) and thermally activated GF (GF-TA).

Table 7. Peak position and assignment in the Raman spectra in Figure 1 of sulfuric acid, and vanadium sulfate and vanadium oxide, respectively, as solid powder and dissolved in sulfuric acid.

H_2SO_4		VOSO_4 in H_2SO_4 (solid)		V_2O_5 in H_2SO_4 (solid)	
Peak (cm^{-1})	Assignment	Peak (cm^{-1})	Assignment	Peak (cm^{-1})	Assignment
				(525)	$\nu_s(\text{V-O-V})$
590	$\nu_s(\text{HSO}_4^-)$	600	$\nu_s(\text{HSO}_4^-)$ near $\text{V}^{\text{IV}}\text{O}_2^+$	595	$\nu_s(\text{HSO}_4^-)$ near $\text{V}^{\text{VO}}_2^+$
		(610-680)	$\text{H}_2\text{O}_6\text{SV}$	(700)	$\nu_{\text{as}}(\text{V-O-V})$
895	$\nu_{\text{as}}(\text{HSO}_4^-)$	900	$\nu_{\text{as}}(\text{HSO}_4^-)$	895	$\nu_{\text{as}}(\text{HSO}_4^-)/\nu_{\text{as}}(\text{V=O})$
		935	$\nu_s(\text{V=O})$ in $\text{V}^{\text{VO}}_2^+$	935	$\nu_s(\text{V=O})$
985	$\nu_s(\text{SO}_4^{2-})$	980	$\nu_s(\text{SO}_4^{2-})$ near $\text{V}^{\text{IV}}\text{O}_2^+$	(955)	$\nu_s(\text{V-O-V})$
		990	$\nu_s(\text{V=O})$	985	$\nu_s(\text{SO}_4^{2-})$
		(1000)	$\nu_s(\text{V=O})$	(995)	$\nu_s(\text{V=O})$
1050	$\nu_s(\text{HSO}_4^-)$	(1025)	$\nu_s(\text{SO}_4^{2-})$	1020	$\nu_s(\text{HSO}_4^-)$ near $\text{V}^{\text{VO}}_2^+$
1085	$\nu_{\text{as}}(\text{HSO}_4^-)$	(1070)	$\nu_{\text{as}}(\text{SO}_4^{2-})$		
		(1115)	$\nu_{\text{as}}(\text{SO}_4^{2-})$		

Solid vanadyl sulfate shows three intense signals related to the symmetric stretching of V=O (1000 cm^{-1}), and the symmetric and asymmetric S–O stretching of the SO_4^{2-} tetrahedra at 1025 and 1115 cm^{-1} , respectively (**Figure 10-1a**). The region from 610 to 680 cm^{-1} is associated with hydrated vanadium sulfate ions.^[249] In its dissolved state, a merged signal of at least two peaks just below 1000 cm^{-1} is visible. The broadening of the signals and the shift in their position can be attributed to the solvation of the ions, *i.e.*, their new coordination environment comprising water and sulfate species.^[228] The band at 990 cm^{-1} arises from a stretching vibration of the V=O bond in the vanadyl-aqua complex,^[250,251] whereas the sharper signal at 980 cm^{-1} results from the symmetric stretching of a sulfate ion in the second coordination sphere of the hydrated complex.

V_2O_5 powder was used to resolve the structure of undissociated pentavalent vanadium (**Figure 10-1b**). The strongest signal at 995 cm^{-1} corresponds to the symmetric stretching of V=O bonds. A symmetric and asymmetric part of a V–O–V vibration at 525 and 700 cm^{-1} defines the dimeric structure of V_2O_5 .^[252] At 955 cm^{-1} a second bridging vibration, formed *via* another oxygen atom, is recognized, which is weak due to its low polarizability. The interactions of ions with the aqueous solvation shell again results in a broadening and shifting of spectral features for the dissolved salt. Several intense features at 595 , 900 , 1050 , and 1090 cm^{-1} can be associated with H_2SO_4 , since a higher concentration had to account for the low solubility of V_2O_5 . A strong peak at 935 cm^{-1} corresponds to a symmetric V=O vibration and at 1020 cm^{-1} , the vibration of VO_2^+ against SO_4^{2-} anions in its second coordination sphere is observed.^[253] Due to the complexity of the different signals, it is not always easy to separate salt and solvent. At 895 cm^{-1} , for instance, an HSO_4^- stretching overlaps with the asymmetric stretching of the VO_2^+ ion.^[254]

To draw reliable conclusions about the processes occurring at the solid–liquid interface, not only the dissolved electrolyte species but also signals from the carbonaceous electrode must be known. Several materials were initially selected as substrates to propose general conclusions independent of the electrode structure: (i) pristine and thermally oxidized GF as industrially relevant electrodes, (ii) HOPG as a model system to directly compare basal and edge planes of graphite (**Figure S55**), and according to the previous study, (iii) zigzag edge modified graphene to specifically address the effect of highly active edge sites. The basal plane of graphite reveals an intense G and 2D band at 1581 and 2665 cm^{-1} , along with weaker defect-related features at 1330 and 1620 cm^{-1} for the D and D' bands (**Figure 10-1c**). In contrast, for edge plane exposed HOPG, the signals originating from the latter are very strong. It is moreover

possible to distinguish between zigzag and armchair geometries for the edge regions, as shown theoretically and experimentally.^[255] While up to 1200 cm⁻¹ zigzag edges are predominant, above that the armchair orientation becomes apparent; both are present on the scratched HOPG to a not quantifiable extent.

The modification of graphene by a monolayer of zigzag nanoribbons (T-G) is not enough to make these features visible in the spectra (**Figure 10-1d**). Instead, the higher number of edges shows only a slight increase in the relative intensity of the D band. The disruption of the graphene layer stacking by the nanoribbon shifts the G band to lower and the 2D band to higher wavenumbers. For graphitic fibers, the D to G ratio can be used to estimate the disorder of the sample^[94], exhibiting an increase from 2.00 on GF to 2.65 on GF-TA due to the damaged induced by the thermal activation (**Figure 10-1e**). The 2D band additionally loses intensity, while the D' band, which is used to characterize the defects present primarily as edge sites^[95], rises.

10.2 Electrocatalytic Activity of the Substrates

CV curves were recorded to investigate the possible potential range in which different spectral changes will be suspected in the *operando* measurements. An active electrocatalyst reduces the overpotential required for the $V^VO_2^+/V^{IVO}2^+$ oxidation as close to the thermodynamic minimum as possible. This is easily demonstrated by comparing HOPG exposed to the electrolyte before and after carving of the basal plane. Only for the latter sample does the CV show a clear oxidation wave before a steep current rise resulting from carbon corrosion, while for the inactive basal plane these two signals blend into each other (**Figure 10-2a**). The edge-rich HOPG also shows the dependence of electrocatalytic activity for vanadium oxidation on graphitic defects.

The enhancement of the activity after modification with zigzag edges is due to changes in the electronic properties, more precisely to a decrease in the work function of the electrode.^[256] Both the pristine and modified graphene possess a characteristic double-peak structure, resulting from variations in the activity of the basal plane and edge regions (**Figure 10-2b**). It is found that the synthetic edges not only outperform the natural activity of graphene by shifting both oxidation waves to lower potentials, but also the HOPG exposed at the edges. After thermal activation of GF, the potential separation between the oxidation and reduction peak in the CV for GF-TA decreases due to the enhanced reaction kinetics resulting from additional surface defects (**Figure 10-2c**).^[200]

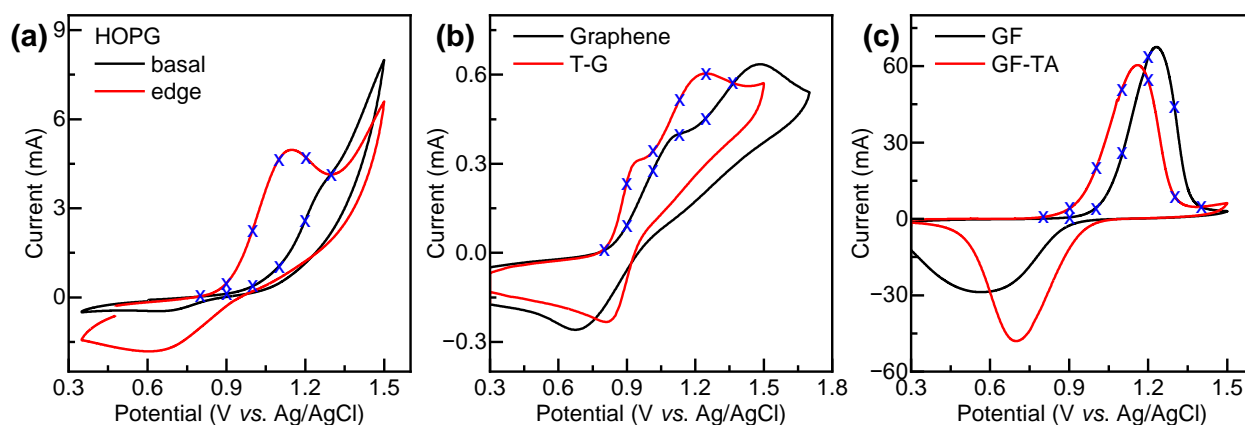


Figure 10-2. Electrochemical activity of the substrates used. **(a)** Basal and edge plane exposed HOPG; **(b)** pristine and tetracene-modified graphene; **(c)** pristine and thermally activated GF. The blue crosses indicate the potential of Raman spectra acquisition.

The electrochemical measurements identified two sample types diverging in electrocatalytic activity for each material class, which thus allows meaningful comparison of spectral differences under working conditions. Spectral features in the following can finally be associated with potential-dependent conversion products of electrolyte species according to **Figure 10-1a,b**, intrinsic variances in the electrode structure as displayed in **Figure 10-1c-e**, or unknown surface reaction intermediates because of the electrocatalytic activity (**Figure 10-2**).

10.3 *Operando* Raman Spectra

Two different laser wavelengths were used to find a compromise between signal intensity and spectral resolution of the Raman features. While the lower wavelength of the green light (532 nm) usually provides higher intensity for low cross-sectional area modes, the red laser (633 nm) is often preferred for carbon-based materials as it delivers higher resolution of overlapping, especially defect-related peaks.^[94] Initial *operando* Raman spectra of GF revealed three important general aspects using the green laser (Figure S56 and Figure S57): (i) the discussed spectra do not show major focal deviations, which means that the differences in relative intensities can be fully associated with changes due to the applied potential. (ii) No structural variations were observed in the graphite-related signals, regardless of the potential. (iii) the large amount of fluorescence below 500 cm^{-1} impeded the investigation of the low wavenumber region. Therefore, only the spectral range relevant for the electrolyte features is displayed in **Figure 10-3**.

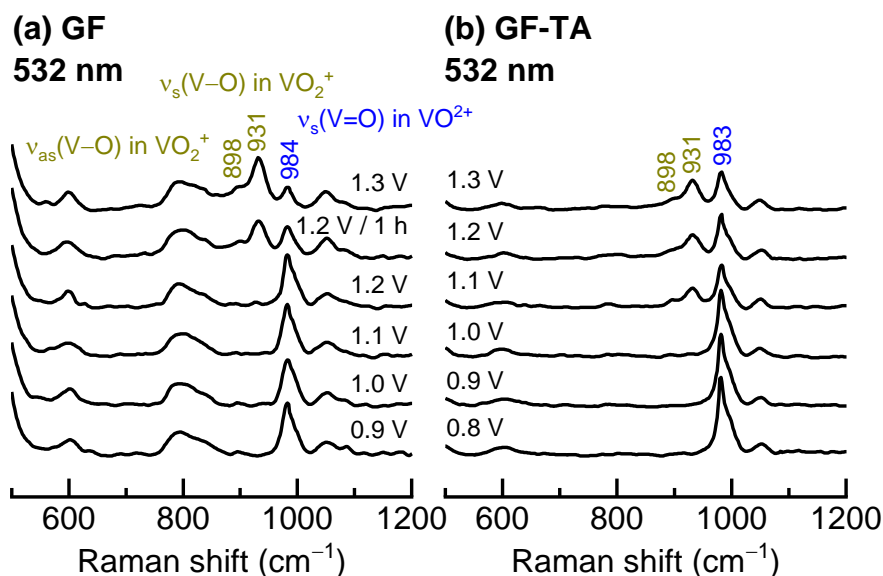


Figure 10-3. Stacked *operando* Raman spectra of (a) GF and (b) GF-TA recorded with a laser wavelength of 532 nm.

From the spectrum of GF in **Figure 10-3a**, the features at about 600, 1050, and 1090 cm^{-1} , associated with vibrations of the sulfate groups in the electrolyte, are present throughout the experiment without major changes. At 984 cm^{-1} , the signal related to the symmetric stretching of the V=O bond in $\text{V}^{\text{IV}}\text{O}_2^+$ loses intensity after holding the potential at 1.2 V vs. Ag/AgCl for 1 h. Two additional bands appeared simultaneously at 931 and 898 cm^{-1} , both related to the symmetric and asymmetric stretching of oxygen in $\text{V}^{\text{VO}_2^+}$. Minor changes in the spectral pattern between 780 and 870 cm^{-1} are observed as a weak peak at ~ 860 cm^{-1} , which was recognized by Gvozdk and Stevenson as an interaction between the $\text{V}^{\text{VO}_2^+}$ ion and sulfuric acid species.^[245] They associated potential-dependent changes in this region predominantly with V–O–V oscillations of various dimeric compounds and introduced a vibrational feature at about 740 cm^{-1} associated with $\text{V}^{\text{VO}_2^+}$ species chemisorbed to oxygen groups on the electrode surface. In our case, no such signals were detected in this wavenumber range.

Spectra were also obtained for the more active GF-TA to analyze the influence of electrocatalytic activity on the spectral pattern (**Figure 10-3b**). The transition from aqueous tetravalent to pentavalent vanadium ions can be equally followed by a peak transition from 983 to 931 cm^{-1} . Changes in the pattern at a lower potential of 1.1 V vs. Ag/AgCl directly reflect the higher activity of the sample. In addition, no features were detected in the previously discussed region between 780 and 870 cm^{-1} , suggesting that the activity is not directly dependent on interactions with an oxygen-functionalized surface. Consequently, the measurements on GF and GF-

TA showed potential-dependent changes in the oxidation of vanadium species, which were followed according to the spectral pattern of the electrolyte shown in **Figure 10-1a,b**.

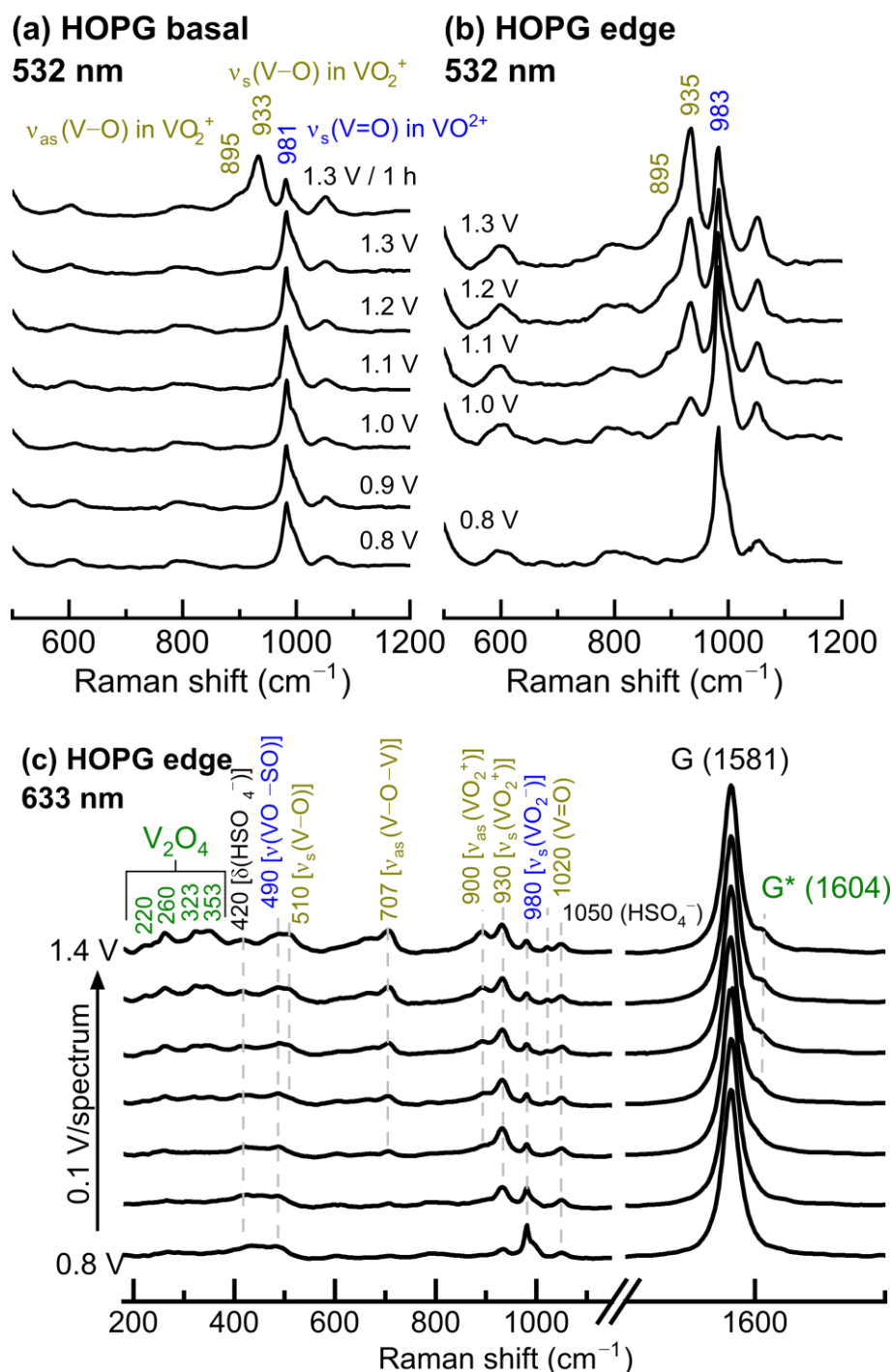


Figure 10-4. Stacked *operando* Raman spectra of HOPG. **(a)** Basal and **(b)** edge plane exposed HOPG recorded with a laser wavelength of 532 nm; **(c)** Edge plane exposed HOPG recorded with a wavelength of 633 nm.

To investigate the processes at graphitic defects in more detail, cleaved and scratched HOPG was studied. **Figure 10-4a** presents the Raman spectra for HOPG exposed in the basal plane, showing the transition from symmetric stretching of the $V=O$ bond in $V^{IV}O_2^+$ (981 cm^{-1}) to the

double-peak structure formed by symmetric and asymmetric stretching of the VVO_2^+ ion (933 and 895 cm^{-1}) at a high potential of 1.3 V vs. Ag/AgCl. A weak signal from the interaction of the pentavalent vanadium ion with sulfuric acid occurs at $\sim 860\text{ cm}^{-1}$. Residual characteristics, if present, are of such low intensity that further interpretation is not reliable. Direct comparison with the spectra of edge plane HOPG in **Figure 10-4b** reveals two increasing signals at 935 and 895 cm^{-1} at only 1.0 V vs. Ag/AgCl, consistent with the higher electrocatalytic activity (**Figure 10-1c**). The peak transition in this wavenumber range can therefore be considered as an activity indicator that sets in at the edge regions at earlier potentials than in the basal plane.

Due to the fluorescence occurring below 500 cm^{-1} and the static carbon signals, the spectra for edge plane exposed HOPG were again measured with a lower laser excitation energy (**Figure 10-4c**). From 0.9 V vs. Ag/AgCl, the symmetric (930 cm^{-1}), followed by the asymmetric stretching of VVO_2^+ (900 cm^{-1}) occurs at slightly higher potentials. As a new weak feature between the stretching of V=O in $V^{IV}O^{2+}$ (980 cm^{-1}) and HSO_4^- , a newly discovered band at 1020 cm^{-1} is associated with the interplay between VVO_2^+ and sulfuric acid anions.^[254] Complementing the known pentavalent vibrational modes, there is a feature at 707 cm^{-1} originating from the asymmetric stretching of the V–O–V bonds. It is accompanied by a weak shoulder at $\sim 670\text{ cm}^{-1}$ and its symmetric part at $\sim 510\text{ cm}^{-1}$, which resembles the pattern of V_2O_5 powder (**Figure 10-1b**).

The possibility that the energy input from the laser exposure led to the precipitation of oxidized vanadium compounds could be ruled out for three reasons: the observed pattern could be (i) reliably reproduced at other locations on the electrode that had not been previously illuminated, and (ii) successfully reversed by lowering the potential at the same location (**Figure S58**). At a reversal potential of 0.8 V, features of both $V^{IV}O^{2+}$ and VVO_2^+ were visible, but at 0.0 V vs. Ag/AgCl, the modes originating from the uncharged electrolyte were observed. (iii) In previous experiments, a green laser with higher energy was used. Nevertheless, no signals indicative of solid V_2O_5 were detected in these cases.

In a next step, the low wavenumber region previously overshadowed by fluorescence is evaluated. The observed pattern that develops at potentials above 1.0 V vs. Ag/AgCl is best described by the vibrational bands of β - V_2O_5 that can be generated by applying temperatures above $200\text{ }^\circ\text{C}$ and high pressures up to 8 GPa to α - V_2O_5 .^[257,258] All V_2O_5 polymorphs can be considered as an assembly of VO_x polyhedral, but while the alpha phase consists of VO_5 structures, vanadium is coordinated 6-fold in the beta phase. Crystallographic and theoretical data defined the latter as parallel chains of V_2O_4 , held together by weak interactions, justifying its

designation as a V_2O_5 .^[258] All features observed below 400 cm^{-1} can be associated with the distortion of these V_2O_4 ladders.^[257]

The double peak structure at 323 and 353 cm^{-1} corresponds to an in-plane stretching of a $V=O$ bond (323 cm^{-1}) and two oxygen atoms in the coordination sphere of a vanadium center (353 cm^{-1}) as ladder breathing (**Figure 10-4c**).^[258,259] The vibration at 260 cm^{-1} originates either from an in-plane vibration of an edge-shared oxygen (lit.: 243 to 253 cm^{-1}) or from an out-of-plane motion of the $V-O-V$ bond (lit.: 271 to 272 cm^{-1}).^[258,259] With similar uncertainty, the 220 cm^{-1} mode can be associated with in-plane stretching of $V=O$ (lit.: 220 to 222 cm^{-1}) or displacement of adjacent layers (lit.: 228 cm^{-1}).^[258,259] Assignment of such low-wavenumber modes is generally difficult, especially since the instability of numerous V_2O_5 polymorphs under ambient conditions complicates experimental characterization. Intense ladder modes of atmospherically stable α - V_2O_5 are found at lower wavenumbers of 285 and 305 cm^{-1} , which excludes its presence and thus precipitation.^[258] Additionally, distinct features at 406 , 483 , and 528 cm^{-1} , which are characteristic for α - V_2O_5 , are absent.

The modes could also be described by γ' - V_2O_5 , whose structure is very similar to β - V_2O_5 , but without the translationally equivalence of adjacent layers.^[260] Its ladder modes lie at 350 and 333 cm^{-1} , originating from the in-plane vibration of vanadium atoms, the distortion of vanadium along the chain at $\sim 260\text{ cm}^{-1}$, and the out-of-plane motion of oxygen in the $V-O-V$ bond at $\sim 220\text{ cm}^{-1}$.^[260] Regardless of the final classification, vanadium species are considered to be dimeric, *i.e.*, they consist of two VO_2 ions connected by an oxygen bridge. Reaction intermediates of dimeric origin were postulated earlier, assuming that they occur at oxygen groups on the electrode.^[245] However, in our case, there were none of these potential-dependent changes between 740 and 820 cm^{-1} associated with the interaction of vanadium and surface oxygen.

Instead, the carbon related vibrations reveal an altered shape at oxidative potentials (**Figure 10-4c**): a shoulder above the G mode at 1604 cm^{-1} , referred to as G^* , occurs simultaneously with the electrolyte conversion. Its origin could theoretically have two reasons: (i) changes in the local electronic structure resulting from the presence of charged species such as vanadium ions lead to a shift in the G band, as it can also be observed in the doping of graphene.^[261-263] (ii) Intercalation of ions, such as sulfuric acid, between graphite layers, causing a splitting of the G band because of an increased force constant of the graphite lattice.^[264-266] To clarify this conflict, graphene was employed as an electrode since it provides multiple intercalation sites. For the green laser, the transition of the electrolyte species above 1.2 V vs. Ag/AgCl is observed

without additional changes in the carbon components (Figure S59). The spectral change, however, is accompanied by a growing G* band at $\sim 1600\text{ cm}^{-1}$ when the sample is illuminated with red light (Figure S60). The wavelength sensitivity of the feature can already be associated with a surface process and not with intercalation, since the latter effect does not depend on the excitation energy.^[267] Further measurements using pure sulfuric acid as an electrolyte definitely exclude intercalation, since no spectral changes over the entire potential range were observed with the red laser (Figure S61). The growth of the G* band is therefore interpreted as an electronic interaction between the carbon atoms in the graphite structure and the vanadium ions from the electrolyte.

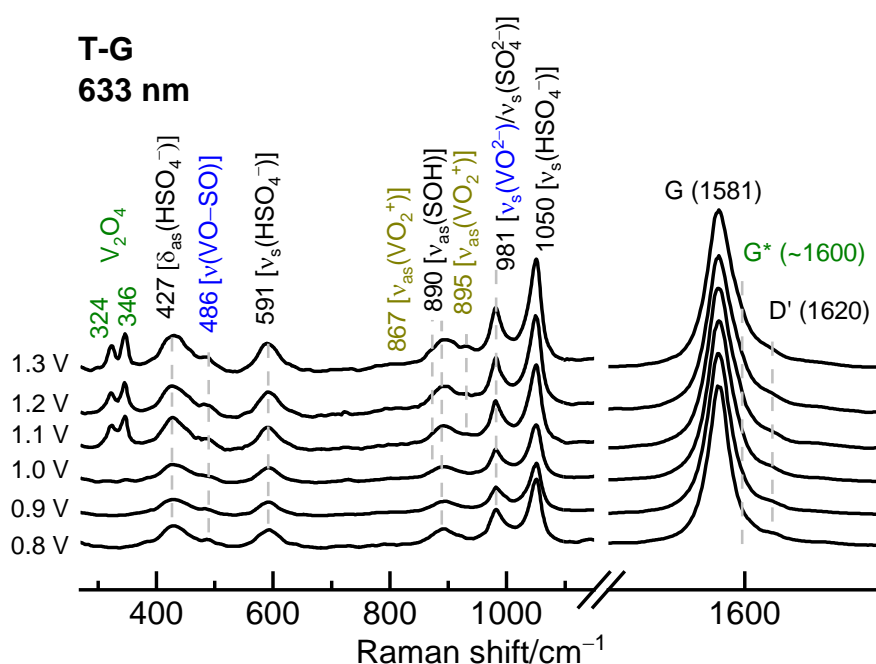


Figure 10-5. Stacked *operando* Raman spectra of T-G recorded with a laser wavelength of 633 nm.

Finally, to distinguish between oxidized electrolyte species and reaction intermediates, the measurement in **Figure 4c** was repeated at an edge-free location directly adjacent to the previously characterized edge site. A transformation of the electrolyte species at 937 cm^{-1} already occurs at about 1.0 V vs. Ag/AgCl, as it was the case for the edge-related spectra, but not for the previously characterized basal plane (**Figure 10-4a** and Figure S62). Oxidized $\text{V}^{\text{VO}_2^+}$ ions thus diffuse from the active site at the edge to the spot illuminated by the laser. No other vibrational features and no potential-dependent structural changes associated with carbon were detected, allowing two conclusions: (i) the ladder vibrations and potentially the V–O–V mode at 707 cm^{-1} belong to a reaction intermediate formed during the oxidation of $\text{V}^{\text{VO}_2^+}$, and

(ii) the growing G^* band demonstrates the interaction of vanadium ions with graphite at graphitic edge sites only, which is crucial for charge transfer.

Additional *operando* Raman spectra were recorded for zigzag edge-modified graphene (T-G) to verify the conclusions about edge-related reaction intermediates. To decrease electrolyte-induced signals while improving the resolution of intermediates, the concentration of dissolved species was reduced. Consequently, the overall spectrum at low potentials is dominated by H_2SO_4 features (**Figure 10-5**). Due to its lower electrocatalytic activity (**Figure 10-2b**), minor changes were observed for pristine graphene at higher potentials due to the absence of surface intermediates (Figure S60). For T-G, however, at 1.1 V vs. Ag/AgCl, the stretching of HSO_4^- at 890 cm^{-1} is accompanied by two asymmetric stretching vibrations associated with VVO_2^+ ions at 867 and 895 cm^{-1} , indicating electrolytic transformation by the oxidation of $V^{IV}O_2^+$. Moreover, the pronounced double-peak structure associated with the V_2O_4 ladder modes at 324 and 346 cm^{-1} is evidence for the presence of adsorbed dimeric species at edge sites during the reaction. Again, no additional spectral features associated with the interaction of vanadium ions with surface oxygen were observed. Instead, a growing G^* band at $\sim 1600\text{ cm}^{-1}$ at higher potentials proves the direct interaction of vanadium with the electrode edges.

10.4 Conclusions

In this chapter, *operando* Raman spectroscopy was used to follow the electrocatalytic oxidation from $V^{IV}O_2^+$ to VVO_2^+ , which is considered the kinetic bottleneck in vanadium flow batteries. By systematically analyzing all solid and dissolved compounds involved, the resulting signals and potential-dependent structural changes were successfully separated and related to the oxidation of the electrolyte, the reaction intermediates, and the interactions of vanadium ions and carbon atoms. The oxidation of dissolved vanadium species can be followed by a transition of vibrational bands associated with VVO_2^+ instead of $V^{IV}O_2^+$ complexes just below 1000 cm^{-1} , whose starting potential corresponds to the electrocatalytic activity of the electrode. Moreover, several vibrations were observed at the active edge regions below 500 cm^{-1} , related to the ladder modes of V_2O_4 structures, suggesting reaction intermediates of dimeric origin. No previously ascribed interaction with surface oxygen was observed for active electrodes. Instead, an additional signal was visible above the graphite-related G band at $\sim 1600\text{ cm}^{-1}$, corresponding to the direct electronic interaction of carbon atoms from the substrate and vanadium ions in the electrolyte. In summary, vanadium ions primarily react directly at non-functionalized carbon edge sites as dimeric species.

11 Concluding Remarks

11.1 Summary and Final Conclusions

This work contributed an in-depth understanding of the kinetic processes at the graphite–electrolyte interface in vanadium flow batteries. The electrocatalytic activity of industrially relevant graphite felt and related carbon-based materials, such as graphene, polycyclic aromatic hydrocarbons, and highly ordered pyrolytic graphite, was studied. The activity-determining properties of graphite-based electrodes for efficient oxidation and reduction of solvated vanadium ions were determined in terms of surface chemistry, microstructure, and electronic structure by various microscopic and spectroscopic experimental techniques and theoretical calculations.

This thesis started with a literature review on the influence of surface oxygen and its effects on the electrocatalytic activity. Based on conflicting initial results, the surface chemistry and microstructural properties of several treated electrodes were characterized before and after electrochemistry, in which graphitic defects were identified as the most likely activity descriptor. These results contributed to a paradigm change that provided the impetus for subsequent studies. Oxygen-free electrodes were prepared to fully trace the origin of the electrocatalysis to hydrogen-terminated defects instead of oxygen groups. It was found that not only does initial oxygen affect the activity negatively, but also that deoxygenated electrodes are more resistant to carbon corrosion under oxidizing conditions in the acidic electrolyte. Based on these findings, a new reaction mechanism, including hydrogen terminated defects instead of oxygen functional groups, was introduced.

Pyrenes with different oxygen groups were used to show systematically that chemical functionalization of edge sites influenced the electrocatalytic activity. Deteriorated redox kinetics for hydroxyl groups were exhibited, while carboxylic groups seemed to have a minor effect on the charge transfer. However, it was not always possible to relate the original functionalization to the outcome because the microstructure of the outermost surface layer was also affected differently regarding the surface group. Surface defects were thus again found to serve as a good descriptor for the electrocatalytic activity in this case. To differentiate between the origin of disorder, zero-dimensional point defects were introduced by thermochemical heteroatom substitution, which showed the importance of considering all electrode properties after an

activation treatment. Low doping concentrations below one percent were enough to increase the full cell performance when the graphitization level was high and high oxygenation was inhibited.

Building on the approach introduced for pyrenes, various molecular structures using polycyclic aromatic hydrocarbons with different edge geometries were examined. The activity was related not only to the architecture of the defects but also to the electronic structure. It was found that higher conjugated zigzag edges increased the electrocatalytic activity for the oxidation of vanadium ions. These experiments allowed to postulate a link between the work function and the electrocatalytic activity. The basal plane of graphite and hydrogen and oxygen terminated edges were additionally compared by density functional theory calculations to investigate their interactions with solvated vanadium ions. It was shown that the adsorption energies of the trivalent and tetravalent vanadium complexes were lower for zigzag than for armchair edges. While additional oxygen functionalities further improved the adsorption properties, charge transfer was found to occur most likely at hydrogen terminated zigzag edges because of more occupied electronic states near the Fermi level. In addition, a positive adsorption energy for the pentavalent vanadium complex showed favorable desorption and thus release of an active site after oxidation at zigzag geometries.

Finally, *operando* Raman spectroscopy was used to identify reaction intermediates under realistic reaction conditions. For several graphite-based electrodes, the electrocatalytic activity was directly related to a potential-dependent signal conversion of the electrolyte compounds. Several vibrational modes in the low wavenumber region, associated with dimeric vanadium species as reaction intermediates, were identified for active edge sites. In addition, vanadium ions have been shown to interact directly with the electrode surface by adsorption and thus influence of the local electronic structure of graphite, which changed the graphite-related signal.

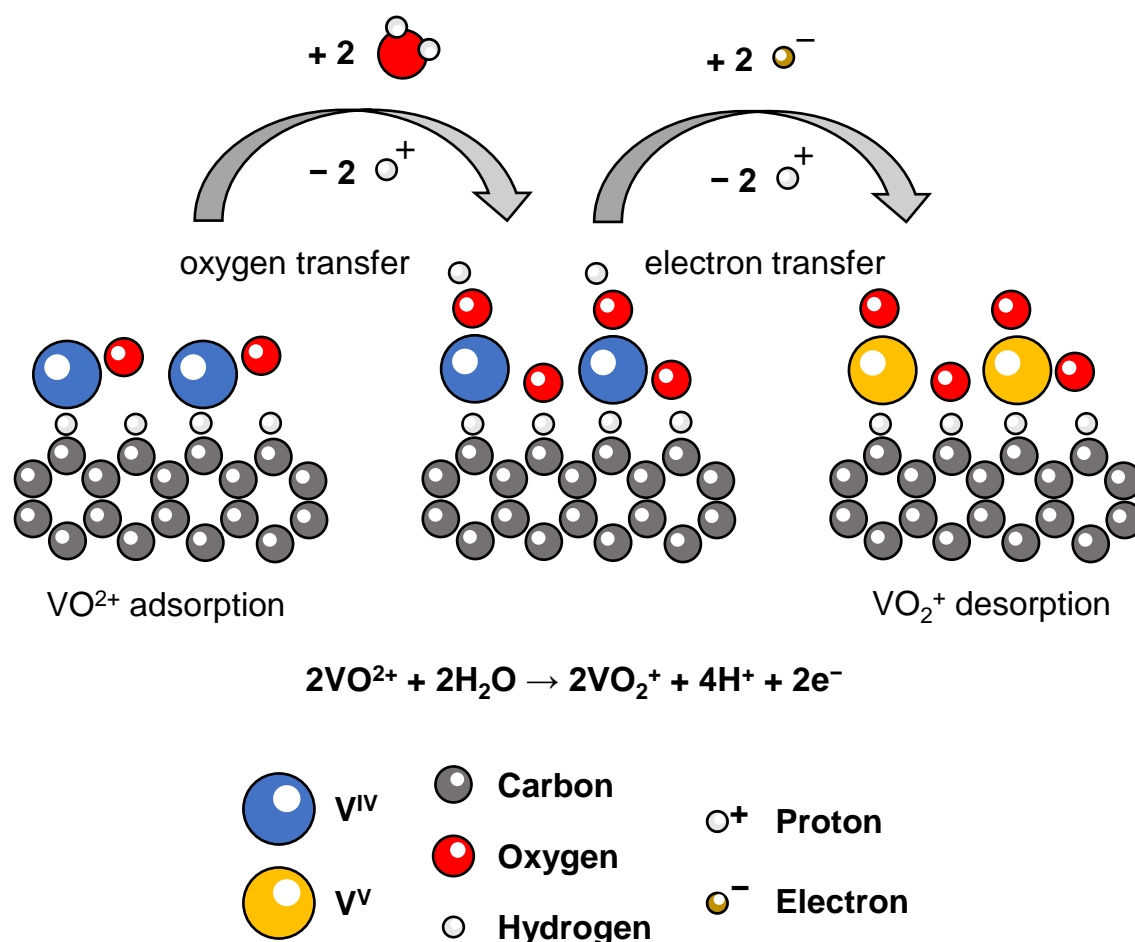


Figure 11-1. Concluding reaction mechanism for efficient oxidation of vanadium dimers at hydrogen terminated zigzag edge sites.

Based on the experimental and theoretical results of this work, an innovative reaction mechanism for the vanadium oxidation in the positive half-cell of a VFB is proposed (**Figure 11-1**). The VO^{2+} ions adsorb and react predominantly as dimeric species at hydrogen terminated zigzag edge sites. It has been shown that larger sizes of the π -conjugated system are helpful for the reaction, suggesting that neighboring ions are not directly adjacent but omit at least one edge carbon atom because of the size of the covalently bonded oxygen and water molecules in the first coordination sphere. After adsorption, an additional oxygen atom from the solvation shell is covalently bonded to the vanadium ion under the release of two protons. Adjacent vanadium ions are bridged by one of these oxygen atoms, as evidenced by V–O–V vibrations and V_2O_4 -like ladder modes observed by *operando* Raman spectroscopy. The additional hydrogen atoms leave the adsorbent because two electrons are transferred from the vanadium ions to the carbon substrate. Because of their positive adsorption energy at the zigzag edges, the

generated VO_2^+ ions readily leave the substrate, freeing the reaction sites for subsequent adsorption of unoxidized vanadium species.

11.2 Outlook on Future Research Possibilities

In this work, various aspects of vanadium redox reactions and the necessary structural properties of graphite as an efficient electrocatalyst have been understood. However, the greater challenge is to successfully transfer these insights gained on model systems to real electrodes. To benefit from these fundamental findings, it will be crucial to develop new activation techniques for three-dimensional felt electrodes.

These treatments should be non-oxidative to reduce the oxygen concentration of a pristine electrode. Since the functionality of surface oxygen groups has most probably been refuted in this work, it is unnecessary and even detrimental to the charge transfer characteristics and long-term stability to have these groups on the electrode at all. In fact, the goal especially in the positive half-cell should be to resist the formation of surface oxygen despite the oxidative conditions that are a direct result of the applied potential and the acidic electrolyte. To this end, the deoxygenation strategy proposed here could be coupled with a further activation that increases the surface area to produce long-living and highly active electrodes.

One consequence of the treatment should be an increase in the electrochemically active surface area due to the introduction of micropores accessible to the electrolyte. It has been demonstrated that a wide range of pores from 60 to 160 μm are beneficial for the mass transfer and pressure drop.^[268] However, the pores created on the surface of graphite felts by conventional activations are much smaller; a significant fraction to a point below 2 nm, where the access of solute species is inhibited.^[269] Therefore, it is critical to understand pores of different nanometers as they interact with molecules, to the point where they could serve as active sites themselves due to confinement effects.^[270,271] In addition, various theoretical and experimental approaches should be considered at the fundamental level to understand the structure of the electrolyte at such pores.

Surface defects need to be introduced to transfer electrons between the electrode and vanadium ions in the electrolyte successfully. This could go toward more fundamental research: whereas in this work, edge defects and their influence and heteroatom substitution^[272] were studied, it is much more difficult to introduce carbon vacancies into graphite under ambient conditions; a mild plasma treatment may be worth trying.^[273,274] It was shown here multiple

times that vacancies could contribute to accelerated charge transfer for the vanadium redox reaction, as their presence was often consistent with the electrocatalytic activity. Considering the metal-like electronic structure of argon-ion bombarded pyrolytic graphite, they could work exceptionally well for vanadium reduction in the negative half-cell where electrons must be provided by the electrode.

Finally, strategies should be developed to implement zigzag edges in the surface structure of graphite. The size of the π -conjugated system between the edges should be explored in more detail to ensure optimal electrocatalytic properties. In this respect, new low-cost synthetic routes for polycyclic aromatic hydrocarbons could be helpful, since their application on sp^2 hybridized carbon can be easily achieved by a simple immersion procedure.

With respect to other technologies that rely on graphite as an electrode material, the results of this work may assist in challenging existing reaction mechanism and understanding new kinetic processes. Deoxygenated electrodes may be of interest for non-aqueous flow batteries, and targeted defect implementation and edge site geometries are likely to be important for a variety of electrochemical energy storage and conversion devices. The study of the electronic structure proved to be a powerful tool for investigating activity-determining factors without introducing new conflicts over surface chemistry and microstructural properties. Finally, *operando* Raman spectroscopy provides comprehensive results on the structural changes of atoms and ions in the electrode and electrolyte simultaneously, and can achieve insightful findings for many types of electrode–electrolyte interfaces.

References

- [1] M. Rychcik, M. Skyllas-Kazacos, *J. Power Sources* **1988**, *22*, 59.
- [2] M. Lopez-Atalaya, G. Codina, J. R. Perez, J. L. Vazquez, A. Aldaz, *J. Power Sources* **1992**, *39*, 147.
- [3] P. K. Leung, C. Ponce-de-León, C. Low, A. A. Shah, F. C. Walsh, *J. Power Sources* **2011**, *196*, 5174.
- [4] M. Krishna, E. J. Fraser, R. Wills, F. C. Walsh, *J. Energy Storage* **2018**, *15*, 69.
- [5] B. Hu, C. DeBruler, Z. Rhodes, T. L. Liu, *J. Am. Chem. Soc.* **2017**, *139*, 1207.
- [6] X. Wei, W. Duan, J. Huang, L. Zhang, B. Li, D. Reed, W. Xu, V. Sprenkle, W. Wang, *ACS Energy Lett.* **2016**, *1*, 705.
- [7] K. Mizushima, P. C. Jones, P. J. Wiseman, J. B. Goodenough, *Mater. Res. Bull.* **1980**, *15*, 783.
- [8] M. S. Whittingham, *Science* **1976**, *192*, 1126.
- [9] A. Yoshino, *Angew. Chem. Int. Ed.* **2012**, *51*, 5798.
- [10] M. Skyllas-Kazacos, *J. Electrochem. Soc.* **1986**, *133*, 1057.
- [11] M. Skyllas-Kazacos, *J. Electrochem. Soc.* **1987**, *134*, 2950.
- [12] M. Rychcik, M. Skyllas-Kazacos, *J. Power Sources* **1987**, *19*, 45.
- [13] I. A. Jumare, *J. Energy Storage* **2020**, *27*, 101130.
- [14] T. Wilberforce, A. Alaswad, A. Palumbo, M. Dassisti, A. G. Olabi, *Int. J. Hydrogen Energy* **2016**, *41*, 16509.
- [15] L. Trahey, F. R. Brushett, N. P. Balsara, G. Ceder, L. Cheng, Y.-M. Chiang, N. T. Hahn, B. J. Ingram, S. D. Minter, J. S. Moore, K. T. Mueller, L. F. Nazar, K. A. Persson, D. J. Siegel, K. Xu, K. R. Zavadil, V. Srinivasan, G. W. Crabtree, *PNAS* **2020**, *117*, 12550.
- [16] G. Kear, A. A. Shah, F. C. Walsh, *Int. J. Energy Res.* **2012**, *36*, 1105.
- [17] X. Han, L. Lu, Y. Zheng, X. Feng, Z. Li, J. Li, M. Ouyang, *eTransportation* **2019**, *1*, 100005.
- [18] J. J. H. Togonon, P.-C. Chiang, H.-J. Lin, W.-C. Tsai, H.-J. Yen, *Carbon Trends* **2021**, *3*, 100035.
- [19] L. L. Zhang, X. S. Zhao, *Chem. Soc. Rev.* **2009**, *38*, 2520.
- [20] S. Li, C. Cheng, A. Thomas, *Adv. Mater.* **2017**, *29*.
- [21] P. R. Wallace, *Phys. Rev.* **1947**, *71*, 622.
- [22] J. L. Lado, N. García-Martínez, J. Fernández-Rossier, *Synth. Met.* **2015**, *210*, 56.
- [23] B. Partoens, F. M. Peeters, *Phys. Rev. B* **2006**, *74*.
- [24] N. B. Luque, W. Schmickler, *Electrochim. Acta* **2012**, *71*, 82.

- [25] D. Wei, Y. Liu, Y. Wang, H. Zhang, L. Huang, G. Yu, *Nano Lett.* **2009**, *9*, 1752.
- [26] Z. Luo, S. Lim, Z. Tian, J. Shang, L. Lai, B. MacDonald, C. Fu, Z. Shen, T. Yu, J. Lin, *J. Mater. Chem.* **2011**, *21*, 8038.
- [27] C. G. Vayenas, S. Bebelis, S. Ladas, *Nature* **1990**, *343*, 625.
- [28] A. M. Ismail, E. Csapó, C. Janáky, *Electrochim. Acta* **2019**, *313*, 171.
- [29] T. Liu, C. Xi, C. Dong, C. Cheng, J. Qin, S. Hu, H. Liu, X.-W. Du, *J. Phys. Chem. C* **2019**, *123*, 28319.
- [30] Y. Cai, L. Tao, G. Huang, N. Zhang, Y. Zou, S. Wang, *Chin. J. Catal.* **2021**, *42*, 938.
- [31] C. H. Choi, H.-K. Lim, M. W. Chung, G. Chon, N. Ranjbar Sahraie, A. Altin, M.-T. Sougrati, L. Stievano, H. S. Oh, E. S. Park, F. Luo, P. Strasser, G. Dražić, K. J. J. Mayrhofer, H. Kim, F. Jaouen, *Energy Environ. Sci.* **2018**, *11*, 3176.
- [32] B. Sun, M. Skyllas-Kazacos, *Electrochim. Acta* **1992**, *37*, 1253.
- [33] B. Sun, M. Skyllas-Kazacos, *Electrochim. Acta* **1992**, *37*, 2459.
- [34] N. Pour, D. G. Kwabi, T. Carney, R. M. Darling, M. L. Perry, Y. Shao-Horn, *J. Phys. Chem. C* **2015**, *119*, 5311.
- [35] G. Wei, W. Su, Z. Wei, X. Fan, J. Liu, C. Yan, *Electrochim. Acta* **2016**, *204*, 263.
- [36] W. Yuan, Y. Zhou, Y. Li, C. Li, H. Peng, J. Zhang, Z. Liu, L. Dai, G. Shi, *Sci. Rep.* **2013**, *3*, 2248.
- [37] D. W. Boukhvalov, M. I. Katsnelson, *Nano Lett.* **2008**, *8*, 4373.
- [38] A. Hassan, A. S. Haile, T. Tzedakis, H. A. Hansen, P. de Silva, *ChemSusChem* **2021**, *14*, 3945.
- [39] K. A. Ritter, J. W. Lyding, *Nat. Mater.* **2009**, *8*, 235.
- [40] Y. Lin, Q. Lu, F. Song, L. Yu, A. K. Mechler, R. Schlögl, S. Heumann, *Angew. Chem. Int. Ed.* **2019**, *58*, 8917.
- [41] H. Radinger, *ChemPhysChem* **2021**, *22*, 2498.
- [42] A. B. Soliman, H. S. Abdel-Samad, S. S. Abdel Rehim, H. H. Hassan, *Sci. Rep.* **2016**, *6*, 22056.
- [43] P. Simon, Y. Gogotsi, *Nat. Mater.* **2008**, *7*, 845.
- [44] H. R. Byon, B. M. Gallant, S. W. Lee, Y. Shao-Horn, *Adv. Funct. Mater.* **2013**, *23*, 1037.
- [45] K. J. Kim, S.-W. Lee, T. Yim, J.-G. Kim, J. W. Choi, J. H. Kim, M.-S. Park, Y.-J. Kim, *Sci. Rep.* **2014**, *4*, 6906.
- [46] K. J. Kim, M.-S. Park, Y.-J. Kim, J. H. Kim, S. X. Dou, M. Skyllas-Kazacos, *J. Mater. Chem. A* **2015**, *3*, 16913.
- [47] Y. Wu, R. Holze, *Batteries* **2018**, *4*, 47.
- [48] J. Maruyama, T. Hasegawa, S. Iwasaki, T. Fukuhara, M. Nogami, *J. Electrochem. Soc.* **2013**, *160*, A1293-A1298.
- [49] K. Amini, J. Gostick, M. D. Pritzker, *Adv. Funct. Mater.* **2020**, *30*, 1910564.

- [50] W. Li, J. Liu, C. Yan, *Carbon* **2013**, *55*, 313.
- [51] S. Zhong, C. Padeste, M. Kazacos, M. Skyllas-Kazacos, *J. Power Sources* **1993**, *45*, 29.
- [52] Y. Li, J. Parrondo, S. Sankarasubramanian, V. Ramani, *J. Phys. Chem. C* **2019**, *123*, 6370.
- [53] A. M. Pezeshki, J. T. Clement, G. M. Veith, T. A. Zawodzinski, M. M. Mench, *J. Power Sources* **2015**, *294*, 333.
- [54] W. Zhang, J. Xi, Z. Li, H. Zhou, Le Liu, Z. Wu, X. Qiu, *Electrochim. Acta* **2013**, *89*, 429.
- [55] L. Yue, W. Li, F. Sun, L. Zhao, L. Xing, *Carbon* **2010**, *48*, 3079.
- [56] Z. Zhang, J. Xi, H. Zhou, X. Qiu, *Electrochim. Acta* **2016**, *218*, 15.
- [57] Z. He, Y. Jiang, W. Meng, F. Jiang, H. Zhou, Y. Li, J. Zhu, L. Wang, L. Dai, *Appl. Surf. Sci.* **2017**, *423*, 111.
- [58] L. Estevez, D. Reed, Z. Nie, A. M. Schwarz, M. I. Nandasiri, J. P. Kizewski, W. Wang, E. Thomsen, J. Liu, J.-G. Zhang, V. Sprenkle, B. Li, *ChemSusChem* **2016**, *9*, 1455.
- [59] J. Noack, N. Roznyatovskaya, J. Kunzendorf, M. Skyllas-Kazacos, C. Menictas, J. Tübke, *J. Energy Chem.* **2018**, *27*, 1341.
- [60] H. Fink, J. Friedl, U. Stimming, *J. Phys. Chem. C* **2016**, *120*, 15893.
- [61] J. Friedl, U. Stimming, *Electrochim. Acta* **2017**, *227*, 235.
- [62] M. V. Holland-Cunz, J. Friedl, U. Stimming, *J. Electroanal. Chem.* **2018**, *819*, 306.
- [63] S. Rümmler, M. Steimecke, S. Schimpf, M. Hartmann, S. Förster, M. Bron, *J. Electrochem. Soc.* **2018**, *165*, A2510-A2518.
- [64] C. Choi, H. Noh, S. Kim, R. Kim, J. Lee, J. Heo, H.-T. Kim, *J. Storage Mater.* **2019**, *21*, 321.
- [65] R. Schweiss, C. Meiser, F. W. T. Goh, *ChemElectroChem* **2017**, *4*, 1969.
- [66] P. Mazúr, J. Mrlík, J. Beneš, J. Pocič, J. Vrána, J. Dundálek, J. Kosek, *J. Power Sources* **2018**, *380*, 105.
- [67] G. Zhang, A. S. Cuharuc, A. G. Güell, P. R. Unwin, *Phys. Chem. Chem. Phys.* **2015**, *17*, 11827.
- [68] M. Park, I.-Y. Jeon, J. Ryu, J.-B. Baek, J. Cho, *Adv. Energy Mater.* **2015**, *5*, 1401550.
- [69] Z. Jiang, K. Klyukin, V. Alexandrov, *Phys. Chem. Chem. Phys.* **2017**, *19*, 14897.
- [70] Z. Jiang, K. Klyukin, V. Alexandrov, *ACS Appl. Mater. Interfaces* **2018**, *10*, 20621.
- [71] S. M. Taylor, A. Pătru, D. Perego, E. Fabbri, T. J. Schmidt, *ACS Appl. Energy Mater.* **2018**, *1*, 1166.
- [72] A. C. Ferrari, D. M. Basko, *Nat. Nanotechnol.* **2013**, *8*, 235.
- [73] M. S. Dresselhaus, A. Jorio, A. G. Souza Filho, R. Saito, *Philos. Trans. R. Soc. London, Ser. A* **2010**, *368*, 5355.
- [74] J. Melke, P. Jakes, J. Langner, L. Riekehr, U. Kunz, Z. Zhao-Karger, A. Nefedov, H. Sezen, C. Wöll, H. Ehrenberg, C. Roth, *Carbon* **2014**, *78*, 220.

- [75] T. J. Rabbow, M. Trampert, P. Pokorny, P. Binder, A. H. Whitehead, *Electrochim. Acta* **2015**, *173*, 17.
- [76] N. Roznyatovskaya, J. Noack, K. Pinkwart, J. Tübke, *Curr. Opin. Electrochem.* **2020**, *19*, 42.
- [77] J. Langner, M. Bruns, D. Dixon, A. Nefedov, C. Wöll, F. Scheiba, H. Ehrenberg, C. Roth, J. Melke, *J. Power Sources* **2016**, *321*, 210.
- [78] C. Gao, N. Wang, S. Peng, S. Liu, Y. Lei, X. Liang, S. Zeng, H. Zi, *Electrochim. Acta* **2013**, *88*, 193.
- [79] H. R. Jiang, W. Shyy, M. C. Wu, R. H. Zhang, T. S. Zhao, *Appl. Energy* **2019**, *233-234*, 105.
- [80] L. Zeng, T. Zhao, L. Wei, *Adv. Sustainable Syst.* **2018**, *2*, 1700148.
- [81] J. Friedl, C. M. Bauer, A. Rinaldi, U. Stimming, *Carbon* **2013**, *63*, 228.
- [82] W. Wang, Z. Wei, W. Su, X. Fan, J. Liu, C. Yan, C. Zeng, *Electrochim. Acta* **2016**, *205*, 102.
- [83] H. Kabir, I. O. Gyan, I. Francis Cheng, *J. Power Sources* **2017**, *342*, 31.
- [84] X. Li, K. Huang, S. Liu, N. TAN, L. Chen, *Trans. Nonferrous Met. Soc. China* **2007**, *17*, 195.
- [85] M. A. Miller, A. Bourke, N. Quill, J. S. Wainright, R. P. Lynch, D. N. Buckley, R. F. Savinell, *J. Electrochem. Soc.* **2016**, *163*, A2095-A2102.
- [86] A. Bourke, M. A. Miller, R. P. Lynch, X. Gao, J. Landon, J. S. Wainright, R. F. Savinell, D. N. Buckley, *J. Electrochem. Soc.* **2016**, *163*, A5097-A5105.
- [87] K. J. Kim, Y.-J. Kim, J.-H. Kim, M.-S. Park, *Mater. Chem. Phys.* **2011**, *131*, 547.
- [88] D. Dixon, D. J. Babu, A. Bhaskar, H.-M. Bruns, J. J. Schneider, F. Scheiba, H. Ehrenberg, *Beilstein J. Nanotechnol.* **2019**, *10*, 1698.
- [89] L. Xue, Y. Li, X. Liu, Q. Liu, J. Shang, H. Duan, L. Dai, J. Shui, *Nat. Commun.* **2018**, *9*, 3819.
- [90] M. S. Dresselhaus, A. Jorio, R. Saito, *Annu. Rev. Condens. Matter Phys.* **2010**, *1*, 89.
- [91] L. G. Cançado, A. Jorio, E. H. M. Ferreira, F. Stavale, C. A. Achete, R. B. Capaz, M. V. O. Moutinho, A. Lombardo, T. S. Kulmala, A. C. Ferrari, *Nano Lett.* **2011**, *11*, 3190.
- [92] F. Tuinstra, J. L. Koenig, *J. Chem. Phys.* **1970**, *53*, 1126.
- [93] R. P. Vidano, D. B. Fischbach, L. J. Willis, T. M. Loehr, *Solid State Commun.* **1981**, *39*, 341.
- [94] M. A. Pimenta, G. Dresselhaus, M. S. Dresselhaus, L. G. Cançado, A. Jorio, R. Saito, *Phys. Chem. Chem. Phys.* **2007**, *9*, 1276.
- [95] A. Eckmann, A. Felten, A. Mishchenko, L. Britnell, R. Krupke, K. S. Novoselov, C. Casiraghi, *Nano Lett.* **2012**, *12*, 3925.
- [96] B. M. Weckhuysen, *Chem. Commun.* **2002**.
- [97] M. A. Bañares, M. O. Guerrero-Pérez, J. L. G. Fierro, G. G. Cortez, *J. Mater. Chem.* **2002**, *12*, 3337.

- [98] V. Calvino-Casilda, M. A. Bañares, in *Catalysis*, Vol. 24 (Eds.: J. J. Spivey, M. Gupta), Royal Society of Chemistry. Cambridge **2012**, p. 1.
- [99] M. O. Guerrero-Pérez, M. A. Bañares, *Catal. Today* **2006**, *113*, 48.
- [100] S. Damyanova, L. M. Gomez, M. A. Bañares, J. L. G. Fierro, *Chem. Mater.* **2000**, *12*, 501.
- [101] I. E. Wachs, C. A. Roberts, *Chem. Soc. Rev.* **2010**, *39*, 5002.
- [102] Z. Q. Li, C. J. Lu, Z. P. Xia, Y. Zhou, Z. Luo, *Carbon* **2007**, *45*, 1686.
- [103] D. S. Sholl, J. A. Steckel, *Density Functional Theory*, John Wiley & Sons, Inc, Hoboken, NJ, USA **2009**.
- [104] K. Honkala, A. Hellman, I. N. Remediakis, A. Logadottir, A. Carlsson, S. Dahl, C. H. Christensen, J. K. Nørskov, *Science* **2005**, *307*, 555.
- [105] R. Schweinfest, A. T. Paxton, M. W. Finnis, *Nature* **2004**, *432*, 1008.
- [106] K. Umemoto, R. M. Wentzcovitch, P. B. Allen, *Science* **2006**, *311*, 983.
- [107] M. Born, R. Oppenheimer, *Ann. Phys.* **1927**, *389*, 457.
- [108] W. Koch, M. C. Holthausen, *A Chemist's Guide to Density Functional Theory*, Wiley **2001**.
- [109] J. Enkovaara, C. Rostgaard, J. J. Mortensen, J. Chen, M. Duřak, L. Ferrighi, J. Gavnholt, C. Glinsvad, V. Haikola, H. A. Hansen, H. H. Kristoffersen, M. Kuisma, A. H. Larsen, L. Lehtovaara, M. Ljungberg, O. Lopez-Acevedo, P. G. Moses, J. Ojanen, T. Olsen, V. Petzold, N. A. Romero, J. Stausholm-Møller, M. Strange, G. A. Tritsarlis, M. Vanin, M. Walter, B. Hammer, H. Häkkinen, G. K. H. Madsen, R. M. Nieminen, J. K. Nørskov, M. Puska, T. T. Rantala, J. Schiøtz, K. S. Thygesen, K. W. Jacobsen, *J. Phys. Condens. Matter* **2010**, *22*, 253202.
- [110] Blöchl, *Phys. Rev. B Condens. Matter.* **1994**, *50*, 17953.
- [111] P. E. Blöchl, C. J. Först, J. Schimpl, *Bull. Mater. Sci.* **2003**, *26*, 33.
- [112] A. Hjorth Larsen, J. Jørgen Mortensen, J. Blomqvist, I. E. Castelli, R. Christensen, M. Duřak, J. Friis, M. N. Groves, B. Hammer, C. Hargus, E. D. Hermes, P. C. Jennings, P. Bjerre Jensen, J. Kermode, J. R. Kitchin, E. Leonhard Kolsbjerg, J. Kubal, K. Kaasbjerg, S. Lysgaard, J. Bergmann Maronsson, T. Maxson, T. Olsen, L. Pastewka, A. Peterson, C. Rostgaard, J. Schiøtz, O. Schütt, M. Strange, K. S. Thygesen, T. Vegge, L. Vilhelmsen, M. Walter, Z. Zeng, K. W. Jacobsen, *J. Phys. Condens. Matter* **2017**, *29*, 273002.
- [113] H. S. Lipson, Stokes A. R., *Proc. R. Soc. Lond. A* **1942**, *181*, 101.
- [114] J. J. Mortensen, K. Kaasbjerg, S. L. Frederiksen, J. K. Nørskov, J. P. Sethna, K. W. Jacobsen, *Phys. Rev. Lett.* **2005**, *95*, 216401.
- [115] Z. González, P. Álvarez, C. Blanco, S. Vega-Díaz, F. Tristán-López, L. P. Rajukumar, R. Cruz-Silva, A. L. Elías, M. Terrones, R. Menéndez, *Sustainable Energy Technol. Assess.* **2015**, *9*, 105.

- [116]W. Li, J. Liu, C. Yan, *Electrochim. Acta* **2012**, *79*, 102.
- [117]L. Dai, Y. Jiang, W. Meng, H. Zhou, L. Wang, Z. He, *Appl. Surf. Sci.* **2017**, *401*, 106.
- [118]Z. He, G. Cheng, Y. Jiang, L. Wang, L. Dai, *J. Electrochem. Soc.* **2018**, *165*, A932-A938.
- [119]R.-H. Huang, C.-H. Sun, T. Tseng, W. Chao, K.-L. Hsueh, F.-S. Shieu, *J. Electrochem. Soc.* **2012**, *159*, A1579-A1586.
- [120]D.-S. Yang, J. Y. Lee, S.-W. Jo, S. J. Yoon, T.-H. Kim, Y. T. Hong, *Int. J. Hydrogen Energy* **2018**, *43*, 1516.
- [121]C. Noh, S. Moon, Y. Chung, Y. Kwon, *J. Mater. Chem. A* **2017**, *5*, 21334.
- [122]O. V. Kharissova, B. I. Kharisov, E. G. de Casas Ortiz, *RSC Adv.* **2013**, *3*, 24812.
- [123]S. Manzetti, J.-C. P. Gabriel, *Int. Nano Lett.* **2019**, *9*, 31.
- [124]E. Ramos, W. A. Pardo, M. Mir, J. Samitier, *Nanotechnology* **2017**, *28*, 135702.
- [125]P. Bilalis, D. Katsigiannopoulos, A. Avgeropoulos, G. Sakellariou, *RSC Adv.* **2014**, *4*, 2911.
- [126]D. Baskaran, J. W. Mays, M. S. Bratcher, *Chem. Mater.* **2005**, *17*, 3389.
- [127]C. Pramanik, J. R. Gissinger, S. Kumar, H. Heinz, *ACS Nano* **2017**, *11*, 12805.
- [128]T. Fujigaya, N. Nakashima, *Sci. Technol. Adv. Mater.* **2015**, *16*, 24802.
- [129]N. Minami, Y. Kim, K. Miyashita, S. Kazaoui, B. Nalini, *Appl. Phys. Lett.* **2006**, *88*, 93123.
- [130]F. Loghin, A. Rivadeneyra, M. Becherer, P. Lugli, M. Bobinger, *Nanomaterials* **2019**, *9*.
- [131]T. Zheng, G. Wang, N. Xu, C. Lu, Y. Qiao, D. Zhang, X. Wang, *Nanomaterials* **2018**, *8*.
- [132]Y.-R. Son, S.-J. Park, *Sci. Rep.* **2018**, *8*, 17601.
- [133]Y. Wang, Y. Liu, K. Wang, S. Song, P. Tsiakaras, H. Liu, *Appl. Catal., B* **2015**, *165*, 360.
- [134]J. Romanos, M. Beckner, T. Rash, L. Firlej, B. Kuchta, P. Yu, G. Suppes, C. Wexler, P. Pfeifer, *Nanotechnology* **2012**, *23*, 15401.
- [135]P. Puech, M. Kandara, G. Paredes, L. Moulin, E. Weiss-Hortala, A. Kundu, N. Ratel-Ramond, J.-M. Plewa, R. Pellenq, M. Monthieux, *C - J. Carbon Res.* **2019**, *5*, 69.
- [136]R. Wang, Y. Li, Y.-L. He, *J. Mater. Chem. A* **2019**, *7*, 10962.
- [137]G. Wang, C. Feng, *Polymers* **2017**, *9*.
- [138]R. Blyth, H. Buqa, F. Netzer, M. Ramsey, J. Besenhard, P. Golob, M. Winter, *Appl. Surf. Sci.* **2000**, *167*, 99.
- [139]F. G. Pacheco, A. A. Cotta, H. F. Gorgulho, A. P. Santos, W. A. Macedo, C. A. Furtado, *Appl. Surf. Sci.* **2015**, *357*, 1015.
- [140]Z. He, L. Liu, C. Gao, Z. Zhou, X. Liang, Y. Lei, Z. He, S. Liu, *RSC Adv.* **2013**, *3*, 19774.
- [141]M. Park, J. Ryu, Y. Kim, J. Cho, *Energy Environ. Sci.* **2014**, *7*, 3727.
- [142]A. Gaunand, F. Coeuret, *Electrochim. Acta* **1978**, *23*, 1197.
- [143]A. Gaunand, D. Hutin, F. Coeuret, *Electrochim. Acta* **1977**, *22*, 93.

- [144] R. Banerjee, N. Bevilacqua, A. Mohseninia, B. Wiedemann, F. Wilhelm, J. Scholta, R. Zeis, *J. Storage Mater.* **2019**, *26*, 100997.
- [145] A. Kossenko, S. Lugovskoy, M. Averbukh, *Materials (Basel, Switzerland)* **2018**, *11*.
- [146] T.-C. Chang, J.-P. Zhang, Y.-K. Fuh, *J. Power Sources* **2014**, *245*, 66.
- [147] J. González-García, P. Bonete, E. Expósito, V. Montiel, A. Aldaz, R. Torregrosa-Maciá, *J. Mater. Chem.* **1999**, *9*, 419.
- [148] L. Gao, H. Lu, H. Lin, X. Sun, J. Xu, D. Liu, Y. Li, *Chem. Res. Chin. Univ.* **2014**, *30*, 441.
- [149] R. J. Rice, R. L. McCreery, *Anal. Chem.* **1989**, *61*, 1637.
- [150] A. Peigney, C. Laurent, E. Flahaut, R. R. Bacsa, A. Rousset, *Carbon* **2001**, *39*, 507.
- [151] M. E. Lee, H.-J. Jin, Y. S. Yun, *RSC Adv.* **2017**, *7*, 43227.
- [152] A. Ganguly, S. Sharma, P. Papakonstantinou, J. Hamilton, *J. Phys. Chem. C* **2011**, *115*, 17009.
- [153] H. R. Thomas, S. P. Day, W. E. Woodruff, C. Vallés, R. J. Young, I. A. Kinloch, G. W. Morley, J. V. Hanna, N. R. Wilson, J. P. Rourke, *Chem. Mater.* **2013**, *25*, 3580.
- [154] H. P. Mungse, O. P. Sharma, H. Sugimura, O. P. Khatri, *RSC Adv.* **2014**, *4*, 22589.
- [155] A. Mezzi, S. Kaciulis, *Surf. Interface Anal.* **2010**, *42*, 1082.
- [156] S. Kaciulis, A. Mezzi, P. Calvani, D. M. Trucchi, *Surf. Interface Anal.* **2014**, *46*, 966.
- [157] A. J. Barlow, S. Popescu, K. Artyushkova, O. Scott, N. Sano, J. Hedley, P. J. Cumpson, *Carbon* **2016**, *107*, 190.
- [158] C.-J. Kim, W. Khan, S.-Y. Park, *Chem. Phys. Lett.* **2011**, *511*, 110.
- [159] O. Akhavan, *Carbon* **2010**, *48*, 509.
- [160] C.-H. Chuang, S. C. Ray, D. Mazumder, S. Sharma, A. Ganguly, P. Papakonstantinou, J.-W. Chiou, H.-M. Tsai, H.-W. Shiu, C.-H. Chen, H.-J. Lin, J. Guo, W.-F. Pong, *Sci. Rep.* **2017**, *7*, 42235.
- [161] L. Tang, X. Li, R. Ji, K. S. Teng, G. Tai, J. Ye, C. Wei, S. P. Lau, *J. Mater. Chem.* **2012**, *22*, 5676.
- [162] C. Hontoria-Lucas, A. J. López-Peinado, J. D. López-González, M. L. Rojas-Cervantes, R. M. Martín-Aranda, *Carbon* **1995**, *33*, 1585.
- [163] C. Mattevi, G. Eda, S. Agnoli, S. Miller, K. A. Mkhoyan, O. Celik, D. Mastrogiovanni, G. Granozzi, E. Garfunkel, M. Chhowalla, *Adv. Funct. Mater.* **2009**, *19*, 2577.
- [164] D. W. Boukhvalov, M. I. Katsnelson, *J. Am. Chem. Soc.* **2008**, *130*, 10697.
- [165] A. Bagri, C. Mattevi, M. Acik, Y. J. Chabal, M. Chhowalla, V. B. Shenoy, *Nat. Chem.* **2010**, *2*, 581.
- [166] L. Chen, Z. Xu, J. Li, B. Zhou, M. Shan, Y. Li, L. Liu, B. Li, J. Niu, *RSC Adv.* **2014**, *4*, 1025.
- [167] S. Park, K.-S. Lee, G. Bozoklu, W. Cai, S. T. Nguyen, R. S. Ruoff, *ACS Nano* **2008**, *2*, 572.

- [168]M. Jin, T. H. Kim, S. C. Lim, D. L. Duong, H. J. Shin, Y. W. Jo, H. K. Jeong, J. Chang, S. Xie, Y. H. Lee, *Adv. Funct. Mater.* **2011**, *21*, 3496.
- [169]F. R. McFeely, S. P. Kowalczyk, L. Ley, R. G. Cavell, R. A. Pollak, D. A. Shirley, *Phys. Rev. B* **1974**, *9*, 5268.
- [170]M. K. Rabchinskii, S. A. Ryzhkov, D. A. Kirilenko, N. V. Ulin, M. V. Baidakova, V. V. Shnitov, S. I. Pavlov, R. G. Chumakov, D. Y. Stolyarova, N. A. Besedina, A. V. Shvidchenko, D. V. Potorochin, F. Roth, D. A. Smirnov, M. V. Gudkov, M. Brzhezinskaya, O. I. Lebedev, V. P. Melnikov, P. N. Brunkov, *Sci. Rep.* **2020**, *10*, 6902.
- [171]K. Endo, S. Koizumi, T. Otsuka, T. Ida, T. Morohashi, J. Onoe, A. Nakao, E. Z. Kurmaev, A. Moewes, D. P. Chong, *J. Phys. Chem. A* **2003**, *107*, 9403.
- [172]H. K. Jeong, C. Yang, B. S. Kim, K. Kim, *EPL* **2010**, *92*, 37005.
- [173]S. Stankovich, D. A. Dikin, R. D. Piner, K. A. Kohlhaas, A. Kleinhammes, Y. Jia, Y. Wu, S. T. Nguyen, R. S. Ruoff, *Carbon* **2007**, *45*, 1558.
- [174]Z. Fan, K. Wang, T. Wei, J. Yan, L. Song, B. Shao, *Carbon* **2010**, *48*, 1686.
- [175]D. Tashima, E. Yamamoto, N. Kai, D. Fujikawa, G. Sakai, M. Otsubo, T. Kijima, *Carbon* **2011**, *49*, 4848.
- [176]X. You, M. Misra, S. Gregori, A. K. Mohanty, *ACS Sustainable Chem. Eng.* **2018**, *6*, 318.
- [177]Y.-T. Kim, Y. Ito, K. Tadai, T. Mitani, U.-S. Kim, H.-S. Kim, B.-W. Cho, *Appl. Phys. Lett.* **2005**, *87*, 234106.
- [178]M. J. Bleda-Martínez, J. A. Maciá-Agulló, D. Lozano-Castelló, E. Morallón, D. Cazorla-Amorós, A. Linares-Solano, *Carbon* **2005**, *43*, 2677.
- [179]Z. Li, H. Peng, R. Liu, Y. Mo, B. Cao, W. Lai, X. Li, L. Pan, Y. Chen, *J. Power Sources* **2020**, *457*, 228022.
- [180]H. Radinger, J. Pfisterer, F. Scheiba, H. Ehrenberg, *ChemElectroChem* **2020**, *7*, 4745.
- [181]Z. Yang, S. Bhowmick, F. G. Sen, A. Banerji, A. T. Alpas, *Sci. Rep.* **2018**, *8*, 121.
- [182]L. Jiang, J. Wang, P. Liu, W. Song, B. He, *RSC Adv.* **2018**, *8*, 11216.
- [183]P. Restuccia, M. Ferrario, M. C. Righi, *Carbon* **2020**, *156*, 93.
- [184]G. Levita, P. Restuccia, M. C. Righi, *Carbon* **2016**, *107*, 878.
- [185]S. Seiler, C. E. Halbig, F. Grote, P. Rietsch, F. Börrnert, U. Kaiser, B. Meyer, S. Eigler, *Nat. Commun.* **2018**, *9*, 836.
- [186]S. Wang, C. Wang, X. Ji, *RSC Adv.* **2017**, *7*, 52252.
- [187]Y. Liang, Z. Tao, J. Chen, *Adv. Energy Mater.* **2012**, *2*, 742.
- [188]Z. Song, H. Zhou, *Energy Environ. Sci.* **2013**, *6*, 2280.

- [189] S. Bandyopadhyay, C. Singh, P. Jash, M. W. Hussain, A. Paul, A. Patra, *Chem. Commun.* **2018**, *54*, 6796.
- [190] N. Lalaoui, P. Rousselot-Pailley, V. Robert, Y. Mekmouche, R. Villalonga, M. Holzinger, S. Cosnier, T. Tron, A. Le Goff, *ACS Catal.* **2016**, *6*, 1894.
- [191] B. R. Lydon, A. Germann, J. Y. Yang, *Inorg. Chem. Front.* **2016**, *3*, 836.
- [192] Y. Zhang, C. Liu, W. Shi, Z. Wang, L. Dai, X. Zhang, *Langmuir* **2007**, *23*, 7911.
- [193] K. C. Etika, F. D. Jochum, P. Theato, J. C. Grunlan, *J. Am. Chem. Soc.* **2009**, *131*, 13598.
- [194] K. C. Etika, F. D. Jochum, M. A. Cox, P. Schattling, P. Theato, J. C. Grunlan, *Macromolecules* **2010**, *43*, 9447.
- [195] J. Liu, R. Wang, L. Cui, J. Tang, Z. Liu, Q. Kong, W. Yang, J. Gooding, *J. Phys. Chem. C* **2012**, *116*, 17939.
- [196] J. Luan, A. Zhang, Y. Zheng, L. Sun, *Composites, Part A* **2012**, *43*, 1032.
- [197] J. C. Bachman, R. Kaviani, D. J. Graham, D. Y. Kim, S. Noda, D. G. Nocera, Y. Shao-Horn, S. W. Lee, *Nat. Commun.* **2015**, *6*, 7040.
- [198] B. Anothumakkool, P.-L. Taberna, B. Daffos, P. Simon, Y. Sayed-Ahmad-Baraza, C. Ewels, T. Brousse, J. Gaubicher, *J. Mater. Chem. A* **2017**, *5*, 1488.
- [199] S. Ghosh, X. An, R. Shah, D. Rawat, B. Dave, S. Kar, S. Talapatra, *J. Phys. Chem. C* **2012**, *116*, 20688.
- [200] H. Radinger, A. Ghamlouche, H. Ehrenberg, F. Scheiba, *J. Mater. Chem. A* **2021**, *9*, 18280.
- [201] L. Eifert, Z. Jusys, R. Banerjee, R. J. Behm, R. Zeis, *ACS Appl. Energy Mater.* **2018**, *1*, 6714.
- [202] L. Eifert, Z. Jusys, R. J. Behm, R. Zeis, *Carbon* **2020**, *158*, 580.
- [203] X. Gu, S. Tian, Q. Zhou, J. Adkins, Z. Gu, X. Li, J. Zheng, *RSC Adv.* **2013**, *3*, 25989.
- [204] A. Xu, L. Shi, L. Zeng, T. S. Zhao, *Electrochim. Acta* **2019**, *300*, 389.
- [205] H. R. Jiang, W. Shyy, L. Zeng, R. H. Zhang, T. S. Zhao, *J. Mater. Chem. A* **2018**, *6*, 13244.
- [206] R. Wang, Y. Li, Y. Wang, Z. Fang, *Appl. Energy* **2020**, *261*, 114369.
- [207] S. Park, H. Kim, *J. Mater. Chem. A* **2015**, *3*, 12276.
- [208] V. Pasala, J. N. Ramavath, C. He, V. K. Ramani, K. Ramanujam, *ChemistrySelect* **2018**, *3*, 8678.
- [209] L. Wang, Z. Sofer, M. Pumera, *ACS Nano* **2020**, *14*, 21.
- [210] K. J. Kim, H. S. Lee, J. Kim, M.-S. Park, J. H. Kim, Y.-J. Kim, M. Skyllas-Kazacos, *ChemSusChem* **2016**, *9*, 1329.
- [211] F. Niu, L.-M. Tao, Y.-C. Deng, Q.-H. Wang, W.-G. Song, *New J. Chem.* **2014**, *38*, 2269.
- [212] T. H. Lim, S. Y. Yeo, *Sci. Rep.* **2017**, *7*, 4733.
- [213] W. Cheng, X. Liu, N. Li, J. Han, S. Li, S. Yu, *RSC Adv.* **2018**, *8*, 11222.

- [214]N. Sreekanth, M. A. Nazrulla, T. V. Vineesh, K. Sailaja, K. L. Phani, *Chem. Commun.* **2015**, 51, 16061.
- [215]R. E. Smith, T. J. Davies, N. d. B. Baynes, R. J. Nichols, *J. Electroanal. Chem.* **2015**, 747, 29.
- [216]D. S. Aaron, Q. Liu, Z. Tang, G. M. Grim, A. B. Papandrew, A. Turhan, T. A. Zawodzinski, M. M. Mench, *J. Power Sources* **2012**, 206, 450.
- [217]M.-A. Goulet, M. Eikerling, E. Kjeang, *Electrochem. Commun.* **2015**, 57, 14.
- [218]M. R. Ammar, N. Galy, J. N. Rouzaud, N. Toulhoat, C. E. Vaudey, P. Simon, N. Moncoffre, *Carbon* **2015**, 95, 364.
- [219]B. Lesiak, L. Kövér, J. Tóth, J. Zemek, P. Jiricek, A. Kromka, N. Rangam, *Applied Surface Science* **2018**, 452, 223.
- [220]W. S. Werner, A. Bellissimo, R. Leber, A. Ashraf, S. Segui, *Surf. Sci.* **2015**, 635, L1-L3.
- [221]K. Ganesan, S. Ghosh, N. Gopala Krishna, S. Ilango, M. Kamruddin, A. K. Tyagi, *Phys. Chem. Chem. Phys.* **2016**, 18, 22160.
- [222]S. Fujii, M. Ziatdinov, M. Ohtsuka, K. Kusakabe, M. Kiguchi, T. Enoki, *Faraday Discuss.* **2014**, 173, 173.
- [223]S. Fujii, T. Enoki, *Acc. Chem. Res.* **2013**, 46, 2202.
- [224]Y.-W. Son, M. L. Cohen, S. G. Louie, *Phys. Rev. Lett.* **2006**, 97, 216803.
- [225]V. Barone, O. Hod, G. E. Scuseria, *Nano Lett.* **2006**, 6, 2748.
- [226]Nakada, Fujita, Dresselhaus, *Phys. Rev. B Condens. Matter.* **1996**, 54, 17954.
- [227]M. Meskinfam Langroudi, C. S. Pomelli, R. Giglioli, C. Chiappe, M. Aysla Costa de Oliveira, B. Mecheri, S. Licoccia, A. D'Epifanio, *J. Power Sources* **2019**, 420, 134.
- [228]Z. Jiang, K. Klyukin, V. Alexandrov, *J. Chem. Phys.* **2016**, 145, 114303.
- [229]F. Sepehr, S. J. Paddison, *Chem. Phys. Lett.* **2013**, 585, 53.
- [230]F. A. Cotton, L. R. Falvello, R. Llusar, E. Libby, C. A. Murillo, W. Schwotzer, *Inorg. Chem.* **1986**, 25, 3423.
- [231]J. Krakowiak, D. Lundberg, I. Persson, *Inorganic Chemistry* **2012**, 51, 9598.
- [232]J. Selbin, *Coordination Chemistry Reviews* **1966**, 1, 293.
- [233]C. J. Ballhausen, B. F. Djurinskij, K. J. Watson, *J. Am. Chem. Soc.* **1968**, 90, 3305.
- [234]F. Sepehr, S. J. Paddison, *J. Phys. Chem. A* **2015**, 119, 5749.
- [235]M. Bühl, M. Parrinello, *Chem. Eur. J.* **2001**, 7, 4487.
- [236]J. Krakowiak, D. Lundberg, I. Persson, *Inorg. Chem.* **2012**, 51, 9598.
- [237]J. H. Warner, G.-D. Lee, K. He, A. W. Robertson, E. Yoon, A. I. Kirkland, *ACS Nano* **2013**, 7, 9860.
- [238]I. Kroner, M. Becker, T. Turek, *ChemElectroChem* **2020**, 7, 4314.

- [239]H. Radinger, P. Connor, R. Stark, W. Jaegermann, B. Kaiser, *ChemCatChem* **2021**, *13*, 1175.
- [240]H. Radinger, P. Connor, S. Tengeler, R. W. Stark, W. Jaegermann, B. Kaiser, *Chem. Mater.* **2021**, *33*, 8259.
- [241]M. Inaba, H. Yoshida, Z. Ogumi, *J. Electrochem. Soc.* **1996**, *143*, 2572.
- [242]M. Anji Reddy, M. Helen, A. Groß, M. Fichtner, H. Euchner, *ACS Energy Lett.* **2018**, *3*, 2851.
- [243]I. Oda, H. Ogasawara, M. Ito, *Langmuir* **1996**, *12*, 1094.
- [244]B. D. Smith, D. E. Irish, P. Kedzierzawski, J. Augustynski, *J. Electrochem. Soc.* **1997**, *144*, 4288.
- [245]N. A. Gvozdik, K. J. Stevenson, *Electrochim. Acta* **2021**, *383*, 138300.
- [246]R. A. Cox, Ü. L. Haldna, K. L. Idler, K. Yates, *Can. J. Chem.* **1981**, *59*, 2591.
- [247]K. Tomikawa, H. Kanno, *J. Phys. Chem. A* **1998**, *102*, 6082.
- [248]O. R. Hunt, A. D. Ward, M. D. King, *RSC Adv.* **2013**, *3*, 19448.
- [249]G. T. Stranford, R. A. Condrate, *J. Solid State Chem.* **1985**, *56*, 394.
- [250]N. Kausar, R. Howe, M. Skyllas - Kazacos, *J. Appl. Electrochem.* **2001**, *31*, 1327.
- [251]K. Kanamori, Y. Ookubo, K. Ino, K. Kawai, H. Michibata, *Inorg. Chem.* **1991**, *30*, 3832.
- [252]M. B. Smirnov, E. M. Roginskii, K. S. Smirnov, R. Baddour-Hadjean, J.-P. Pereira-Ramos, *Inorg. Chem.* **2018**, *57*, 9190.
- [253]C. Madic, G. M. Begun, R. L. Hahn, J. P. Launay, W. E. Thiessen, *Inorg. Chem.* **1984**, *23*, 469.
- [254]C. Sun, K. Vezzù, G. Pagot, A. Nale, Y. H. Bang, G. Pace, E. Negro, C. Gambaro, L. Meda, T. A. Zawodzinski, V. Di Noto, *Electrochim. Acta* **2019**, *318*, 913.
- [255]J. Kim, N. Lee, Y. H. Min, S. Noh, N.-K. Kim, S. Jung, M. Joo, Y. Yamada, *ACS Omega* **2018**, *3*, 17789.
- [256]H. Radinger, V. Trouillet, F. Bauer, F. Scheiba, *ACS Catal.* **2022**, *12*, 6007.
- [257]P. Shvets, O. Dikaya, K. Maksimova, A. Goikhman, *J. Raman Spectrosc.* **2019**, *50*, 1226.
- [258]R. Baddour-Hadjean, M. B. Smirnov, K. S. Smirnov, V. Y. Kazimirov, J. M. Gallardo-Amores, U. Amador, M. E. Arroyo-de Dompablo, J. P. Pereira-Ramos, *Inorg. Chem.* **2012**, *51*, 3194.
- [259]Z. Bo, S. Qing, H. De-Yan, *Chin. Phys. B* **2009**, *18*, 4988.
- [260]R. Baddour-Hadjean, M. B. Smirnov, V. Y. Kazimirov, K. S. Smirnov, J.-P. Pereira-Ramos, *J. Raman Spectrosc.* **2015**, *46*, 406.

- [261]Q. Hao, S. M. Morton, B. Wang, Y. Zhao, L. Jensen, T. Jun Huang, *Appl. Phys. Lett.* **2013**, *102*, 11102.
- [262]S. Lee, M. Kim, S.-Y. Cho, D.-J. Lee, H.-M. Kim, K.-B. Kim, *Nanotechnology* **2020**, *31*, 95708.
- [263]S. S. Nanda, M. J. Kim, K. S. Yeom, S. S. A. An, H. Ju, D. K. Yi, *TrAC, Trends Anal. Chem.* **2016**, *80*, 125.
- [264]M. Inaba, H. Yoshida, Z. Ogumi, T. Abe, Y. Mizutani, M. Asano, *J. Electrochem. Soc.* **1995**, *142*, 20.
- [265]V. A. Sethuraman, L. J. Hardwick, V. Srinivasan, R. Kostecki, *J. Power Sources* **2010**, *195*, 3655.
- [266]S. Jovanovic, P. Jakes, S. Merz, R.-A. Eichel, J. Granwehr, *Electrochem. Sci. Adv.* **2021**.
- [267]A. Moissette, A. Burneau, J. Dubessy, H. Fuzellier, M. Lelaurain, *Carbon* **1995**, *33*, 1223.
- [268]D. Zhang, A. Forner-Cuenca, O. O. Taiwo, V. Yufit, F. R. Brushett, N. P. Brandon, S. Gu, Q. Cai, *J. Power Sources* **2020**, *447*, 227249.
- [269]K. V. Greco, J. K. Bonesteel, N. Chanut, C. Tai-Chieh Wan, Y.-M. Chiang, F. R. Brushett, *ACS Appl. Energy Mater.* **2021**, *4*, 13516.
- [270]J. Wordsworth, T. M. Benedetti, A. Alinezhad, R. D. Tilley, M. A. Edwards, W. Schuhmann, J. J. Gooding, *Chem. Sci.* **2019**, *11*, 1233.
- [271]C. Andronesco, J. Masa, R. D. Tilley, J. J. Gooding, W. Schuhmann, *Curr. Opin. Electrochem.* **2021**, *25*, 100644.
- [272]H. Radinger, M. Hartmann, M. Ast, J. Pfisterer, M. Bron, H. Ehrenberg, F. Scheiba, *Electrochim. Acta* **2022**, *409*, 139971.
- [273]G. W. Hinman, A. Haubold, J. O. Gardner, J. K. Layton, *Carbon* **1970**, *8*, 341.
- [274]E. Bourelle, H. Konno, M. Inagaki, *Carbon* **1999**, *37*, 2041.
- [275]L. Dong, F. Hou, X. Zhong, R. Wang, J. Chen, L. Wang, *Composites, Part A* **2013**, *55*, 74.
- [276]G. Lou, Y. Wu, X. Zhu, Y. Lu, S. Yu, C. Yang, H. Chen, C. Guan, L. Li, Z. Shen, *ACS Appl. Mater. Interfaces* **2018**, *10*, 42503.
- [277]P. Barathi, A. S. Kumar, *Langmuir* **2013**, *29*, 10617.
- [278]A. R. MacIntosh, G. Jiang, P. Zamani, Z. Song, A. Riese, K. J. Harris, X. Fu, Z. Chen, X. Sun, G. R. Goward, *J. Phys. Chem. C* **2018**, *122*, 6593.
- [279]L. Jia, Y. Chen, S. Lei, S. Mo, Z. Liu, X. Shao, *Energy Procedia* **2014**, *61*, 1348.
- [280]B. B. Berkes, A. Jozwiuk, H. Sommer, T. Brezesinski, J. Janek, *Electrochem. Commun.* **2015**, *60*, 64.
- [281]B. B. Berkes, A. Jozwiuk, M. Vračar, H. Sommer, T. Brezesinski, J. Janek, *Anal. Chem.* **2015**, *87*, 5878.

- [282]W. Li, Z. Zhang, Y. Tang, H. Bian, T.-W. Ng, W. Zhang, C.-S. Lee, *Adv. Sci.* **2016**, *3*, 1500276.
- [283]P. Han, H. Wang, Z. Liu, X. Chen, W. Ma, J. Yao, Y. Zhu, G. Cui, *Carbon* **2011**, *49*, 693.
- [284]J. F. Moulder, J. Chastain (Eds.), *Handbook of X-ray photoelectron spectroscopy: A reference book of standard spectra for identification and interpretation of XPS data*, Perkin-Elmer Corporation, Eden Prairie, Minn. **1992**.

List of Abbreviations

BET	Brunauer–Emmett–Teller
CC	Carbon Cloth
CF	Carbon Felt
CMC	Carboxymethyl Cellulose
CP	Carbon Paper
CV	Cyclic Voltammetry
DEMS	Differential Electrochemical Mass Spectrometry
DFT	Density Functional Theory
DMSO	Dimethyl Sulfoxide
DOS	Density of States
EDLC	Electrical Double Layer Capacitance
EIS	Electrochemical Impedance Spectroscopy
FWHM	Full Width at Half Maximum
GC	Glassy Carbon
GF	Graphite Felt
HOPG	Highly Ordered Pyrolytic Carbon
IPA	Isopropyl Alcohol
MWCNT	Multi-Walled Carbon Nanotube
OFG	Oxygen Functional Group
PAH	Polycyclic Aromatic Hydrocarbon
PAN	Polyacrylonitrile
PDOS	Projected Density of States
REELS	Reflection Electron Energy Loss Spectroscopy
SEM	Scanning Electron Microscopy
SHE	Standard Hydrogen Electrode
UPS	UV Photoelectron Spectroscopy
VB	Valence Band
WF	Work Function
XPS	X-ray Photoelectron Spectroscopy
XRD	X-ray Diffraction

List of Symbols

a_{Ox}	Activity of oxidized species	α	Charge transfer coefficient
a_{Red}	Activity of reduced species	ΔE_p	Peak potential separation
d	Distance of lattice planes	η	Overpotential
E^0	Standard redox potential	λ	Wavelength
E_{Bin}	Binding energy	ν	Frequency
E_{F}	Fermi level energy	ν_{as}	Asymmetric stretching mode
E_{Kin}	Kinetic energy	ν_{s}	Symmetric stretching mode
E_{redox}	Redox potential	Φ	Work function
E_{Vac}	Vacuum level energy	Ψ	Wavefunction
E_{VBM}	Valence band maximum energy		
F	Faraday constant		
G	Gibb's energy		
h	Planck constant		
$I(\text{D})$	D band intensity		
$I(\text{D}')$	D' band intensity		
$I(\text{G})$	G band intensity		
i_p	Peak current		
iR	Internal resistance		
j	Current density		
j_0	Exchange current density		
n	Number of electrons		
R_{CT}	Charge Transfer Resistance		
T	Temperature		
V	Potential energy		
V_{H}	Hartree potential		
V_{XC}	Exchange correlation potential		

Appendix A: Experimental Details

Sample Preparation

In general: Sheets of PAN-based pristine GF (GFD 4.6, SGL Carbon) or thermally activated GF-TA, respectively, were cut out of A4 sheets and cleaned by sonication in acetone and ultrapure water (Milli-Q, $18.2 \text{ M}\Omega \text{ cm}^{-1}$) for 10 min each, followed by drying at $80 \text{ }^\circ\text{C}$ overnight.

Prior to electrochemical half-cell measurements, GF was centrifuged for 5 min at 800 rpm in the corresponding electrolyte. As positive electrolyte, $0.1 \text{ M V}^{\text{IV}}\text{O}_2^+$ was prepared by dissolving VO_2SO_4 powder (Alfa Aesar) in $2 \text{ M H}_2\text{SO}_4$ (Emsure). To obtain the negative electrolyte, the positive half-cell electrolyte was reduced in a single cell assembly (MicroFlow cell, ElectroCell). It was added to both half-cell tanks, pumped through the single cell in a circuit, and charged at 1.6 V . The $\text{V}^{\text{IV}}\text{O}_2^+$ is thus oxidized to $\text{V}^{\text{VO}_2^+}$ on one side and reduced to V^{III} on the other. At a termination current of 5 mA cm^{-2} , it was assumed that all the vanadium on the negative side was reduced to V^{III} .

Chapter 4: Multi-walled carbon nanotube (MWCNT) dispersions were prepared by dissolving 1 mg mL^{-1} CMC in Milli-Q and adding 2 mg mL^{-1} MWCNTs (Baytubes, BAYER) in a 180 min sonication process. Alkaline etching solutions were prepared by dissolving KOH (Emplura) in Milli-Q. For a combined process, the MWCNT dispersion was mixed with 8 M KOH in equal parts. To prepare the desired sample, pieces of GF were immersed in the different solution or dispersion, followed by a vacuum treatment to ensure thorough wetting. A freeze-drying step was incorporated to improve the distribution of MWCNTs and the KOH activating agent on the felt.^[275,276] The wet samples were transferred to a freeze-dryer (LyoQuest -85, Telstar), frozen at $-85 \text{ }^\circ\text{C}$ for 24 h, followed by drying for at least 48 h. The dry samples were heated in a batch type furnace in Ar atmosphere, by ramping with 3 K min^{-1} to $800 \text{ }^\circ\text{C}$ for 1 h. Afterwards, the samples were cleaned with diluted H_2SO_4 and Milli-Q and dried again over night at $80 \text{ }^\circ\text{C}$.

Chapter 5: Sheets of GF and GF-TA (=GF-SA) were heated in a gas tight sealed quartz glass tube with $5 \text{ }^\circ\text{C h}^{-1}$ to the desired temperature ($500, 800, 900, \text{ and } 980 \text{ }^\circ\text{C}$) for 3 h under Ar/ H_2 atmosphere. The samples were consequently labelled with the corresponding deoxygenation temperature in addition to the kind of felt electrode. After thermal deoxygenation, the gas inlet and outlet of the glass tube were sealed to transfer the samples under inert atmosphere to an Ar-filled glove box. Therein, the felts were prepared for further examination. The use of the

hydrogen saturation to prevent spontaneous re-oxygenation has been tested by performing XPS to the samples deoxygenated at 980 °C, after they were in contact with air for 5 min (Figure S32). Both kind of felts (GF-980 and GF-SA-980) showed minor to no increase of surface oxygen species.

Chapter 6: Pyrene-modified GF has been prepared by a dipping procedure: cleaned GF and deoxygenated GF-980 were immersed in a solution containing 5 mM of the corresponding pyrene derivative (all Sigma-Aldrich), pyrene (purity = 98%), 1-Hydroxypyrene (98%), 1-Pyrenemethanol (97%), 1-Pyrenecarboxylic acid (97%), 1-Pyrenebutyric acid (97%), and 1-Acetylpyrene (97%) dissolved in DMSO (Emsure, 99.7%). After 24 h, the felts were thoroughly washed with Milli-Q and dried at 80 °C. GF-PYR=O was synthesized by an electrochemical procedure published elsewhere for pyrene-functionalized MWCNTs.^[277] Briefly, GF-PYR was subjected to an applied potential of 1.0 V vs. Ag/AgCl in a pH 7 phosphate buffer solution.

Chapter 7: To prepare graphene containing dispersions, 4 mg of pristine graphene (Dasheng graphene Co. Ltd., China), graphene treated at 3000 °C (G3000, Dasheng graphene Co. Ltd., China), boron and phosphorus-doped graphene powders (BG and PG-1, Sigma-Aldrich) were dispersed, respectively, in 990 μ L Milli-Q and 10 μ L Nafion (5 wt%, Sigma-Aldrich) under ultrasonication for 90 min. 10 μ L of the obtained homogeneous dispersion were drop coated with an Eppendorf pipette onto GC electrodes (ALS Co., Ltd.). Prior, GC was polished with Al suspension (0.05 μ m, MasterPrep, Buehler) on a polishing pad to mirror finish, and cleaned in acetone and Milli-Q under ultrasound. The coated electrodes were dried in ambient for at least 1 h, rinsed with Milli-Q to remove residuals, and dried under N₂ afterwards.

Phosphorus-doped graphene (PG-2) was synthesized based on a method published elsewhere.^[278] Briefly, 30 mg G3000 were dispersed in a solution containing 50 mL IPA and 150 mg triphenylphosphine (TPP, Sigma-Aldrich) for 2 h under ultrasound. The solvent was evaporated on a hot plate. The residual powder was homogenized in a mortar and heated in an Al₂O₃ crucible with a ramp of 5 °C min⁻¹ to 1000 °C for 90 min under Ar atmosphere. After washing and drying, the final PG-2 was obtained.

To prepare graphene-modified electrodes, CMC was dissolved in Milli-Q to a concentration of 1 mg mL⁻¹, and subsequently, 2 mg mL⁻¹ graphene was added. The dispersion was ultrasonicated for 180 min to distribute the material homogeneously and durably.^[279] The cleaned GF was dipped in the solution, thoroughly wetted by applying vacuum to the vessels, ultrasonicated for 20 min, reversed, and ultrasonicated again for the same time. Afterwards, the samples

were frozen overnight at $-85\text{ }^{\circ}\text{C}$ and then freeze-dried for 48 h. The samples were subsequently heat-treated under Ar atmosphere at $800\text{ }^{\circ}\text{C}$ for 3 h to carbonize the binder.

The directly modified GF was fabricated by soaking the pristine felt with a TPP containing DMSO solution (12.5 , 25 , and 50 mg mL^{-1}). The wet sample underwent the same freeze-drying process as described above and was subsequently heat-treated at 200 to $1000\text{ }^{\circ}\text{C}$ under Ar, either in an autoclave, in an open system, or in a closed graphite crucible with small holes.

Chapter 8: G3000 was used as a substrate to prepare model catalysts with armchair and zigzag edge sites. PAHs (phenanthrene, anthracene, chrysene, and tetracene; all with a purity $\geq 99\%$) were obtained from Sigma Aldrich and used according to literature.^[40] PAHs and graphene were dispersed in DMSO under ultrasound and stirred overnight. The product was filtered, washed with Milli-Q several times to remove excess PAHs and DMSO, and dried at $80\text{ }^{\circ}\text{C}$. To form a dispersion for electrochemical measurements, 4 mg of the product were dispersed in a mixture of $390\text{ }\mu\text{L}$ IPA and $10\text{ }\mu\text{L}$ Nafion solution.

Chapter 10: Raman spectra of the electrolytes were measured by placing a drop of the solution ($2\text{ M H}_2\text{SO}_4$, 1 M VO^{2+} in $0.1\text{ M H}_2\text{SO}_4$, sat. VO^{2+} in $2\text{ M H}_2\text{SO}_4$) on a microscope slide. Wet GF was placed on a gold coin as current collector and assembled into the cell. HOPG ($5\times 5\text{ mm}$) was cleaved with a tape prior to characterization to receive a fresh basal plane. A blade was used to scratch the surface of HOPG to produce kinks and edges (Figure S55). To guarantee wetting of these defects, electrolyte was dropped onto HOPG and pressed into the channels with a glass plate before the sample was assembled. Carbon dispersions were evaluated by dropping them onto gold coins using a spin coater. $10\text{ }\mu\text{L}$ of the dispersion were drop-wise added onto the rotating disk before it was dried for several hours at room temperature.

Analytical Methods

Cyclic voltammetry (CV) of GF was measured with a BioLogic VSP potentiostat, using Ag/AgCl in 3 M KCl ($E_{\text{Ag/AgCl}} = 0.210\text{ V vs. RHE}$) as reference electrode, in the custom-built cell described in Chapter 3. The electrolyte filled half-cell has been bubbled with Ar prior to, and the surface above the electrolyte during the experiments. An electrochemical surface conditioning step was performed to remove loose adsorbates on the surface of GF by scanning $20\times$ either from 0 to -0.3 V (negative) or from 0 to 0.5 V vs. Ag/AgCl (positive half-cell) with 100 mV s^{-1} . The CV data has been iR -corrected regarding the electrolyte resistance, which was assessed by EIS at the OCP.

A three-electrode glass cell was used to measure powders drop-casted on GC electrodes. The sample served as the working, a graphite rod (redox.me) as the counter, and Ag/AgCl as the reference electrode. Before the electrochemical testing, the electrolyte was deaerated with Ar.

The CV curves in Chapter 10 were collected using another custom-built sample holder from the Martin Luther University Halle-Wittenberg, allowing larger sample sizes to be investigated.

Electrochemical impedance spectroscopy (EIS) was recorded with a voltage amplitude of 10 mV at an applied potential of 0.9 V and -0.45 V vs. Ag/AgCl. The spectra were fitted with the RelaxIS 3 software (rhd instruments), usually using the equivalent circuit diagram displayed in Figure S25.

Electrical double layer capacitance (EDLC) measurements were conducted in a (usually) non-faradaic potential window of 0.15 to 0.25 V vs. Ag/AgCl. The potential was kept at 0.2 V vs. Ag/AgCl for 2 min, before the range was scanned 10× with scan rates of 10 to 250 mV s⁻¹. The current at 0.2 V vs. Ag/AgCl was used in a current vs. scan rate plot to assess the EDLC using the slope of the linear relationship between both factors.

Raman spectroscopy was performed on a LabRAM HR Evolution spectrometer (HORIBA Scientific) equipped with a HeNe (632.8 nm, $E_{\text{laser}} = 1.99$ eV) and a 532 nm Nd:YAG laser ($E_{\text{laser}} = 2.33$ eV), further using a 600 g mm⁻¹ grating and a 50× or 100× magnification objective. On each sample, several spectra were taken on random positions to obtain a standard deviation value. By using a smaller magnifying lens, the deviation of the intensity ratios could be reduced. However, the signal intensity in general is lower and thus more difficult to analyze because thereby the part of light scattered from basal planes is increased while the resolution and intensity from edge sites is decreased. For deconvolution, the spectra were subtracted by a spline background (BG), normalized to the highest signal and deconvoluted with absolute Lorentzian (D, G, D') and Gaussian-Lorentzian (D* and D'') peak shapes using the CasaXPS software.

Operando Raman spectroscopy was carried out using a commercial Raman cell (TSC Raman, rhd instruments). A gold-coated copper ring is used as counter, Ag/AgCl (3 M KOH) as reference electrode. As electrolyte, 1 M VO²⁺ in 0.1 M H₂SO₄ was used if not noted otherwise. At the start of a measurement, several points on the sample were tested regarding the signal intensity ratio between carbon (D, G) and electrolyte-related signals to find the optimum height and focus on the electrode–electrolyte interface. Subsequently, a potential of 0 V vs. Ag/AgCl is applied for about 10 min. Afterwards, the potential is usually increased from 0.8 to 1.4 V vs. Ag/AgCl in

steps of 0.1 V. At each potential, a Raman spectrum is acquired after the current response equalized.

Field-emission scanning electron microscopy (FE-SEM) was performed using a Carl Zeiss Merlin microscope at acceleration voltages of 5 to 15 kV and a probe current of 150 to 500 pA.

X-ray diffraction (XRD) patterns were measured using a STOE STADI P powder diffractometer with monochromatic Cu-K α radiation ($\lambda = 1.54056 \text{ \AA}$) in transmission geometry.

X-ray photoelectron spectroscopy (XPS) was performed using a K-alpha+ and an Escalab spectrometer (Thermo Fisher Scientific) with monochromatic Al-K α radiation ($E = 1486.6 \text{ eV}$) at a spot size of ~ 400 and $600 \text{ }\mu\text{m}$, respectively. Survey spectra were recorded with a pass energy of 200 eV, detail spectra with 50 eV. The Thermo Avantage software was used for data acquisition and spectral deconvolution, determining a Shirley BG with the implemented smart BG function. The asymmetry of sp^2 hybridized graphitic carbon was evaluated with a tail mix of 80 to 90% and a tail exponent of 0.03 to 0.1, considering a smaller FWHM of 0.8 to 0.9 eV. All other components were fitted using conventional Voigt peak profiles (70 to 30% Gaussian-Lorentzian) with FWHM values up to 1.8 eV, restricting the position regarding the sp^2 signal and the relative FWHM to sp^3 carbon.

The concentration of oxygen was analyzed by quantifying all O 1s and C 1s components present on the surface of a sample. For the investigation of the D-parameter, the C KLL Auger region was scanned $100\times$ with a pass energy of 100 eV and a step size of 0.5 eV. The D-parameter can be determined by the binding energy distance between the maximum and minimum in the first-derivative plot of the obtained spectrum. The VB region was studied with a pass energy of 50 eV at a step size of 0.2 eV. The E_{VBM} was assessed by the intercept of two straight lines: one horizontal at the baseline, and one diagonal along the threshold-edge of the VB spectra up to $\sim 10 \text{ eV}$. Both the Auger and the VB region were normalized to the maximum signal to enhance the comparability.

For **UV photoelectron spectroscopy (UPS)**, a helium gas discharge lamp ($E = 21.22 \text{ eV}$) was used to generating photoelectrons in the VB with high resolution. Spectra were recorded with a pass energy of 2 eV and a step size of 0.1 eV. To determine the WF, a bias voltage of 4 to 6 V was applied. By fitting the threshold close to E_{F} and the cutoff energy, the E_{VBM} and the WF were determined, respectively.

Reflection electron energy loss spectroscopy (REELS) was measured using monoenergetic electrons ($E = 1$ keV), scanning the elastic and the inelastic peaks with a pass energy of 5 and 10 eV, respectively, at a step size of 0.02 eV. To compare the pattern of multiple samples, the inelastic signals were normalized to the intensity of the corresponding elastic peak.

For the investigation of the **electrical conductivity under compression**, a uniaxial compression device (zwickiLine, Zwick/Roell) with a 100 N load cell was used. The thickness at no compression of GF was calculated by the distance of the compression tools at 0.1 N. By knowing the thickness at a given force, the compression is derived. The test machine was coupled with a custom-built cell described in Chapter 3 to measure the electrical conductivity. Gold coated copper pins connected to a potentiostat (BioLogic SP-300) were attached to the load cell; insulating plates made from yttrium stabilized zirconium oxide prevent short circuiting through the compression device. The voltage was measured at a current of 100 mA, and the area specific resistance was calculated by $\rho_{el} = RA$, with R being the electrical resistance and A the felt contact area. To receive a standard deviation, three samples were tested for each modification.

UV-Vis spectroscopy (Hitachi U-3010 Spectrophotometer) in a range of 900 to 190 nm using quartz cuvettes (Hellma 100-QS), and **dynamic light scattering** (Zetasizer Pro, Malvern Panalytical) were performed to characterize the quality of the MWCNT dispersions and the size of the dispersed particles.

The gas evolution of pyrene-modified GF was studied by **Differential electrochemical mass spectrometry (DEMS)**. A setup as described in previous literature^[280,281] was modified to hold a sealed glass container containing an Ag/AgCl (3 M KCl) reference, pristine GF as counter and the sample as the working electrode, 10 mL of electrolyte (0.1 M VOSO₄ in 2 M H₂SO₄) and carrier gas inlet and outlet tubes. The gas inlet tube was lowered to the bottom of the container, so that the incoming carrier gas was bubbled through the electrolyte, while the outgoing tube was located directly above the electrolyte surface. The tube fittings were additionally sealed by silicon grease. For measurements, a linear voltage sweep from 0.6 to 1.8 V was performed at 0.5 mV s⁻¹. A constant stream of He carrier gas (purity 6.0, 10 mL min⁻¹) passed the cell. The extracted gas mixture went through a cold trap at -30 °C to remove H₂O, and analyzed using a mass spectrometer (Omni Star GSD 320, Pfeiffer Vacuum GmbH), monitoring the evolution of H₂ ($m/z = 2$), O₂ ($m/z = 32$), CO₂ ($m/z = 44$) as well as of various possible pyrene fragments ($m/z = 81, 87, 94, 95, 100, 101, 109$). For each fragment, a datapoint was recorded every 9 s.

Calibration was performed by passing a calibration gas of known composition through the cell. A complete measurement including calibration is shown in Figure S33.

Polarization Curves of GF and GF-P under operational conditions were conducted by using an in-house designed single-cell VFB, assembled as zero-gap architecture. A graphite foil (GF-176, Graphite Materials GmbH) served as current collector. The electrodes ($1 \times 1 \text{ cm}^2$) were fixed by a Teflon® (DuPont de Nemours Corp) spacer-layer, which was sandwiched between graphite foil and a membrane (Fumasep® FS-930, Fumatech BWT GmbH). A double headed peristaltic pump (323Du, Watson-Marlow Pumps Group) ensured a continuous flow of the electrolyte (1.6 M V, $V^{\text{III}}/V^{\text{IV}} \approx 0.8/0.8$ M, 3 M H_2SO_4 , 0.4 L per half-cell, GfE GmbH). The current collectors were connected to the potentiostat (Reference 3000, Gamry instruments) *via* gilded steel clamps (BU-60G, Mueller Electric Europe LTD, UK). The electrochemical protocol consisted of three steps:

- 1) charging of the electrolyte: the electrolyte was galvanostatically charged at a current density of 68 mA cm^{-2} and a flow rate of 70 mL min^{-1} to a state of charge (SoC) $\approx 50\%$ in an external cell. At an OCP of 1.4 V, the electrolytes were directed *via* three-way valves to other liquid lines, which were connected to the actual test cell, containing the electrode.
- 2) equilibration of the electrode: the potentiostat generated short time alternating galvanostatic pulses of 1 s, whereby the step size was 1 mA cm^{-2} . When the cell-voltage reached $\pm 200 \text{ mV}$ of the OVP, one of ten equilibration cycle was finished.
- 3) the actual characterization *via* the polarization curve method: the first galvanostatic discharge step at -10 mA cm^{-2} was generated for 30 s. Subsequently, steps with -20 , -30 , -40 mA cm^{-2} , *etc.*, (30 s each), resulted in a staircase-like current *vs.* time profile. During these steps, the cell voltage was recorded. The discharge polarization curve was stopped at a cell voltage of 0 V.

To show cell voltages at steady state conditions and to exclude the influence of capacitive voltages, the voltage values over the last 10 s of each step were averaged. During the first polarization curve, the flow rate was 130 mL min^{-1} . Afterwards, an identical charging polarization curve was performed. Subsequently, the routine was repeated at flow rates of 100 and 70 mL min^{-1} . Current collectors, membranes and the electrolyte were exchanged for each sample.

Appendix B: Supporting Information

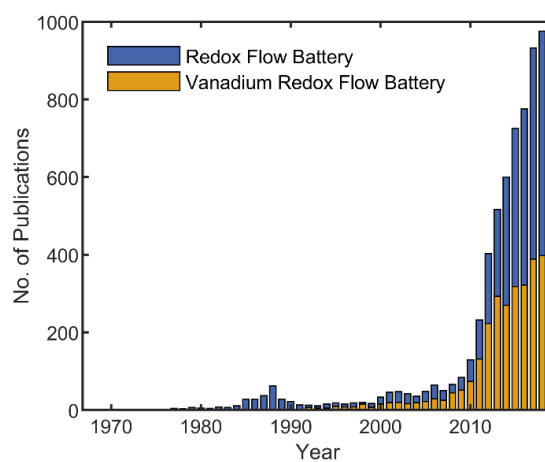


Figure S1. Number of publications over the last 40 years. Results are based on a SciFinder analysis, in which the keywords “redox flow battery” and “vanadium redox flow battery” are entered.

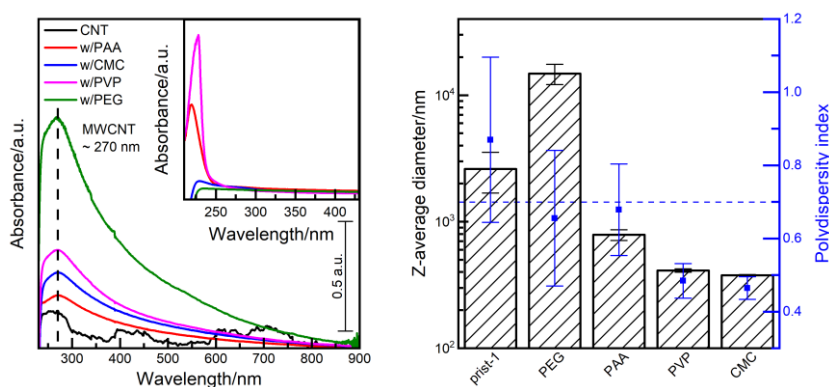


Figure S2. UV-Vis spectroscopy and DLS analysis of MWCNT dispersions with different polymers in a 1/1 ratio. The dispersion with a concentration of 1 mg ml⁻¹ was diluted with 20 additional parts H₂O for the measurements. While PEG and polyvinylpyrrolidone PVP revealed more intense absorption signals, their particle size and PDI are higher compared to CMC.

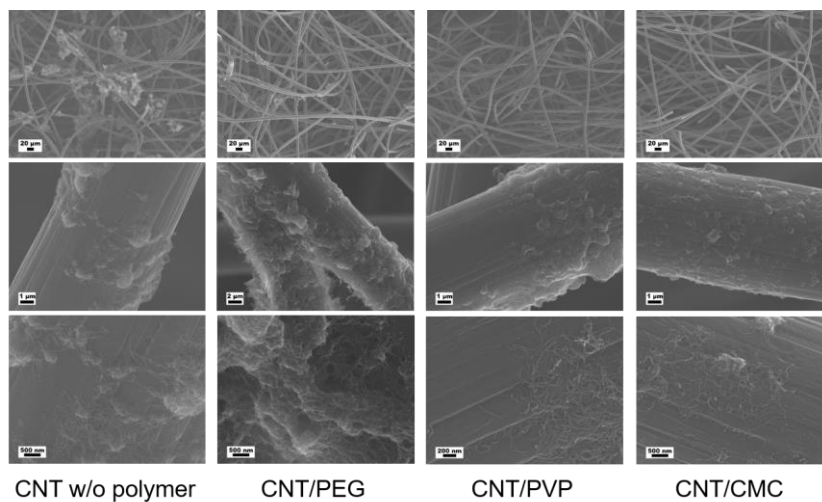


Figure S3. SEM of GF loaded with different MWCNT/polymer dispersions. Low magnification pictures reveal big aggregates in the fiber pores, especially for loading without polymer dispersant. Detailed pictures at high magnifications show the distribution of MWCNTs along the fiber, which is especially successful for PVP and CMC.

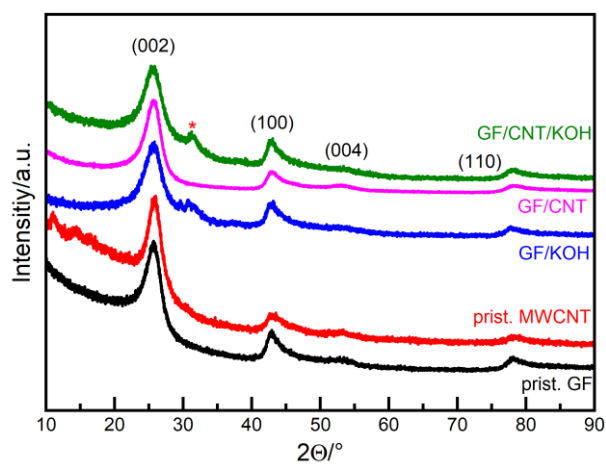


Figure S4. XRD patterns of pristine and modified GF and pristine MWCNTs. The graphite-related reflections are indicated. The red star marks a reflection related to K_2CO_3 .

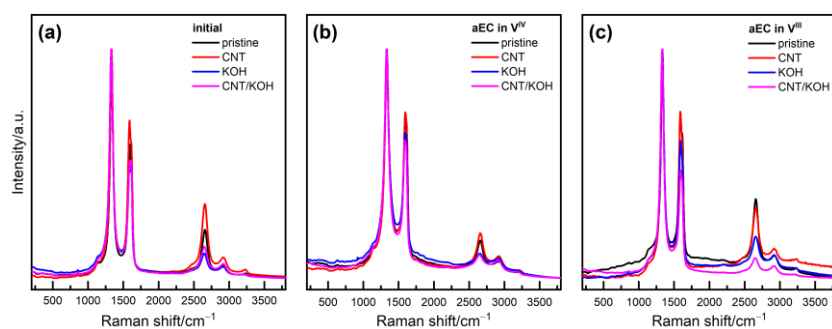


Figure S5. Raman survey spectra of pristine and modified GF. (a) In their initial state, and after cycling in the (b) positive and the (c) negative half-cell.

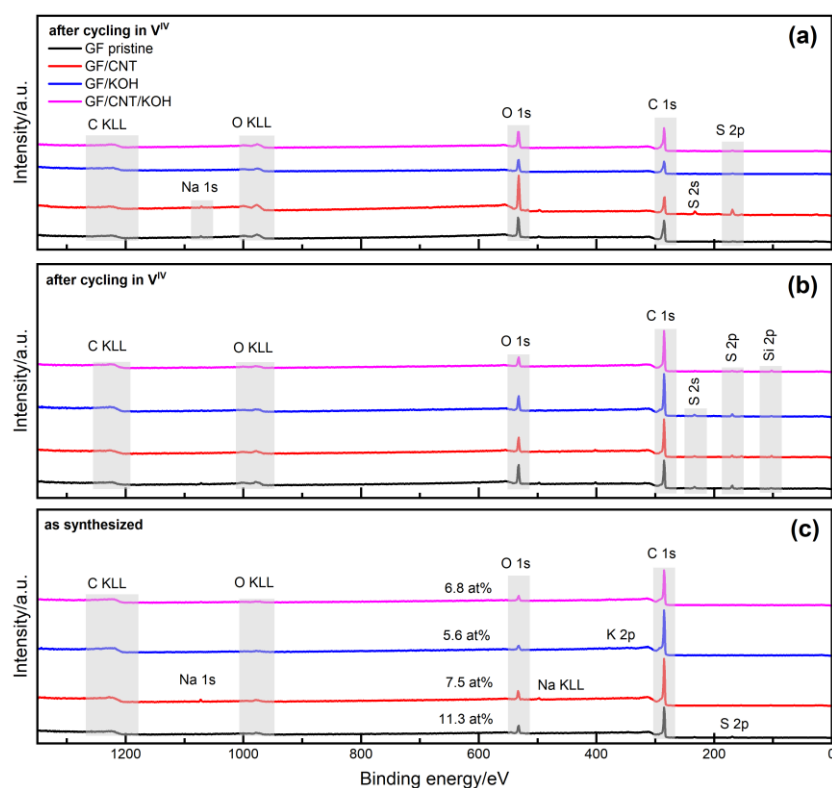


Figure S6. Survey spectra of pristine and modified GF, after electrochemical cycling (a) in V^{IV}O²⁺, (b) in V^{III}, and (c) prior to any electrochemical treatment. From left to right, several regions were identified: C KLL Auger, Na 1s core level, O KLL Auger, O 1s core level, Na KLL Auger, K 2p core level, C 1s core level, S 2s and 2p core level, and Si 2p core level. The major components of all samples are oxygen and carbon, only moderate amounts of sulfur are present on GF, and traces of sodium and potassium on GF/CNT and GF/KOH, respectively. While sulfur can be attributed to the cleaning process with diluted H₂SO₄ and potassium to residuals from the KOH activation, low concentrations of sodium and silicon are found in many XP spectra of GF as ambient contaminations and impurities.

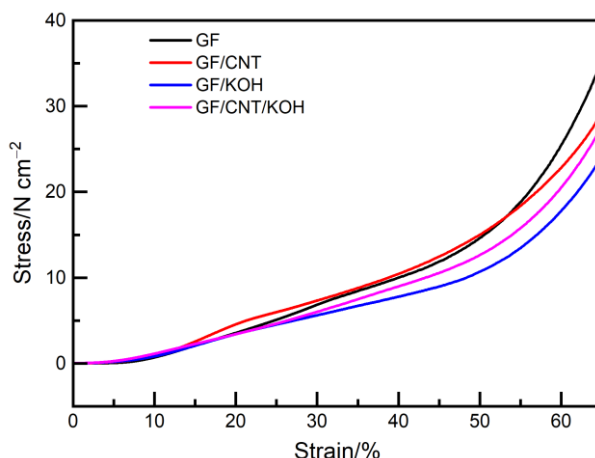


Figure S7. Mechanical stability of GF under mechanical compression. The pressure stability was measured with the same setup used for the investigation of the electrical conductivity.

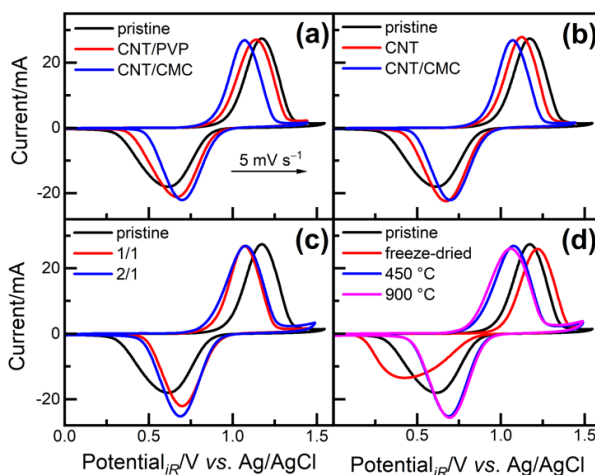


Figure S8. CV curves for the $V^{V}O_2^+/V^{IV}O_2^+$ redox reaction of pristine and MWCNT-modified GF. Comparison of (a) MWCNT/polymer solutions after heating at 450 °C, (b) activity with and without CMC after heating at 450 °C, (c), ratio of MWCNT to polymer after heating at 450 °C, and (d) temperature treatment after modification. From the UV-Vis, DLS, and SEM results, PVP and CMC were selected as promising candidates for successfully distributing and bonding MWCNTs and were therefore studied electrochemically. A CNT/CMC modified GF, after carbonization of the binder, revealed lower ΔE_p and higher reversibility compared to CNT/PVP. The influence of the binder has been investigated by testing a sample without CMC, resulting in decreased redox activity, associated with a worse distribution and bigger aggregates of MWCNTs. The ideal ratio of MWCNTs to binder was evaluated by doubling the CNT/CMC ratio. The higher MWCNT/binder ratio resulted in a broader redox wave with higher reversibility and a lower onset potential. The necessity to carbonize the binder is shown, because modified GF exhibits even lower activity than pristine GF because of covered active sites. An increased carbonization temperature from 450 to 900 °C had no significant positive effect on the activity.

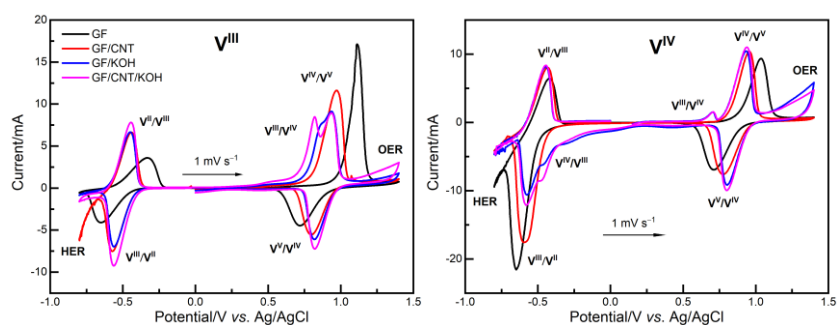


Figure S9. CV curves of pristine and modified GF in 0.1 M V^{III} (left) and 0.1 M $V^{IV}O_2^+$ (right) over the complete potential range between hydrogen in the cathodic and oxygen evolution on the anodic side. All signals in the diagram have been assigned to the corresponding vanadium redox reactions. GF and GF/CNT reveal higher peak currents of the $V^{IV}O_2^+/V^{IV}O_2^+$ oxidation in the negative, and the V^{III}/V^{II} reduction in the positive electrolyte, respectively, because of the overlap of these redox reactions with the preceding $V^{IV}O_2^+/V^{III}$ oxidation and $V^{IV}O_2^+/V^{III}$ reduction. These reactions are separated for more electrocatalytically active GF/KOH and GF/CNT/KOH.

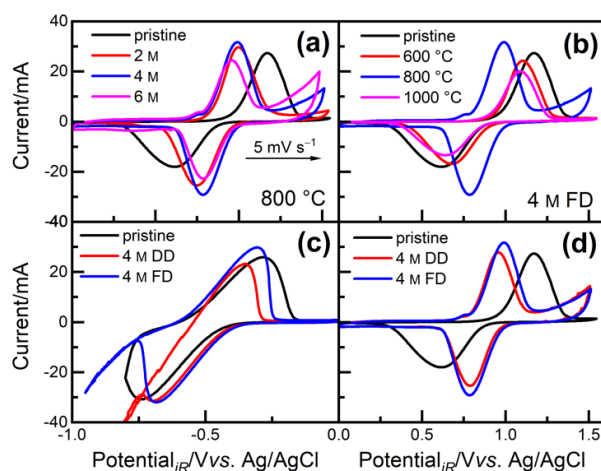


Figure S10. CV curves of GF/KOH prepared under various conditions. Comparison of (a) KOH solutions with different molarities after freeze-drying and calcination at 800 °C; (b) calcination temperatures after freeze-drying using 4 M KOH; (c,d) freeze-dried (FD) and directly dried (DD, drying cabinet at 80 °C) electrodes using 4 M KOH and calcination temperatures of 800 °C for the (c) V^{III}/V^{II} and (d) $V^{IV}O_2^+/V^{IV}O_2^+$ redox reactions. For the negative and the positive half-cell, an increased peak current was observed for freeze-dried electrodes, attributed to a better distribution of KOH and therefore more uniform activation of GF.

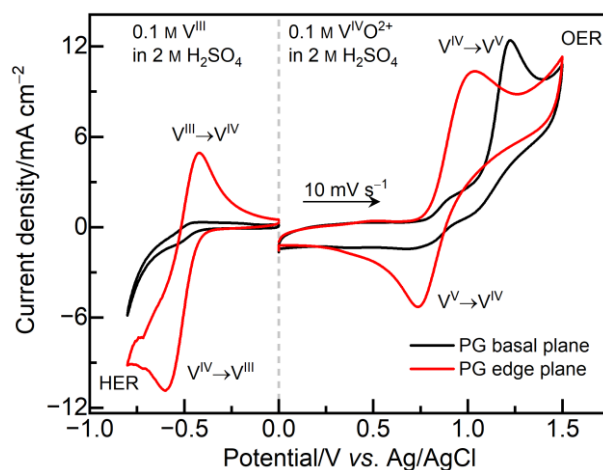


Figure S11. Electrochemical performance of basal plane and edge plane exposed HOPG electrodes in both half-cells.

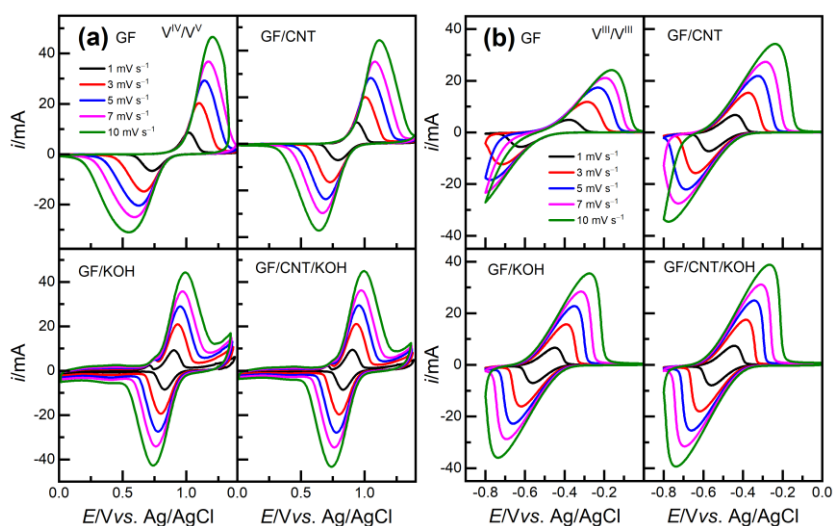


Figure S12. CV curves at different scan rates from 1 to 10 mV s^{-1} of pristine and modified GF for the (a) positive and (b) negative half-cell.

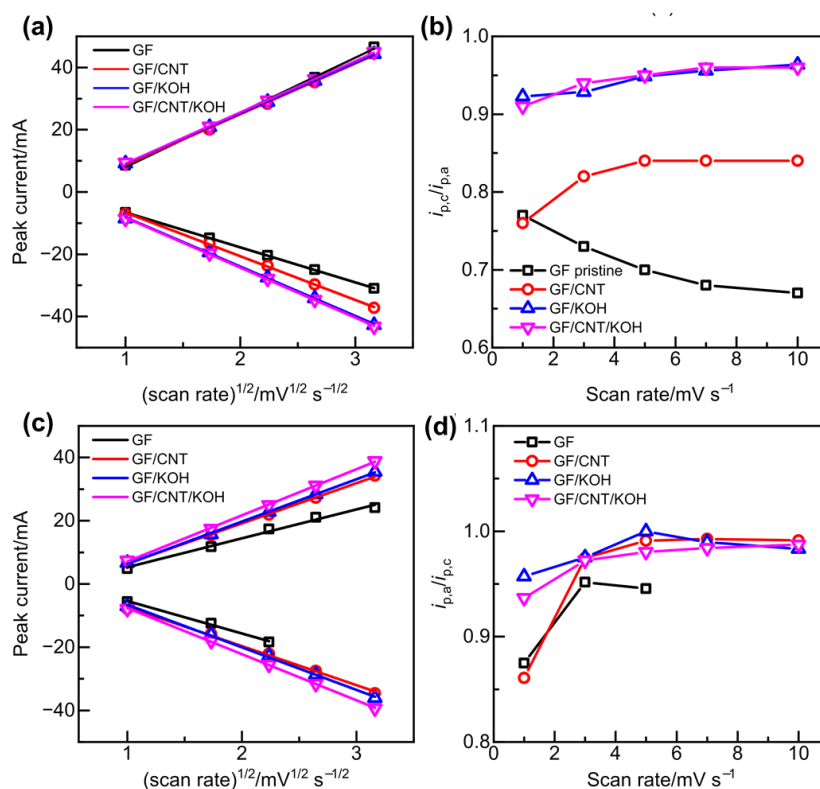


Figure S13. Randles–Sevcik plots and redox reaction reversibility in the (a,b) positive and (c,d) negative half-cell. The mass-transfer properties of the electrodes were studied by graphically verifying the Randles–Sevcik equation. Positive half-cell: a linear fit suggests that the $\text{VVO}_2^+/\text{V}^{\text{IV}}\text{O}_2^+$ redox reaction is limited by diffusion.^[119,282] The reductive fit reveals a $\sim 70\%$ higher slope for the KOH activated samples, signifying faster reaction kinetics at the electrode.^[141] This shows a positive influence of edge sites on the kinetics and shows a hindering effect of oxygen for the $\text{VVO}_2^+/\text{V}^{\text{IV}}\text{O}_2^+$ reduction.^[60] To address the reversibility of the redox process, the $i_{p,c}/i_{p,a}$ ratio for the $\text{VVO}_2^+/\text{V}^{\text{IV}}\text{O}_2^+$ redox couple was calculated. For GF, the current ratio decreased at higher scan rates, while the current ratio of GF/CNT slightly increased. In contrast, a high reversibility with peak current ratios >0.9 at all scan rates for GF/KOH and GF/CNT/KOH is observed. Negative half-cell: given by the linear fit of the Randles–Sevcik plots, the slope of GF/CNT/KOH is $\sim 65\%$ higher for both anodic and cathodic currents, showing a faster mass transfer in the combinatorial treated electrode. The $i_{p,a}/i_{p,c}$ ratios for the $\text{V}^{\text{III}}/\text{V}^{\text{II}}$ redox couple quickly rise close to 1 for the modified electrodes. In contrast, for GF the peak values are not applicable anymore $>5 \text{ mV s}^{-1}$.

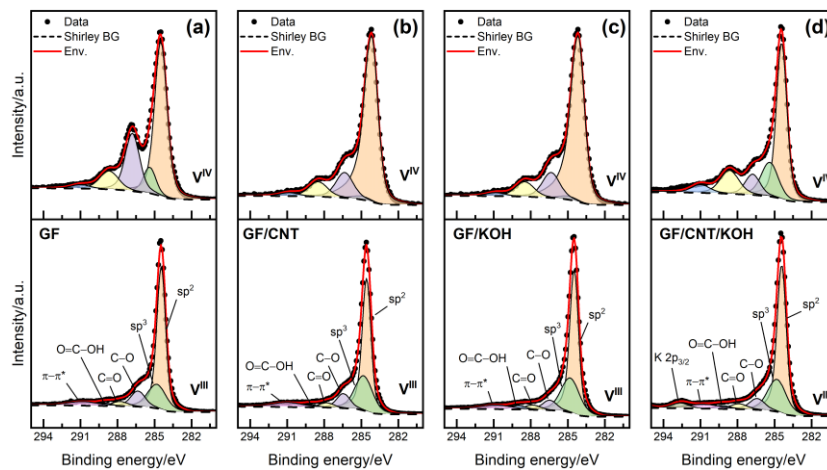


Figure S14. Detail spectra in the C 1s region of (a) GF, (b) GF/CNT, (c) GF/KOH, and (d) GF/CNT/KOH, after cycling in the positive (top row), and in the negative (bottom row) half-cell.

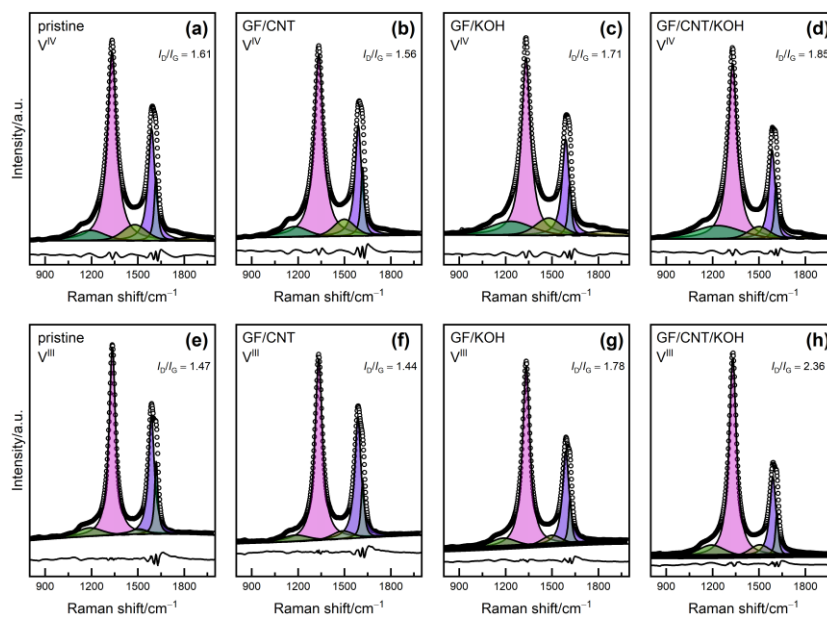


Figure S15. Deconvoluted Raman spectra of pristine and modified GF after cycling in the (a–d) positive and the (e–h) negative half-cell.

Table S1. Initial oxygen concentration of pristine and modified GF. The composition compared to all surface species (including carbon, rounded to 0.5 at%) and the relative composition regarding the three main functional groups (O–C, O=C, O=C–O, rounded to the full percentage) is given.

Sample	O–C/at%	O=C/at%	O=C–O/at%	O–C/rel. at%	O=C/rel. at%	O=C–O/rel. at%
GF	4.5	6	1	40	53	7
GF/CNT	4.5	1	2	59	17	25
GF/KOH	2	2.5	0.5	53	34	15
GF/CNT/KOH	2	1.5	0.5	40	47	13

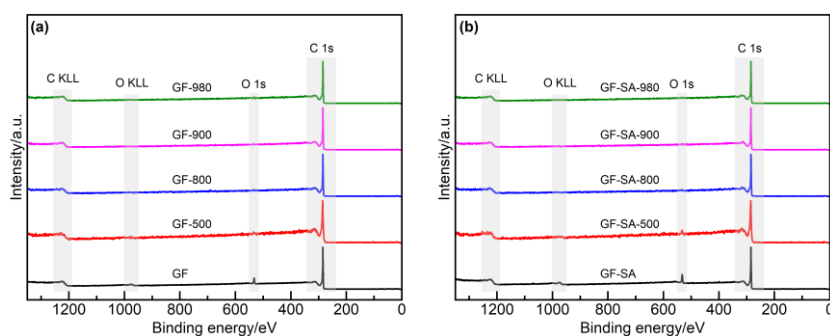


Figure S16. Survey spectra of the deoxygenation procedure. Spectra are given regarding the previous temperature treatment for (a) GF and (b) GF-SA. Only carbon and oxygen were detected as chemical compounds, as it is deduced from the carbon Auger C KLL (~1223 eV) and core level region C 1s (~285 eV), and equally from the oxygen Auger O KLL (1013-978 eV) and core level O 1s (~531 eV). Deoxygenation can be observed in the surveys, as the contribution from the O 1s and the O KLL signals vanish after the temperature treatment.

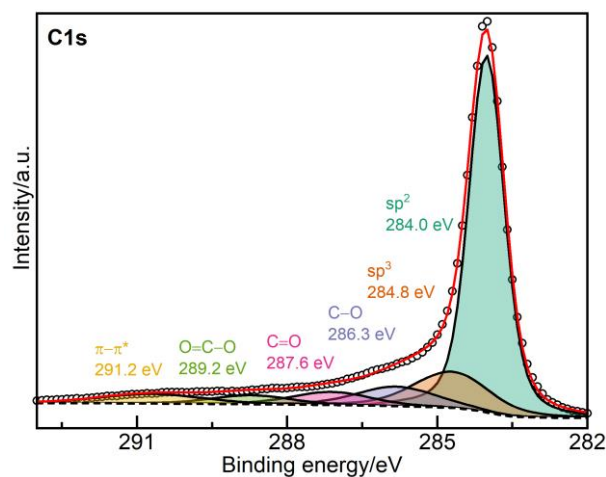


Figure S17. C 1s detail spectrum of GF. Six different carbon-related peak components were deconvoluted and stated in the picture: sp^2 carbon at 284 eV, sp^3 carbon at 284.8 eV, ether and hydroxyl groups at 286.3 eV, carbonyls at 287.6 eV, and carboxylic groups at 289.2 eV; the additional sp^2 carbon related shake-up satellite is located at 291.2 eV.^[58,152,166,167] The spectrum is binding energy corrected regarding the position of sp^2 carbon.

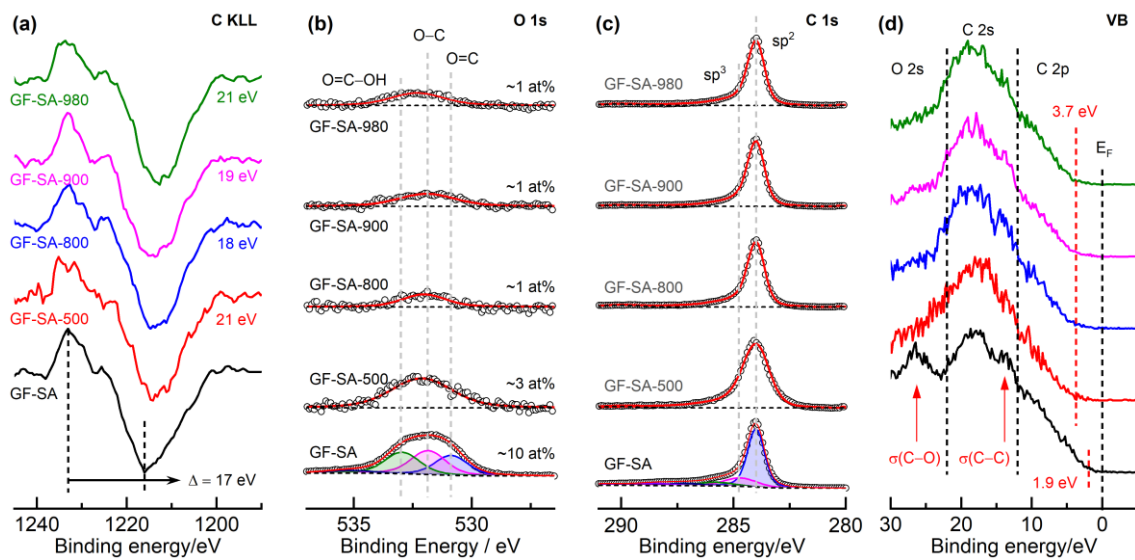


Figure S18. XPS investigation of thermally deoxygenated GF-SA. (a) First derivative of the C KLL Auger region to determine the D-parameter. (b) O 1s detail spectra, indicating the position of the respective oxygen group and the relative oxygen content. (c) C 1s detail spectra, showing the position of sp^2 and sp^3 hybridized carbon. (d) VB spectra, displaying the O 2s, C 2s and C 2p regions and the evaluated E_{VBM} .

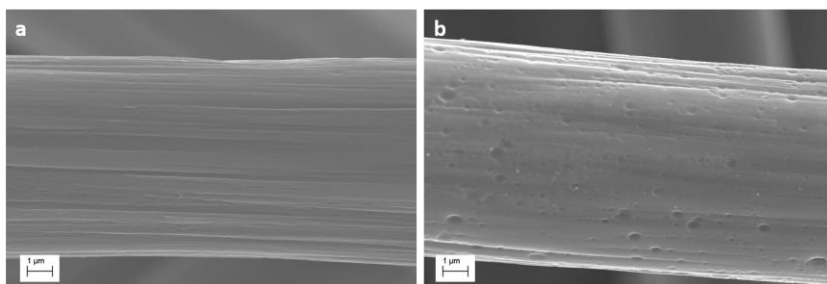


Figure S19. SEM of thermally deoxygenated GF-980 and GF-SA-980.

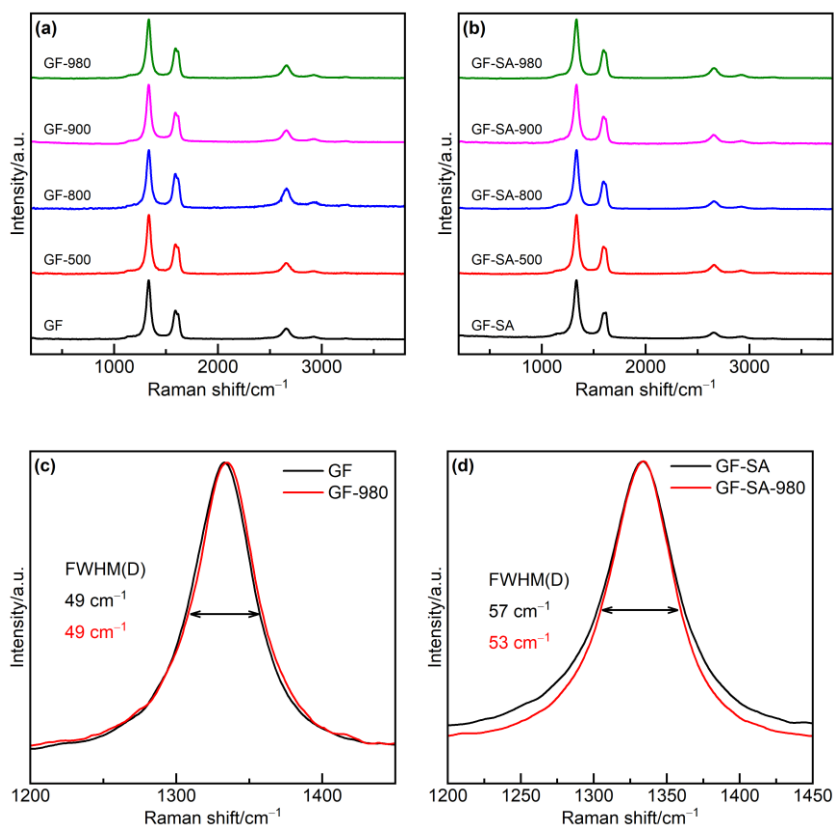


Figure S20. Raman spectra of (a) GF and (b) GF-SA prior to and after each corresponding deoxygenation step. The spectra in the picture are normalized to the D band, but not BG-corrected or deconvoluted. (c,d) Depiction of the D band of pristine and fully deoxygenated GF and GF-SA electrodes to evaluate the FWHM.

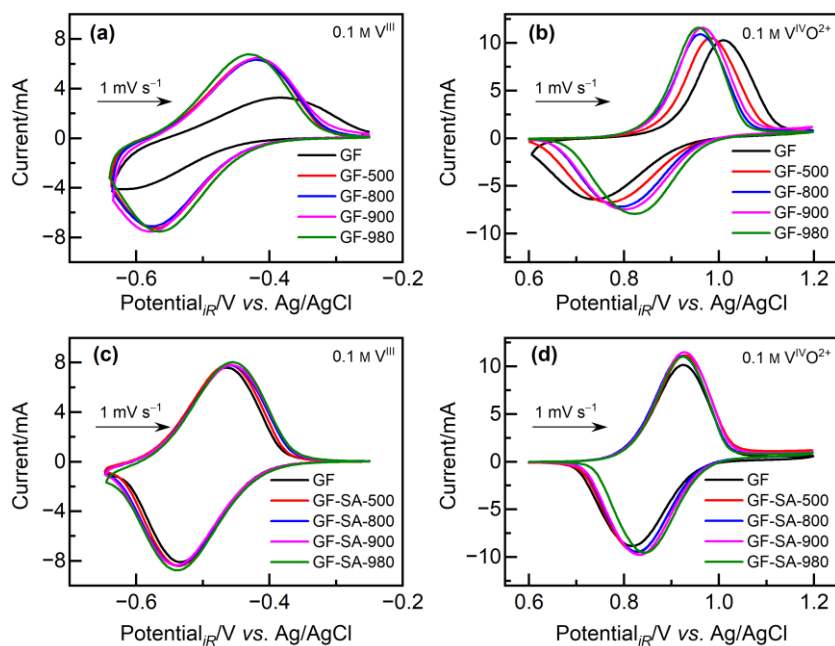


Figure S21. Electrocatalytic activity for the V^{III}/V^{II} and the $V^{VO_2^+}/V^{VO_2^{2+}}$ redox couple. CV curves were recorded for (a,b) pristine and deoxygenated GF and (c,d) GF-SA.

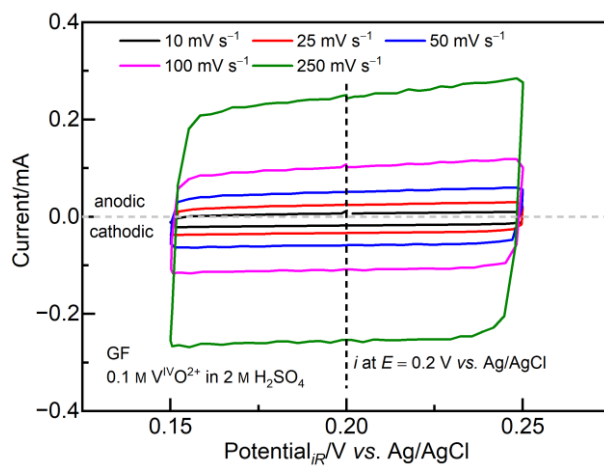


Figure S22. Example of the used CV method to evaluate the EDLC. CV curves were recorded in the positive electrolyte in a non-faradaic potential region with varying scan rates.

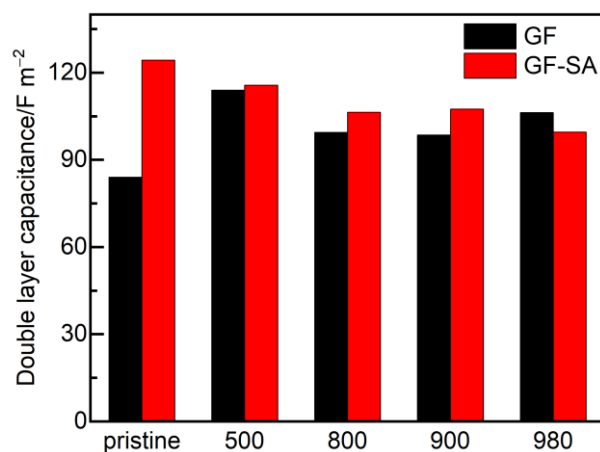


Figure S23. Normalized EDLC of GF. The surface area of the felt was measured by BET; the weight of the electrode was determined prior to electrochemical cycling.

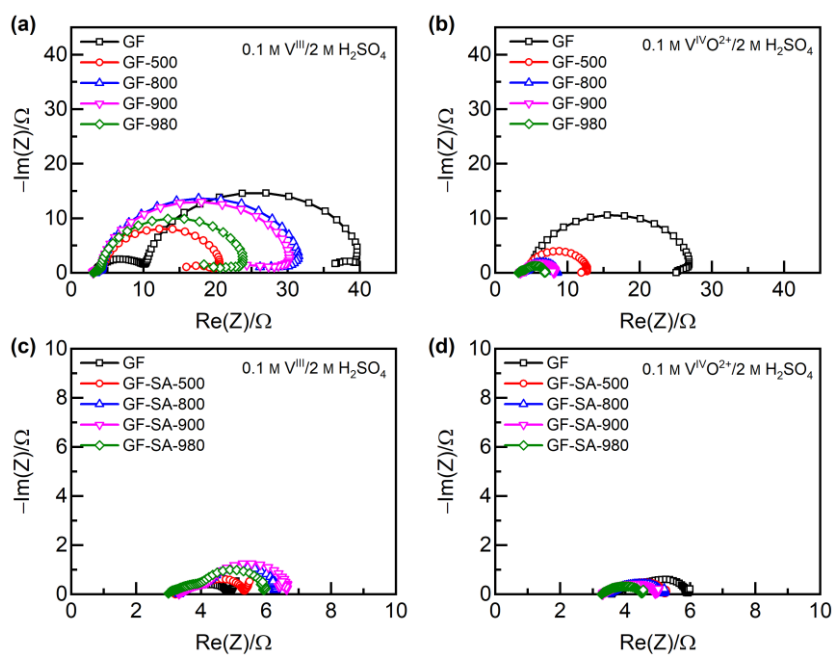


Figure S24. Nyquist plots of EIS measurements. Displayed are the negative and positive half-cell measurements at an applied potential of -0.45 and 0.9 V vs. Ag/AgCl for pristine and deoxygenated (a,b) GF and (c,d) GF-SA.

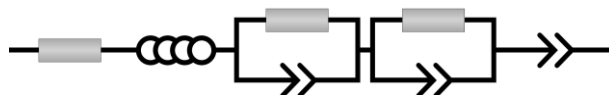


Figure S25. Equivalent circuit diagram used for the deconvolution of the EIS data. The graph displays following elements: an inductance and the electrolyte resistance in series, followed by two resistance/constant phase elements in parallel, one for the glassy carbon/felt, and one for the felt/electrolyte interface, and in the end one constant phase element for the diffusion. Not for all spectra every element was necessary.

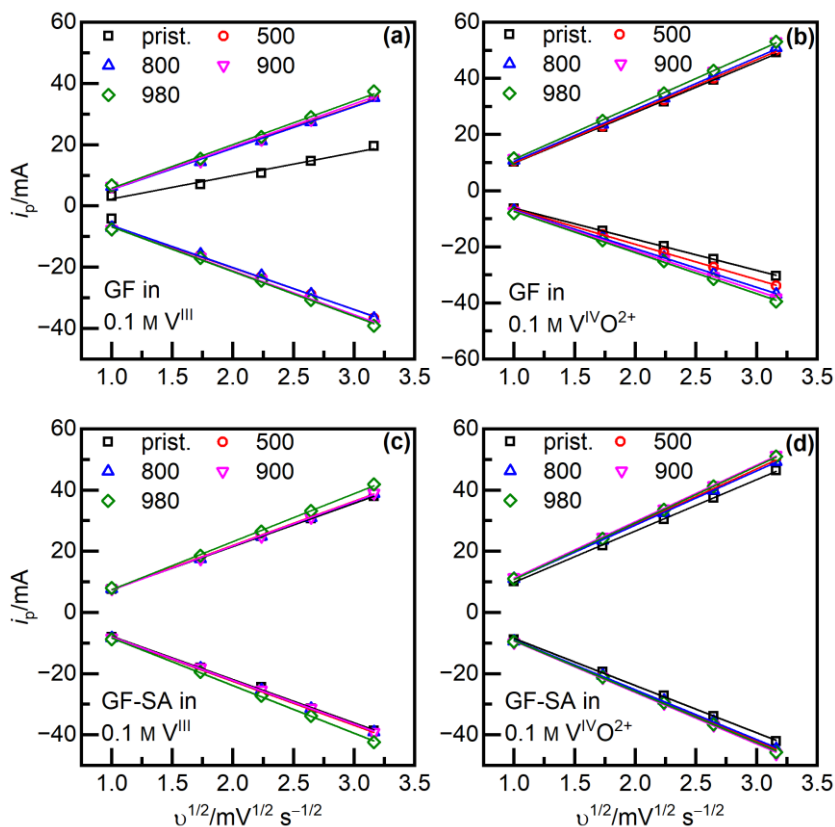


Figure S26. Randles–Sevcik plots; CV data for pristine and deoxygenated (a,b) GF and (c,d) GF-SA. The data has been determined from the peak currents at various scan rates. Mass transfer properties have been investigated by graphically verifying the Randles–Sevcik equation, which shows a linearity of i_p vs. $v^{1/2}$ for all electrodes in both half-cells, indicating a chemically reversible redox process limited by diffusion.^[119,282,283] A higher slope suggests a faster mass transfer process, which has been observed especially for the V^{III}/V^{II} redox reaction after deoxygenation.^[141] The most rapid mass transfer is achieved for felts deoxygenated at 980 °C, which is another indicator of the hindering effect of OFGs.

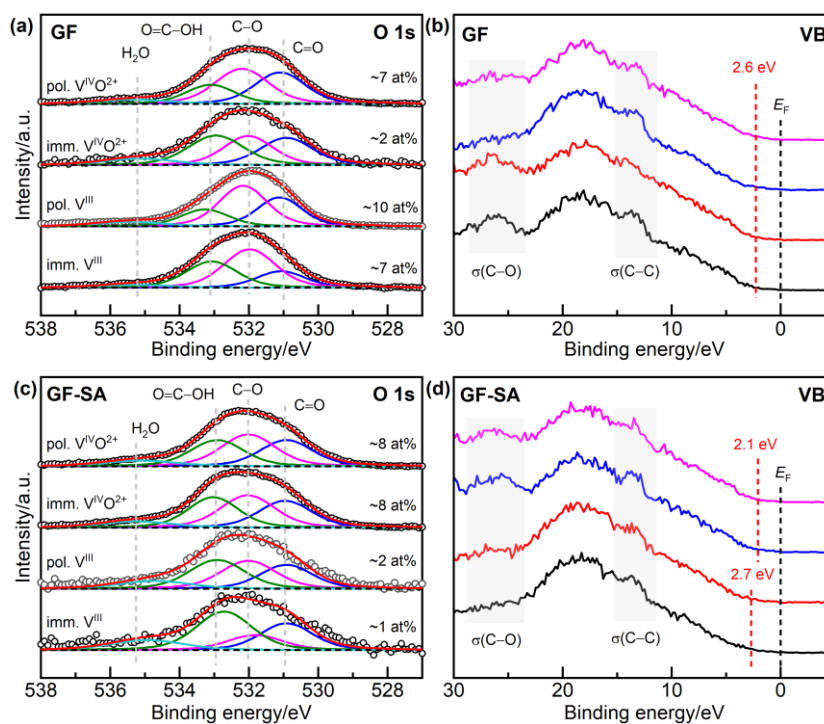


Figure S27. XPS and electronic structure of GF and GF-SA. Electrodes have either been immersed for 3 h or polarized at -0.6 and 1.2 V vs. Ag/AgCl in 0.1 M V^{III} and $V^{IVO^{2+}}$ for 1 h, respectively. The figure displays the O 1s detail spectra and the VB region of (a,b) GF and (c,d) GF-SA, each after deoxygenation at 980 °C and respective electrolyte treatment.

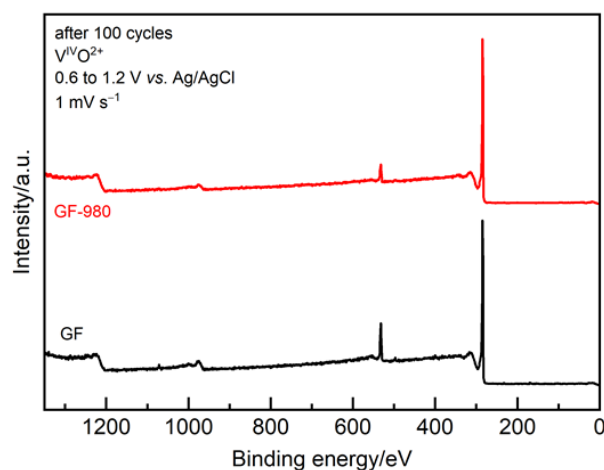


Figure S28. Survey spectra of $100\times$ cycled pristine (GF) and deoxygenated (GF-980) electrodes. Only carbon and oxygen were detected as chemical compounds.

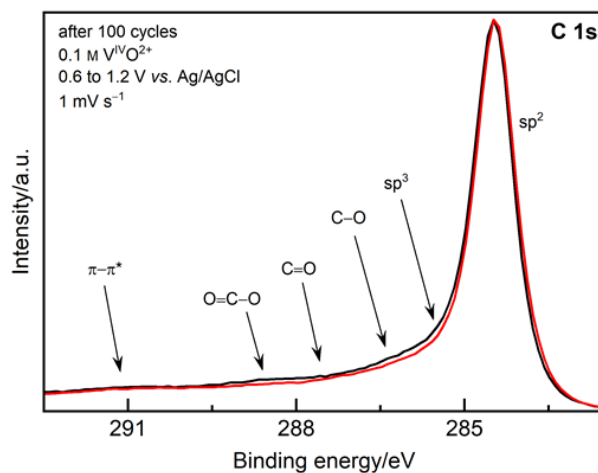


Figure S29. Normalized C 1s spectra of GF (black) and GF-980 (red). Because of its complexity, the C 1s region is not used for quantitative fitting, but a direct comparison of the normalized spectra yields qualitatively an increased sp^3 carbon signal and various carbon-oxygen signals that are more pronounced for GF.

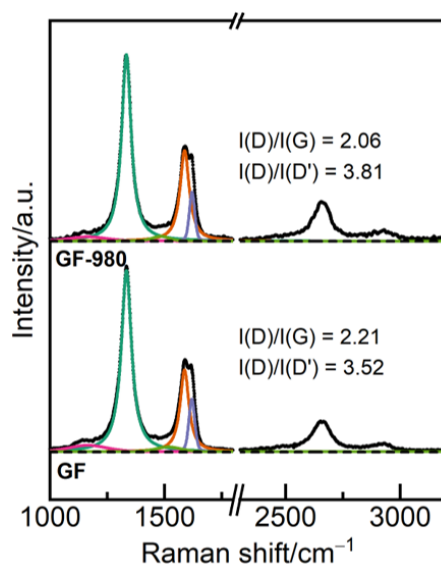


Figure S30. Deconvoluted Raman spectra after long-term cycling. Band intensity ratios are indicated: while the $I(D)/I(D')$ ratio stays unchanged compared to the electrode before cycling, the $I(D)/I(G)$ ratio changes.

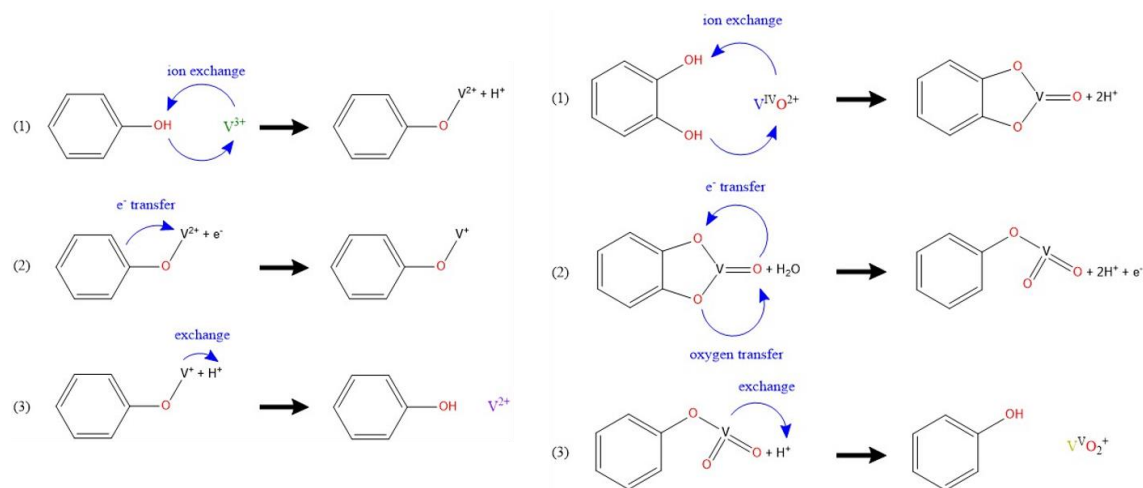


Figure S31. Old reaction mechanism *via* hydroxyl groups, first proposed in 1992.^[32] The left panel displays the mechanism in the negative half-cell *via* an ion exchange mechanism, followed by the electron transfer and another ion exchange mechanism. The left panel shows the mechanism in the positive half-cell in a similar order, but with two initial hydroxyl groups at the electrode surface.

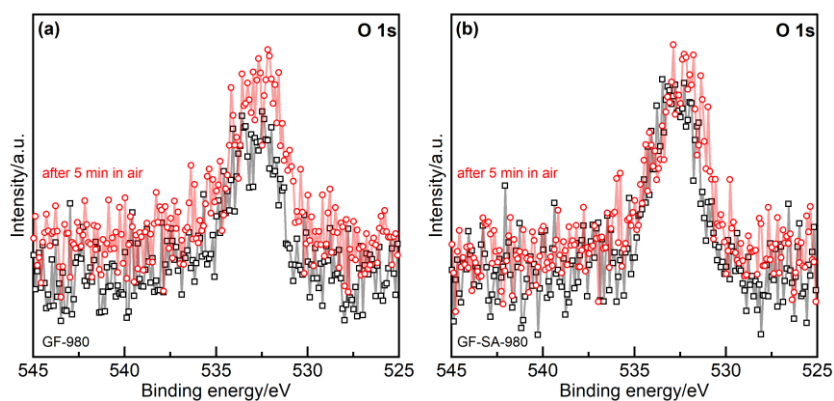


Figure S32. O 1s detail spectra to examine the self-oxidation of deoxygenated (a) GF and (b) GF-SA in contact with air. Previously measured GF was exposed to atmosphere for 5 min in the load lock of the XPS chamber. Afterwards, spectra were recorded again at the same spot.

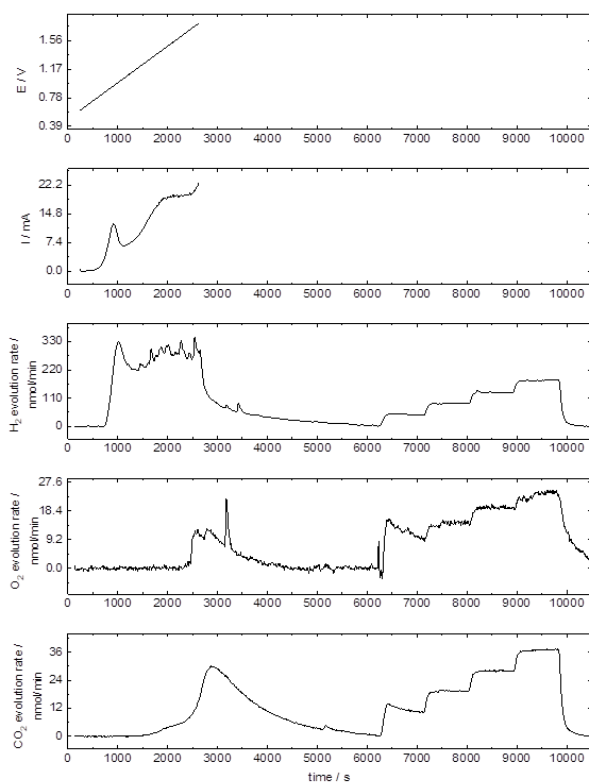


Figure S33. DEMS measurement and calibration curve for pyrene-coated GF. Different concentrations of calibration gas were added to the carrier gas stream to get reference levels for a calibration curve.

Table S2. Integrated gas evolution during DEMS measurements.

Electrode	Total CO ₂ evolution (μmol)	Total charge passed (C)	Ratio ($\mu\text{mol/C}$)
GF	1.4	22.08	0.0634
GF-980	1.2	30.16	0.0398
GF-PYR	0.7	26.95	0.0258
GF-PYR-COOH	1.4	40.98	0.0342

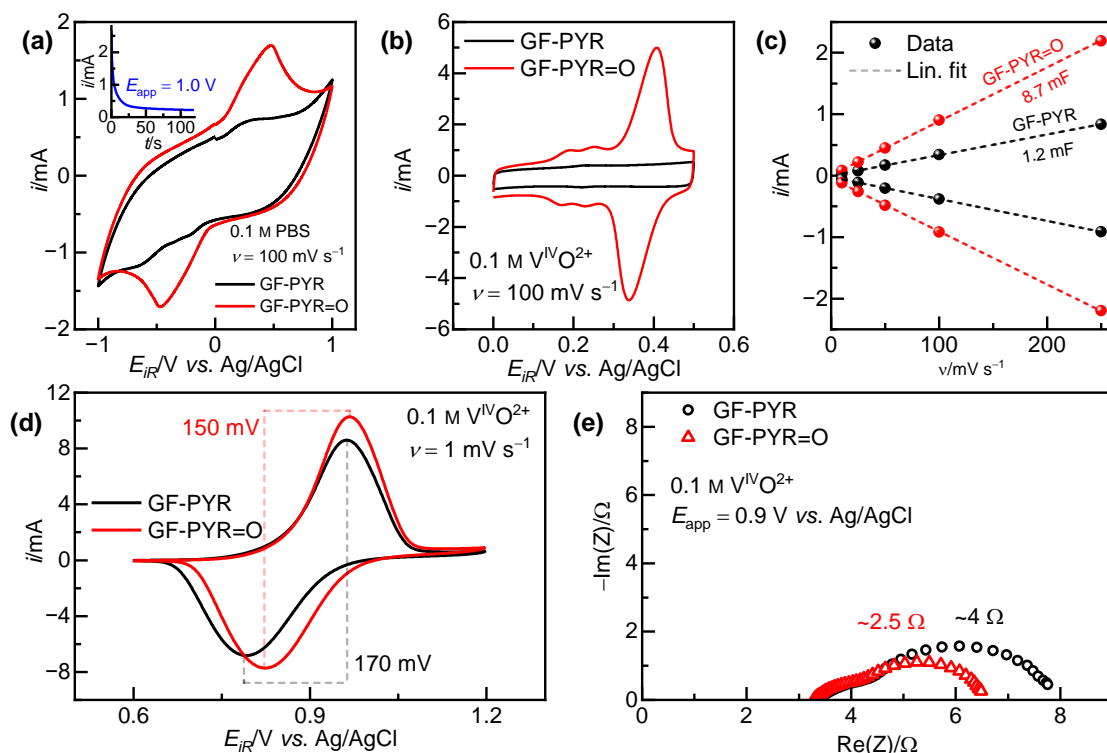


Figure S34. Electrochemical preparation and characterization of GF-PYR=O. (a) Protocol to prepare and show the functionalization. (b) Capacitive behavior in a non-faradaic potential range. (c) EDLC; (d,e) Electrocatalytic activity in the positive half-cell evaluated using (d) CV and (e) EIS. The possibility of electrochemically altering the functionalization of a pyrene-modified electrode and thus its electrocatalytic properties was studied. Therefore, a procedure proposed for the carbonyl functionalization of pyrene-modified MWCNTs was used.^[277] After the chronoamperometric treatment in phosphate buffer solution, additional redox peaks showcasing the successful treatment were visible not only in the treatment solution (Figure S34a) but also in the vanadium-containing electrolyte (Figure S34b). Another investigation of the EDLC (Figure S34c) revealed that the initial low capacitance of GF-PYR (1.2 mF) is increased over seven times to 8.7 mF for GF-PYR=O, which is more than it was observed for GF-PYR-COOH before (7.3 mF). The higher active surface area is also reflected in the peak currents measured by CV (Figure S34d). While the position of the $V^{VO_2^+}/V^{VO_2^+}$ oxidation peak remains unchanged, the corresponding reduction reaction is favored for GF-PYR=O, leading to a by 20 mV reduced ΔE_p . The R_{CT} is lowered by 1.5 Ω after the electrochemical treatment. This last experiment demonstrates that pyrene-modified GF uncovers a completely new range of electrode treatments, which might alter the electrocatalytic activity of GF in a targeted manner.

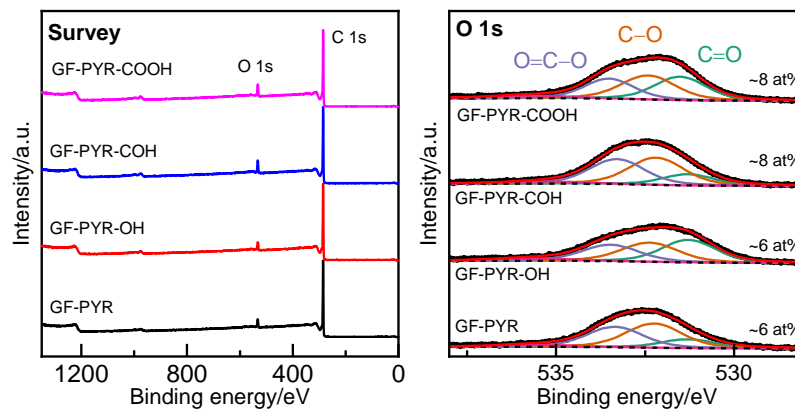


Figure S35. Surface chemical composition of pristine and pyrene-modified GF-980. (a) Survey and (b) O 1s detail spectra.

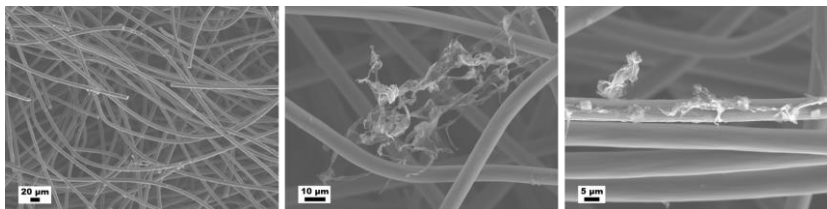


Figure S36. SEM of PG-1 attached to GF at different magnifications.

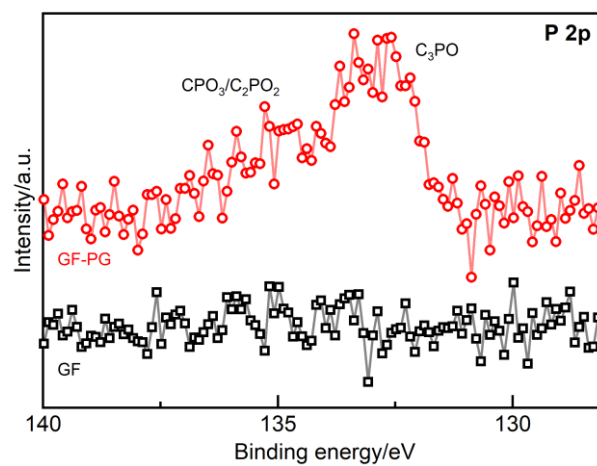


Figure S37. P 2p spectra of GF and GF-PG.

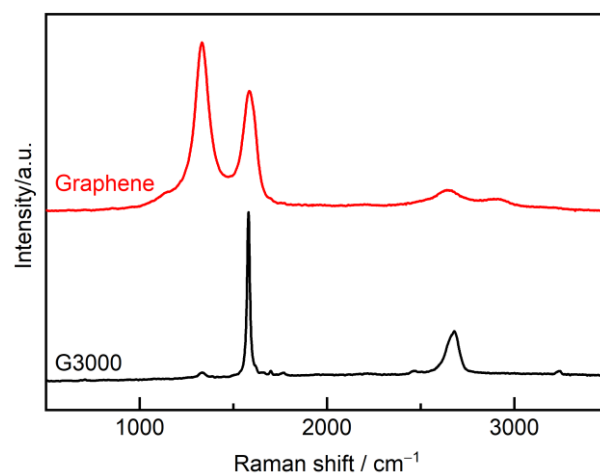


Figure S38. Raman spectra of G3000 and graphene.

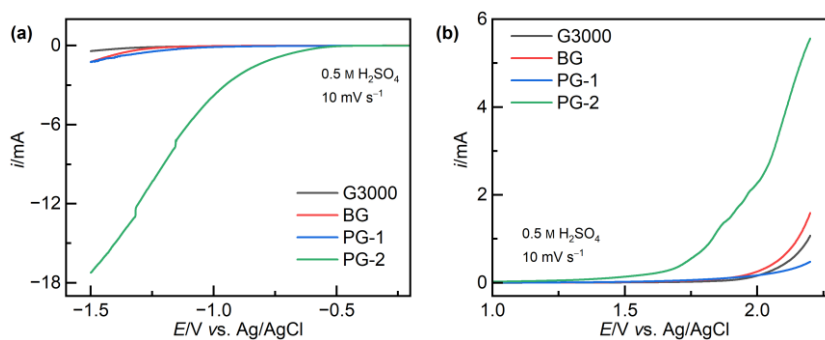


Figure S39. LSV curves of G3000 and doped graphenes. (a) hydrogen and (b) oxygen evolution in H_2SO_4 . Additional to the current onset at a lower potential for PG-2, the evolution of hydrogen and oxygen is further seen in the ragged slope of the curve, which is because of the bubble formation on the surface of the electrode.

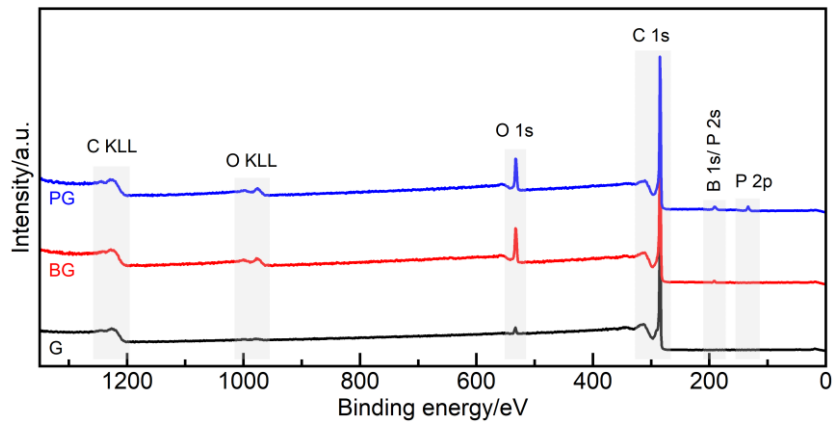


Figure S40. Survey spectra of graphene and commercial doped graphene. From left to right, we detected carbon and oxygen Auger C KLL (~ 1223 eV) and O KLL (1013–978 eV), oxygen core level O 1s (~ 531 eV), carbon core level C 1s (~ 285 eV), boron core level B 1s overlapping with phosphorus core level P 2s (~ 192 eV), and phosphorus multiplet P 2p (~ 133 eV).^[284]

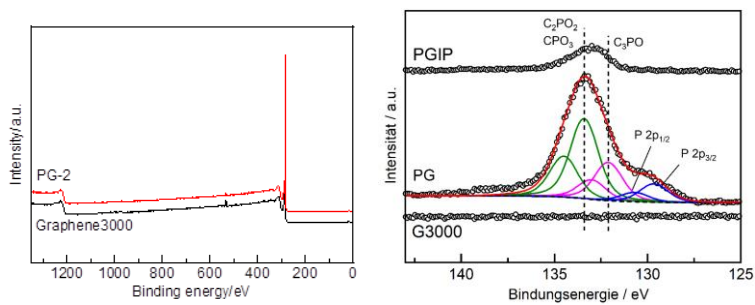


Figure S41. XP survey and P 2p detail spectra of G3000, commercial PG-1 (PG) and the synthesized PG-2 (PGIP).

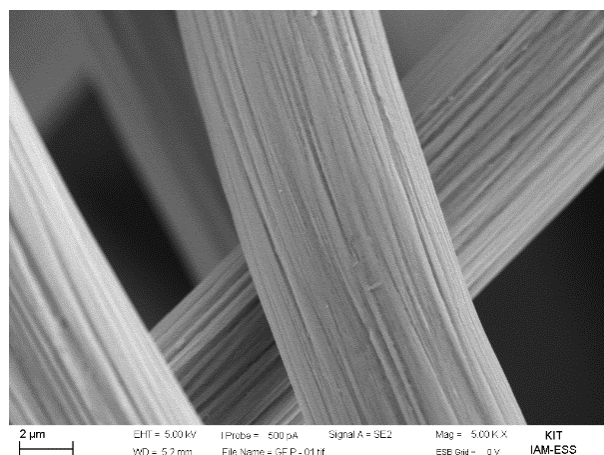


Figure S42. SEM image of GF-P.

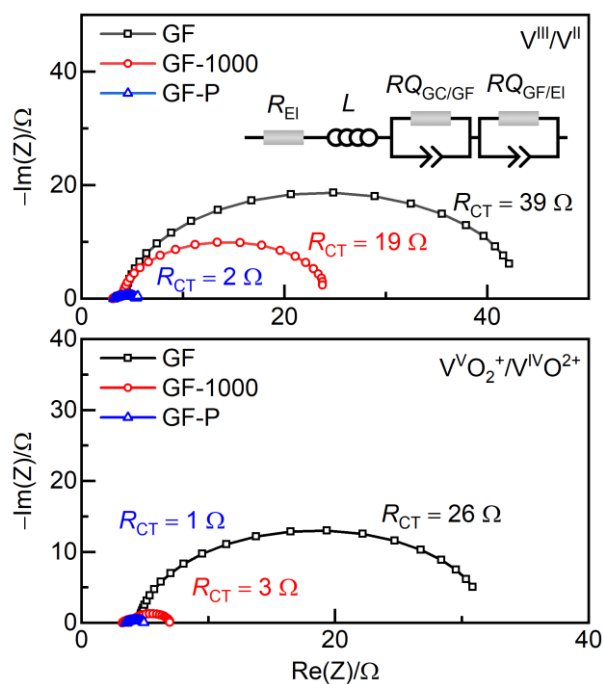


Figure S43. EIS of pristine (GF), thermally treated (GF-1000) and phosphorus doped GF (GF-P). R_{CT} is assessed at the second semi-circle at an applied potential of 0.9 V vs. Ag/AgCl in the positive, and -0.45 V vs. Ag/AgCl in the negative half-cell.

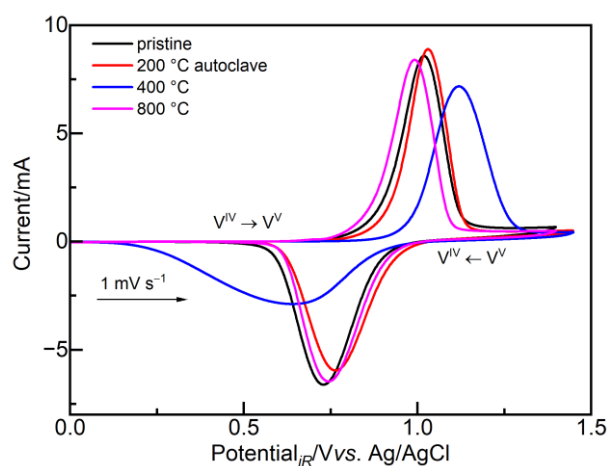


Figure S44. Electrocatalytic activity of GF and GF-P (synthesized by using a 25 mg mL^{-1} TPP in DMSO solution), heat-treated at different temperatures.

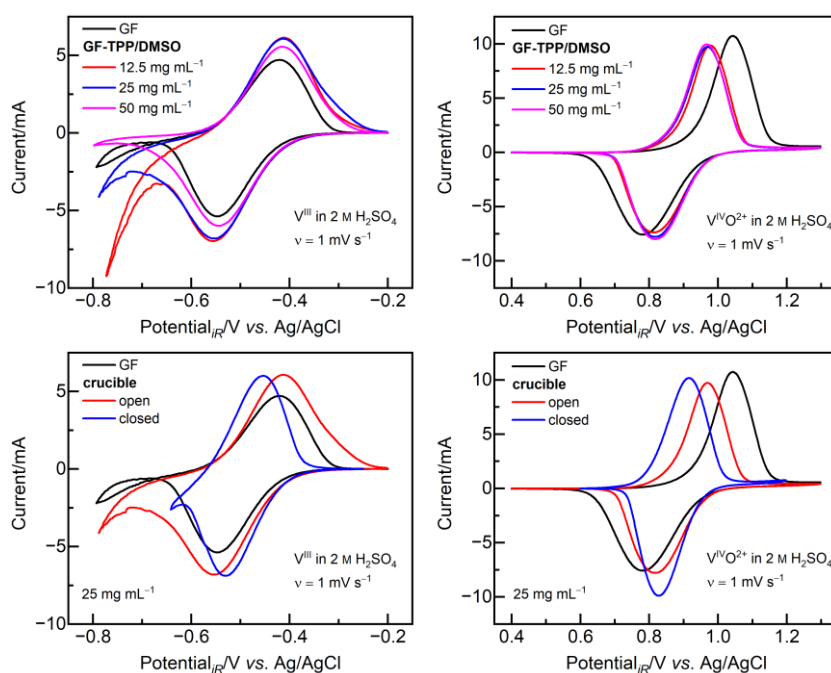


Figure S45. Electrocatalytic activity of GF and GF-P, synthesized under varying conditions. All samples were heat-treated at $1000 \text{ }^\circ\text{C}$ under Ar atmosphere. CV was conducted in the negative (left side) and positive half-cell (right side). In the top row, different concentrations of TPP in DMSO were tested. In the bottom row, the felts were calcined with and without using a closed graphite crucible.

Table S3. Elemental composition of the heat-treated graphene and doped graphene.

Sample	C/%	N/%	H/%	S/%
G3000	98.2	0.1	1.31	0.00
BG	76.2	0.09	1.06	0.24
PG-1	77.9	0.2	1.04	0.00
PG-2	97.8	0.19	0.25	0.00

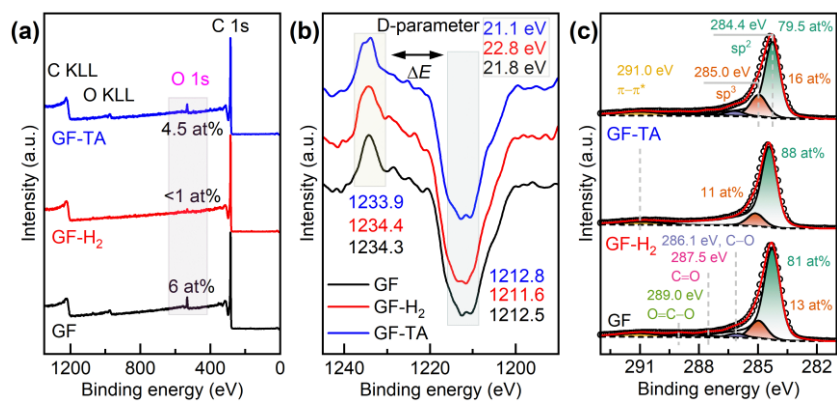


Figure S46. XP spectra of pristine and activated GF. (a) Surveys, revealing that in both cases only carbon and oxygen are present. (b) D-parameter evaluated from the first-derivative of the carbon Auger C KLL. (c) C 1s detail spectra showing the ratio of sp^2 and sp^3 hybridized carbon.

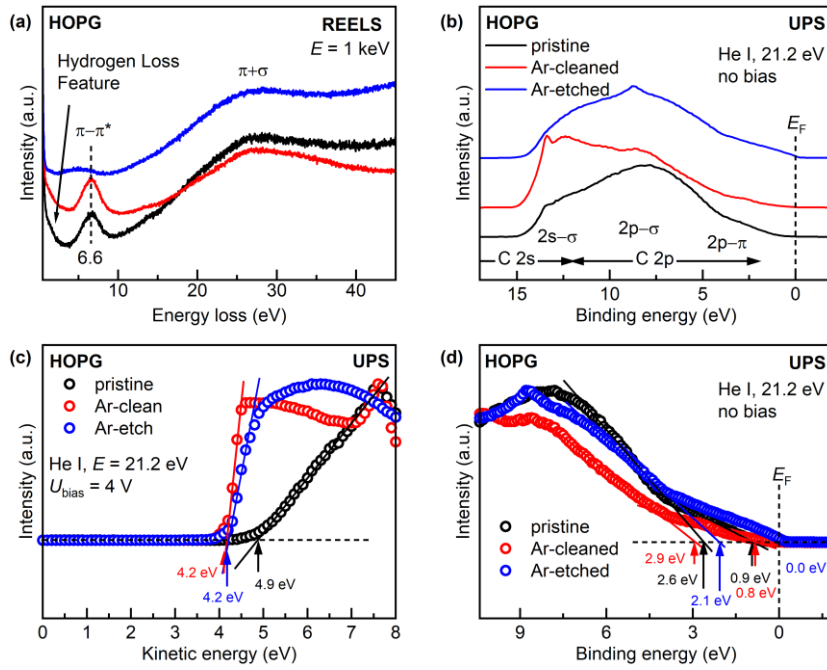


Figure S47. Electronic structure of oxidized, Ar-cleaned, and Ar-etched HOPG. (a) Integrity of the π -conjugated system analyzed by the $\pi-\pi^*$ transition in REELS, showing the difference between the intact system of pristine and cleaned HOPG compared with the vanishing signal for ion-bombarded HOPG. (b) DOS below the E_F probed by UPS to investigate the valence electrons of the C 2p and C 2s orbitals. (c) At an applied external bias, the cutoff energy of the valence electrons yields the WF. (d) Detailed investigation of the threshold energies close to E_F to determine the VBM of the $2p-\pi$ and $2p-\sigma$ electrons.

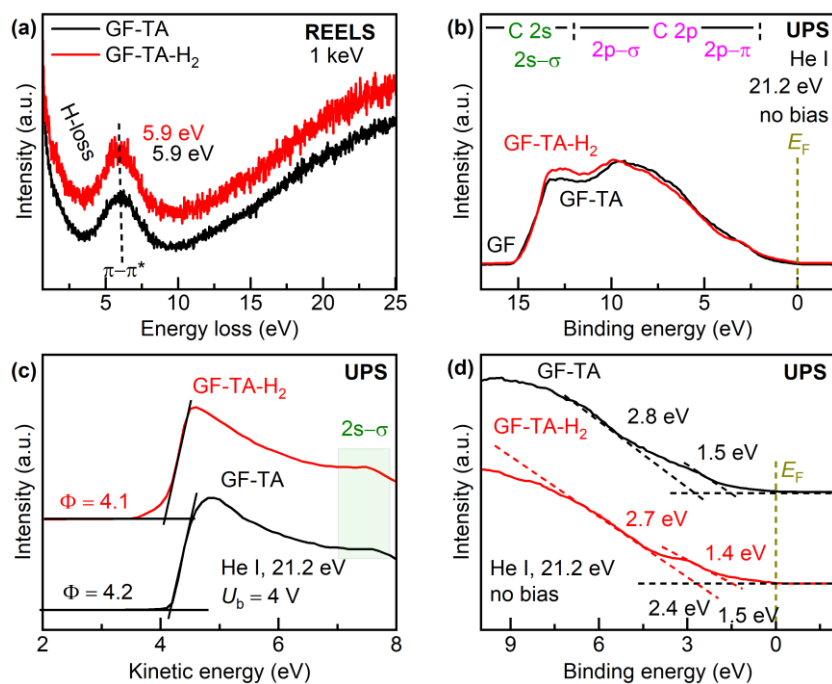


Figure S48. Electronic structure of GF-TA and GF-TA-H₂. (a) Integrity of the π -conjugated system analyzed by the π - π^* transition using REELS. (b) DOS below E_F probed by UPS to investigate the valence electrons of the C 2p and C 2s orbitals. (c) At an applied external bias, the cutoff energy of the valence electrons yields the WF. (d) Detailed investigation of the threshold energies close to E_F to determine the E_{VBM} of the $2p$ - π and $2p$ - σ electrons.

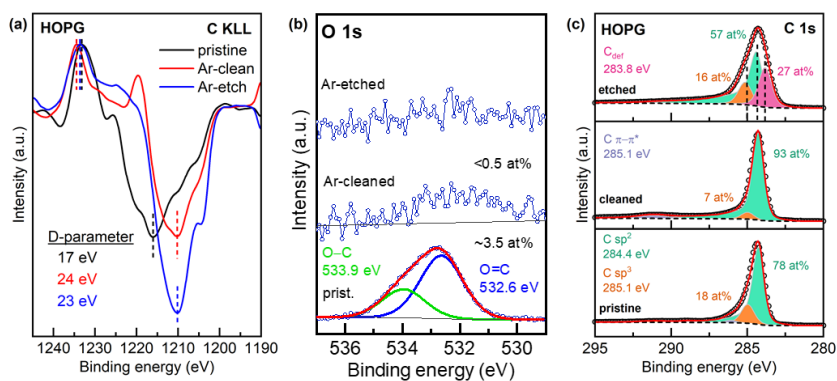


Figure S49. XPS of oxidized, Ar-cleaned, and Ar-etched HOPG. (a) Evaluation of the D-parameter shows a graphitic degree for cleaned and ion bombarded HOPG, but not the oxidized sample. (b) O 1s detail spectra to illustrate the removal of contamination after cleaning and bombarding. (c) C 1s detail spectra showing the ratio of sp^2 to sp^3 carbon, and the resulting signal for deficient carbon (C_{def}) after Ar-sputtering.

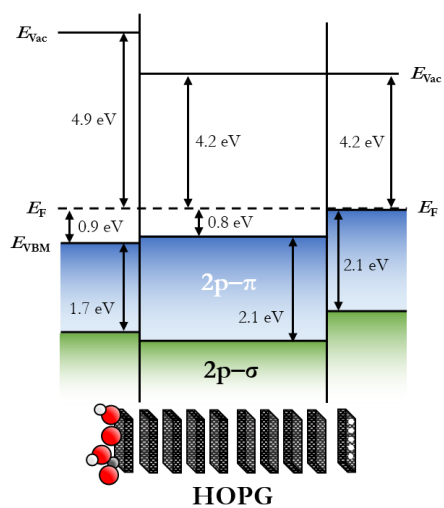


Figure S50. Band diagram of oxidized (left), Ar-cleaned (middle), and Ar-etched (right) HOPG.

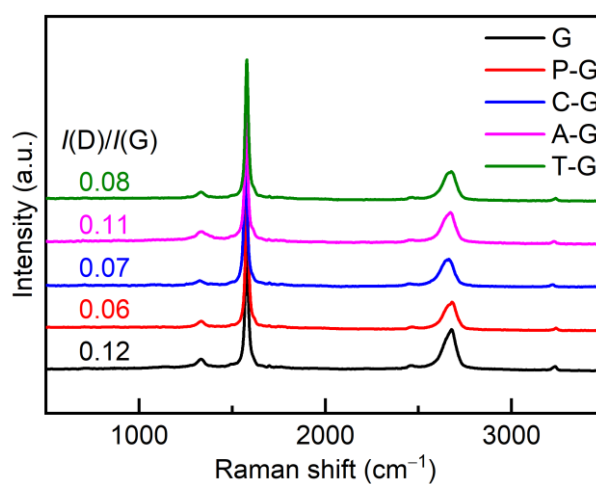


Figure S51. Raman spectra of pristine and PAH-modified graphene.

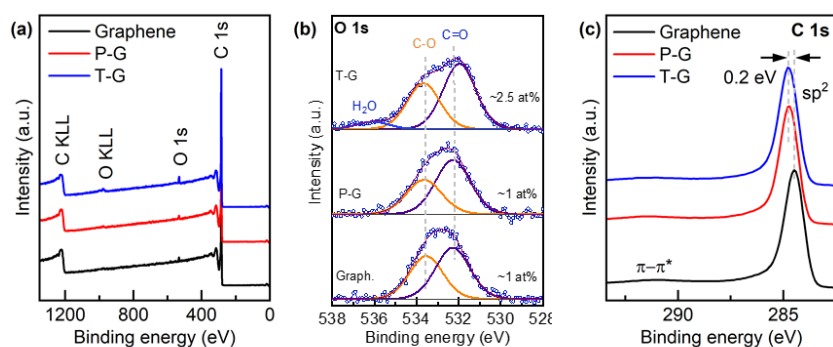


Figure S52. XP spectra of pristine and PAH-modified graphene. (a) Surveys, revealing that in both cases only carbon and oxygen are present. (b) O 1s detail spectra to illustrate the slight increase of surface oxidation for the more reactive zigzag edge sites. (c) C 1s detail spectra showing the peak shift of sp^2 hybridized carbon.

Table S4. Average distances (R in Å) and angles O-V-O (\angle in $^\circ$) for the first hydration shell of $[V^{II}(H_2O)_6]^{2+}$ and $[V^{III}(H_2O)_6]^{3+}$ compared to calculations and experimental data (XRD). The type of oxygen atom is specified according to its geometric position and coordination, where O_w describes the classification in a water molecule, “ax” denotes axial and “eq” equatorial (see Figure 9-1a).

Complex	$R(V-O_{w,ax/eq})$	$\angle(O_{w,ax}-V-O_{w,ax})$	$\angle(O_{w,ax/eq}-V-O_{w,eq})$
$[V^{II}(H_2O)_6]^{2+}$	2.19–2.20	179.6	89.7–90.3
Lit.	2.13–2.23	170.9–179.2	89.8–90.7
$[V^{III}(H_2O)_6]^{3+}$	2.19–2.21	179.5	89.7–90.2
Lit.	2.00–2.10	172.0	90.0–91.7

Table S5. Analogue to Table S4 for $[V^{IV}O(H_2O)_5]^{2+}$ (see Figure 9-1b).

Complex	$R(V-O_{ax})$	$R(V-O_{w,ax})$	$R(V-O_{w,eq})$	$\angle(O-V-O_{w,eq})$	$\angle(O_{w,ax}-V-O_{w,eq})$	$\angle(O_{w,eq}-V-O_{w,eq})$
$[V^{IV}O(H_2O)_5]^{2+}$	1.68	2.44	2.19/2.22	101.4/92.2	78.6/87.1	157.2/174.3
Lit.	1.57–1.72	2.20–2.36	2.03–2.12		97.4–98.0	169.6–174.2

Table S6. Analogue to Table S4 for $[V^VO_2(H_2O)_4]^+$ (see Figure 9-1c). Two values from equatorial water arise because of one O_w being next to and one O_w averse to O_{eq} .

Complex	$R(V-O_{ax})$	$R(V-O_{eq})$	$R(V-O_{w,ax})$	$R(V-O_{w,eq})$	$\angle(O_{ax}-V-O_{eq})$	$\angle(O_{ax}-V-O_{w,eq})$	$\angle(O_{w,ax}-V-O_{w,eq})$
$[V^VO_2(H_2O)_4]^+$	1.68	1.69	2.35	2.26/2.51	120	89.5/83.9	91.4/71.4
Lit.	1.61–1.73		2.22–2.32				

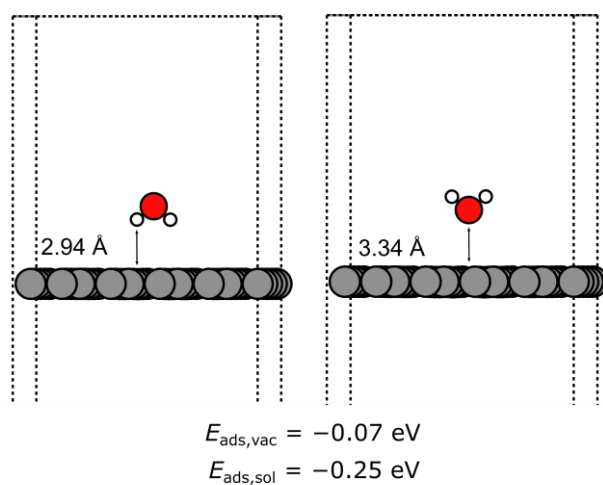
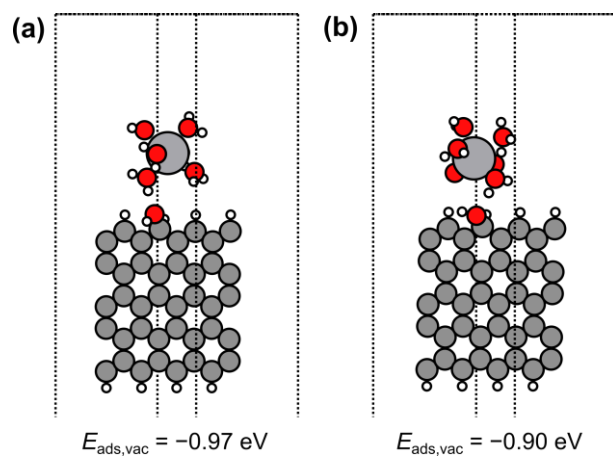


Figure S53. Relaxed structures of adsorbed water at the basal plane of graphene.

Figure S54. Relaxed structures of adsorbed (a) $[\text{V}^{\text{III}}(\text{H}_2\text{O})_6]^{3+}$ and (b) $[\text{V}^{\text{IV}}\text{O}(\text{H}_2\text{O})_5]^{2+}$ at HOH-terminated zigzag edges.

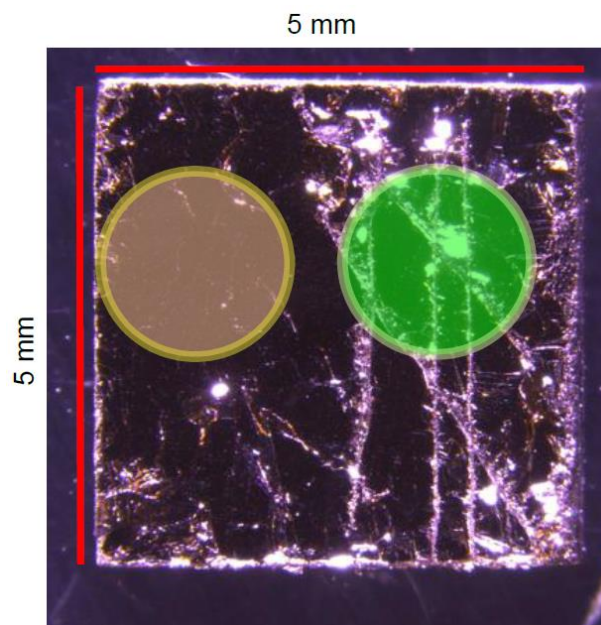


Figure S55. Optical microscope image of HOPG. Freshly cleaved (yellow) and scratched (green) regions are shown.

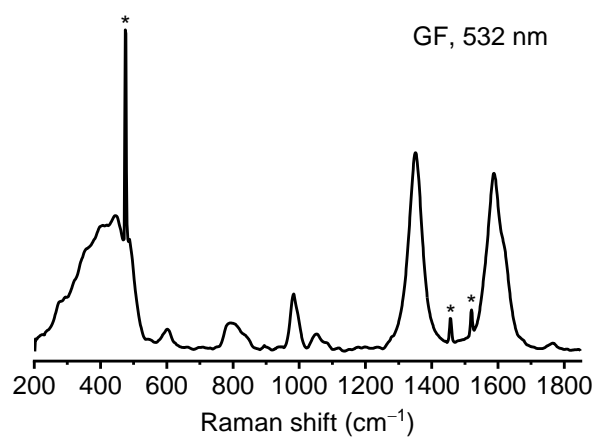


Figure S56. *Operando* Raman spectrum of GF displaying the complete range of acquisition using the green laser.

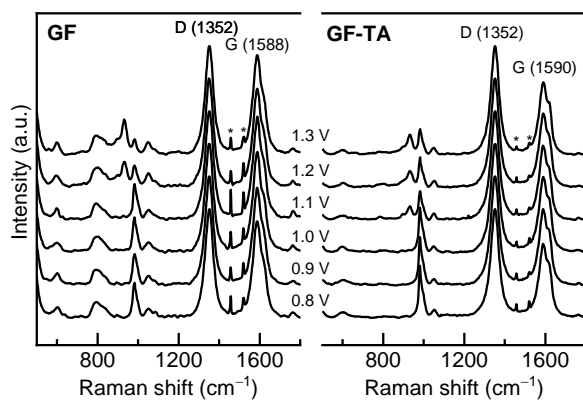


Figure S57. Stacked *operando* Raman spectra of (a) GF and (b) GF-TA recorded with a laser wavelength of 532 nm, showing an expanded range compared to Figure 10-3.

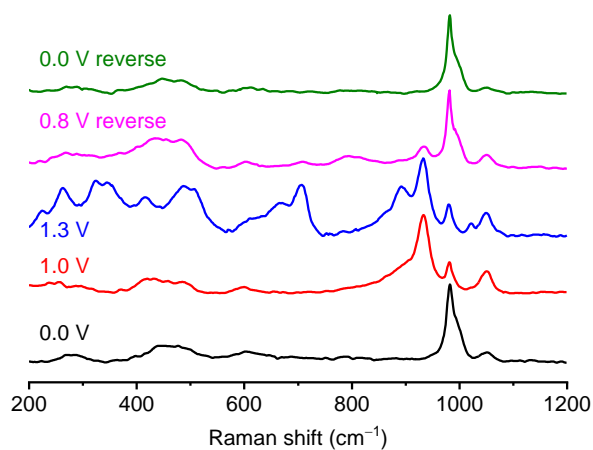


Figure S58. *Operando* Raman spectra of edge exposed HOPG, illustrating the reversibility of the pattern observed at 1.3 V vs. Ag/AgCl.

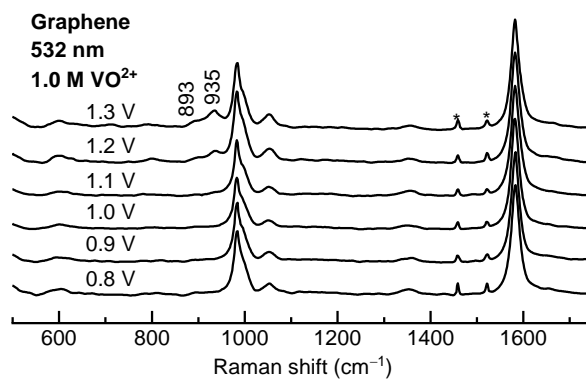


Figure S59. *Operando* Raman spectra of graphene using the green laser and high vanadium ion concentration.

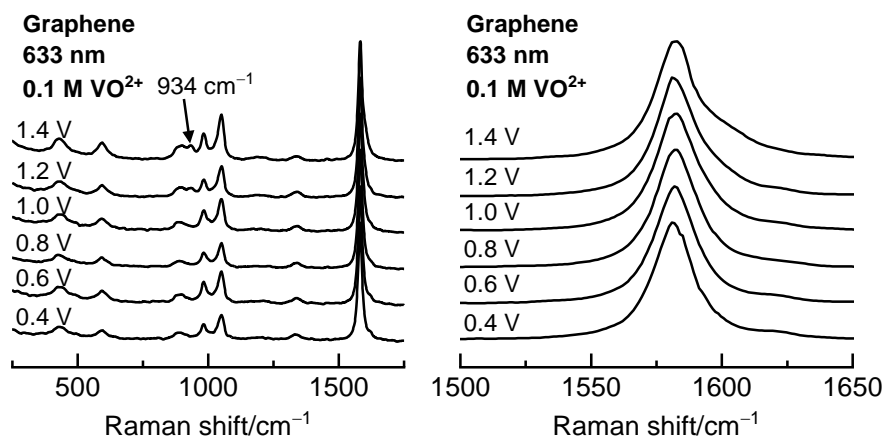


Figure S60. *Operando* Raman spectra of graphene using a red laser and low vanadium ion concentration.

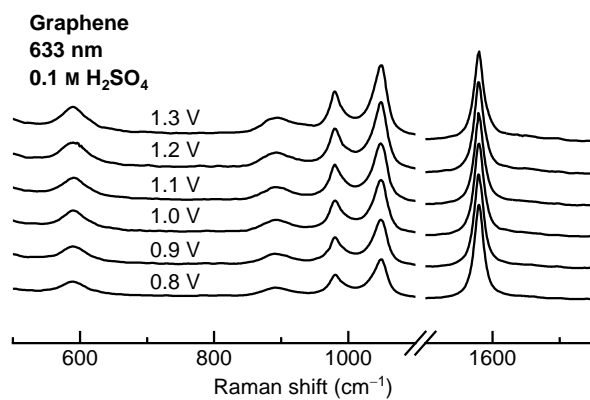


Figure S61. *Operando* Raman spectra of graphene using red laser and sulfuric acid as electrolyte.

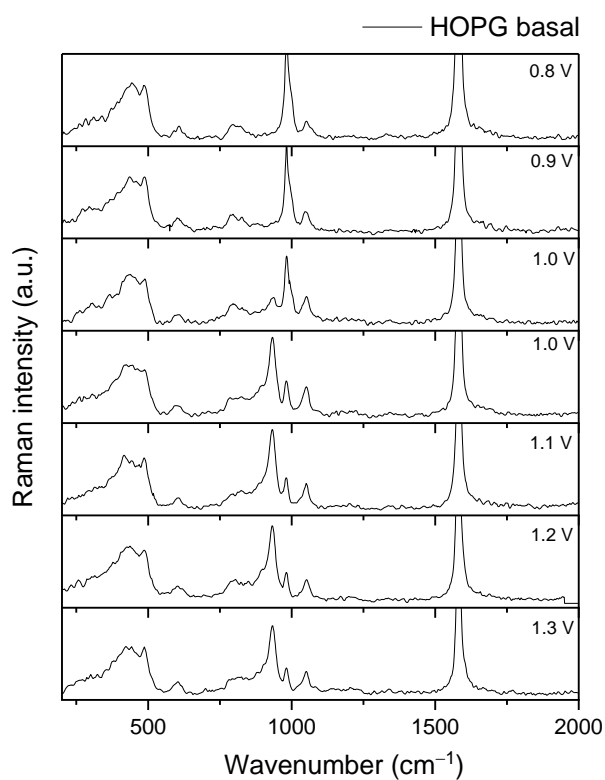


Figure S62. *Operando* Spectra of basal plane HOPG, measured using the 633 nm laser at a spot directly next to the active edge site.

Appendix C: List of Publications and Presentations

Peer-Reviewed Articles

- 10.) A. Lindner, **H. Radinger**, F. Scheiba, H. Ehrenberg, „Structure–activity correlation of thermally activated graphite electrodes for vanadium flow batteries”, *RSC Adv.* **2022**, *12*, 14119.
DOI: [10.1039/D2RA02368G](https://doi.org/10.1039/D2RA02368G)
- 9.) **H. Radinger**, V. Trouillet, F. Bauer, F. Scheiba, “Work Function Describes the Electrocatalytic Activity of Graphite for Vanadium Oxidation”, *ACS Catal.* **2022**, *12*, 6007.
DOI: [10.1021/acscatal.2c00334](https://doi.org/10.1021/acscatal.2c00334)
- 8.) **H. Radinger**, M. Hartmann, M. Ast, M. Bron, H. Ehrenberg, F. Scheiba, “Understanding the Properties for Efficient Phosphorus-doping of Graphite Electrodes in Vanadium Flow Batteries”, *Electrochim. Acta* **2022**, *409*, 139971.
DOI: [10.1016/j.electacta.2022.139971](https://doi.org/10.1016/j.electacta.2022.139971)
- 7.) M. Bauer, K. Pfeifer, X. Luo, **H. Radinger**, F. Scheiba, H. Ehrenberg, “Functionalization of Graphite Electrodes with Diazonium Salts for Lithium-Ion Batteries”, *ChemElectroChem*, **2021**.
DOI: [10.1002/celec.202101434](https://doi.org/10.1002/celec.202101434), Cover:
- 6.) **H. Radinger**, “2021: A Surface Odyssey. Role of Oxygen Functional Groups on Activated Carbon-Based Electrodes in Vanadium Flow Batteries”, *ChemPhysChem*, **2021**, *22*, 2498.
DOI: [10.1002/cphc.202100623](https://doi.org/10.1002/cphc.202100623)
- 5.) **H. Radinger**, P. Connor, S. Tengeler R. Stark, W. Jaegermann, B. Kaiser, “Importance of Nickel Oxide Lattice Defects for Efficient Oxygen Evolution Reaction”, *Chem. Mater.*, **2021**, *33*, 8259.
DOI: [10.1021/acs.chemmater.1c02406](https://doi.org/10.1021/acs.chemmater.1c02406)
- 4.) **H. Radinger**, A. Ghamlouche, H. Ehrenberg, F. Scheiba, “Origin of the Catalytic Activity at Graphite Electrodes in Vanadium Flow Batteries”, *J. Mater. Chem. A* **2021**, *9*, 18280.
DOI: [10.1039/D1TA04316A](https://doi.org/10.1039/D1TA04316A), Cover: [10.1039/D1TA90189C](https://doi.org/10.1039/D1TA90189C)
- 3.) **H. Radinger**, P. Connor, R. Stark, W. Jaegermann, B. Kaiser, “Manganese Oxide as an Inorganic Catalyst for the Oxygen Evolution Reaction Studied by X-Ray Photoelectron and Operando Raman Spectroscopy”, *ChemCatChem* **2021**, *13*, 1175.
DOI: [10.1002/cctc.202001756](https://doi.org/10.1002/cctc.202001756), Cover: [10.1002/cctc.202100028](https://doi.org/10.1002/cctc.202100028)
- 2.) **H. Radinger**, J. Pfisterer, F. Scheiba, H. Ehrenberg, “Influence and Electrochemical Stability of Oxygen Groups and Edge Sites in Vanadium Redox Reactions”, *ChemElectroChem* **2020**, *7*, 4745.
DOI: [10.1002/celec.202001387](https://doi.org/10.1002/celec.202001387)
- 1.) Poschmann, H. Groß, R. Amin, C. Fritsch, T. Dankwort, **H. Radinger**, S. Indris, L. Kienle, W. Bensch, “CuCo₂S₄ deposited on TiO₂: controlling the pH value boosts the photocatalytic hydrogen evolution”, *Eur. J. Inorg. Chem.* **2020**, *38*, 3692.
DOI: [10.1002/ejic.202000555](https://doi.org/10.1002/ejic.202000555)

Conference Paper

2.) **H. Radinger**, J. Pfisterer, F. Scheiba, H. Ehrenberg, "Surface and Activity Enhancement of Graphite Felt Electrodes", *The International Flow Battery Forum* **2021**.

1.) B. Kaiser, S. Tao, S. Wagner, **H. Radinger**, S. Tengeler, W. Jaegermann, "Nickeloxide Nanoparticles and Thin Films as Catalysts for (Photo-)Electrochemical Water Splitting: A Surface Science Study", *nanoGe Fall Meeting* **2018**.

DOI: [10.29363/nanoge.fallmeeting.2018.233](https://doi.org/10.29363/nanoge.fallmeeting.2018.233)

Oral Presentations

8.) **H. Radinger**, F. Scheiba, H. A. Hansen, H. Ehrenberg, "Surface Properties of Graphite for Electrocatalysis of Vanadium Redox Reactions", *241st Electrochemical Society Meeting* **2022**, Vancouver, Canada.

7.) **H. Radinger**, P. Connor, S. Tengeler, R. Stark, W. Jaegermann, B. Kaiser, „Transition Metal Oxides for the Oxygen Evolution Reaction Studied by X-ray Photoelectron and Operando Raman Spectroscopy", *European Materials Research Society* **2021**, virtual.

6.) **H. Radinger**, A. Lindner, F. Scheiba, H. Ehrenberg, "The Graphite–Electrolyte Interface in Vanadium Flow Batteries", *European Materials Research Society* **2021**, virtual.

5.) **H. Radinger**, A. Lindner, F. Scheiba, H. Ehrenberg, "The Graphite–Electrolyte Interface in Vanadium Flow Batteries", *GDCh Wissenschaftsforum Chemie* **2021**, virtual.

4.) **H. Radinger**, A. Ghamlouche, F. Scheiba, H. Ehrenberg, "Disproving the Electrocatalytic Role of Initial Oxygen Functional Groups in Comparison to Stable Defects on Graphite Electrodes in Vanadium Flow Batteries", *Materials Research Society* **2020**, virtual.

3.) **H. Radinger**, A. Ghamlouche, F. Scheiba, H. Ehrenberg, "Systematic analysis of oxygen functional groups and graphitic defects on vanadium flow battery electrodes", *Electrochemical Society PRiME* **2020**, virtual.

DOI: [10.1149/MA2020-02453753mtgabs](https://doi.org/10.1149/MA2020-02453753mtgabs)

2.) **H. Radinger**, P. Connor, S. Tengeler, W. Jaegermann, B. Kaiser, "Manganese Oxide OER Catalysts Investigated with X-Ray Photoelectron- and operando Raman Spectroscopy", *European Materials Research Society* **2019**, Nice, France.

1.) **H. Radinger**, F. Scheiba, H. Ehrenberg, "Conductive Carbon Coatings for Metal Bipolar Plates", *German Israeli Battery School* **2019**, Berlin, Germany.

Poster Presentations

3.) **H. Radinger**, J. Pfisterer, F. Scheiba, H. Ehrenberg, "Surface and Activity Enhancement of Graphite Felt Electrodes", *The International Flow Battery Forum* **2021**, virtual.

2.) **H. Radinger**, F. Scheiba, H. Ehrenberg, "A Computer-Aided Design Approach for the Characterization of Bipolar Plates for Vanadium Flow Batteries", *3. Flow Battery Colloquium* **2019**, Karlsruhe, Germany.

1.) **H. Radinger**, P. Connor, S. Tengeler, B. Kaiser, W. Jaegermann, “Molybdenum-doping of Magnetron Sputtered Manganese Oxide Catalysts for Water Splitting Applications”, *International School of Materials for Sustainable Development and Energy* **2018**, Erice, Italy